CORTICAL REPRESENTATION OF TOUCH:
FROM WHOLE CELL RECORDINGS TO NETWORK SIMULATIONS IN SILICO

Chao Huang

Cortical Representation of Touch:

from Whole Cell Recordings to Network Simulations *in silico*

Proefschrift

ter verkrijging van de graad van doctor
aan de Radboud Universiteit Nijmegen
op gezag van de rector magnificus,
volgens besluit van het college van decanen
in het openbaar te verdedigen op dinsdag 26 april 2016
om 16.30 uur precies

door

Chao Huang
Geboren op 20 november 1984
te Yunnan, China

Promotor:

Prof. dr. T. Celikel

Copromotor:

Dr. B. Englitz

Manuscriptcommissie:

Prof. dr. P. H. E. Tiesinga

Prof. dr. H. Mansvelder (VU University)

Dr. R. Petersen (The University of Manchester, Verenigd Koninkrijk)

Cortical Representation of Touch:

from Whole Cell Recordings to Network Simulations *in silico*

Doctoral Thesis

to obtain the degree of doctor
from Radboud University Nijmegen
on the authority of the Rector Magnificus,
according to the decision of the Council of Deans
to be defended in public on Tuesday April 26, 2016
at 16.30 hours

by

Chao Huang
Born on November 20, 1984
in Yunnan, China

Supervisor:

Prof. dr. T. Celikel

Co-supervisor:

Dr. B. Englitz

Manuscript Committee:

Prof. dr. P. H. E. Tiesinga

Prof. dr. H. Mansvelder (VU University)

Dr. R. Petersen (The University of Manchester, U. K.)

TABLE OF CONTENTS

Chapter 1. INTRODUCTION

The principal function of a neuron is to process and communicate information. To achieve this function each neuron integrates information across thousands of synaptic inputs. The information that originates from the presynaptic pool of neurons (or “senders” as commonly called in the field of communication theory) is communicated in the form of action potentials (e.g. “messages”), and targets postsynaptic neurons (i.e. receivers).

A mechanistic understanding of neural information processing requires quantification of the spatio-temporal distribution of synaptic inputs, as synaptic inputs are summed across dendrites and the soma of the postsynaptic neurons, as well as the information communicated with the downstream neurons through action potentials. In the neocortex, due to the fact that each neuron communicates monosynaptically with a few thousand presynaptic partners, often across different brain regions (DeFelipe & Farinas 1992), it has traditionally been difficult to address the nature of information processing, information transfer and information recovery systematically.

Sensory systems offer unique opportunities to study information processing in neural circuits; If the primary function of the sensory circuit is to faithfully and reliably represent the environment, a substantial part of the sensory information in the periphery should be represented throughout the sensory circuits in the form of neural signals. Furthermore, since sensory systems are commonly organized in the form of topographical maps, where sensory receptors in the periphery are represented by topographically organized groups of neurons along the sensory axis, at least part of the sensory information is spatially filtered by the structural organization of the sensory nuclei. In the visual system, for example, projections of the retina ganglion cells target the primary visual cortex (V1), via the lateral geniculate nucleus, in an orderly fashion such that adjacent spots on the retina are represented by adjacent neurons in the lateral geniculate nucleus and the primary visual cortex, forming the retinotopic map. Similar types of topographic maps can be found in the auditory and somatosensory system, where adjacent neurons represent sensory receptors located adjacently along the length of the cochlea or the body, respectively. The most prominent example of such sensory maps is found in the whisker system of rodents, where facial whiskers on the snout are represented as topographical maps along the brainstem, thalamus and cortex. This structured organization between the sensory receptors in the periphery and the neurons in the central nervous system allows precise mapping of the origins of the sensory information each neuron receives, as well as the nature of the information. Taking advantage of this organizational principle of the whisker system, I here study the fundamental mechanisms of information processing, while systematically quantifying the information existing along different stages of the neural networks using experimental and computational methods.

Recording neural activity

Despite the recent advances in optical imaging of neural activity (Denk et al 1990, 1994, Komai et al 2006, Hillman 2007, Grienberger & Konnerth 2012, Andermann et al 2013, Badura et al 2014), the gold standard in analysis of neural activity is the electrical recordings of neural responses. The voltage signal across the membrane of a neuron can be measured with intracellular recording techniques, i.e. sharp electrodes or whole-cell patch clamp recordings. The signal naturally includes both the subthreshold (postsynaptic potentials, PSPs) and suprathreshold (i.e. action potential or spikes) responses. While quantitative analysis of the synaptic inputs onto a postsynaptic neuron can be performed by studying the PSP, statistics of the action potentials in respect to the stimulus determine the information that each neuron transfers to its postsynaptic partners. The recorded neuron can further be identified by morphological reconstructions based on dye filling (Snow et al 1976, Somogyi & Soltesz 1986, Brecht et al 2003, de Kock et al 2007, Fino & Yuste 2011, Oberlaender et al 2012, and molecularly characterized using single-cell RT-PCR(Porter et al 1998, Wang et al 2004). When combined with cell-targeted expression of fluorescent proteins, single cell whole-cell recordings can also be performed in a cell-type specific manner (Komai et al 2006). Because the intracellular environment of the recorded cell is accessible through the recording pipette, the cell can be independently manipulated pharmacologically and/or electrophysiologically without significantly affecting the local network activity (Brecht 2004).

Traditionally, it is difficult to establish and maintain stable current and voltage clamp under in *vivo* conditions, especially in awake, behaving animals. Recent developments in miniaturized implantable amplifiers (Lee et al 2006) and the adoption of head restrained protocols (Petersen et al 2003, Lefort et al 2009, O’Connor et al 2010, Crochet et al 2011, Atallah et al 2012, Li et al 2015) now enable the intracellular recording in awake behaving animals, gaining valuable insight on how behaviour-relevant information is processed at both subthreshold and suprathreshold levels in a single neuron. However, because the recording duration is often too short to characterize neural responses against a large library of stimuli, and the membrane state undergoes modulated changes across different behavioral and attentional states, the use of *in vivo* chronic recordings for the analysis of neural information processing is limited to anesthesized preparations.

The electrical activity generated by the neurons can also be measured extracellularly with one or several electrodes inserted into the brain of a living animal and placed close to neurons of interest. If the impedance of the electrode is high enough, spikes emitted from different neurons can be isolated. Compared to the intracellular recording techniques mentioned above, the extracellular recordings are technically simpler, mechanically more stable and can be relatively easily employed in freely behaving animals to study the target group of neurons for extended periods. In fact, this technique has been and will continue to be the dominant technique in the field of system and cognitive neuroscience, and several key findings, including the discovery of visual neuron receptive field (Hubel & Wiesel 1962), hippocampal place cells (O'Keefe & Dostrovsky 1971), have been described using extracellular recordings of the neural responses. Due to the extracellular sampling of the electrical activity, however, recordings with extracellular electrodes only allow isolation of neuronal signals by the frequency component of the signal while separating local field potentials (LFP) from action potentials (AP). Hence, extracellular recordings could provide information transmitted via action potentials without attributing to the information that is received by a given neuron.

Growing evidence suggests that sensory neurons represent information using sparse coding (for reviews see Olshausen & Field 2004, Barth & Poulet 2012, Petersen & Crochet 2013) as such a small subgroup of highly active neurons in a majority of less active cells encode sensory stimuli (de Kock et al 2007, O'Connor et al 2010, Yassin et al 2010, Crochet et al 2011). The extracellular recording techniques is more likely to identify these highly active neurons while ignoring less active ones (Hromadka et al 2008, see Shoham et al 2006 for discussion), resulting in overestimation of average firing rates, skewing the information content of the neural representations.

A key difference between the LFP and AP is that the LFP reflects the summation of electrical activity of neurons located within a few hundred microns to a few millimeters around the electrode (Katzner et al 2009, Pesaran 2009, see Einevoll et al 2013 for review), while APs represent the spiking activity of local neurons. The majority of the LFP signal (the power spectrum of LFPs usually exhibits $1/f$ frequency scaling) is thought to be generated by synchronized synaptic currents arising on cortical neurons (Einevoll et al 2013). Accordingly, simultaneously recorded single neuron membrane potentials in most cortical neurons and LFPs from adjacent electrode demonstrate a close correspondence (Poulet & Petersen, 2008)

The power spectrum of the LFPs is also strongly modulated by behavioral states (e.g. awake vs. anesthetized, attention etc.) since the correlation pattern of synaptic inputs is dependent on behavioral states, making the LFP signals a good indicator of the states of the experimental subjects. However, it should be noted that other sources, which includes calcium spikes, after-spike hyperpolarization and glial cells, can also contribute to LFPs, though mainly in the low-frequency range (Einevoll et al 2013). As a result, the LFPs are inherently ambiguous and difficult to interpret compared to spikes or subthreshold membrane potentials. However, the LFP signals are readily available in many experimental protocols ranging from glass pipette recordings to multi-electrode arrays and can be measured simultaneously with single unit activities, while providing unique information about the key integrative synaptic activities that cannot be gathered by observing spiking activity alone (Belitski et al 2008, Einevoll et al 2013, Panzeri et al 2015).

Neural coding: Single neuron’s perspective

Every neuron integrates spatio-temporally distributed, presynaptic activity patterns in its soma as PSPs and eventually generates APs. The information in the presynaptic activity patterns can be studied by observing the membrane potential dynamics and the spiking activities of the neuron, respectively. Traditionally most experimental research has focused on action potentials due to experimental limitations (see above).

Experiments on early sensory cortices have found that sensory evoked spiking activity in excitatory neuron population is generally low, especially in superficial layers (L2/3), a phenomenon believed to be an indication of sparse coding (see e,g, Olshausen & Field 2004, Barth & Poulet 2012, Petersen & Crochet 2013 for in-depth reviews). In the barrel cortex of rodents for example stimulating a single whisker under anesthesia generates only 0.1-0.3 action potentials/trial in a Layer (L)4 neuron of the corresponding principal barrel column (Brecht & Sakmann 2002, Brecht et al 2003, Celikel et al 2004). The sparseness of the evoked representations is preserved in L2/3. The deflection of the principal whisker evokes 0.03-0.2 spikes/stimulus (Brecht et al 2003, Celikel et al 2004), independent from the recording method or the experimental condition studied (Allen et al 2003, Celikel et al 2004, de Kock et al 2007, Kerr et al 2007, O’Connor et al 2010, Crochet et al 2011). Stimulation of the principal whisker almost always elicits the strongest response, while the representation of surround whiskers is often weak and unreliable (Brecht et al 2003, Manns et al 2004). In agreement with these observations, information theoretic analysis has found that information carried by single neurons’ spikes about stimulus location (i.e. which whisker is stimulated) is low (Petersen et al 2001, Panzeri et al 2001), since only the response to principal whisker stimulation is (relatively) reliable. The neurons located in deeper layers generally show higher levels of spontaneous and evoked activity, however the median of sensory evoked response is still lower than 1 spikes/stimulus (Manns et al 2004, de Kock 2007, O’Connor et al 2010). This coding principle is not specific to the barrel cortex. Neurons in the primary auditory (DeWeese et al 2003, Hromadka et al 2008), primary visual (Vinje & Gallant 2003, Greenberg et al 2008, Willmore et al 2011), olfactory (Poo & Isaacson 2009, Stettler and Axel 2009) and gustatory (Chen et al 2011) cortices display similar sparse response properties, suggesting that sparse coding is a general principle employed in sensory processing throughout the sensory pathways (Barlow 1972, Olshausen & Field 2004). Conversely, sparse coding principles have been demonstrated to impose neural filter properties consistent with the naturally observed ones (Olshausen & Field 1996, Lewicki 2002, Smith & Lewicki 2006)

Interestingly, while the overwhelming proportion of the population activity is sparse, there exists a small population of neurons that are highly active under the experimental condition - they fire reliably when the stimulus is delivered, and usually fire more than one action potentials (de Kock et al 2007, O'Connor et al 2010, Yassin et al 2010, Crochet et al 2011). Multiple mechanisms could underlie this highly active neuron population (Barth & Poulet 2012). They are possibly strongly wired into the neural circuit (Lefort et al 2009, O'Connor et al 2010), receiving stronger excitatory (or weaker inhibitory) drive compared to surrounding weakly active cells. The neuronal intrinsic properties could further shape the probability of spiking (Conners et al 1982, Nowak et al 2003). One important question remains is that whether these highly active neurons are sharply tuned for certain stimuli under specific context, or they represent a subgroup of broadly tuned, unselective neurons.

Since the discovery of receptive fields in the visual system (Hubel & Wiesel 1962), the selectivity of cortical neurons in primary sensory cortices has been well documented. Recent experimental evidence also argues that in the visual (Ohki et al 2005, Willmore et al 2011), somatosensory (Andermann & Moore 2006, Ramirez et al 2014) and auditory (Rothschild et al 2010) cortices neurons display a even a higher degree of stimulus selectivity, in particular when they are studied using complex otherwise naturalistic stimuli (Vinje & Gallant 2000, 2002, Ramirez et al 2014) or under specific behavior context (O'Connor et al 2010). On the other hand, some studies have reported highly active neurons with broad receptive field, which contain high amount of sensory information (Foffani et al 2008, Ince et al 2013), although in these studies the type of the neurons (excitatory vs inhibitory) investigated is ambiguous. In summary, the observed highly active neuron population could be a mixture of neurons that are highly selective to a specific stimulus tested under a given behavioral context as well as neurons that are broadly tuned.

From the information encoding perspective, high (and heterogeneous) stimulus selectivity of neuronal spiking representations suggests that different neurons encode distinct stimulus information that complements each other. Thus, pooling spiking response from a heterogeneous population ('population code') can often steadily increase the information about the stimulus depending on the pooled population size. In addition, the correlation structure between individual neurons could significantly affect the population encoding (see Averbeck et al 2006 for review). The heterogeneity of stimulus selectivity also suggests that during the decoding process preserving the identities of pooled neuron population could maximize the information encoded in populations (Ince et al 2013). However, the heterogeneity of response strength implies that the amount of information carried by different neurons would differ significantly as highly active neurons, despite being out-numbered by sparsely active neurons, encode the majority of information in the population in any given trial (Ince et al 2013). This is consistent with the observation that in many behavioral experiments the spiking response from only a small number of highly active cells can accurately predict the animal's behavior (Stuttgen & Schwarz 2008, O’Connor et al 2010, Niessing & Friedrich 2010, Mayrhofer et al 2015, Peron et al 2015).

Intracellular information transfer

While most sensory neurons have sparse suprathreshold representations, they have reliable and broadly tuned subthreshold representations. In the barrel cortex of anesthetized rodents, over 90% of neurons that exhibit subthreshold depolarization upon principal whisker stimulation also responds to stimulation of more than 8 other surrounding whiskers (Brecht et al 2003). Experiments performed in different sensory modalities across animal states and behavior context show similarly broad subthreshold receptive fields with monosynaptic PSP amplitudes ranging over 2-8 mV per stimulus (Carandini & Ferster 2000, Volgushev et al 2000, Tan et al 2004, Crochet et al 2011). The broad and efficacious subthreshold representation is in sharp contrast to the sparse and often unreliable representation at the suprathreshold level, and is consistent with wide-spread and numerous synaptic connections cortical neurons receive (Bruno & Sakmann 2006). As a consequence, information represented in the subthreshold activity could be much richer compared with those represented in spikes (de Ruyter van Steveninck & Laughlin 1996, Dhingra & Smith 2004). This information in the subthreshold response could propagate through the network even in the absence of spiking as changes in membrane potential is passed onto neighbouring cells via gap junctions (Galarreta & Hestrin 2001) and/or by tonically active, membrane potential modulated neurotransmitter release (Rien et al 2011). And finally, subthreshold signals, especially those generated by mass population activity that is often measured by LPFs, can capture information about intrinsically driven state changes that cannot be inferred from spiking activity of a few neurons (Einevoll et al 2013).

The subthreshold responses can be thought as the somatic aggregate of the synaptic information neurons receive (however the input might have been filtered through the non-linear dendritic computation mechanisms – Mel 1993, London & Häusser 2005, Brunel et al 2014) while spikes carry the information each neuron transmits to its postsynaptic partners; Thus an analytical comparison between the two provides a quantitative description of the intracellular information transfer (see Chapter 5 of this thesis).

It has long been speculated that sensory neurons preferentially transmit those messages (spikes) that carry unique information to reduce the redundancy in the transmitted information while increasing the channel capacity (Attneave 1954, Barlow 1961). Following this argument, if neurons represent redundant information in their subthreshold responses, they should not transmit all the available information to their postsynaptic partners. The nature of transmitted information could depend on the computation performed by the postsynaptic partners (Felleman & Essen 1991). The excitatory neuron population in L2/3 of rodent barrel cortex contains two intermingled subpopulations that specifically target the secondary somatosensory cortex (S2) or the primary motor cortex (M1) (Chen et al 2013, Yamashita et al 2013). When the animal is actively using its whiskers to palpate an object, the whisker contacts are reliably (but differently) represented in the subthreshold response of both neuronal subpopulations. During an episode of repetitive whisker contacts, while M1-projection neurons only spike transiently after the first contact, S2-projection neurons generate spikes (relatively) robustly to each whisker contact (Yamashita et al 2013). Discrimination analysis further indicates that spikes from M1-projection neurons contain more information about the presence of the stimulus, while spikes from S2-projections neurons contain more information about stimulus features (Chen et al 2013).

What are the neural mechanisms that transform the strong and broadly tuned subthreshold representation into the sparse and selective spiking representation? Inhibition plays an important role in shaping sensory responses of cortical neurons by suppressing the activity of excitatory neurons. Sensory stimulation evokes precisely timed excitatory and inhibitory drives onto cortical excitatory neurons, with inhibition usually being stronger and slightly delayed compared to excitation, which allows a short window of opportunity during which the excitatory drives can summate and drive spiking activity (Gabernet et al 2005, Okun & Lampl 2008). The exact temporal shifts between excitation and inhibition vary across different sensory modalities, ranging from ~ 1ms in somatosensory cortex (Gabernet et al 2005) to ~1-4 ms in auditory cortex (Wehr & Zador 2003), ~10 ms in olfactory cortex (Poo & Isaacson 2009), and longer in visual cortex (Hirsch et al 1998). Comparing inhibitory and excitatory receptive fields in the same neuron generally shows that the tuning of inhibitory inputs are either matched (Zhang et al 2003, Wehr & Zador 2003, Okun & Lampl 2008) or more broadly tuned (Poo & Isaacson 2009, Liu et al 2011). Furthermore, a few simultaneously activated excitatory neurons could induce strong and widespread inhibition on the neural network (Kapfer et al 2007). The sensory evoked inhibition that is strong, widespread and tightly coupled with excitation serves many functions, which include controlling precise timing of response (Wehr & Zador 2003, Gabernet et al 2005, Okun & Lampl 2008), preventing runaway excitation (Kapfer et al 2007), sharpen stimulus selectivity (Zhang et al 2003, Poo & Isaacson 2009, Liu et al 2011), and overall increasing the sparseness of sensory response (Haider et al 2013).

The spike threshold can also transform broadly tuned subthreshold response into sparse and more selective spike response through the so-called ‘iceberg’ effect (Rose & Blakemore 1974): since the membrane potential is usually well below the spike threshold, only sufficiently large excitatory input can drive the membrane potential to reach spike threshold for spike generation, thus generating more sharply tuned spiking response compared to the subthreshold response. The spike threshold and the inhibition work synergistically, with inhibition that is tightly coupled to excitation suppresses sensory evoked response to mostly below spike threshold, thus spikes are only sparsely generated (de la Rocha et al. Science 2010). Indeed, whole-cell recording in head restrained behaving mice has shown that whisker contact reliably drives the neuronal membrane potential to a fixed value, which is independent of pre-contact membrane potential, below spike threshold in most excitatory neurons. Only in a small fraction (~10%) of excitatory neurons the contact induced a membrane potential response which is on average above the spike threshold, and these neurons fire reliably (Crochet et al 2011). Inhibition that is more broadly tuned compared with excitation can further sharpen the neuronal selectivity (Zhang et al 2003, Poo & Isaacson 2009, Liu et al 2011). Interestingly, the spike threshold is not fixed but rather depends on the temporal profile of the membrane depolarization, such that fast depolarizations produce spikes at lower thresholds, and slower depolarizations at higher thresholds (Azouz & Gray 2000, Azouz & Gray 2003, De Polavieja et al 2005, Wilent & Contreras 2005, Goldberg et al 2008, Fontaine et al 2014). This type of spike threshold adaptation effectively reduces the membrane time constant, making the neuron more likely to spike in response to synchronized inputs (Fontaine et al 2014). The effect of an adaptive spike threshold on neuronal information processing will be analyzed in Chapter 4 of this thesis.

Cell type specific neural representations

It is widely speculated that around 20% of all neocortical neurons are inhibitory (see Markram et al 2004, Ascoli et al 2008); although recent studies (Meyer et al 2011), including the data presented in Chapter 3 of this thesis suggest that inhibitory neuron density is only ~12% in the barrel cortex. The interneuron population shows a striking diversity in terms of their electrophysiological, biochemical and morphological properties (see Markram et al 2004). Based on the immunoreactivity to parvalbumin (PV), somatostatin (SST) and the ionotropic serotonin receptor subunit 5-HT$_{3A}$R, neocortical interneurons can be separated into three largely non-overlapping groups (Lee et al 2010). In L2/3, the 5-HT$_{3A}$R+ cells account for ~50% of the total interneuron population, and generally have broad action potential waveform with adapting firing patterns. They can be further divided into at least 4 subgroups: 1) the neuroglia cells (Tamas et al 2003, Olah et al 2009, Wozny & Williams 2011), which mediate slow inhibition via volume transmission and can be identified by co-immunostaining with alpha-Actin-2 (Tamas et al 2003); 2) Calretinin (CR)+/ vasoactive intestinal polypeptide (VIP)+ multipolar cells (Caputi et al 2009) with regular firing pattern, 3) CR+ bipolar cells (Caputi et al 2009, Xu et al 2006) with bursting firing pattern and 4) VIP+/CR- bipolar cells (Porter et al 1998) which also show bursting firing pattern. These groups of interneurons preferentially inhibit other interneurons.

PV+ interneurons account for an additional ~30% of the L2/3 interneuron population, and can be further divided into 3 subgroups: 1) fast-spiking (FS) basket cells which preferentially target the soma or the proximal dendrites of pyramidal neurons. They are densely and reciprocally connected to nearby pyramidal cells (Holmgren et al 2003, Packer & Yuste 2011). FS PV+ interneurons in L4 of the rodent barrel cortex can be further divided into three clusters based on differential axonal projection patterns (Koelbl et al 2015). 2) bursting basket cells which are less densely connected in the network but innervate PV+ FS cells, hence suppressing their inhibitory drive in the network (Blatow et al 2003). 3) FS chandelier cells, which specifically target the axon initial segment (Zhu et al 2004, Taniguchi et al 2013).

The remaining ~20% of interneuron are SST+ Martinotti cells (Wang et al 2004), which innervate distal dendrites of pyramidal neurons. They are densely connected with the pyramidal neurons in the local network (Fino & Yuste 2011) and receive facilitating input from pyramidal neurons (Kapfer et al 2007) and little inputs from L4 excitatory neurons (Helmstaedter et al 2008).

The different types of interneurons tend to form gap junctions (preferentially) with other interneurons belonging to the same group but not with different types, as such bursting PV+ cells form gap junctions with other bursting PV+ cells but not with FS PV+ cells (Blatow et al 2003). The connectivity as well as synaptic properties between different types of interneurons also appears to be cell type-specific. In the mouse visual cortex, for example, PV+ cells strongly innervate each other as well as the pyramidal neurons but provide little inhibition to other groups of interneurons. SST+ cells, on the other hand, do not innervate other SST+ cells, but provide inhibition to all other types of interneurons (Pfeffer et al 2013). The short-term synaptic dynamics has also been shown to be cell-type specific (Gupta et al 2000).

Compared to pyramidal neurons, and with the exception of SST+ cells, interneurons receive stronger and larger number of feed-forward excitation (Helmstaedter et al 2008). The recurrent excitation onto interneurons is also stronger compared to those made onto excitatory neurons (Holmgren et al 2003, Avermann et al 2011). Consistent with these connectivity features, both spontaneous and sensory evoked spiking activity is much higher in interneurons (Swadlow 1989, Gentet et al 2010, Hofer et al 2011). SST+ interneurons’ encoding of touch is the exception to this norm, as they are inhibited by the whisker contact (Gentet et al 2010).

The stimulus selectivity of excitatory neurons is maintained in part by network motifs. The visual cortical excitatory neurons form non-random sub-networks such that neurons selective to the same stimulus features are more likely to connect with each other (Ko et al 2011). This type of functionally specific connectivity pattern is largely absent at least in the PV+ interneuron populations, and experimental evidence suggests that the spiking responses in interneurons are less selective or more broadly tuned (Swadlow 1989, Bruno & Simons 2002, Sohya et al 2007, Wu et al 2008, Liu et al 2009, Hofer et al 2011, but also see Runyan et al 2010), and can be approximated by the average tuning of adjacent excitatory neurons (Kerlin et al 2010).

In summary, compared with excitatory neurons, sensory evoked spiking activity in interneurons are dense (as opposed to sparse), more reliable and less selective. This difference is partially due to higher excitability in interneurons, as some interneuron population has the same level of subthreshold tuning compared with excitatory neurons (Bruno & Simons 2002, Cardin et al 2007, Wu et al 2008, Nowak et al 2008). However it is important to note that there is a wide distribution of firing rate and stimulus selectivity in each group of interneuron population, just like in the excitatory neural population. PV+ interneurons generally show strong, unselective and short latency response, whereas in visual cortex SST+ interneurons show weak, more selective and delayed response (Ma et al 2010), while in barrel cortex they are inhibited by whisker contacts (Gentet et al 2012).

Excitatory and inhibitory neurons could encode different features of the stimulus in their spiking activity. With their high excitability, high sensitivity, broad tuning, short onset latency and reliable and highly synchronized (Swadlow 2003) stimulus evoked firing, FS PV+ interneurons could reliably encode stimulus onset, whereas the sparse and temporally distributed excitatory neurons' spikes could encode finer features about the stimulus (see Conclusions). The high firing rates of interneurons could also suggest that they might preferentially employ rate coding. Most decoding analyses based on ideal observers assume that the decoder has the knowledge of stimulus onset timing, whereas in real neural networks it is not trivial for the postsynaptic neurons to access such information. It has been proposed that the peak of the population activity could be potentially used as a temporal reference for decoding (Panzeri & Diamond 2010); however given the response properties outlined above of FS PV+ interneurons could be a better temporal reference for decoders in biological networks or *in silico*.

The focus of the thesis

Despite our ever-increasing understanding of the rules of communication in neural circuits, the anatomical complexity of the circuits and the lack of analytical insight into the intracellular information transfer delay the progress in providing a mechanistic description of sensory processing in the brain. Thus, in this thesis, I will experimentally study and computationally address the nature of intra- and inter-neuronal information transfer along the somatosensory axis to mechanistically determine how information is aggregated, transferred and recovered in sensory circuits.

The thesis consists of six chapters, including this introductory chapter. **Chapter 2** describes a simple optical design for the visualization of cortical representation of touch in single trial resolution. Furthermore, by taking advantage of the spontaneous oscillations in the blood-flow, we derive novel algorithms that enable structural mapping of the neurovasculature during functional imaging experiments. We finally combine these developments to show how to map cortical representation of touch even though stimulus representation might be confounded by neurovasculature. This approach is then utilized in the subsequent chapters for mapping the barrel cortex prior to *in vivo* experiments.

With six cortical layers and ~12000 neurons in a cortical column, each whisker touch recruits complex circuits spanning multiple columns. **Chapter 3** aims to build a computational model of the somatosensory cortex to ultimately reduce the dimensionality in this network, provide a test-bed for the empirical studies and develop a biologically realistic network structure for computational studies. To achieve these goals in this chapter we first describe how to reconstruct the somatosensory cortex in soma resolution by combining multi-channel (i.e. triple or quadruple) immunohistochemistry with serial mosaic scanning confocal microscopy. With this accurate information on the node of the network and the experimental evidence in the literature on the pairwise connectivity of neurons in the barrel cortex, we then build a structural network that replicates circuit organization in the barrel cortex at the current level of certainty allowed by the barrel cortex literature. The neuronal dynamics in this *in silico* network are then realized using a modified quadratic neural model, the so called Izhikevich neuron. In the second part of the chapter, we then extensively characterize the neural representations *in silico* and test them against the neural representation in the biological cortical columns.

The modification that we introduce in the Izhikevich model is to rescue the model neuron from a fixed spiking threshold. In **Chapter 4,** we first show experimentally that spiking threshold is inversely correlated with the first derivative of the membrane potential, i.e. faster membrane depolarization leads to action potentials generated at lower voltages. Subsequently, we conduct an information theoretic analysis to investigate the consequences of an adaptive threshold for the representation of incoming information, for both rate and pattern codes. This analysis is further extended to the dependence on the cortical state.

With an accurate model of the network representations *in silico* **Chapter 5** addresses the nature of intra- and inter-neuronal information processing in the somatosensory cortex. By combining *in vivo* and *in vitro* whole-cell recording of neural representations with network simulations *in silico* this chapter shows that as the sensory information is transferred from one loci to another (let it be a subcortical nuclei or cortical layer) the circuit reconstructs the stimulus with high fidelity enabling accurate representation of the sensory stimulus (in our set of stimuli) in single neuron resolution even four synapses away from the sensory periphery, albeit only in its subthreshold representations.

Finally, **Chapter 6** brings together all the observations to provide a novel theory of sensory information processing along neural circuits which argues that sensory information is processed in parallel by inhibitory and excitatory cortical circuits as such the two information bearing channels enable multiplexed sensing in the somatosensory system.

References

Allen, C. B., Celikel, T., & Feldman, D. E. (2003). Long-term depression induced by sensory deprivation during cortical map plasticity in vivo. *Nature Neuroscience*, *6*(3), 291–9.

Andermann, M. L., & Moore, C. I. (2006). A somatotopic map of vibrissa motion direction within a barrel column. *Nature Neuroscience*, *9*(4), 543–51.

Andermann, M. L., Gilfoy, N. B., Goldey, G. J., Sachdev, R. N. S., Wölfel, M., McCormick, D. A., … Levene, M. J. (2013). Chronic cellular imaging of entire cortical columns in awake mice using microprisms. *Neuron*, *80*(4), 900–13.

Andersen, R. A., Musallam, S., & Pesaran, B. (2004). Selecting the signals for a brain-machine interface. *Current Opinion in Neurobiology*, *14*(6), 720–6.

Ascoli, G. A., Alonso-Nanclares, L., Anderson, S. A., Barrionuevo, G., Benavides-Piccione, R., Burkhalter, A., … Yuste, R. (2008). Petilla terminology: nomenclature of features of GABAergic interneurons of the cerebral cortex. *Nature Reviews. Neuroscience*, *9*(7), 557–68.

Atallah, B. V, Bruns, W., Carandini, M., & Scanziani, M. (2012). Parvalbumin-expressing interneurons linearly transform cortical responses to visual stimuli. *Neuron*, *73*(1), 159–70.

Attneave, F. (1954). Some informational aspects of visual perception. *Psychological Review*, *61*(3), 183–93.

Averbeck, B. B., Latham, P. E., & Pouget, A. (2006). Neural correlations, population coding and computation. *Nature Reviews. Neuroscience*, *7*(5), 358–66.

Avermann, M., Tomm, C., Mateo, C., Gerstner, W., & Petersen, C. C. H. (2012). Microcircuits of excitatory and inhibitory neurons in layer 2/3 of mouse barrel cortex. *Journal of Neurophysiology*, *107*(11), 3116–34.

Azouz, R., & Gray, C. M. (2000). Dynamic spike threshold reveals a mechanism for synaptic coincidence detection in cortical neurons in vivo. *Proceedings of the National Academy of Sciences of the United States of America*, *97*(14), 8110–8115.

Azouz, R., & Gray, C. M. (2003). Adaptive coincidence detection and dynamic gain control in visual cortical neurons in vivo. *Neuron*, *37*(3), 513–523.

Badura, A., Sun, X. R., Giovannucci, A., Lynch, L. A., & Wang, S. S.-H. (2014). Fast calcium sensor proteins for monitoring neural activity. *Neurophotonics, 1*(2), 025008.

Barlow, H. B. (1961). Possible principles underlying the transformation of sensory messages. Sensory Communication, Ed W.Rosenblith Ch13 , pp. 217-234 .M.I.T. Press, Cambridge, Mass.

Barlow, H. B. (1972). Single units and sensation: a neuron doctrine for perceptual psychology? *Perception*, *1*(4), 371–94.

Barth, A. L., & Poulet, J. F. A. (2012). Experimental evidence for sparse firing in the neocortex. *Trends in Neurosciences*, *35*(6), 345–55.

Barthó, P., Hirase, H., Monconduit, L., Zugaro, M., Harris, K. D., & Buzsáki, G. (2004). Characterization of neocortical principal cells and interneurons by network interactions and extracellular features. *Journal of Neurophysiology*, *92*(1), 600–8.

Belitski, A., Gretton, A., Magri, C., Murayama, Y., Montemurro, M. A., Logothetis, N. K., & Panzeri, S. (2008). Low-frequency local field potentials and spikes in primary visual cortex convey independent visual information. *The Journal of Neuroscience : The Official Journal of the Society for Neuroscience*, *28*(22), 5696–709.

Blatow, M., Rozov, A., Katona, I., Hormuzi, S. G., & Meyer, A. H. (2003). A novel network of multipolar bursting interneurons generates theta frequency oscillations in neocortex. *Neuron*, *38,* 805–817.

Brecht, M., Roth, A., & Sakmann, B. (2003). Dynamic receptive fields of reconstructed pyramidal cells in layers 3 and 2 of rat somatosensory barrel cortex. *The Journal of Physiology*, *553*(Pt 1), 243–65.

Brecht, M., & Sakmann, B. (2002). Dynamic representation of whisker deflection by synaptic potentials in spiny stellate and pyramidal cells in the barrels and septa of layer 4 rat somatosensory cortex. *The Journal of Physiology, 543*(1), 49–70.

Brecht, M., Schneider, M., Sakmann, B., & Margrie, T. W. (2004). Whisker movements evoked by stimulation of single pyramidal cells in rat motor cortex. *Nature*, *427*(6976), 704–10.

Brunel, N., Hakim, V., & Richardson, M. J. E. (2014). Single neuron dynamics and computation. *Current Opinion in Neurobiology*, *25*, 149–55.

Bruno, R. M., & Sakmann, B. (2006). Cortex is driven by weak but synchronously active thalamocortical synapses. *Science*, *312*(5780), 1622–7.

Bruno, R. M., & Simons, D. J. (2002). Feedforward mechanisms of excitatory and inhibitory cortical receptive fields. *The Journal of Neuroscience*, *22*(24), 10966–75.

Caputi, A., Rozov, A., Blatow, M., & Monyer, H. (2009). Two calretinin-positive GABAergic cell types in layer 2/3 of the mouse neocortex provide different forms of inhibition. *Cerebral Cortex*, *19*(6), 1345–59.

Carandini, M., & Ferster, D. (2000). Membrane potential and firing rate in cat primary visual cortex. *The Journal of Neuroscience : The Official Journal of the Society for Neuroscience*, *20*(1), 470–84.

Cardin, J. A., Palmer, L. A., & Contreras, D. (2007). Stimulus feature selectivity in excitatory and inhibitory neurons in primary visual cortex. *The Journal of Neuroscience*, *27*(39), 10333–44.

Celikel, T., Szostak, V. a, & Feldman, D. E. (2004). Modulation of spike timing by sensory deprivation during induction of cortical map plasticity. *Nature Neuroscience*, *7*(5), 534–41.

Chen, J. L., Carta, S., Soldado-Magraner, J., Schneider, B. L., & Helmchen, F. (2013). Behaviour-dependent recruitment of long-range projection neurons in somatosensory cortex. *Nature*, *499*(7458), 336–40.

Chen, X., Gabitto, M., Peng, Y., Ryba, N. J. P., & Zuker, C. S. (2011). A Gustotopic Map of Taste Qualities in the Mammalian Brain. *Science*, *333*(6047), 1262–1266.

Connors, B. W., Gutnick, M. J., & Prince, D. A. (1982). Electrophysiological properties of neocortical neurons in vitro. *Journal of Neurophysiology*, *48*(6), 1302–20.

Crochet, S., Poulet, J. F. A., Kremer, Y., & Petersen, C. C. H. (2011). Synaptic mechanisms underlying sparse coding of active touch. *Neuron*, *69*(6), 1160–75.

De Kock, C. P. J., Bruno, R. M., Spors, H., & Sakmann, B. (2007). Layer- and cell-type-specific suprathreshold stimulus representation in rat primary somatosensory cortex. *The Journal of Physiology*, *581*(Pt 1), 139–54.

De Polavieja, G. G., Harsch, A., Kleppe, I., Robinson, H. P. C., & Juusola, M. (2005). Stimulus history reliably shapes action potential waveforms of cortical neurons. *The*

Journal of Neuroscience, *25*(23), 5657–65.

De Ruyter van Steveninck, R. R., & Laughlin, S. B. (1996). The rate of information transfer at graded-potential synapses. *Nature*, *379*(6566), 642–645.

DeFelipe, J., & Fariñas, I. (1992). The pyramidal neuron of the cerebral cortex: morphological and chemical characteristics of the synaptic inputs. *Progress in Neurobiology*, *39*(6), 563–607.

Denk, W., Strickler, J. H., & Webb, W. W. (1990). Two-photon laser scanning fluorescence microscopy. *Science (New York, N.Y.)*, *248*(4951), 73–6.

Denk, W., Delaney, K. R., Gelperin, A., Kleinfeld, D., Strowbridge, B. W., Tank, D. W., & Yuste, R. (1994). Anatomical and functional imaging of neurons using 2-photon laser scanning microscopy. *Journal of Neuroscience Methods*, *54*(2), 151–62

Dhingra, N. K., & Smith, R. G. (2004). Spike generator limits efficiency of information transfer in a retinal ganglion cell. *The Journal of Neuroscience*, *24*(12), 2914–22.

Einevoll, G. T., Kayser, C., Logothetis, N. K., & Panzeri, S. (2013). Modelling and analysis of local field potentials for studying the function of cortical circuits. *Nature Reviews Neuroscience*, *14*(11), 770–85.

Felleman, D. J., & Van Essen, D. C. (1991). Distributed hierarchical processing in the primate cerebral cortex. *Cerebral Cortex*, *1*(1), 1–47.

Fino, E., & Yuste, R. (2011). Dense inhibitory connectivity in neocortex. *Neuron*, *69*(6), 1188–203.

Foffani, G., Chapin, J. K., & Moxon, K. A. (2008). Computational role of large receptive fields in the primary somatosensory cortex. *Journal of Neurophysiology*, *100*(1), 268–80.

Fontaine, B., Peña, J. L., & Brette, R. (2014). Spike-threshold adaptation predicted by membrane potential dynamics in vivo. *PLoS Computational Biology*, *10*(4), e1003560.

Gabernet, L., Jadhav, S. P., Feldman, D. E., Carandini, M., & Scanziani, M. (2005). Somatosensory integration controlled by dynamic thalamocortical feed-forward inhibition. *Neuron*, *48*(2), 315–27.

Galarreta, M., & Hestrin, S. (2001). Electrical synapses between GABA-releasing interneurons. *Nature Reviews Neuroscience*, *2*(6), 425–33.

Gentet, L. J., Kremer, Y., Taniguchi, H., Huang, Z. J., Staiger, J. F., & Petersen, C. C. H. (2012). Unique functional properties of somatostatin-expressing GABAergic neurons in mouse barrel cortex. *Nature Neuroscience*, *15*(4), 607–12.

Goldberg, E. M., Clark, B. D., Zagha, E., Nahmani, M., Erisir, A., & Rudy, B. (2008). K+ channels at the axon initial segment dampen near-threshold excitability of neocortical fast-spiking GABAergic interneurons. *Neuron*, *58*(3), 387–400.

Greenberg, D. S., Houweling, A. R., & Kerr, J. N. D. (2008). Population imaging of ongoing neuronal activity in the visual cortex of awake rats. *Nature Neuroscience*, *11*(7), 749–51.

Grienberger, C., & Konnerth, A. (2012). Imaging calcium in neurons. *Neuron*, *73*(5), 862–85.

Gupta, a., Wang, Y., & Markram, H. (2000). Organizing principles for a diversity of GABAergic interneurons and synapses in the neocortex. *Science*, *287*(5451), 273–8.

Haider, B., Häusser, M., & Carandini, M. (2013). Inhibition dominates sensory responses in the awake cortex. *Nature*, *493*(7430), 97–100.

Harvey, C. D., Coen, P., & Tank, D. W. (2012). Choice-specific sequences in parietal cortex during a virtual-navigation decision task. *Nature*, *484*(7392), 62–8.

Helmstaedter, M., Staiger, J. F., Sakmann, B., & Feldmeyer, D. (2008). Efficient recruitment of layer 2/3 interneurons by layer 4 input in single columns of rat somatosensory cortex. *The Journal of Neuroscience*, *28*(33), 8273–84.

Hillman, E. M. C. (2007). Optical brain imaging in vivo: techniques and applications from animal to man. *Journal of Biomedical Optics*, *12*(5), 051402.

Hirsch, J. A., Alonso, J. M., Reid, R. C., & Martinez, L. M. (1998). Synaptic integration in striate cortical simple cells. *The Journal of Neuroscience*, *18*(22), 9517–28.

Hofer, S. B., Ko, H., Pichler, B., Vogelstein, J., Ros, H., Zeng, H., … Mrsic-Flogel, T. D. (2011). Differential connectivity and response dynamics of excitatory and inhibitory neurons in visual cortex. *Nature Neuroscience*, *14*(8), 1045–1052.

Holmgren, C., Harkany, T., Svennenfors, B., & Zilberter, Y. (2003). Pyramidal cell communication within local networks in layer 2/3 of rat neocortex. *The Journal of Physiology*, *551*(Pt 1), 139–53.

Hromádka, T., Deweese, M. R., & Zador, A. M. (2008). Sparse representation of sounds in the unanesthetized auditory cortex. *PLoS Biology*, *6*(1), e16.

Hubel, D. H., & Wiesel, T. N. (1962). Receptive fields, binocular interaction and functional architecture in the cat's visual cortex. *The Journal of Physiology*, *160*(1), 106.

Ince, R. A. A., Panzeri, S., & Kayser, C. (2013). Neural codes formed by small and temporally precise populations in auditory cortex. *The Journal of Neuroscience*, *33*(46), 18277–87.

Kapfer, C., Glickfeld, L. L., Atallah, B. V, & Scanziani, M. (2007). Supralinear increase of recurrent inhibition during sparse activity in the somatosensory cortex. *Nature Neuroscience*, *10*(6), 743–53.

Katzner, S., Nauhaus, I., Benucci, A., Bonin, V., Ringach, D. L., & Carandini, M. (2009). Local origin of field potentials in visual cortex. *Neuron*, *61*(1), 35–41.

Kerlin, A. M., Andermann, M. L., Berezovskii, V. K., & Reid, R. C. (2010). Broadly tuned response properties of diverse inhibitory neuron subtypes in mouse visual cortex. *Neuron*, *67*(5), 858–71.

Kerr, J. N. D., de Kock, C. P. J., Greenberg, D. S., Bruno, R. M., Sakmann, B., & Helmchen, F. (2007). Spatial organization of neuronal population responses in layer 2/3 of rat barrel cortex. *The Journal of Neuroscience*, *27*(48), 13316–28.

Ko, H., Hofer, S. B., Pichler, B., Buchanan, K. A., Sjöström, P. J., & Mrsic-Flogel, T. D. (2011). Functional specificity of local synaptic connections in neocortical networks. *Nature*, *473*(7345), 87–91.

Koelbl, C., Helmstaedter, M., Lübke, J., & Feldmeyer, D. (2015). A barrel-related interneuron in layer 4 of rat somatosensory cortex with a high intrabarrel connectivity. *Cerebral Cortex*, *25*(3), 713–25.

Komai, S., Denk, W., Osten, P., Brecht, M., & Margrie, T. W. (2006). Two-photon targeted patching (TPTP) in vivo. *Nature Protocols*, *1*(2), 647–652.

Lee, A. K., Manns, I. D., Sakmann, B., & Brecht, M. (2006). Whole-cell recordings in freely moving rats. *Neuron*, *51*(4), 399–407.

Lee, S., Hjerling-Leffler, J., Zagha, E., Fishell, G., & Rudy, B. (2010). The largest group of superficial neocortical GABAergic interneurons expresses ionotropic serotonin receptors. *The Journal of Neuroscience*, *30*(50), 16796–808.

Lefort, S., Tomm, C., Floyd Sarria, J.-C., & Petersen, C. C. H. (2009). The excitatory neuronal network of the C2 barrel column in mouse primary somatosensory cortex. *Neuron*, *61*(2), 301–16.

Lewicki, M. S. (2002). Efficient coding of natural sounds. *Nature Neuroscience*, *5*(4), 356–363.

Li, N., Chen, T.-W., Guo, Z. V., Gerfen, C. R., & Svoboda, K. (2015). A motor cortex circuit for motor planning and movement. *Nature*, *519*(7541), 51–6.

Liu, B., Li, P., Li, Y., Sun, Y. J., Yanagawa, Y., Obata, K., … Tao, H. W. (2009). Visual receptive field structure of cortical inhibitory neurons revealed by two-photon imaging guided recording. *The Journal of Neuroscience*, *29*(34), 10520–32.

Liu, B., Li, Y., Ma, W., Pan, C., Zhang, L. I., & Tao, H. W. (2011). Broad inhibition sharpens orientation selectivity by expanding input dynamic range in mouse simple cells. *Neuron*, *71*(3), 542–54.

London, M., & Häusser, M. (2005). Dendritic computation. *Annual Review of Neuroscience*, *28*, 503–32.

Ma, W., Liu, B., Li, Y., Huang, Z. J., Zhang, L. I., & Tao, H. W. (2010). Visual representations by cortical somatostatin inhibitory neurons--selective but with weak and delayed responses. *The Journal of Neuroscience*, *30*(43), 14371–9.

Manns, I. D., Sakmann, B., & Brecht, M. (2004). Sub- and suprathreshold receptive field properties of pyramidal neurones in layers 5A and 5B of rat somatosensory barrel cortex. *The Journal of Physiology*, *556*(Pt 2), 601–22.

Markowitz, D. A., Wong, Y. T., Gray, C. M., & Pesaran, B. (2011). Optimizing the decoding of movement goals from local field potentials in macaque cortex. *The Journal of Neuroscience*, *31*(50), 18412–22.

Markram, H., Toledo-Rodriguez, M., Wang, Y., Gupta, A., Silberberg, G., & Wu, C. (2004). Interneurons of the neocortical inhibitory system. *Nature Reviews Neuroscience*, *5*(10), 793–807.

Mayrhofer, J. M., Haiss, F., Helmchen, F., & Weber, B. (2015). Sparse, reliable, and long-term stable representation of periodic whisker deflections in the mouse barrel cortex. *NeuroImage*.

Mel, B. W. (1993). Synaptic integration in an excitable dendritic tree. *Journal of Neurophysiology*, *70*(3), 1086–101.

Meyer, H. S., Schwarz, D., Wimmer, V. C., Schmitt, A. C., Kerr, J. N. D., Sakmann, B., & Helmstaedter, M. (2011). Inhibitory interneurons in a cortical column form hot zones of inhibition in layers 2 and 5A. *Proceedings of the National Academy of Sciences of the United States of America*, *108*(40), 16807–12.

Niessing, J., & Friedrich, R. W. (2010). Olfactory pattern classification by discrete neuronal network states. *Nature*, *465*(7294), 47–52.

Nowak, L. G., Azouz, R., Sanchez-Vives, M. V, Gray, C. M., & McCormick, D. A. (2003). Electrophysiological classes of cat primary visual cortical neurons in vivo as revealed by quantitative analyses. *Journal of Neurophysiology*, *89*(3), 1541–66.

Nowak, L. G., Sanchez-Vives, M. V, & McCormick, D. A. (2008). Lack of orientation and direction selectivity in a subgroup of fast-spiking inhibitory interneurons: cellular and synaptic mechanisms and comparison with other electrophysiological cell types. *Cerebral Cortex*, *18*(5), 1058–78.

O’Connor, D. H., Peron, S. P., Huber, D., & Svoboda, K. (2010). Neural activity in barrel cortex underlying vibrissa-based object localization in mice. *Neuron*, *67*(6), 1048–61.

O’Keefe, J., & Dostrovsky, J. (1971). The hippocampus as a spatial map. Preliminary evidence from unit activity in the freely-moving rat. *Brain Research*, *34*(1), 171–175.

Oberlaender, M., Ramirez, A., & Bruno, R. M. (2012). Sensory experience restructures thalamocortical axons during adulthood. *Neuron*, *74*(4), 648–55.

Ohki, K., Chung, S., Ch’ng, Y. H., Kara, P., & Reid, R. C. (2005). Functional imaging with cellular resolution reveals precise micro-architecture in visual cortex. *Nature*, *433*(7026), 597–603.

Okun, M., & Lampl, I. (2008). Instantaneous correlation of excitation and inhibition during ongoing and sensory-evoked activities. *Nature Neuroscience*, *11*(5), 535–7.

Oláh, S., Füle, M., Komlósi, G., Varga, C., Báldi, R., Barzó, P., & Tamás, G. (2009). Regulation of cortical microcircuits by unitary GABA-mediated volume transmission. *Nature*, *461*(7268), 1278–81.

Olshausen, B. A., & Field, D. J. (2004). Sparse coding of sensory inputs. *Current Opinion in Neurobiology*, *14*(4), 481–7.

Olshausen, B. A., & Field, D. J. (1996). Emergence of simple-cell receptive field properties by learning a sparse code for natural images. *Nature*, *381*(6583), 607–9.

Packer, A. M., & Yuste, R. (2011). Dense, unspecific connectivity of neocortical parvalbumin-positive interneurons: a canonical microcircuit for inhibition? *The Journal of Neuroscience*, *31*(37), 13260–71.

Panzeri, S., Petersen, R. S., Schultz, S. R., Lebedev, M., & Diamond, M. E. (2001). The role of spike timing in the coding of stimulus location in rat somatosensory cortex. *Neuron*, *29*(3), 769–77.

Panzeri, S., Macke, J. H., Gross, J., & Kayser, C. (2015). Neural population coding: combining insights from microscopic and mass signals. *Trends in Cognitive Sciences*, *19*(3), 162–172.

Panzeri, S., & Diamond, M. E. (2010). Information Carried by Population Spike Times in the Whisker Sensory Cortex can be Decoded Without Knowledge of Stimulus Time. *Frontiers in Synaptic Neuroscience*, *2*, 17.

Peron, S. P., Freeman, J., Iyer, V., Guo, C., & Svoboda, K. (2015). A Cellular Resolution Map of Barrel Cortex Activity during Tactile Behavior. *Neuron*, *86*(3), 783–799.

Pesaran, B. (2009). Uncovering the mysterious origins of local field potentials. *Neuron*, *61*(1), 1–2.

Petersen, C. C. H., & Crochet, S. (2013). Synaptic computation and sensory processing in neocortical layer 2/3. *Neuron*, *78*(1), 28–48.

Petersen, C. C. H., Hahn, T. T. G., Mehta, M., Grinvald, A., & Sakmann, B. (2003). Interaction of sensory responses with spontaneous depolarization in layer 2/3 barrel cortex. *Proc. Natl. Acad. Sci. USA*, *100*, 13638–13643.

Petersen, R. S., Panzeri, S., & Diamond, M. E. (2001). Population coding of stimulus location in rat somatosensory cortex. *Neuron*, *32*, 503–514.

Pfeffer, C. K., Xue, M., He, M., Huang, Z. J., & Scanziani, M. (2013). Inhibition of inhibition in visual cortex: the logic of connections between molecularly distinct interneurons. *Nature Neuroscience*, *16*(8), 1068–76.

Poo, C., & Isaacson, J. S. (2009). Odor representations in olfactory cortex: “sparse” coding, global inhibition, and oscillations. *Neuron*, *62*(6), 850–61.

Porter, J. T., Cauli, B., Staiger, J. F., Lambolez, B., Rossier, J., & Audinat, E. (1998). Properties of bipolar VIPergic interneurons and their excitation by pyramidal neurons in the rat neocortex. *The European Journal of Neuroscience*, *10*(12), 3617–28.

Poulet, J. F. A., & Petersen, C. C. H. (2008). Internal brain state regulates membrane potential synchrony in barrel cortex of behaving mice. *Nature*, *454*(7206), 881–5. doi:10.1038/nature07150

Ramirez, A., Pnevmatikakis, E. A., Merel, J., Paninski, L., Miller, K. D., & Bruno, R. M. (2014). Spatiotemporal receptive fields of barrel cortex revealed by reverse correlation of synaptic input. *Nature Neuroscience*, *17*(6), 866–75.

Ray, S., & Maunsell, J. H. R. (2011). Different origins of gamma rhythm and high-gamma activity in macaque visual cortex. *PLoS Biology*, *9*(4), e1000610.

Richert, M., Nageswaran, J. M., Dutt, N., & Krichmar, J. L. (2011). An Efficient Simulation Environment for Modeling Large-Scale Cortical Processing. *Frontiers in Neuroinformatics*, *5*, 19.

Rien, D., Kern, R., & Kurtz, R. (2011). Synaptic transmission of graded membrane potential changes and spikes between identified visual interneurons. *The European Journal of Neuroscience*, *34*(5), 705–16.

Rose, D., & Blakemore, C. (1974). Effects of bicuculline on functions of inhibition in visual cortex. *Nature*, *249*(455), 375–7.

Rothschild, G., Nelken, I., & Mizrahi, A. (2010). Functional organization and population dynamics in the mouse primary auditory cortex. *Nature Neuroscience*, *13*(3), 353–360.

Runyan, C. A., Schummers, J., Van Wart, A., Kuhlman, S. J., Wilson, N. R., Huang, Z. J., & Sur, M. (2010). Response Features of Parvalbumin-Expressing Interneurons

Suggest Precise Roles for Subtypes of Inhibition in Visual Cortex. *Neuron*, *67*(5), 847–857.

Schomburg, E. W., Anastassiou, C. A., Buzsáki, G., & Koch, C. (2012). The spiking component of oscillatory extracellular potentials in the rat hippocampus. *The Journal of Neuroscience : The Official Journal of the Society for Neuroscience*, *32*(34), 11798–811.

Shoham, S., O'Connor, D. H., & Segev, R. (2006). How silent is the brain: is there a "dark matter" problem in neuroscience? *Journal of Comparative Physiology. A, Neuroethology, Sensory, Neural, and Behavioral Physiology*, *192*(8), 777–84.

Smith, E. C., & Lewicki, M. S. (2006). Efficient auditory coding. *Nature*, *439*(7079), 978–82.

Snow, P. J., Rose, P. K., & Brown, A. G. (1976). Tracing axons and axon collaterals of spinal neurons using intracellular injection of horseradish peroxidase. *Science*, *191*(4224), 312–3.

Sohya, K., Kameyama, K., Yanagawa, Y., Obata, K., & Tsumoto, T. (2007). GABAergic neurons are less selective to stimulus orientation than excitatory neurons in layer II/III of visual cortex, as revealed by in vivo functional Ca2+ imaging in transgenic mice. *The Journal of Neuroscience*, *27*(8), 2145–9.

Somogyi, P., & Soltész, I. (1986). Immunogold demonstration of GABA in synaptic terminals of intracellularly recorded, horseradish peroxidase-filled basket cells and clutch cells in the cat's visual cortex. *Neuroscience*, *19*(4), 1051–65.

Stettler, D. D., & Axel, R. (2009). Representations of odor in the piriform cortex. *Neuron*, *63*(6), 854–64.

Stüttgen, M. C., & Schwarz, C. (2008). Psychophysical and neurometric detection performance under stimulus uncertainty. *Nature Neuroscience*, *11*(9), 1091–1099.

Swadlow, H. A. (1989). Efferent neurons and suspected interneurons in S-1 vibrissa cortex of the awake rabbit: receptive fields and axonal properties. *Journal of Neurophysiology*, *62*(1), 288–308.

Swadlow, H. A. (2003). Fast-spike Interneurons and Feedforward Inhibition in Awake Sensory Neocortex. *Cerebral Cortex*, *13*(1), 25–32.

Tamás, G., Lorincz, A., Simon, A., & Szabadics, J. (2003). Identified sources and targets of slow inhibition in the neocortex. *Science*, *299*(5614), 1902–5.

Tan, A. Y. Y., Zhang, L. I., Merzenich, M. M., & Schreiner, C. E. (2004). Tone-evoked excitatory and inhibitory synaptic conductances of primary auditory cortex neurons. *Journal of Neurophysiology*, *92*(1), 630–43.

Taniguchi, H., Lu, J., & Huang, Z. J. (2013). The spatial and temporal origin of chandelier cells in mouse neocortex. *Science*, *339*(6115), 70–4.

Vinje, W. E., & Gallant, J. L. (2000). Sparse coding and decorrelation in primary visual cortex during natural vision. *Science*, *287*(5456), 1273–6.

Vinje, W. E., & Gallant, J. L. (2002). Natural stimulation of the nonclassical receptive field increases information transmission efficiency in V1. *The Journal of Neuroscience*, *22*(7), 2904–15.

Volgushev, M., Pernberg, J., & Eysel, U. T. (2000). Comparison of the selectivity of postsynaptic potentials and spike responses in cat visual cortex. *The European Journal of Neuroscience*, *12*(1), 257–63.

Wang, Y., Toledo-Rodriguez, M., Gupta, A., Wu, C., Silberberg, G., Luo, J., & Markram, H. (2004). Anatomical, physiological and molecular properties of Martinotti cells in the somatosensory cortex of the juvenile rat. *The Journal of Physiology*, *561*(Pt 1), 65–90.

Wehr, M., & Zador, A. M. (2003). Balanced inhibition underlies tuning and sharpens spike timing in auditory cortex. *Nature*, *426*(6965), 442–6.

Wilent, W. B., & Contreras, D. (2005). Stimulus-dependent changes in spike threshold enhance feature selectivity in rat barrel cortex neurons. *The Journal of Neuroscience*, *25*(11), 2983–91.

Willmore, B. D. B., Mazer, J. A., & Gallant, J. L. (2011). Sparse coding in striate and extrastriate visual cortex. *Journal of Neurophysiology*, *105*(6), 2907–19.

Wozny, C., & Williams, S. R. (2011). Specificity of synaptic connectivity between layer 1 inhibitory interneurons and layer 2/3 pyramidal neurons in the rat neocortex. *Cerebral Cortex*, *21*(8), 1818–26.

Wu, G. K., Arbuckle, R., Liu, B.-H., Tao, H. W., & Zhang, L. I. (2008). Lateral sharpening of cortical frequency tuning by approximately balanced inhibition. *Neuron*, *58*(1), 132–43.

Xu, X., Roby, K. D., & Callaway, E. M. (2006). Mouse cortical inhibitory neuron type that coexpresses somatostatin and calretinin. *The Journal of Comparative Neurology*, *499*(1), 144–60.

Yamashita, T., Pala, A., Pedrido, L., Kremer, Y., Welker, E., & Petersen, C. C. H. (2013). Membrane potential dynamics of neocortical projection neurons driving target-specific signals. *Neuron*, *80*(6), 1477–90.

Yassin, L., Benedetti, B. L., Jouhanneau, J.-S., Wen, J. A., Poulet, J. F. A., & Barth, A. L. (2010). An embedded subnetwork of highly active neurons in the neocortex. *Neuron*, *68*(6), 1043–50.

Zhang, L. I., Tan, A. Y. Y., Schreiner, C. E., & Merzenich, M. M. (2003). Topography and synaptic shaping of direction selectivity in primary auditory cortex. *Nature*, *424*(6945), 201–5.

Zhu, Y., Stornetta, R. L., & Zhu, J. J. (2004). Chandelier cells control excessive cortical excitation: characteristics of whisker-evoked synaptic responses of layer 2/3 nonpyramidal and pyramidal neurons. *The Journal of Neuroscience*, *24*(22), 5101–8.

Chapter 2. FUNCTIONAL IMAGING OF WHISKER REPRESENTATIONS IN THE BARREL CORTEX

Abstract

Functional imaging of intrinsic signals allows minimally invasive spatiotemporal mapping of stimulus representations in the cortex; but representations are often corrupted by stimulus-independent spatial artifacts, especially those originating from the blood vessels. In this method chapter we present novel algorithms for unsupervised identification of cerebral vascularization, allowing blind separation of stimulus representations from noise, and detail how to locate cortical region of interest for subsequent electrophysiological experiments. These algorithms commonly take advantage of the temporal fluctuations in global reflectance to extract anatomical information. More specifically, the phase of low frequency oscillations relative to global fluctuations reveals local vascular identity. Arterioles can be reconstructed using their characteristically high power in those frequencies corresponding to respiration, heartbeat, and vasomotion signals. By treating the vasculature as a dynamic flow network, we finally demonstrate that direction of blood perfusion can be quantitatively visualized. Application of these methods for removal of stimulus-independent changes in reflectance permits isolation of stimulus-evoked representations even if the representation spatially overlaps with blood vessels. The algorithms can further be expanded to extract temporal information on blood flow, monitoring of revascularization following a focal stroke, and distinguish arterioles from venules and parenchyma.

Introduction

Functional imaging of intrinsic signals allows quantitative analysis of neural representations by taking advantage of the coupling between vascular response and neural activity (Lieke et al. 1989; Parri and Crunelli 2003; Roy and Sherrington 1890; Sheth et al. 2005; Villringer and Dirnagl 1995). These minimally invasive hemodynamic imaging techniques commonly have low signal to noise ratio (SNR), slow time course, and require averaging across multiple trials to obtain reproducible results (Bonhoeffer and Grinvald 1996; Mayhew et al. 1999; Vanzetta et al. 2005; Zepeda et al. 2004; Zheng et al. 2001).

The noise in intrinsic signals exists in both spatial and temporal domains. Slow changes in wide-scale regional cerebral blood flows (CBF (Cannestra et al. 1996; Dirnagl et al. 1989; Narayan et al. 1995; Villringer et al. 1989)), slow oscillations in the diameters of arterioles (i.e. vasomotion (Chambers and Zweifach 1947; Kalatsky and Stryker 2003; Zepeda et al. 2004)), and higher frequency oscillations resulting from respiration and heartbeat (Lieke et al. 1989; Mayhew et al. 1996; Reidl et al. 2007) introduce temporally varying and spatially structured fluctuations to intrinsic signal measurements. Among the different sources of noise, those that closely match the time-course of the vascular response to neural activity (i.e. $0.02<f<0.2$ Hz) have an order of magnitude larger amplitude than stimulus-evoked responses (Bonhoeffer and Grinvald 1996; Carmona et al. 1995; Zepeda et al. 2004), and have proven more difficult to overcome (Schiessl et al. 2008; Vanzetta et al. 2005) because bandpass filtering risks the loss of information from the underlying signal. This noise can be attenuated by phase-locking the stimulus onset to oscillations, subtracting the pre-stimulus background, and averaging evoked responses across multiple trials (Grinvald et al. 1991), which reduce the magnitude of stimulus-independent oscillations with uncorrelated phase by the square root of the number of trials (Narayan et al. 1994). Assuming greater spatial homogeneity of the slow spontaneous fluctuations in the signal, one can further reduce the noise in evoked responses by subtracting the median from each frame (Blasdel and Salama 1986; Frostig et al. 1990; Ts'o et al. 1990). This procedure corrects for the slow global changes in reflectance as a function of time (Bonhoeffer and Grinvald 1996). The combination of these approaches results in an averaged time series of hemodynamic response, which may be used to map the spatial location, amplitude and time course of the evoked responses.

Even after these corrections, however, there often remains a spatially structured vasculature artifact that interferes with extraction of evoked representations (Spitzer et al. 2001). Early application of Principal Component Analysis (PCA) helped to isolate the stimulus-evoked responses from stimulus-independent noise (Cannestra et al. 1996; Geladi et al. 1989; Vanzetta et al. 2004; Zheng et al. 2001), using the implicit assumption that evoked representations would be localized and elliptical, and the vasculature noise would appear in branching vessel structures that are quantitatively similar to vessel maps. While improving the quality of the mapping signal, these linear PCA methods still leave residual signals from the vasculature that confound quantitative analysis of evoked representations. This is an inevitable consequence of PCA – even the ideal time-course eigenvector of the stimulus-evoked response can produce an arteriole corrupted spatial representation due to the physiologically coupled role of arterioles as the source of blood flow to the evoked neural response. For this reason, several variations of independent component analysis (ICA), such as extended spatial decorrelation (ESD (Molgedey and Schuster 1994; Schiessl et al. 2008; Stetter et al. 2000)), sub-space correlation (SSC (Zheng et al. 2001)), and spontaneous independent component analysis (sICA (Reidl et al. 2007)), have been applied to the principal components to separate stimulus-evoked representations from spatially distinct stimulus-independent "noise". While these algorithms can successfully isolate the vasculature artifact, because they produce images with unit-less dimensions, and are highly non-linear by their nature, subsequent quantitative analysis of the physiological signals is often difficult (Reidl et al. 2007; Schiessl et al. 2008; Stetter et al. 2000).

For these reasons, there is a niche for approaches that would identify vasculature for isolation of stimulus-evoked representations from non-specific changes in hemodynamic responses within the well-understood domain of reflectance units (Carmona et al. 1995; Frostig et al. 1990; Reidl et al. 2007; Schiessl et al. 2008; Stetter et al. 2000; Vanzetta et al. 2005; Zheng et al. 2001). To this end, a binary classification of the pixels that carry the largest stimulus-independent changes (i.e. lowest SNR) offers several distinct advantages. First, binary removal of pixels with a greater stimulus-independent component permits de-noising without changing image units, allowing a direct extraction and quantitative interpretation of evoked representations. Second, as Carmona and colleagues originally observed (Carmona et al. 1995), even if one does not require common units for quantitative comparison of spatial representations across trials, conditions, or experiments, initial removal of stimulus-independent artifacts before applying PCA minimizes the overlap between stimulus-evoked and stimulus-independent representations. Third, there remains an interest in the dynamics of the stimulus-evoked vasculature response (Drew et al. 2011; Golanov et al. 1994; Jones et al. 2001). Binary classification of pixels representing the vasculature may facilitate more targeted investigations into the dynamic temporal response of arterioles and venules upon stimulus presentations and allow mechanistic explanation of stimulus representations using functional imaging of intrinsic signals.

Here we introduce three novel algorithms that reconstruct vasculature pattern from temporal variations in intrinsic signals. The methods are unsupervised, allow blind source separation of the stimulus-independent noise in intrinsic signals and particularly suitable for automation of image processing steps for quantitative analysis of neural representations. We furthermore show that these algorithms can be expanded to distinguish arterioles from venules, quantify the time course of blood flow in identified vasculatures and allow reconstruction of stimulus-evoked representations even if the evoked representation spatially overlaps with vasculature.

Materials and Methods

Adult C57Bl6 mice (22-24 g; Taconic Farms, CA- USA) from either sex were used according to the animal welfare guidelines of the National Institute of Health and the Animal Care and Use Committee at the University of Southern California.

Animal preparation

Mice were anesthetized with Ketamine and Xylazine (i.p. 100 mg/kg ketamine, 15 mg/kg xylazine) and placed on a heating pad to maintain the core body temperature at 36.5(±0.2)°C during the experiment. Following a medial skin incision, skull above the right primary somatosensory cortex was thinned to ~100 µm thickness (-1.5 to -4.5 from bregma; -3 to -6 from midline) using a dental drill. Skull transparency was maintained throughout the imaging session by application of a thin layer of mineral oil (330760; Sigma-Aldrich, MO- USA) as necessary.

Data acquisition

All data acquisition and instrument control were performed using custom written routines in Labview (National Instruments, TX- USA). Two light-guide coupled high-power light emitting diodes were used to visualize cerebral vascularization (530 nm; LCS-0530-05-22; Mightex, CA- USA) and to image intrinsic signals (625 nm; LCS-0625-03-22; Mightex, CA- USA). We chose 625 nm light for intrinsic observation it provides a strong signal to noise ratio in evoked experiments and because the physiological etiology of the signal at this wavelength has been well characterized (Frostig et al 1990). Images were acquired at 60 fps using a Pike-032B (Allied Vision Technologies, MA- USA) with custom thermoelectric cooling and digitized at 16-bit with 320 x 480 pixel resolution. Field of view was magnified (4x; 7 µm/pixel) using a custom made macroscope (Figure 2.1) attached to the camera. The camera was placed perpendicular to the imaging plane and focused ~200 µm below the cortical surface. To visualize whisker-evoked changes in intrinsic signals, a single whisker (i.e. left C2) was deflected (amplitude= 8 degrees) using a computer controlled piezoelectric actuator every 15s with a 5 Hz square pulse train for 3s. In addition, spontaneous changes in intrinsic signals were observed for a period of 5 min. All data were acquired continuously.

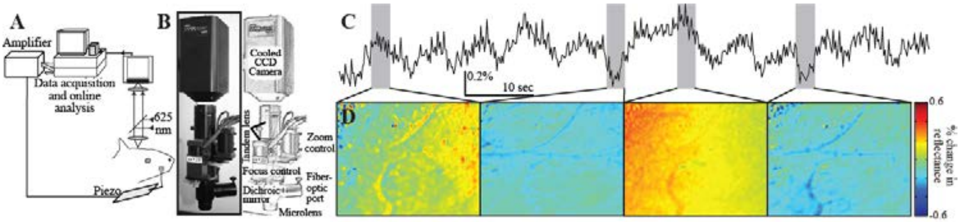

Figure 2.1. Experimental setup and representative data. (A) Spontaneous and sensory-evoked changes in reflectance of 625 nm wavelength light was measured in vivo under anesthesia. Whisker deflections were delivered using a piezoelectric actuator. (B) Custom-made macroscope for intrinsic optical imaging. (C) Spontaneous low frequency oscillations in mean pixel reflectance over a 60 second period. (D) Representative images reconstructed from averaged reflectance over 2 second time intervals during low and high "states" of the light reflectance.

Data analysis

Data analysis was performed using MATLAB (MathWorks, MA- USA). The collection of MATLAB functions and a representative raw data set are available online (http://jn.physiology.org/content/109/12/3094.figures-only) as supplementary materials. For vascular identification analyses, individual images collected under 625 nm illumination during spontaneous observation were down-sampled at 8 Hz by averaging pixel values in 0.125 s frames. Background reflectance was calculated for each pixel across the period of observation (e.g. 60 s) by averaging, and percent change in reflectance (Y) was calculated after subtraction of the background and smoothed (Y_s) using a Gaussian filter ($\sigma = 70$ μm). The 70 μm standard deviation of the Gaussian filter was chosen to maximally reduce local video noise with a minimal blurring effect on larger scale image features (e.g. vessels, neural responses), and might be reduced when trying to identify smaller vessels. Sample frames of Y_s are shown in Figure 2.1C (bottom panels). Finally, global reflectance, G, was calculated as the median value of each frame in Y_s to track spontaneous changes in intrinsic signals across the field of view (see Figure 2.1C top panel).

Spatial Reconstruction from Spectral Power (SRSP)

SRSP is based on reconstruction of the spectral power in pixel reflectance oscillations across the field of view. This approach is feasible given the previous observations that distinct sources (i.e. heart-rate, breathing, vasomotion) that contribute to changes in intrinsic signals oscillate at different frequencies (Carmona et al. 1995; Mayhew et al. 1996; Schiessl et al. 2008) (also see below). To isolate contributions of each source to changes in Y_s, we computed the Fourier power spectrum ($\tilde{Y}_s$). As shown in Figure 2.2, the power contained in frequency peaks of $\tilde{Y}_s$ differs for regions of interest (ROI) containing arterioles, venules, or capillaries. We use this information to construct a map of arterioles by integrating over the frequency domain for each pixel (Figure 2.2B-E, lower panels):

$$SRSP\ image(i,j) = \int_{0.2}^{4} \tilde{Y}_s^{i,j}\,(f)df$$

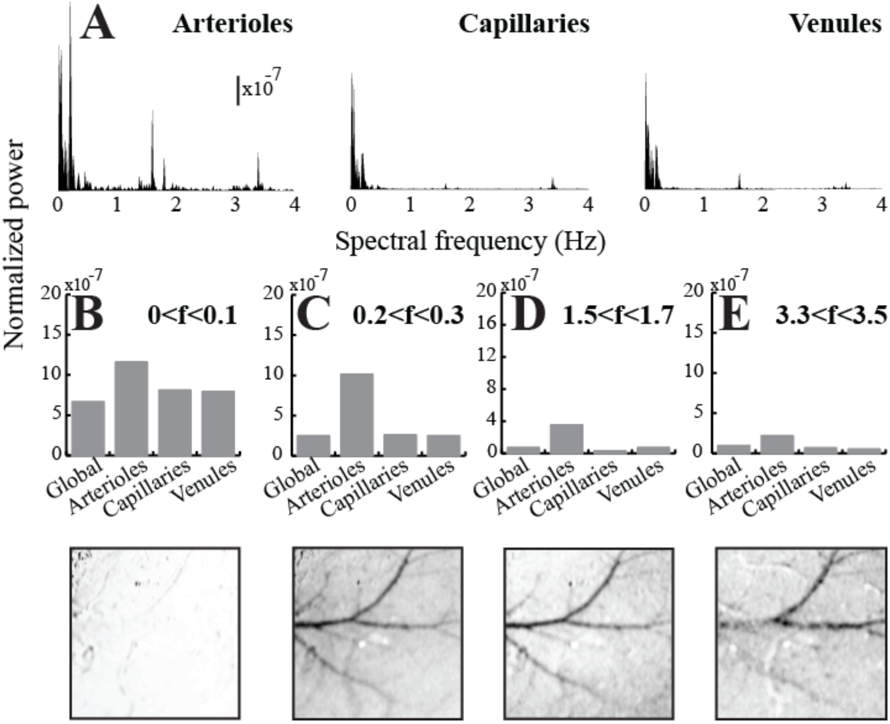

Figure 2.2. Spectral power of oscillations varies across vasculatures. (A) Fourier power spectrum of the mean light reflectance across frequencies for identified arterioles, capillaries and venules. Spectral power across the entire image is shown as the change in mean pixel reflectance (i.e. global reflectance). Reconstruction of the ROI from bandpass filtered data at 0<f<0.1 (B), 0.2<f<0.3 (C), 1.5<f<1.7 (D), and 3.3<f<3.5 (E). Histograms show the power in different vasculature across the same four Fourier spectrum peaks.

Maximal Covariance after Shift (MCS)

MCS is based on calculation of the phase of low frequency fluctuations in each pixel with respect to the global reflectance, G. Because these low frequency fluctuations propagate through the blood vessels, the phase of upstream arterioles leads and the phase of downstream venules lags the global phase. As a result, spatial reconstruction of phase information across the ROI correlates well with vascular classification.

For phase computation, we take advantage of the fact that two oscillating signals will have higher covariance when their respective phases are aligned. Both G and Y_s were band-pass filtered to remove frequency components greater than 1 Hz, and sphered to zero mean and unit variance, giving $\hat{G}$ and $\hat{Y}_s$. By shifting the $\hat{Y}_s$ forward or backward in time with respect to $\hat{G}$, we were able to modulate the phase offset and search for the phase shift that maximizes the covariance between $\hat{G}$ and $\hat{Y}$. Rather than searching for the maximum over each independent shift, we increased the robustness of the phase estimation by maximizing over the quadratic regression of covariance values for shifts within a narrow window (i.e. ∈ [-0.25,0.25] seconds). After finding the phase of each pixel, we then reconstruct the field of view:

$$MCS\ image(i,j) = \underset{shift\,\in[-0.25,0.25]}{\operatorname{argmax}}\ \hat{G}(t) * \hat{Y}_s^{i,j}(t + shift)$$

Local Coherence with Global Flux (LCGF)

The phase differences in the vasomotion signal identified by MCS indicate that the instantaneous flow rate through each cross section of the vascular network is not necessarily uniform. Necessarily, haemoglobin entering the field of view must travel through the arterioles before exiting through the venules. Because, during periods of increasing blood supply, the activity of the arterioles precedes that of the venules, we expected for a positive correlation between the signal from arteriole vessels and the change in global reflectance, and a negative correlation between the signal from venules and the change in global reflectance. As a result, we found that the sign of this correlation was indicative of vessel type. To reduce high frequency noise, we first low-pass filter the global reflectance at 1 Hz and then calculate:

$$LCGF\ image(i,j) = Y_s^{i,j}(t) * \partial G$$

where LCGF is the local coherence with global flux, and ∂G is the frame-by-frame change in global reflectance G after low-pass filtering.

Spontaneous Principal Component Analysis (sPCA)

Principal Component Analysis (PCA) was performed on spontaneous oscillations in reflectance as described before for stimulus-evoked representations (Biswal and

Kannurpatti 2009; Carmona et al. 1995; Everson et al. 1998; Mayhew et al. 2001; Narayanan and Laubach 2009; Reidl et al. 2007; Schiessl et al. 2008; Stetter et al. 2000; Vanzetta et al. 2004; Zepeda et al. 2004) with minor modifications. Low pass filtered (f<0.2 Hz) Y_s was down-sampled at 1 Hz and continuously recorded data was segmented into 15s long periods. The number of segments used for analysis depended on the time-course, and varied between 1-20. A composite segment, X, was formed as the average of each segment, sphered to zero mean and unit variance. The eigenvectors, V, of the covariance matrix of X were calculated, and the principal components, shown in 3E, were generated by multiplying X by the nth eigenvector, with the Component 1 having maximal variance.

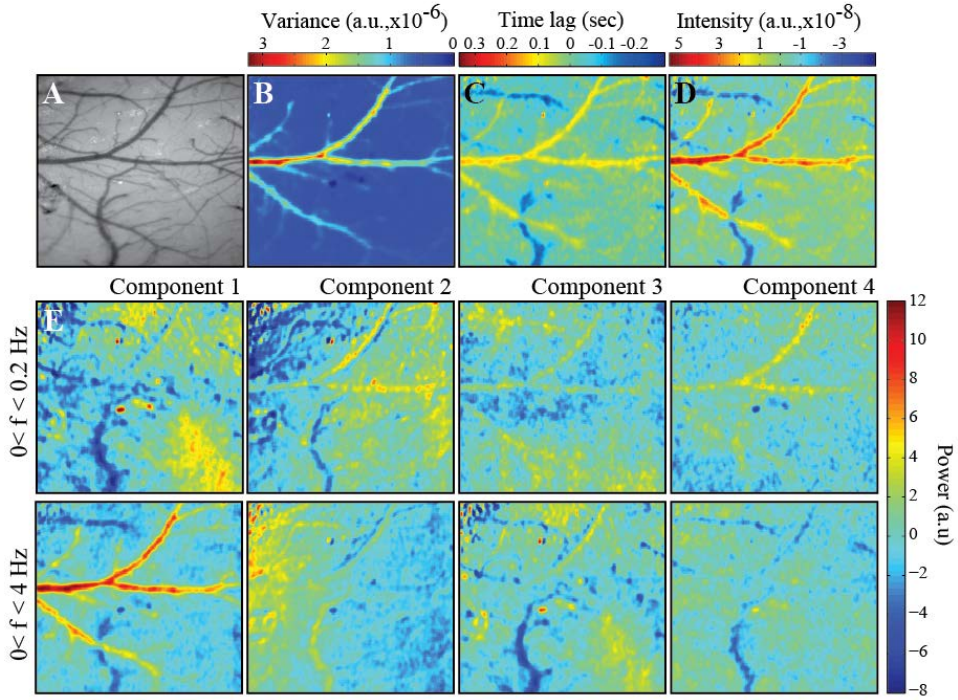

Figure 2.3. Reconstruction of the cerebral vasculature from low frequency spontaneous oscillations in light reflectance. (A) Cerebral vasculature visualized under 530 nm illumination, presented herein as a reference. (B) Power of oscillations in 0.2<f<4 Hz reconstructed into a 2D spatial representation. Note that this "Variance" method successfully detects larger arterioles with a typical branch diameter of >35µm. (C) Reconstruction of the phase offset in each pixel relative to the global reflectance with MCS. (D) Reconstruction of the coherence between regional CBV and global CBF into LCGF image. (E) First 4 Principal Components generated from low-passed (<0.2 Hz; upper panel) and band-passed (0<f<4 Hz;

lower panel) percent change in reflectance.

Direct visualization of vasculature under green light

A single frame of reflectance at 530 nm was used for direct visualization of the vasculature for reference purposes. To compensate for slowly varying reflectance properties, including uneven illumination, a Gaussian filter (σ = 140 μm) was applied. Subtraction of the smoothed image from the raw image produced a corrected image where vascularization is visualized (see i.e. Figure 2.3A).

Mutual information calculations

For quantitative analysis of the success in identification of vasculature using the aforementioned algorithms, we calculated the mutual information (MI) between the vasculature as identified under 530 nm anatomical illumination (P) and each reconstruction based on functional imaging at 625 nm (Q; Figure 2.4). To calculate the MI images, P and Q were first thresholded to produce binary maps, B_P and B_Q. Pixels in the highest x_P or x_Q percentiles, respectively, were assigned a value of 1, and all other pixels were assigned a value of 0. The entropy in Q was calculated as:

$$H(Q) = -f_{Q=0}\log_2\left(f_{Q=0}\right) - f_{Q=1}\log_2(f_{Q=1})$$

In addition, the entropy in Q given the elements of P was calculated using the probabilities (f) of a 0 or 1 occurring in Q given a 0 or 1 occurring in the same location of P:

$$\begin{aligned}H(Q|P) = -f_{P=0}[f_{Q=0|P=0}\log_2(f_{Q=0|P=0}) + f_{Q=1|P=0}\log_2\left(f_{Q=1|P=0}\right)] \\ - f_{P=1}[f_{Q=0|P=1}\log_2(f_{Q=0|P=1}) + f_{Q=1|P=1}\log_2\left(f_{Q=1|P=1}\right)]\end{aligned}$$

From these quantities, the mutual information was calculated as the difference between the original entropy in Q and the entropy in Q given P:

$$MI(Q,P) = H(Q) - H(Q|P)$$

This calculation was repeated for a range of threshold values, $x_P \in [1:30]$ and $x_Q \in [1:30]$, producing a mutual information matrix that quantitatively compares the success of vasculature classification algorithms against a common reference image.

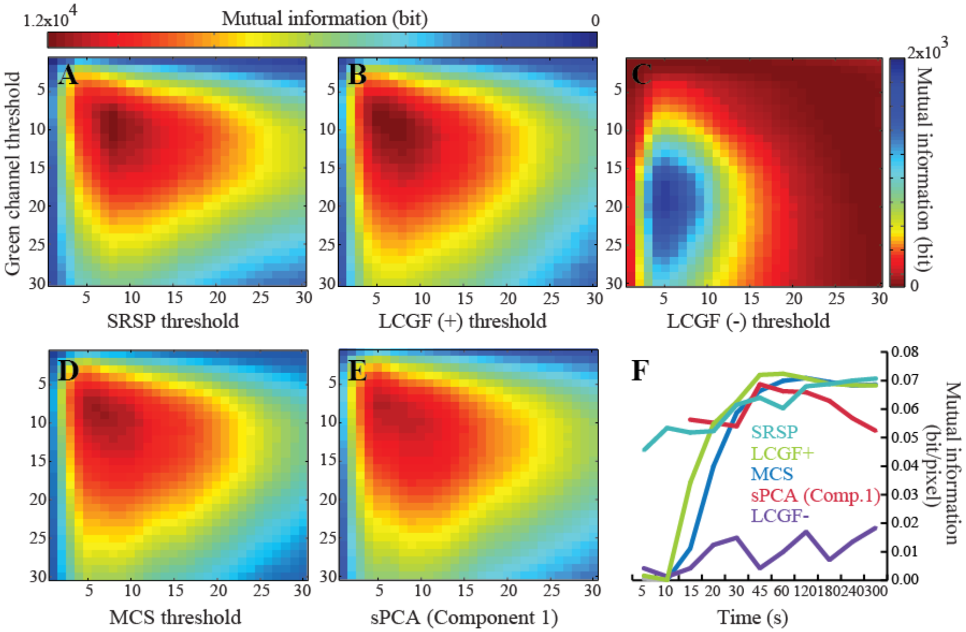

Figure 2.4. Analysis of the mutual information between vasculature identified using structural imaging at 530 nm and reconstructed images from functional imaging at 625 nm. (A-E) Plot of the mutual information (MI) between binary thresholds of the green image and reconstructions from (A) SRSP arterioles (300 s observation), (B) LCGF arterioles (60 s observation) (C) LCGF venules (60 s observation), (D) MCS arterioles (120 s observation), and (E) sPCA (Component 2, 0<f<4 Hz) (45 s observation). Observation windows were chosen to showcase each method at its best performing time-course for arterioles. (F) The relationship between MI and sampling duration.

Analysis of sensory evoked responses

To exemplify the use of vasculature identification algorithms for reconstruction of sensory evoked representations, whisker deflection evoked changes in intrinsic signals were studied as described above. Individual images collected at 60 Hz, under 625 nm illumination, were down-sampled (by averaging) into 0.5 second frames for analysis. In each trial (duration: 15 sec) the background reflectance was determined by averaging the last 6 frames prior to whisker deflection onset for the First Frame analysis (Frostig et al. 1990; Mayhew et al. 1996; Narayan et al. 1994; Obermayer and Blasdel 1993; Schiessl et al. 2008; Sheth et al. 2005). For each trial, the percent change in evoked reflectance, *E*, was identified by subtracting the background image and then dividing by it. The reflectance video was then averaged across 20 trials (E_{av}) to reduce the noise in spontaneous signals not phase-locked to the stimulus.

To generate the response containing stimulus-independent pixels, E_{av} was smoothed using a Gaussian filter (σ = 70 µm), and the median of each frame was subtracted to reduce the effect of low frequency noise. Figure 2.5D (left) shows a representative image, averaged from 1.5-2 seconds after stimulus onset.

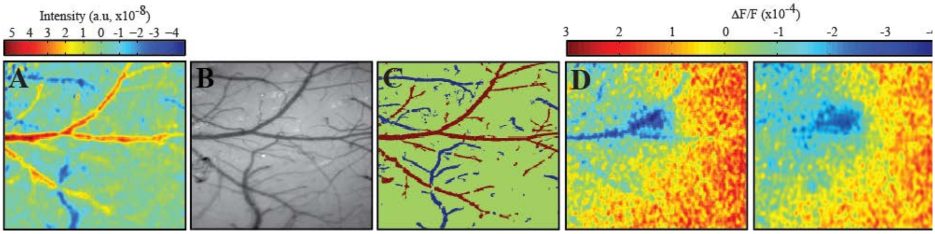

Figure 2.5. Application of vasculature identification techniques for classification of blood vessels, and removal of blood vessel artifacts from evoked responses. (A) Reconstruction of the coherence between local CBV and global CBF into LCGF image. (B) Raw image collected at 530 nm. (C) Back projection of LCGF values onto vessels identified under 530 nm produces a map of arterioles (red) and venules (blue). (D) Extraction of the vasculature artifact from whisker evoked representations in the mouse primary somatosensory cortex. Left: Image of the percent change in reflectance between 1.5-2 seconds after stimulus onset averaged over 20 trials shows corruption of functional response by arterioles. Right: Whisker evoked response, after the removal of vessels identified by SRSP and recovery of removed pixels using a bilinear interpolation function.

Removal of the vasculature artifact from evoked representations

To reconstruct sensory representations with reduced vasculature noise, pixels that preferentially carry stimulus-independent signal, i.e. arteriole pixels, were identified by thresholding the LCGF image (Fig 3D; threshold: top 15%). To prevent these arteriole pixels from corrupting their surroundings during smoothing, we removed them before applying the Gaussian filter. For image smoothing after pixel removal, we developed a specialized routine: First, a binary map was created with zeros marking the identified arteriole pixels and ones marking all other pixels. Each frame of E_{av} was multiplied by the binary map, Gaussian filtered (σ = 70 µm), and again multiplied by the binary map to give pre-adjusted frames. To correct for bias that resulted from introduction of the zero values (see above), the same Gaussian filter was applied to the binary map, resulting in an adjustment image with all values between 0 and 1. Dividing the pre-adjusted frames by the adjustment image (with the exclusion that 0/0 = 0), and subtracting the median from each frame gave the final images where stimulus-independent arteriole signal is excluded. To refill the gaps denoting vasculature, each frame was bilinearly interpolated and smoothed using a Gaussian filter ($\sigma = 49$ µm). The final frame representing the averaged evoked response between 1.5 and 2 seconds after stimulus is shown in Figure 2.5D (right).

Results

We developed image-processing algorithms for unsupervised identification of cerebral vascularization by visualizing temporally varying fluctuations in reflectance across the field of view. One of the main applications for these algorithms is to extract stimulus-independent changes in intrinsic signals to improve quantitative analysis of sensory-evoked representations in brain mapping experiments.

Spectral power of spontaneous oscillations vary across vasculatures

To investigate the temporal characteristics of changes in light reflectance across cerebral vasculature, we plotted the Fourier Power spectrum of the signal in pixels corresponding to arterioles, venules, capillaries, as well as the global reflectance, *G*, across the field-of-view (Figure 2.2A). Each power spectrum is constructed from the mean value of 49 pixels in a 7x7 region of interest (ROI). Spectral analysis of the global fluctuations in reflectance shows four distinct peaks at 0.05 Hz, 0.2 Hz, 1.6 Hz, and 3.4 Hz which correspond to rate of regional cerebral blood flow (rCBF), vasomotion, respiration, and heartbeat, respectively (Mayhew et al. 1996; Schiessl et al. 2008). The oscillatory nature of the reflectance varies across the vasculature. While signal recorded in arterioles replicate the spectral signature described for the global reflectance, signals from venules and capillaries oscillate predominantly in lower frequencies ($f<0.5$ Hz; Figure 2.2A).

Given the distinct spectral representation of the vasculature, image reconstruction based on band-pass filtered temporal fluctuations in intrinsic signals should reveal a pattern of vascularization. Figure 2.2B-E (lower panels) show the relative success of spatial reconstructions in narrow-pass (0.1 Hz) filtered data around the frequency peaks noted above. Reconstructions from $0<f<0.1$ Hz reveal little spatial dependency or vascular structure. Power in higher frequencies shows greater contrast between arterioles and other vessels or non vessels (parenchyma; Figure 2.2C-E) with highest SNR at $0.2<f<0.3$ Hz. This contrast may be partially explained by vasomotion at this frequency range (Dirnagl et al. 1989; Mayhew et al. 1999; Spitzer et al. 2001).

Spatial reconstructions in the $1.5<f<1.6$ Hz, which correspond to rate of respiration in mouse under our anesthetic conditions, also outline arterioles although normalized power of oscillations at this range is significantly smaller than the signal observed at $0.2<f<0.3$ Hz. Unlike the other peaks, the 3.4 Hz heartbeat reconstruction is not homogeneous across the arterioles. This difference suggests that pressures imposed by the micro-vascular structure of the arterioles might influence the signal magnitude. The heartbeat signal also contains a lower value for venules than the parenchyma (Figure 2.2E), in part due to the reduced pressure of blood after flowing through the capillaries.

Transforming spectral power information into a single image

In our methods, extraction of the stimulus-independent response is achieved by classification of pixels from a single image. To produce this image, it was necessary to combine spatial reconstructions from frequencies informative of vascular structure (e.g. Figure 2.2C-E), while ignoring frequencies with a low SNR (e.g. Figure 2.2B). The Spatial Reconstruction from Spectral Power (SRSP) algorithm achieves this by linearly summing spatial reconstructions for all frequencies ≥ 0.2 Hz (Figure 2.3B). The result correlates well with the arterioles identified in the snap shot at 530 nm (Figure 2.3A). A linear sum over reconstructions is justified here because it intrinsically weights each frequency by its contribution to the net signal's variance. The frequencies ≥ 0.2 Hz include information from vasomotion, heartbeat, and respiration, and exclude slower changes in rCBF. While the magnitude of slow oscillations <0.2 Hz was not spatially informative, their phase proved to be characteristic of each structure.

Phase of low frequency oscillations varies across vasculatures

Because rCBF may be considered as a physical wave, which originates in arterioles and propagates through vasculature to venules, it can be characterized by the temporal frequency of oscillations and the spatial wavelength between peaks. Empirically, we find that the wavelength of the rCBF signal is wider than the field of view, such that the relative phase of any pixel at a given time uniquely determines its up- or downstream position within the fluid blood flow network. Thus, by analyzing the typical difference between each pixel's phase and the global phase, we can reconstruct an image representative of the vascular structure. Moreover, this information has the potential to identify and distinguish both venules and arterioles from surrounding parenchyma.

Creating a vasculature map from phase information

We applied this theory to our data set using Maximal Covariance after Shift (MCS), which measures two signals' phase offset across a range of frequencies by identifying the time-shift that maximizes their covariance. We found that phase offsets between pixels, after low-pass filtering at <1.0 Hz, (Figure 2.3C) correlated well with vascular identity previously determined from spectral power (Figure 2.3B) and reflectance at 530 nm (Figure 2.3A). In addition, unlike SRSP, MCS classification resulted in separate labeling of arterioles, venules, and parenchyma, expanding the potential uses of spatial classification. Changes in covariance between zero shift and maximal shift were often small (mean = 1.5E-3, max = 4.2E-2, s.d. = 2.8E-3), but highly revealing of structure (Figure 2.3C).

Flow dynamics are representative of vasculatures

A separate motivation for measuring the spatial coherence of signals came specifically from blood flow and volume. In particular, we took advantage of the idea that changes in the total volume of blood throughout the field of view would have opposing correlations with activity in the sources (i.e. arterioles) and sinks (i.e. venules) of the network. We tested this hypothesis in our data set using the Local Coherence with Global Flux (LCGF) algorithm, and found that the resulting map captured much of the vascular structure within the field of view (Figure 2.3D).

Application of spontaneous principal component analysis

Unlike the SRSP, MCS, and LCGF, which attempt to identify vascular structure from distinct physiological phenomena, sPCA works under the principal that the vasculature will have an independent time-course with greater variance than the parenchyma. It is not immediately obvious that these distinctions need be present in spontaneous observation. However, we have shown previously, using the SRSP method, that arterioles have greater power at frequencies ≥ 0.2 Hz (Figure 2.2C-E). If the corresponding variance is sufficient to justify an independent arteriole time-course eigenvector, the back-projection of that arteriole eigenvector into a spatial representation is equivalent to measuring the covariance between each pixel's signal and the arteriole signal. In this case, the results of the MCS method predict that covariance, and therefore the spatial representation, would be strongest in the arterioles, followed by the parenchyma and finally by the venules.

The sPCA algorithm used herein is based on previous implementations of PCA on evoked intrinsic signals (Carmona et al. 1995; Everson et al. 1998; Mayhew et al. 1999; Narayan et al. 1995; Reidl et al. 2007; Schiessl et al. 2008; Stetter et al. 2000; Vanzetta and Grinvald 2001; Zepeda et al. 2004), PET (Pedersen et al. 1994), and fMRI (Biswal and Kannurpatti 2009). Depending on the configuration of input parameters (e.g. period of observation, down-sampling rate, number of components), we found that the spatial representation produced in the first or second of principal component (Figure 2.3E, lower panel Component 1) correlated with the vasculature maps attained by MCS (Figure 2.3C) and LCGF (Figure 2.3D). Subsequent representations (Figure 2.3E, lower panel Components 2-4) were dominated by signal from vasculature, but did not successfully separate venules from arterioles, and produced regional differences in the parenchyma.

Creating a vasculature map from phase information

Given the success of the algorithm, we were interested in determining which frequency sources contributed to the vasculature component. We found it unlikely that heartbeat or respiration were the primary source of classification because they account for a lesser percentage of the total power (Figure 2.2A), and the data was down-sampled to 1 Hz during pre-processing, causing partial attenuation of frequencies during aliasing. To investigate whether vasculature was distinguished by phase offsets of rCBFs or power distributions in vasomotion, we tested sPCA on data low-pass filtered < 0.2 Hz to isolate the rCBF signal before down-sampling. The results (Figure 2.3E, upper panel) do not show a reliable identification of vasculature. Alternatively, initial bandpass filtering $0.2 \leq f < 1.0$ Hz to isolate the vasomotion signal (results not shown) produced a vasculature component distinguishing venules from arterioles just as in the unfiltered data.

Quantitative comparison of vasculature classification methods

To compare the success of the four algorithms that reveal pattern of cerebral vascularization, we employed a mutual information (MI) metric that produced quantitative comparisons directly from binary maps, as opposed to a metric based on analog content of the images compared (e.g. normalized covariance). As a comparator, we used the snap shot of the field of view at 530 nm (Figure 2.3A).

Assumptions of Mutual Information Comparison: Comparison of arteriole identification among the four 625 nm methods revealed similar performance at each method’s optimal time-course (Figure 2.4 A,B,D,E). The mutual information between each of the binary maps produced by the SRSP, MCS, LCGF, and sPCA methods and the 530 nm snapshot are significantly above ($p << 1E-10$) the mutual information that would be produced by a random map, which approximately follows a Chi Square distribution with 1 degree of freedom (Federer 2011). However, interpreting the meaning of relative differences between each method’s mutual information value is challenging for several reasons. First, while stricter binary filters (i.e. pixels in lowest 5%) identified main arterioles for all methods, we observed that the 530 nm snap shot began filling in smaller arterioles or venules at less stringent thresholds while the 625 nm methods preferentially widened main arterioles before identifying smaller vessels. This may account for the saturation in mutual information at 10% thresholds, even though the MI between two identical images saturates at 50% thresholds. Second, the 530 nm snap shot is not an ideal classification image, and maps which have a higher mutual information in respect to the snap shot are not necessarily superior. Third, the snap shot is only justified as a quantitative comparison under the assumption that all 625 nm methods will be penalized relatively equally by the intrinsic differences. It is clear that this assumption is not met for comparisons between venule and arteriole identification, as both the shape and absolute maximum of mutual information for venule identification (Figure 2.4C) was significantly different from that for arterioles. By comparison, however, the arteriole identification from vasculature maps show highly correlated shapes, with the greatest correlation existing between MCS and sPCA ($r = 0.993$, $p < 0.001$ with Bonferroni correction for multiple comparisons), and the least correlation existing between SRSP and LCGF ($r = 0.953$, $p <0.001$ with Bonferroni correction), indicating that the comparison is relatively fair.

Optimal Time-course of Data Recording: Despite these uncertainties, quantitative mutual information evaluation relates well to qualitative performance observations, particularly in measuring the gain or loss of information over increasing periods of observation (Figure 2.4F). SRSP, MCS, and LCGF images from periods greater than one minute were computed by averaging images calculated from each minute of data prior to mutual information calculation. The information of each method is maximal at: 300s (SRSP); 120s (MCS); 60s (LCGF); 45s (sPCA).

Discussion

We have introduced analytical methods for mapping cerebral vasculature using intrinsic functional optical imaging. The algorithms are based on temporal analysis of spontaneous fluctuations in hemodynamic signals, and take advantage of the spectral and phasic changes in reflectance across the vasculature. Compared to the solutions previously developed (Table 1), these algorithms allow unsupervised identification and classification of the vasculature, and produce quantitatively tractable images, e.g. for blind separation of stimulus-independent changes in reflectance from evoked representations (see below).

Principles, underlying assumptions and limitations of our algorithmic solutions

Spatial Reconstructions from Spectral Power (SRSP) is based on the observations (Figure 2.2) that fluctuations in 625 nm reflectance are not uniform across the cortex and throughout the vasculature. The spatial dependence of power distributions may be related to the source of oscillatory changes in reflectance. For the data collected from the mouse somatosensory cortex and presented herein, discrete peaks at 0.2 Hz, 1.6 Hz, and 3.4 Hz correspond to oscillations introduced by vasomotion, respiration, and heartbeat, respectively.

Vasomotion, the spontaneous rhythmic changes in the tone of blood vessels, is closely linked to cyclic changes in cerebral blood flow (CBF) and volume (CBV) throughout the vascular network (Dirnagl et al. 1989; Mayhew et al. 1996). Given the role of arterioles in perfusion and the observation that CBF and CBV changes are largest and can be most readily studied in arterioles (Drew et al. 2011; Vanzetta et al. 2005), one would expect that arterioles would carry a dominant vasomotion signal. Our results agree with this prediction and show significantly stronger signal magnitude, at 0.2 Hz, in the arterioles rather than in venules or capillaries (Figure 2.2B). Interestingly, respiration induced changes in reflectance at 1.6 Hz shows the greatest magnitude difference between the arterioles and parenchyma, providing a strong contrast for arteriole identification. The contrast between arterioles and venules, on the other hand, is maximized at 3.4 Hz which argues that the magnitude of the heart beat on blood flow decreases as blood circulates through capillaries. Unlike vasomotion and respiration induced fluctuations in the intrinsic signals, heart beat induced oscillations show spatial inhomogeneity within the arterioles, which may be due to different pressures imposed by the micro-vascular structure of the arterioles.

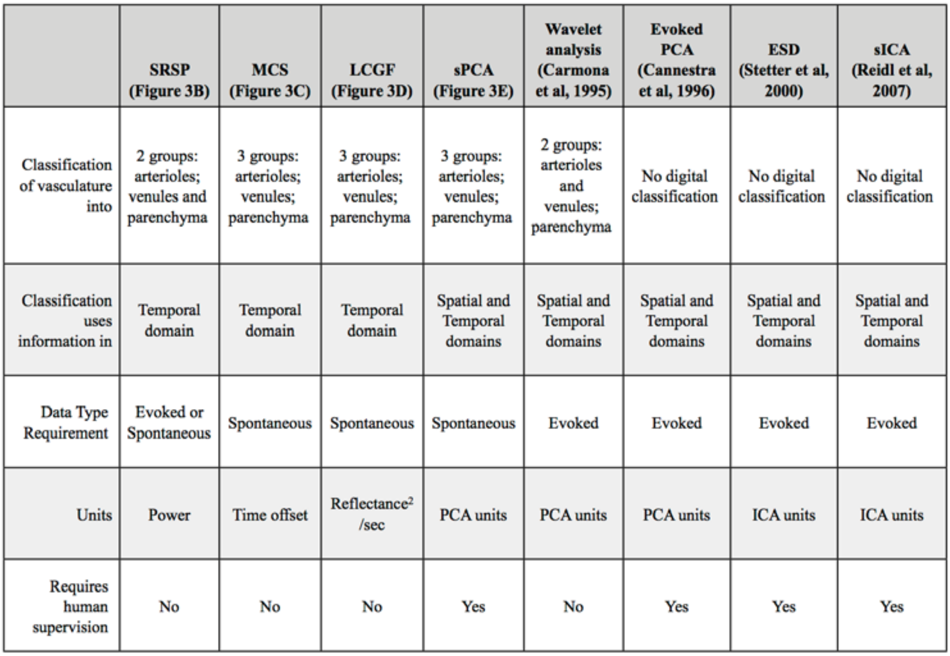

	SRSP (Figure 3B)	**MCS (Figure 3C)**	**LCGF (Figure 3D)**	**sPCA (Figure 3E)**	**Wavelet analysis (Carmona et al, 1995)**	**Evoked PCA (Cannestra et al, 1996)**	**ESD (Stetter et al, 2000)**	**sICA (Reidl et al, 2007)**
Classification of vasculature into	2 groups: arterioles; venules and parenchyma	3 groups: arterioles; venules; parenchyma	3 groups: arterioles; venules; parenchyma	3 groups: arterioles; venules; parenchyma	2 groups: arterioles and venules; parenchyma	No digital classification	No digital classification	No digital classification
Classification uses information in	Temporal domain	Temporal domain	Temporal domain	Spatial and Temporal domains	Spatial and Temporal domains	Spatial and Temporal domains	Spatial and Temporal domains	Spatial and Temporal domains
Data Type Requirement	Evoked or Spontaneous	Spontaneous	Spontaneous	Spontaneous	Evoked	Evoked	Evoked	Evoked
Units	Power	Time offset	Reflectance^2 /sec	PCA units	PCA units	PCA units	ICA units	ICA units
Requires human supervision	No	No	No	Yes	No	Yes	Yes	Yes

Table 2.1. Comparison of image processing algorithms to extract structural anatomical information from functional signals.

Given the greater power in arterioles across the entire spectrum (Figure 2.2), it may appear that taking the variance of each pixel would provide a reliable map of arterioles. However, we find that the greatest contribution to the variance originates from changes in regional CBF at frequencies <0.2 Hz, which show significantly less contrast between the vasculature and parenchyma than other frequency peaks. For this reason, we omit these frequencies from the final SRSP image, integrating over the power spectrum only for frequencies ≥ 0.2 Hz.

The emphasis on information from higher frequency signals for use in vessel identification may be compared to the method employed by Carmona and colleagues (1995) for wavelet analysis. Carmona *et al.*'s processed the raw signal by integrating over the absolute value of the time derivative of each pixel's reflectance. When thinking of the raw signal as the sum of its sinusoidal components, the derivative weights each oscillation by its frequency, numerically penalizing the contribution from low frequency components. While Carmona and colleagues justify the derivative through physiological means, the results of our SRSP method suggest that this weighting has a direct numerical benefit by amplifying the contribution of frequencies with greater signal to noise ratio.

Finally it should be noted that our vasculature reconstruction based on SRSP would been different, albeit only minimally, had we integrated over a log frequency scale rather than a linear one. The decision on how to reconstruct the final SRSP image is fairly arbitrary by nature, as any method taking linear combinations of frequency components could be justified. We chose uniformly weighted integration because of its relative simplicity, its theoretical relationship to the variance, and its success for the conditions of our experiment.

Maximal Covariance after Shift (MCS) algorithm is our attempt to directly visualize the phase differences between the slow oscillations in the global signal and individual pixels. Since the discovery of the slow 0.2 Hz vasomotion oscillation, its spatial coherence has been of interest (e.g. (Mayhew et al. 1996)). Although we have shown that the magnitude of this signal varies across different vasculature (see above), phase differences can be more difficult to visualize, as they require higher temporal resolution for detection. One method to detect phase differences between signals is to investigate the differences between each signal's complex Fourier series. Because each physiological source of the intrinsic signals carry information across frequency range, it is necessary to combine information from more than one frequency band in the discrete Fourier spectrum. In its general form, this combination requires a metric which considers the magnitude and direction of the phase offset, the power contribution with respect to the overall signal variance, and the absolute frequency for each band of the discrete Fourier spectrum across both signals.

To accomplish this complex task, we apply the MCS algorithm, which intrinsically takes these parameters into consideration with a simple and intuitive concept: the phase of two signals will be best aligned when their covariance is maximal. If the two signals are nearly aligned to start with, as is the case for the low frequency oscillations across the field of view, temporally shifting one signal in respect to another will either act to better align their phase, hence increasing the covariance, or further separate the phase, decreasing the covariance. The magnitude and sign of this change depends on the initial separation, allowing computation of each pixel's offset from the global phase across the field of view.

Our data show that the phase distribution of intrinsic signals is not random, but is directly associated with the flow dynamics of the network. While phase of the arteriole signal leads the global phase, the phase of the venule signal follows it. Interestingly, capillary signal's phase is relatively well aligned with the global phase. These observations are consistent with a model of the low frequency oscillations propagating along arteriole-capillary-venule path of the blood flow. The difference in phase may be equated to the time required for the signal to cross the field of view, in our case ~0.25 s. This time window is in agreement with previous observations of the delay between CBV increase and the corresponding increase in CBF (Jones et al. 2001; Malonek et al. 1997).

Local Coherence with Global Flux (LCGF): The phase differences revealed by MCS also indicate that the oscillations seen in the global reflectance (Figure 2.1A) are not uniform throughout the network. Moreover, the net flow through the arterioles can be greater or less than the net flow through the venules - this difference is particularly evident during evoked activity, when blood flow and oxygen levels are increased in isolated loci. When the global flow is positive, the arterioles should be carrying more blood, and the opposite should be true when the total global flow is negative. Therefore, regions with higher local CBV when the global blood volume is increasing are likely to contain arterioles, and regions with higher local CBV when global blood volume is decreasing are likely to contain venules. This relationship may be examined using inner product of local cerebral blood volume in each frame and the derivative of the global blood volume. The scalar result is positive for arterioles and negative for venules (Figure 2.3D).

Spatial vs temporal domain of information in intrinsic signals for vasculature identification

Intrinsic signals are complex. Even single pixel values oscillate at various time scales, which, as we have shown, contain quantitative information regarding the cerebral vasculature. Hemodynamic signals also carry information in the spatial domain. The source of the perfusion to the neural tissue, directionality of network flow, systematic changes in the vasculature size and functional coupling between neighboring regions all contain spatial knowledge which can be used to extract the pattern of vasculature. However, as we have shown, temporal data also contains information about the vasculature. One advantage of the temporal methods is that they are better suited for separate identification of venules and arterioles, which have otherwise similar spatial structure.

A reason for the strong performance of temporal methods is that they include the same implicit, and valuable, assumption used by spatial methods when applying a Gaussian spatial filter before temporal analysis. While designed to decrease detector (i.e. CCD) noise, the Gaussian filter simultaneously enforces the assumption that pixels in the same region will have a similar identity. While this assumption is well justified by physical connectivity of blood vessels, it also causes neighboring adjacent pixels to be too similar to differentiate by further spatial analysis. As a result, most of the local spatial information is lost, placing an upper bound on the potential of continued local analysis in the spatial domain. While spatial analysis on larger scales (e.g. distinguishing between the linear vessels and the elliptical mapping signal) remains relatively unaffected by this limitation, image-wide features are more qualitative by nature, and taking advantage of them quantitatively is both harder to justify theoretically and harder to implement algorithmically. Further spatial analysis is intrinsically penalized by the prior application of the Gaussian filter, however the quality of information in the temporal domain is improved. This is mainly because the underlying physiological signals are spatially homogenous in local regions to begin with, and Gaussian averaging only makes their expression more robust. Essentially, this allows investigation of signals within the frequency domain, which appears to contain independent and otherwise unexploited information.

Our methods use blind source separation, make no further assumptions about the spatial domain, and avoid tampering with image units, therefore it is possible to apply many of the powerful spatially-based methods (see introduction) upon extraction of the stimulus-independent component using the frequency domain. For example, it remains to be seen whether a variation of wavelet analysis or ESD analysis could be used in combination with one or more temporal methods discussed here to enhance the current identification process.

Application of vasculature identification methods in functional brain mapping experiments

There has been a long-standing interest in vessel identification algorithms in functional imaging studies (Carmona et al. 1995; Frostig et al. 1990; Reidl et al. 2007; Schiessl et al. 2008; Stetter et al. 2000; Vanzetta et al. 2005; Zheng et al. 2001). Mapping vasculature in evoked data is particularly important, as its identification will allow removal of vasculature noise from neural representations of the stimulus. Current solutions, such as subtraction of orthogonal stimulus conditions, or application of PCA, ICA, sICA, ESD, and others, commonly remove vessel artifacts without reconstructing the vasculature map or identifying the type of vasculature.

As discussed previously, part of the reason these spatiotemporal algorithms struggle is that the signal in arterioles is dynamically coupled with the evoked signal. While PCA is successful in amplifying the SNR over classical methods, it also carries some of the vessel artifacts into the mapping components (Reidl et al. 2007; Schiessl et al. 2008; Stetter et al. 2000). To clean these components, ICA may be employed to look for distinct spatial sources in the principal components. This process is designed to remove pixels in the stimulus-evoked component that also show up in the vasculature components (Reidl et al. 2007; Schiessl et al. 2008), which is essentially the same objective that our algorithms use. However, unlike binary removal methods, the penalty applied to these pixels in ICA is very hard to adjust for, because it is calculated in the nonlinear domain of ICA.

We have shown that our methods are capable of producing similar results using information from the temporal domain without some of the difficulties associated with previous methods. Once vessel artifacts have been removed from the image, quantitative vessel analysis using classical methods becomes much easier, as algorithms targeted to the evoked response need not worry about the influence of noise from the vasculature.

A further advantage of removing vessels is that the subtraction of the median image after First Frame Analysis (Frostig et al. 1990; Mayhew et al. 2001; Narayan et al. 1994; Obermayer and Blasdel 1993; Schiessl et al. 2008; Sheth et al. 2005) can provide a better approximation of the spontaneous noise. As seen in Figure 2.2, the low frequency noise is stronger in vessels – damaging the spatial homogeneity of the low frequency signal. By removing vessels before the calculation of the median, the median will better represent the noise in vessel free tissue, which is where most of the stimulus-evoked representations reside.

In addition to removing the vasculature noise, we are able to recover some of the lost information under the assumption that a removed pixel would have a similar evoked response to neighboring pixels had it not been overlapped by the vasculature. Conveniently, this assumption appears to be valid when the pixel is within the evoked response. We take advantage of this assumption by bilinearly interpolating values for removed pixels, refilling the gaps in the image (Figure 2.5E).

Algorithms described herein allow direct identification and classification of the cerebral vasculature. Although they were originally developed for the blind separation of vasculature noise from evoked representations to automate quantitative analysis of sensory representations, they are likely to find other applications including measurement of phase-based flow changes to study hemodynamic coupling across large cortical territories and chronic study of revascularization following a stroke.

References

Biswal BB, and Kannurpatti SS. Resting-state functional connectivity in animal models: modulations by exsanguination. *Methods Mol Biol* 489: 255-274, 2009.

Blasdel GG, and Salama G. Voltage-sensitive dyes reveal a modular organization in monkey striate cortex. *Nature* 321: 579-585, 1986.

Bonhoeffer T, and Grinvald A. Optical imaging based on intrinsic signals: The methodology. In: *Brain Mapping: The Methods*, edited by Toga A, and Mazziotta J. San Diego: Academic, 1996, p. 55-97.

Cannestra AF, Blood AJ, Black KL, and Toga AW. The evolution of optical signals in human and rodent cortex. *Neuroimage* 3: 202-208, 1996.

Carmona RA, Hwang WL, and Frostig RD. Wavelet analysis for brain-function imaging. *IEEE Trans Med Imaging* 14: 556-564, 1995.

Chambers R, and Zweifach BW. Intercellular cement and capillary permeability. *Physiol Rev* 27: 436-463, 1947.

Dirnagl U, Kaplan B, Jacewicz M, and Pulsinelli W. Continuous measurement of cerebral cortical blood flow by laser-Doppler flowmetry in a rat stroke model. *J Cereb Blood Flow Metab* 9: 589-596, 1989.

Drew PJ, Shih AY, and Kleinfeld D. Fluctuating and sensory-induced vasodynamics in rodent cortex extend arteriole capacity. *Proc Natl Acad Sci USA* 108: 8473-8478, 2011.

Everson RM, Prashanth AK, Gabbay M, Knight BW, Sirovich L, and Kaplan E. Representation of spatial frequency and orientation in the visual cortex. *Proc Natl Acad Sci USA* 95: 8334-8338, 1998.

Federer A. Estimating networks using mutual information. Thesis: Department of Mathematics, Swiss Federal Institute of Technology Zurich, 2011.

Frostig RD, Lieke EE, Ts'o DY, and Grinvald A. Cortical functional architecture and local coupling between neuronal activity and the microcirculation revealed by in vivo high-resolution optical imaging of intrinsic signals. *Proc Natl Acad Sci USA* 87: 6082-6086, 1990.

Geladi P, Isaksson H, Lindqvist L, Wold S, and Esbensen K. Principal component analysis on multivariate images. *Chemometrics and Intelligent Laboratory Systems* 5: 209-220, 1989.

Golanov EV, Yamamoto S, and Reis DJ. Spontaneous waves of cerebral blood flow associated with a pattern of electrocortical activity. *Am J Physiol* 266: R204-214, 1994.

Grinvald A, Frostig RD, Siegel RM, and Bartfeld E. High-resolution optical imaging of functional brain architecture in the awake monkey. *Proc Natl Acad Sci USA* 88: 11559-11563, 1991.

Jones M, Berwick J, Johnston D, and Mayhew J. Concurrent optical imaging spectroscopy and laser-Doppler flowmetry: the relationship between blood flow, oxygenation, and volume in rodent barrel cortex. *Neuroimage* 13: 1002-1015, 2001.

Kalatsky VA, and Stryker MP. New paradigm for optical imaging: temporally encoded maps of intrinsic signal. *Neuron* 38: 529-545, 2003.

Lieke EE, Frostig RD, Arieli A, Ts'o DY, Hildesheim R, and Grinvald A. Optical imaging of cortical activity: real-time imaging using extrinsic dye-signals and high resolution imaging based on slow intrinsic-signals. *Annu Rev Physiol* 51: 543-559, 1989.

Malonek D, Dirnagl U, Lindauer U, Yamada K, Kanno I, and Grinvald A. Vascular imprints of neuronal activity: relationships between the dynamics of cortical blood flow, oxygenation, and volume changes following sensory stimulation. *Proc Natl Acad Sci U S A* 94: 14826-14831, 1997.

Mayhew J, Johnston D, Martindale J, Jones M, Berwick J, and Zheng Y. Increased oxygen consumption following activation of brain: theoretical footnotes using spectroscopic data from barrel cortex. *Neuroimage* 13: 975-987, 2001.

Mayhew J, Zheng Y, Hou Y, Vuksanovic B, Berwick J, Askew S, and Coffey P. Spectroscopic analysis of changes in remitted illumination: the response to increased neural activity in brain. *Neuroimage* 10: 304-326, 1999.

Mayhew JE, Askew S, Zheng Y, Porrill J, Westby GW, Redgrave P, Rector DM, and Harper RM. Cerebral vasomotion: a 0.1-Hz oscillation in reflected light imaging of neural activity. *Neuroimage* 4: 183-193, 1996.

Molgedey L, and Schuster HG. Separation of a mixture of independent signals using time delayed correlations. *Phys Rev Lett* 72: 3634-3637, 1994.

Narayan SM, Esfahani P, Blood AJ, Sikkens L, and Toga AW. Functional increases in cerebral blood volume over somatosensory cortex. *J Cereb Blood Flow Metab* 15: 754-765, 1995.

Narayan SM, Santori EM, Blood AJ, Burton JS, and Toga AW. Imaging optical reflectance in rodent barrel and forelimb sensory cortex. *Neuroimage* 1: 181-190, 1994.

Narayanan NS, and Laubach M. Methods for studying functional interactions among neuronal populations. *Methods Mol Biol* 489: 135-165, 2009.

Obermayer K, and Blasdel GG. Geometry of orientation and ocular dominance columns in monkey striate cortex. *J Neurosci* 13: 4114-4129, 1993.

Parri R, and Crunelli V. An astrocyte bridge from synapse to blood flow. *Nat Neurosci* 6: 5-6, 2003.

Pedersen F, Bergstrom M, Bengtsson E, and Langstrom B. Principal component analysis of dynamic positron emission tomography images. *Eur J Nucl Med* 21: 1285-1292, 1994.

Reidl J, Starke J, Omer DB, Grinvald A, and Spors H. Independent component analysis of high-resolution imaging data identifies distinct functional domains. *Neuroimage* 34: 94-108, 2007.

Roy CS, and Sherrington CS. On the Regulation of the Blood-supply of the Brain. *J Physiol* 11: 85-158 117, 1890.

Schiessl I, Wang W, and McLoughlin N. Independent components of the haemodynamic response in intrinsic optical imaging. *Neuroimage* 39: 634-646, 2008.

Sheth SA, Nemoto M, Guiou MW, Walker MA, and Toga AW. Spatiotemporal evolution of functional hemodynamic changes and their relationship to neuronal activity. *J Cereb Blood Flow Metab* 25: 830-841, 2005.

Spitzer MW, Calford MB, Clarey JC, Pettigrew JD, and Roe AW. Spontaneous and stimulus-evoked intrinsic optical signals in primary auditory cortex of the cat. *J Neurophysiol* 85: 1283-1298, 2001.

Stetter M, Schiessl I, Otto T, Sengpiel F, Hubener M, Bonhoeffer T, and Obermayer K. Principal component analysis and blind separation of sources for optical imaging of intrinsic signals. *Neuroimage* 11: 482-490, 2000.

Ts'o DY, Frostig RD, Lieke EE, and Grinvald A. Functional organization of primate visual cortex revealed by high resolution optical imaging. *Science* 249: 417-420, 1990.

Vanzetta I, and Grinvald A. Evidence and lack of evidence for the initial dip in the anesthetized rat: implications for human functional brain imaging. *Neuroimage* 13: 959-967, 2001.

Vanzetta I, Hildesheim R, and Grinvald A. Compartment-resolved imaging of activity-dependent dynamics of cortical blood volume and oximetry. *J Neurosci* 25: 2233-2244, 2005.

Vanzetta I, Slovin H, Omer DB, and Grinvald A. Columnar resolution of blood volume and oximetry functional maps in the behaving monkey; implications for FMRI. *Neuron* 42: 843-854, 2004.

Villringer A, and Dirnagl U. Coupling of brain activity and cerebral blood flow: basis of functional neuroimaging. *Cerebrovasc Brain Metab Rev* 7: 240-276, 1995.

Villringer A, Haberl RL, Dirnagl U, Anneser F, Verst M, and Einhaupl KM. Confocal laser microscopy to study microcirculation on the rat brain surface in vivo. *Brain Res* 504: 159-160, 1989.

Zepeda A, Arias C, and Sengpiel F. Optical imaging of intrinsic signals: recent developments in the methodology and its applications. *J Neurosci Methods* 136: 1-21, 2004.

Zheng Y, Johnston D, Berwick J, and Mayhew J. Signal source separation in the analysis of neural activity in brain. *Neuroimage* 13: 447-458, 2001.

Chapter 3. BARREL CORTEX *IN SILICO*

Abstract

With six layers and ~12000 neurons across tens of different classes, a cortical column is a complex network whose function is plausibly greater than the sum of its constituents'. Understanding the function of every single network component will require going beyond the brute-force modulation of neural activity while observing the behavior of a small group of neurons (as most current cutting-edge experimental designs employ). Therefore, in this Chapter, we develop a computational model of the somatosensory cortical column and begin addressing the network mechanisms of touch *in silico*. The development of the model requires three independent approaches starting with the reconstruction of the barrel cortex in soma resolution using multi-channel mosaic scanning confocal microscopy. We then define a mathematical model of the cortical neuron, originally based on the quadratic Izhikevich model, whose action potential threshold adapts to the rate of ongoing network activity impinging onto the postsynaptic neuron. Connecting each neuron in the network using statistical rules of pair-wise connectivity results in a functional cortical column *in silico*. Simulation of whisker touch representations in this network showed that the *in silico* network predicts the population response of touch representations in the barrel cortex *in vivo* while providing new insights on the role of membrane states in gating, otherwise gain-modulation of sensory representations in a layer, column and input specific manner.

Introduction

One of the grand challenges in Neuroscience is to mechanistically describe the cerebral cortical function in any mammalian model system. Over the last century increasing number of studies have focused on elucidating the cerebral cortical organization and function. The majority of these works, however, focused on the anatomy of the cortex and unravelling the structural organization of the cortical networks. By describing the principles of neuronal classification, cell-type specific projection patterns (Lübke & Feldmeyer 2007, Schubert et al 2007, Oberlaender et al 2012a), input-output mapping across cortical layers (Lefort et al 2009), and by functional characterization of the anatomically identified neurons upon simple stimulation conditions, these studies have identified cortical organizational principles across model systems as well as a number of cortical areas (Douglas & Martin 2004). Although such a wiring-diagram approach is critical for a structural description of the network, relating the structure to function requires detailed study of the dynamical processes in single neurons as well as neural populations (Douglas & Martin 2007, O’Connor et al 2009).

The barrel cortex of rodents is an ideal model to bridge what is known about the structural organization of the cortical column with its function in freely behaving animals, for example upon whisker touch with a tactile target (Celikel & Sakmann 2007, Von Heimendahl et al 2007). Whiskers are functionally analogous to human fingers. Just like fingers, they are represented topographically in the cortex as somatosensory and motor maps. A whisker contact with a tactile target activates a trisynaptic network that brings spatially constrained sensory information to the barrel cortex. These topographical projections predominantly terminate at the Layer (L) 4 of the principal cortical column of a given whisker. The feed-forward projections from L4 primarily target L2/3 neurons within the same column, which in turn project to other L2/3 neurons in neighboring columns. These cross-columnar projections are believed to be the principal circuits that form supragranular sensory maps and mediate functional integration of sensory information across individual whiskers (see Brecht 2007, Lübke & Feldmeyer 2007, Schubert et al 2007, Feldmeyer et al 2012 for review).

Neurons in a column share a common principal whisker and have similar receptive fields; the principal whisker of each column evokes the largest amount of activity while the activity induced by surround whisker deflections gradually decreases with the distance between the principal and surrounding whisker of interest (Brecht & Sakmann 2002, Brecht et al 2003). This receptive field organization has dominated our understanding of the functional representations in the barrel cortex although growing evidence suggest that the majority of single neurons’ contribution to sensory representations are neither reliable nor persistent across different whisker contacts with the same object (O’Connor et al

2010, Crochet et al 2011).

With a circuit organization that favors population encoding of the stimulus, and the well-defined cellular anatomy at single neuron resolution, the barrel column is ideally suited as a model system for computational reconstruction. Here we develop a fully functional, biologically constrained network that will ultimately help to understand the line between the structural organization of the network and its functions.

Materials and Methods

Tissue preparation and immunochemistry

Juvenile mice from either sex were perfused using 4% paraformaldehyde before tangential sections were prepared. To ensure that cortical layers were orthogonal to the slicing plane the cortex was removed from the subcortical areas and medio-lateral and rostro-caudal borders trimmed. The remaining neocortex included the entire barrel cortex and was immobilized between two glass slides using four 1.2 mm metal spacers. The rest of the histological process, including post-fixation and sucrose treatment were performed while the neocortex was flattened. All care was given to ensure that the tissue is as flat as possible at the time of placement onto the sliding horizontal microtome. 50 micron sections were cut and processed using standard immunohistochemical protocols. The following antibodies were used: anti-NeuN (Millipore, Chicken), anti-GAD65 (Boehringer Mannheim, Mouse), anti-Somatostatin (SST, Millipore, Rat), anti-Parvalbumin (PV, Swant Antibodies, Goat) at concentrations suggested by the provider.

The imaging was performed using a Leica Confocal microscope (LCS SP2) with a 40X oil-immersion lens (NA 1.4). Each section sequentially cutting across layers was individually scanned with 512x512 pixel resolution; signal in each pixel was average after 4 scans and before it was stored. The alignment of each section was performed manually by trained human observers.

Automated cell counting

All image analysis was done using a custom-written running toolbox on Matlab 2012b with an Image Processing Toolbox add-on (Mathworks).

Nucleus-staining channels (NeuN, Parvalbumin and Calretinin)

Most fluorescence imaging methods, including confocal microscopy, have several shortcomings that make the automated cell identification a challenging task: First, the background intensity of images is often uneven due to light scattering and tissue auto-fluorescence. Shading and bleaching of fluorophores further add to this problem when acquiring multiple confocal images at the same location. Second, intensity variation within a single cell might cause over-segmentation of the cell. Third, the intensity of different neuron population turns to be very different because they absorb fluorescent dye unevenly. Specifically, GAD65+ and SST+ neurons usually have weakly stained nucleus as visualized by anti-NeuN antibody, making non-linear gain modulation necessary in a cell-type specific manner. To overcome these problems and maximize the hit and correct rejection rate over miss and false positives (i.e. (H+CR)/(M+FP)), we have developed the following pipeline:

Pre-processing: The goal of pre-processing is to obtain relatively consistent images from original fluorescent images with varying quality to pass to cell count algorithm, so the same algorithm can process a large variety of images and still get consistent result.

Median filtering: A median filter with 3×3×3 pixel neighbourhood is applied to fluorescent image stacks to smooth intensity distribution within each image stack in 3D. This operation removes local high-frequency intensity variations (Figure 3.1b).

Vignetting correction: Vignetting is the phenomenon of intensity attenuation away from the image center. We use a single-image based vignetting correction method (Zheng et al 2009) to correct for the intensity attenuation (Figure 3.1c). The algorithm extracts vignetting information using segmentation techniques, which separate the vignetting effect from other sources of intensity variations such as texture. The resulting image is foreground, i.e. the cellular processes, on a homogenous background.

Background subtraction: The background illumination can result from non-specific bonding of antibodies or auto-fluorescence of the tissue. To reduce the background noise, local minima in each original grayscale image are filled by morphological filling, and background is estimated by morphological opening with 15 pixel radius disk-shaped structuring element. The radius value is chosen to be comparable to largest object size so the potential object pixels are not affected. The estimated background is then subtracted from original image to enhance the signal-to-noise ratio (SNR) (Figure 3.1d).

Contrast-limited adaptive histogram equalization (CLAHE): CLAHE (Zuiderveld 1994) enhances local contrast within individual images by remapping intensity value of each pixel using a transformation function derived from its neighbourhood. This increases local contrast and amplifies the signal from weakly stained cells, as well as reduces global intensity difference, which partially corrects for the un-even illumination that individual fluorescent images often suffer from (Figure 3.1e). CLAHE is applied using an 8×8 tiles division for each image. Images from channels with very low number of positive staining with high SNR (e.g. Calretinin staining channel) are not processed with CLAHE.

Image segmentation to identify cell nucleus

Black-and-white image transform is applied to grey scale images to separate foreground, i.e regions presumably contain nuclei, from background. In the ideal conditions, if all the objects were stained evenly during immunochemistry, the image pixels' intensity value will be distributed as two well-separated Gaussian distributions. However, objects are usually not evenly stained; specifically, GAD65+ and SST+ neurons usually have weak NeuN staining. As a result, the intensity distribution for object pixels is very broad and cannot be described by a single Gaussian distribution. To reliably identify foreground pixels we calculated threshold values using 2-level Otsu's method (Otsu 1979), which separates the pixels into 3 groups. The group with lowest intensity reliably captures the background pixels, and the other 2 groups are set to foreground. This transformation is directly applied to the 3D image stack to obtain a 3D foreground (Figure 3.1f).

Marker-based watershed segmentation: The B&W transform identified regions that contain cell nuclei, albeit non-specifically, and it does not identify the location and shape of each individual nucleus stained. Therefore image segmentation is needed to identify individual nuclei. The watershed method (Meyer 1994) is an efficient way of segmenting grey scale images, i.e. separates the foreground part of an image obtained by the B&W transformation based on the intensity gradient, and has the advantage of operating on the local image gradient instead of the global gradient. However, a direct application of the watershed method usually results in an over-segmentation of nuclei due to the local intensity variation within individual nuclei. To overcome this problem, the marker-based watershed algorithm is employed, in which markers serving as the starting 'basin' for each object are first placed on the image to be segmented, and the watershed algorithm is then applied to produce one segment (or object) on each marker.

We computed the markers by applying a regional maxima transform on foreground grey-scale images. To ensure at most one marker is placed in each nucleus, the grey-scale image need to be smoothed first to eliminate local intensity variation. This is realized by applying a morphological opening-by-reconstruction operation (Vincent 1993) with 5 pixels radius on foreground grayscale image, which removes small blemishes in each individual nucleus and ensures that the regional maxima transform can find foreground markers accurately.

After identifying the markers, the watershed algorithm is applied (Figure 3.1g). To ensure an accurate detection of cell boundaries, the B&W foreground need to enclose the entire cell object. This image dilation is applied to the B&W foreground to enlarge it by 1 pixel in radius before application of the watershed algorithm. Finally, objects with volume smaller than 400 voxels in total are removed by morphological opening.

Correction for clusters of connected neurons: Clusters of closely located neurons are not always successfully separated without further image processing; especially when closely located neurons all have similar intensity values. In such cases the application of the intensity-based watershed algorithm results in the identification of one instead of many real neurons (see Figure 3.1b). Furthermore, our strategy of augmenting the regional intensity similarity during watershed segmentation actually increases the chance of under-segmentation during clustering. To correct for this under-segmentation we employed the following approach:

a. The volume (total number of voxels) of all identified objects is calculated, and objects with a volume larger than mean+std of the population are labelled as “potential clusters”.

b. For each object in the potential cluster list, the original grey-scale image is retrieved. Then, from all the voxels contained in the object, the 50% voxels with the lowest intensity value are removed, generating a new B&W object with smaller size. Because usually those low-intensity pixels are usually from the periphery region of each individual neuron, the new B&W object has a better separation between different neurons.

c. A Euclidean distance-based 3-D regional maximum transform is then applied to the new, smaller B&W 3-D candidate object, in which the distance from each voxel belongs to the object to the border of the object, is calculated. Assuming neurons have Ellipsoid-like shapes, the peak (largest distance from the border) of this transform will likely be the centre of neurons, even if the object consists of several connected neurons. The regional maximum transform is then applied to locate those peaks in Euclidean distance space. Before the regional maximum transform is applied, the target image is smoothed by the morphological opening-by-reconstruction operation described before with a 1 voxel radius to remove small local variations.

d. If more than one centre is found (in c) the watershed method is applied to the distance transform of the original B&W object, using the identified centres as markers. If only one centre is found then the cluster is judged as a single neuron and removed from the list. Again, the distance metric is smoothed by morphological opening-by-reconstruction operation before the watershed algorithm is applied.

e. Steps a-d are repeated until the “potential cluster list” is empty (Figure 3.1h).

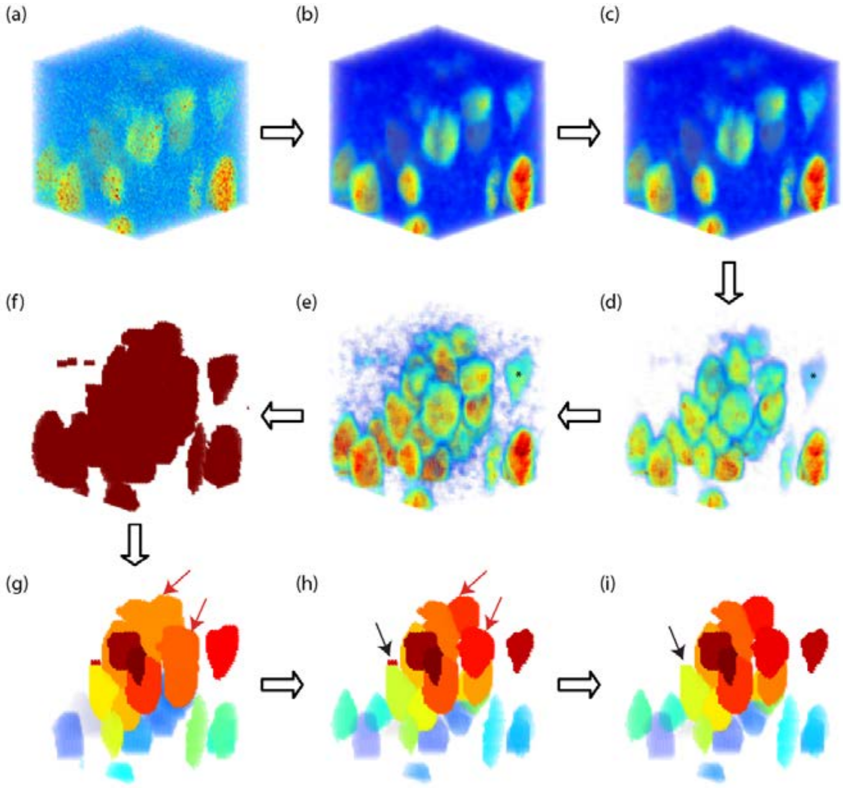

*Figure 3.1. Automatic cell counting for soma-staining channels. The example is an anti-NeuN+ staining volume. (a) Original 3D image stack obtained from Z-scan confocal imaging. (b) Median filtering with a 3-by-3-by-3 pixel neighborhood to reduce local intensity variation in the image. (c) Vignetting correction using single-image based method. (d) Background subtraction to reduce the background intensity level. (e) Contrast-limited adaptive histogram equalization (CLAHE) to enhance local contrast. Notice the contrast enhancement effect on the weakly stained cell marked with * in (d) and (e). (f) Black-and-white (B&W) transform to separate foreground objects from the background. (g) Marker-base watershed segmentation on the BW image. Identified objects are labelled with different colors. Notice the cell clusters pointed with red arrows, which are under-segmented by the watershed algorithm. (h) Cluster-separation using a Euclidean distance transform. The under-segmented clusters in (g) are further segmented, as the red arrows pointed out in (g). (i) Morphological filtering on the identified objects. Small artefacts, such as the one indicated by black arrow in (h), are removed.*

Morphological filtering: Neurons have certain shape and volume. Based on this statistical information, clustered objects can be filtered to remove small artefacts. This is necessary because of the low threshold value used for foreground generation. To remove these artefacts from our reconstructed neurons we first performed a morphological opening with a structure whose size is 1/3 of the size of each object's bounding box. Bounding box is calculated in 3-D hence it is the smallest cube that contains the object. This operation breaks down irregular shapes but keeps relatively regular shapes (sphere, ellipsoid, cuboid) intact. Then, both voxel size (volume) and mean intensity of the objects are fit with a Gaussian mixture model, and the group with the smallest voxel size and lowest mean intensity is judged as artefacts and removed. (Figure 3.1f).

Combining information from different soma-staining channels: Cells identified from each channel are added together to give a cumulative soma counts across all antibody channels. Overlapped objects are judged to be different cells if:

a. The overlapping volume is smaller than 30% of any object volume constituting the cluster;

b. After subtraction the new object preserves the ellipsoid shape.

Cytosol-staining channels (GAD65 and Somatostatin)

The identification of the cells in cytosol-staining channels utilizes reference information gathered from the soma-staining channels, hence the segmentation of cytosolic signals require at least one nuclear channel staining.

The early stages of the images processing for the cyctosol signal localization are identical to those of the soma-staining channels except CLAHE step. Subsequently cell objects were imported from combined soma-staining channels information (Figure 3.2c).

For each cell object, two additional voxels were added to the diameter of the object (Figure 3.2d). This enlarged cell object is used as a mask to detect positive staining in the cytosol-staining channel (Figure 3.2f). Positive staining was defined as connected voxels with a volume of at least 10% of the object and that they have significantly higher intensity compared to the voxels within the 2.5 times diameter of the associated cell (Figure 3.2g). Finally the percentage of positive staining was obtained and used to identify GAD65 or Somatostatin positive cells.

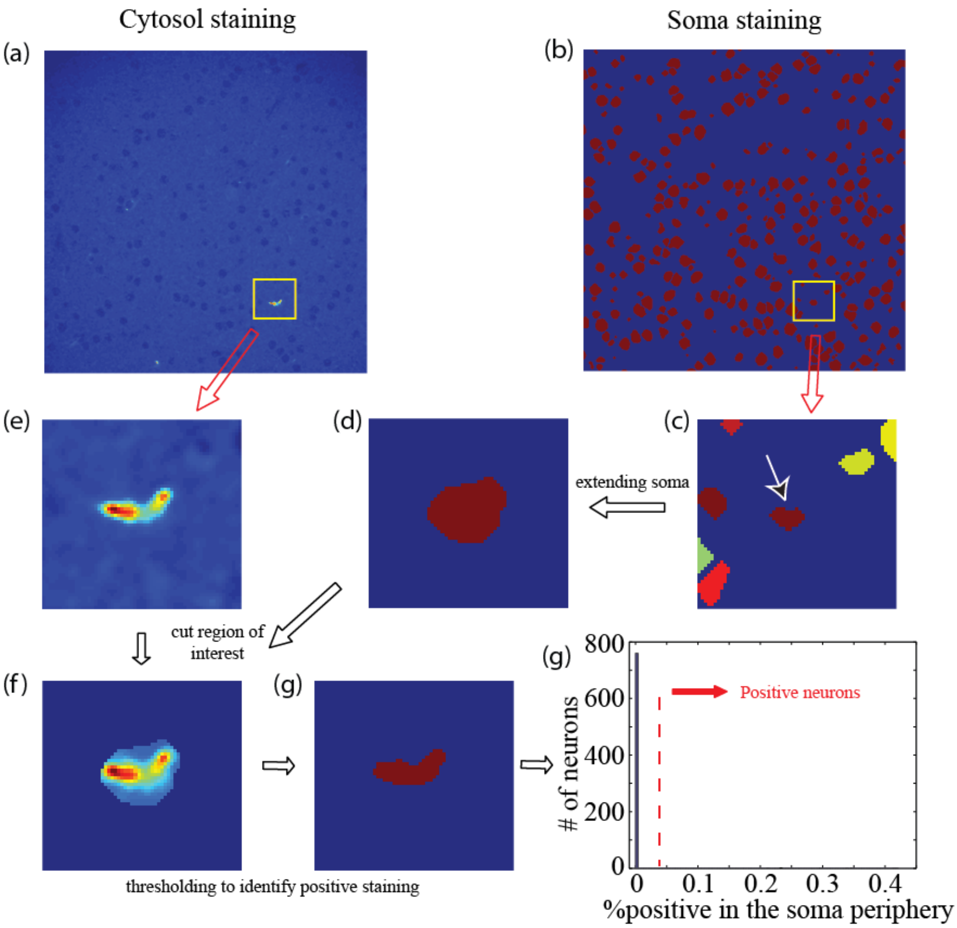

Figure 3.2. Automatic cell counting for cytosol-staining channels. The example shown is a Somatostatin (SST) staining immunofluorecent image. (a, b) Images from SST-channel and identified cell objects from soma-staining channels, at the same position in the image stack. (c) The cell object under analysis, as indicated by the red arrow, with region of interest marked by yellow rectangle in (a) and (b). (d) The cell object under analysis is enlarged by 2-pixels in all directions; other objects are ignored. (e) Corresponding region in the SST channels. (f) The object in (d) is used as mask image to obtain the region of interest in the SST channel. (g) Positive staining is detected as connected pixels with at least 10% volume of object in (d), whose intensity value is two times the standard deviation higher than average pixel intensity in the local image region as shown in (c). (h) Histogram of percentage of positive staining in the SST channel for all the cell objects identified in (b). Cells with a positive percentage higher than 9% are labelled as SST-positive cells.

Performance comparison between computer and the human observer

Three human observers independently counted a number of 3-D images stacks from different antibody staining, using Vaa3D software (Peng et al 2010). Three identical copy of each image stack were placed in the manual counting dataset in a random order; the human observers subsequently confirmed that they did not notice the duplicates in the data set they have analysed. The automated counting result was compared with average human counting result, and the summary of the difference is shown in Table 3.1.

Antibody	# image stacks	Avg. relative difference (%)	Avg. absolute difference (%)
NeuN	13	1.24±2.49	2.32±1.42
PV	7	-0.55±3.49	2.64±2.09
CR	7	-0.47±3.24	2.48±1.91
SST	6	1.19±3.52	2.90±2.01
GAD65	7	1.68±6.76	5.56±3.60

Table 3.1. Comparison of automated counting and manual counting results for different antibody staining. Across all different antibody staining the average relative difference is below 2% when the automated counting results were compared with average results obtained by independent human observers.

Generating an average barrel column

After performing automatic cell counting on individual slices across different cortical depth, we calculated average cell density for different types of cells identified by distinct antibody channels at a given cortical depth as indicated by slice number. Tissue shrinkage was not corrected but the average column size was empirically determined. To account for the differences in cortical thickness across different animals, we then binned the density data from each individual animal into 20 bins, which were subsequently averaged to obtain the average cell density distribution across cortical depth. The layer borders z_{lim} between different cortical layers (L1-L2/3, L2/3-L4, L4-L5, L5-L6) were determined using the same as described previously (Meyer et al 2010), by first fitting a Gaussian function

$$g(z) = c_1 + c_2 e^{-(z-z_0)^2/2\sigma^2}$$

to the NeuN+ cell density profile along cortical depth with manually chosen c_1, c_2 and z_0, and then the respective z_{lim} was calculated from the fitted value σ as

$$z_{lim} = z_0 \pm \sigma\sqrt{2ln2}$$

The L5A-L5B border was determined by manual inspection on NeuN+ cell density. We then calculated the size of an average barrel in C-E rows, 1-3 columns by manually labeling corresponding barrels in anti-GAD65 staining (Figure 3.3). The number of different types of cells in an average barrel from the C-E rows, 1-3 columns was then calculated by the size as well as the corresponding cell density.

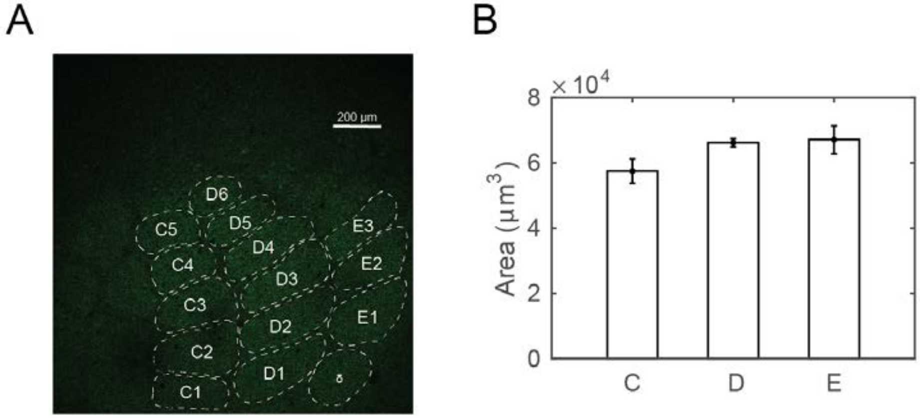

Figure 3.3. Average barrel column. (A) A sample image stained with anti-GAD65 antibody overlaid with manually determined barrel borders. (B) Average area of the Layer 4 across barrel columns C, D, and E.

Neuronal Model.

We used the Izhikevich quadratic model neuron (Izhikevich 2007) in this study:

$$dv/dt \ = \ 0.04 * (v - vr)(v - vt) - u + I$$

where v, vr and vt are the membrane potential, resting membrane potential without stimulus and the spike threshold of the neuron, respectively. u is the recovery variable and its evolution is determined by:

$$du/dt \ = a * [b(v - vr) - u]$$

The model has the following reset condition:

$$\begin{aligned} &if\ v \geq 30 \\ &\quad v \leftarrow c \\ &\quad u \leftarrow u + d \end{aligned}$$

I is the synaptic current the neuron received (see below). a, b, c, d are dimensionless variables which together determine the firing pattern of the model neuron (see Table 3.2; values are from Izhikevich 2003, with slight modification on d to match reported firing rates of different types of neurons). For the simulations a first order Euler method with step size of 0.1 ms was used.

	a	b	c	d
L4 neurons				
Excitatory neurons	0.020±0.006	0.225±0.014	-58.0±2.9	9.0±1.7
Fast-spiking interneuron	0.100±0.012	0.203±0.015	-69.7±3.0	10.6±1.7
Non-fast-spiking interneuron	0.021±0.006	0.255±0.028	-59.9±4.3	8.9±1.1
L2/3 neurons				
Excitatory neurons	0.020±0.006	0.225±0.014	-62.0±4.4	11.0±1.7
PV+ FS neurons	0.100±0.011	0.213±0.015	-69.7±3.0	12.6±1.8
PV+ bursting neurons	0.021±0.006	0.240±0.029	-54.7±2.7	6.9±1.2
Martinotti neuron	0.022±0.006	0.225±0.014	-59.8±4.5	8.3±2.1

Neurogliaform cell	0.021±0.006	0.267±0.015	-85.7±2.7	15.9±1.2
CR+ bipolar cell	0.020±0.006	0.260±0.014	-55.5±3.9	8.2±1.5
CR+ multipolar cell	0.024±0.009	0.200±0.012	-62.1±2.8	11.5±1.6
VIP+/CR- cell	0.021±0.006	0.230±0.015	-57.2±4.2	8.1±1.6

Table 3.2. Model parameters for different types of neurons in the network. All values are mean±std; parameters are normally distributed.

Neural network

The mouse barrel cortex L4-L2/3 network was modeled based on the distribution of different classes of neurons in an average barrel in mouse barrel cortex reconstructed by immunochemical labelling and confocal microscopy (see above). 13 different types of cortical neurons are included in the model (see Thomson & Lamy 2007, Markram et al 2004 for review; also see Oberlaender et al 2012a for different excitatory neuron classes). We included 9 types of neurons in L2/3, 2 excitatory: L2 pyramidal neurons and L3 pyramidal neurons (Brecht et al 2003, Feldmeyer et al 2006); 7 inhibitory: PV+ fast-spiking neurons (Holmgren et al 2003, Packer & Yuste 2011), PV+ bursting neurons (Blatow et al 2003), SST+ Martinotti neurons (Wang et al 2004, Kapfer et al 2007, Fino & Yuste 2011), Neurogliaform cells (Tamas et al 2003, Wozny & Williams 2011), CR+ bipolar neurons (Caputi et al 2009, Xu et al 2006), CR+/VIP+ multipolar neurons (Caputi et al 2009) and VIP+/CR- neurons (Porter et al 1998). In L4 we included 4 types of neurons, 2 excitatory: L4 spiny stellate neurons and L4 star pyramidal neurons (Egger et al 2008, Staiger et al 2004); 2 inhibitory: PV+ fast-spiking neurons and PV- low-threshold spiking neurons (Beierlein et al 2003, Sun et al 2006, Koelbl et al 2015). The distribution of excitatory, PV+, CR+ and SST+ neurons are taken from the anatomical reconstructions; for other cell types, we assigned corresponding number of different neurons in each cluster based on the previous studies (Kawaguchi & Kubota 1997, Uematsu et al 2007). These neurons were distributed in a 640-by-300-by-300 µm region (L4, 210-by-300-by-300; L2/3, 430-by-300-by-300). Note that we scaled the size of the network to match the average dimension of a rat column (Feldmeyer et al 2006), due to the fact that most of the axonal and dendritic projection patterns were measured in rat.

Connectivity was determined using axonal and dendritic projection patterns from the literature (Egger et al 2008, Feldmeyer et al. 2002, Lubke et al. 2003, Feldmeyer et al. 2006, Helmstaedter et al. 2008), which were approximated by 3-D Gaussian functions, with the assumption that the probability that two neurons are connected is proportional to the degree of axonal-dendritic overlap between these two neurons (i.e. a modified version of Peter's rule, Peters et al. 1976, White 1979). For each pre-synaptic *i* and post-synaptic neuron *j*, we calculated the axonal-dendritic overlapping index $I_{i,j}$, which is the sum of the product of the presynaptic axonal distribution A_i and postsynaptic dendritic distribution D_j:

$$I_{i,j} = \int_x \int_y \int_z A_i D_j dxdydz, \qquad x, y \in SD_j$$

where SD_j is the 3-D space contains 99.9% of D_j. We then converted $I_{i,j}$ into connection probability $P_{i,j}$ between neuron *i* and *j*, by choosing a constant k for each unique pre- and post-synaptic cell type pair so that the average connection probability within experimentally measured inter-soma distances (usually 100 μm) matches empirically measured values between these two types of cells (Table 3.3):

$$P_{i,j} = k \times I_{i,j}$$

Finally a binary connectivity matrix was randomly generated using pairwise connection probability $P_{i,j}$, in which connected pairs were labelled as 1 (Figure 3.3).

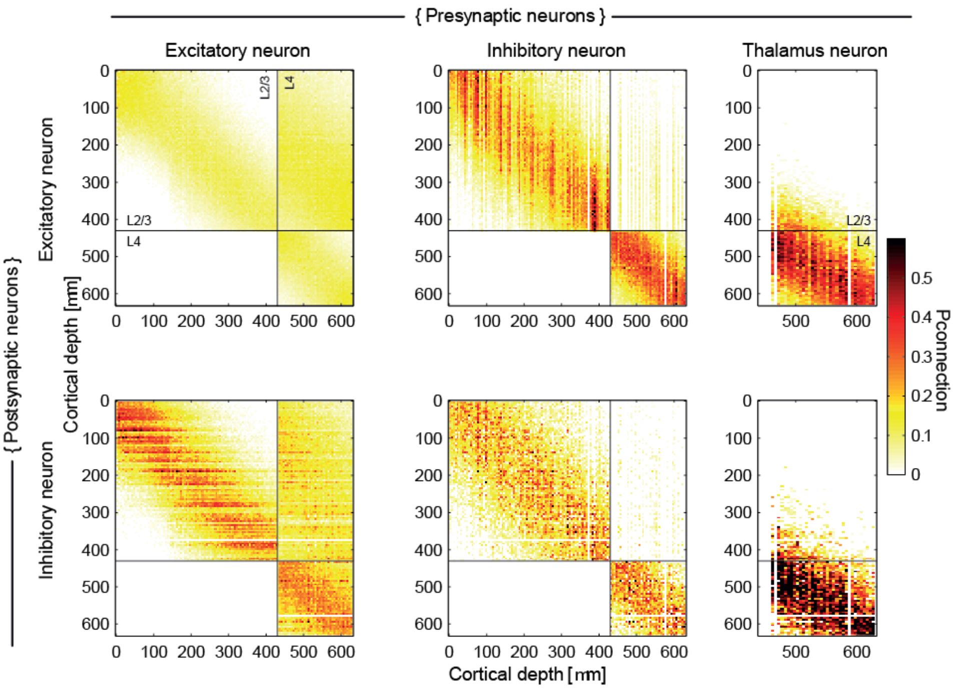

Figure 3.4. Connectivity matrix and connection pattern in the simulated network. Connectivity matrices organized by cell types (excitatory vs. inhibitory) and cortical layer distribution (L2/3 vs. L4), sorted by cell depth from layer 1-layer 2 border. Colour code indicates connection probability between pre- and post-synaptic neuron population ($P_{connection}$) at given cortical depth, binned using a 5-by-5 µm window. In general connection between excitatory and inhibitory neurons, as well as connection between inhibitory neurons is denser compared to excitatory-excitatory connections. Note when presynaptic cell is thalamic neuron, the depth location indicates centre of thalamic axon density distribution, rather than actual cell location.

Synaptic currents in this network were modelled by a double-exponential function. Parameters of those functions were adjusted to match experimentally measured PSPs (peak amplitude, rise time, half width, failure rate, coefficient of variation and pair-pulse ratio) in barrel cortex in *vitro* (Table 3.3; See Thomson & Lamy 2007 for an extensive review). The onset latency was calculated from the distance between cell pairs; the conduction velocity of action potential was set to 190µm/ms (Feldmeyer et al 2002). The short-term synaptic dynamics (pair-pulse depression/facilitation) was modelled as a scalar multiplier to actual synaptic weight, which follows a single exponential dynamic (Izhikevich & Edelman 2007):

$$dx/dt = (1-x)/\tau_x, \qquad x \leftarrow px \text{ when the presynaptic neuron fires.}$$

τ_x was set to 150ms for excitatory synapses and depression inhibitory synapses ($p<1$), and 100ms for facilitating inhibitory synapses ($p>1$). Differences in the activation state of the cortex were included in the model by setting the common initial voltage and the equilibrium potential *vr* of all cells, thus accounting for potential up - and down-states as well as an intermediate state.

Pre-synaptic	**Post-synaptic**	**Am (mV)**	**τ_r (ms)**	**τ_d (ms)**	**PPR**	**FR**	**CV**	**P_{conn}**	**Ref**
Thalamic projections into the L4									
Thalamic	Cortical excitatory	0.95 ± 1.10	1.16 ± 0.27	22.5 ± 27.4	0.76 ± 0.07	0.00 ± 0.01^2	0.23 ± 0.15^2	0.43^3	A, B, C
	Cortical fast spiking	1.62 ± 1.26^1	0.41 ± 0.15	6.74 ± 1.10	0.55 ± 0.12	0.00 ± 0.01^2	0.22 ± 0.12^2	0.5^3	

	Cortical non-fast spiking	0.27 ± 0.19[1]	1.12 ± 0.48	22.5 ± 11.10	0.76 ± 0.07	0.00 ± 0.01[2]	0.72 ± 0.34[2]	0.5[3]	
L4 – L4 connections									
L4 excitatory	L4 excitatory	1.1 ± 1.1	0.88 ± 0.26	12.3 ± 2.2	0.65 ± 0.16	0.11 ± 0.18	0.30 ± 0.19	0.06	A
	L4 fast spiking	2.2 ± 2.2	0.37 ± 0.11	4.9 ± 1.9	0.65 ± 0.16	0.03 ± 0.08	0.27 ± 0.13	0.43	
	L4 low-threshold spiking	0.3 ± 0.5	0.86 ± 0.48	8.9 ± 2.9	1.2 ± 0.3	0.57 ± 0.35	1.04 ± 0.54	0.57	
L4 fast spiking	L4 cells	1.1 ± 0.8	1.5 ± 0.7	24.0 ± 10.8	0.72 ± 0.25	0.03 ± 0.07	0.25 ± 0.11	0.44	
L4 low-threshold spiking	L4 cells	0.48 ± 0.45	2.1 ± 1.0	22.6 ± 13.7	0.99 ± 0.26	0.29 ± 0.26	0.41 ± 0.21	0.35	
L4 – L2/3 connections									
L4 excitatory	L2/3 pyramidal	0.7 ± 0.6	0.8 ± 0.3	12.7 ± 3.5	0.90 ± 0.39	4.9 ± 8.8	0.27 ± 0.13	0.12	D
	PV+ fast-spiking cell	0.96 ± 0.93	0.89 ± 0.31	15.0 ± 8.2	0.99 ± 0.66	20.0 ± 20.0	0.27 ± 0.13 *	0.2[4]	E, F
	PV+ bursting cell	1.2 ± 0.2	0.42 ± 0.1	6.3 ± 2.1	0.84 ± 0.17	13.0 ± 19.8	0.5 ± 0.3*		
	Martinotti neuron	Not connected							

	Neurogliaform cell	0.59 ± 0.21	0.85 ± 0.26	13.0 ± 6.2	0.70 ± 0.18	17.0 ± 14.0	0.5 ± 0.3*	0.2[4]	
	CR+ bipolar cell	1.3 ± 0.9	1.1 ± 0.4	14.0 ± 4.1	1.00 ± 0.62	13.0 ± 19.8	0.5 ± 0.3*		
	CR+ multipolar cell	1.4 ± 1.4	0.79 ± 0.50	8.5 ± 3.1	0.92 ± 0.40	13.0 ± 19.8	0.5 ± 0.3*		
	VIP+/CR- cell	1.3 ± 0.9	1.1 ± 0.4	14.0 ± 4.1	1.00 ± 0.62	13.0 ± 19.8	0.5 ± 0.3*		
L4 fast spiking	L2/3 cells	1.1 ± 0.8	1.5 ± 0.7	24.0 ± 10.8	0.72 ± 0.25	0.03 ± 0.07	0.25 ± 0.11	†	A, V
L4 low-threshold spiking	L2/3 cells	Not connected							N/A
L2/3 – L2/3 connections									
L2/3 pyramidal	L2/3 pyramidal	1.0 ± 0.7	0.7 ± 0.2	15.7 ± 4.5	0.61 ± 0.41	3.2 ± 7.8	0.33 ± 0.18	0.10	F, G
	PV+ fast-spiking cell	0.82 ± 0.49	2.32 ± 1.00	16.25 ± 5.78	0.70 ± 0.14	20.0 ± 20.0	0.6 ± 0.1*	0.65	G, V
	PV+ bursting cell	0.38 ± 0.25	2.76 ± 1.05	19.2 ± 2.2	0.51 ± 0.13	13.0 ± 19.8	0.5 ± 0.3*	0.18	H
	Martinotti neuron	0.25 ± 0.2	2.76 ± 1.05	19.2 ± 2.2	1.91 ± 0.82	50 ± 20	1.04 ± 0.54	0.29	I, J, P
	Neurogliaform cell	0.39± 0.33	2.6 ± 0.5	17.9 ± 4.0	0.83 ± 0.14	20 ± 10	0.6 ± 0.1*	0.29	G, S

	CR+ bipolar cell	1.35± 0.62	0.64 ± 0.27	26.0 ± 8.1	0.83 ± 0.14	28 ± 22	0.39 ± 0.07	0.18	K, N
	CR+ multipolar cell	1.36± 0.78	1.26 ± 0.53	9.5 ± 3.9	1.6 ± 0.7	50 ± 20	0.6 ± 0.1*	0.20	M, N
	VIP+/CR- cell	1.35± 0.62	0.64 ± 0.27	26.0 ± 8.1	0.83 ± 0.14	28 ± 22	0.39 ± 0.07	0.46	M, I
PV+ fast-spiking cell	L2/3 pyramidal	0.52± 0.45	3.5 ± 1.4	43.1 ± 10.2	0.70 ± 0.15	5.1 ± 8.7[5]	0.46 ± 0.17[5]	0.60	G, S
	PV+ fast spiking cell	0.56± 0.43	1.8 ± 0.6	15.8 ± 6.0	0.70 ± 0.15	5.1 ± 8.7[5]	0.46 ± 0.17[5]	0.55	G, S
	others	Not connected							U
PV+ bursting cell	L2/3 pyramidal	1.21 ± 1.18	2.1 ± 1.0	22.6 ± 13.7	1.27 ± 0.60	8.9 ± 11.8[5]	0.53 ± 0.23[5]	0.41	H, O
	PV+ fast-spiking cell	0.77 ± 0.62	2.1 ± 1.0	22.6 ± 13.7	0.86 ± 0.20	5.1 ± 8.7[5]	0.46 ± 0.17[5]	0.26	
	others	1.06 ± 0.83	2.1 ± 1.0	22.6 ± 13.7	1.53 ± 0.63	8.9 ± 11.8[5]	0.53 ± 0.23[5]	0.41	
Martinotti neuron	Martinotti neuron	Not connected							P, T, U
	others	0.29 ± 0.22	3.5 ± 1.1	13.7 ± 9.9	1.80 ± 0.50	26.8 ± 26.3[5]	0.91 ± 0.56[5]	0.71	

Neuroglia form cell	others	0.58 ± 0.1	53.2 ± 10.8	100 ± 19	0.51 ± 0.13	5.1 ± 8.7[5]	0.46 ± 0.17[5]	0.44	Q, O, R
CR+ bipolar cell	L2/3 pyramidal	0.49 ± 0.49[6]	5.4 ± 2.2[6]	56.2 ± 24.1[6]	1.40 ± 0.50	26.8 ± 26.3[5]	0.91 ± 0.56[5]	0.11	L, O, S
	PV+ fast-spiking cell	0.37 ± 0.33[6]	3.1 ± 2.0[6]	20.0 ± 12.1[6]	1.10 ± 0.20	26.8 ± 26.3[5]	0.91 ± 0.56[5]	0.30	
	CR+ bipolar cell	0.49 ± 0.56[6]	4.9 ± 5.4[6]	33.3 ± 12.0[6]	1.42 ± 0.20	26.8 ± 26.3[5]	0.91 ± 0.56[5]	0.32	
	CR+ multipolar cell	0.49 ± 0.56[6]	4.9 ± 5.4[6]	33.3 ± 12.0[6]	1.33 ± 0.30	26.8 ± 26.3[5]	0.91 ± 0.56[5]	0.76	
	others	0.49 ± 0.56[6]	4.9 ± 5.4[6]	33.3 ± 12.0[6]	1.80 ± 0.30	26.8 ± 26.3[5]	0.91 ± 0.56[5]	0.30	
CR+ multipolar cell	L2/3 pyramidal	0.49 ± 0.49[6]	5.4 ± 2.2[6]	56.2 ± 24.1[6]	0.7 ± 0.3	5.1 ± 8.7[5]	0.46 ± 0.17[5]	0.14	L, O, S
	PV+ fast-spiking cell	0.37 ± 0.33[6]	3.1 ± 2.0[6]	20.0 ± 12.1[6]	1.4 ± 0.4	26.8 ± 26.3[5]	0.91 ± 0.56[5]	0.18	
	CR+ bipolar cell	0.49 ± 0.56[6]	4.9 ± 5.4[6]	33.3 ± 12.0[6]	0.98 ± 0.2	8.9 ± 11.8[5]	0.53 ± 0.23[5]	0.41	

	CR+ multipolar cell	0.49 ± 0.56^{6}	4.9 ± 5.4^{6}	33.3 ± 12.0^{6}	0.74 ± 0.30	5.1 ± 8.7^{5}	0.46 ± 0.17^{5}	0.10	
	others	0.49 ± 0.56^{6}	4.9 ± 5.4^{6}	33.3 ± 12.0^{6}	1.1 ± 0.4	8.9 ± 11.8^{5}	0.53 ± 0.23^{5}	0.50	
VIP+/CR- cell	L2/3 pyramidal	0.49 ± 0.49^{6}	5.4 ± 2.2^{6}	56.2 ± 24.1^{6}	1.0 ± 0.3	8.9 ± 11.8^{5}	0.53 ± 0.23^{5}	0.46^{6}	L, O, S
	PV+ fast-spiking cell	0.37 ± 0.33^{6}	3.1 ± 2.0^{6}	20.0 ± 12.1^{6}	1.0 ± 0.3	8.9 ± 11.8^{5}	0.53 ± 0.23^{5}	0.38^{6}	
	others	0.49 ± 0.56^{6}	4.9 ± 5.4^{6}	33.3 ± 12.0^{6}	1.0 ± 0.3	8.9 ± 11.8^{5}	0.53 ± 0.23^{5}	0.38^{6}	

Table 3.3. Features of neural connectivity in the somatosensory (barrel) cortical column. Am, amplitude; τ_r, rise time constant; τ_d, decay time constant; P_{conn}, connection probability; FR, failure rate; PPR, pair-pulse ratio. Values are mean±std.

Notes:

† Same parameters are used as in L4-L4 connections, but extended into L2/3

* Values reflect L4-L4 connections.

** References: (A) Beierlein et al 2003; (B) Gil et al 1999; (C) Bruno & Sakmann 2006; (D) Feldmeyer et al 2002; (E) Helmstaedter et al 2008; (F) Sun et al 2006; (F) Feldmeyer et al 2006; (G) Holmgren et al 2003; (H) Blatow et al 2003; (I) Ali 2003; (J) Kapfer et al 2007; (K) Reyes et al 1998; (L) Rozov et al 2001; (M) Porter et al 1998; (N) Caputi et al 2009; (O) Gupta et al 2000; (P) Fino & Yuste 2011; (Q) Wozny & Williams 2011; (R) Tamas et al 2003; (S) Avermann et al 2012; (T) Packer & Yuste 2011; (U) Pfeffer et al 2013; (V) Koelbl et al 2015.

[1] Values are taken from A, but scaled according to C.

[2] Values are calculated from L4-L4 connections measured in A, based on the difference between L4-L4 synapses and thalamic-L4 synapses reported in B.

[3] Values are for thalamus-L4 connection probability.

[4] Values are taken from E, as average connection probability between L4 excitatory neurons and L2/3 interneurons.

[5] Values are taken from O, based on inhibitory synapse classification.

[6] Values are taken from S, as average values for NFS (non-fast-spiking) interneurons.

Thalamic inputs

To the best of our knowledge as of Feb 1st 2015 there is not any published quantitative work on the cellular organization of the mouse thalamic nuclei. In rat, each barreloid in thalamic VPM nuclei has ~1/18 of the number of neurons compared to corresponding L4 barrel (Meyer et al 2013). Given that in our average barrel column L4 contains ~1600 neuron, we assigned 90 neurons, all excitatory to each barreloid in VPM. The thalamic-cortical connectivity was calculated using the same method as cortical-cortical connectivity discussed above, using published thalamic axon projection patterns (Furuta et al 2011, Oberlaender et al 2012b). The POM pathway was not modeled.

Thalamic stimulation provided in the model was based on population Peristimulus time histograms (PSTHs) collected extracellularly in anesthetized animals in *vivo* in response to a brief, ~400 µm whisker deflection applied to either the principle or one of the surround whiskers (Aguilar & Castro-Alamancos 2005). The PSTHs only specified the population firing rate in the thalamic cells; to generate individual neuron response in different trials we assumed that thalamic neurons fire independent Poisson spike trains in each trial, constrained by the PSTHs.

Spike-timing dependent plasticity

A network of 3-by-1 barrel columns was constructed to simulate spike-timing dependent plasticity in barrel cortex following a single (row) whisker deprivation. Each column was randomly generated using distributions of 13 different types of neurons, and connectivity was calculated using the same method discussed above. The middle column was whisker-deprived, which received surround whisker evoked thalamic input; the two lateral columns were whisker-spared and received principal whisker evoked thalamic input (Aguilar and Castro-Alamancos 2005). The STDP rule for L4-L2/3 excitatory connections was as follows (Celikel et al 2004):

$$dA = -3.7 \times 10^{6} (\mathit{\Delta} t)^2 - 0.0019 \mathit{\Delta} t + 0.77, \quad -250 \leq \mathit{\Delta} t \leq 0$$

$$-4.7 \times 10^{-7} (\mathit{\Delta} t)^3 + 0.00028 (\mathit{\Delta} t)^2 - 0.022 \mathit{\Delta} t + 1.4, \;\; 3 \leq \mathit{\Delta} t \leq 32$$

$$0.5665\Delta t/3 - 0.23, \qquad 0 < \Delta t < 3$$

Δt is the timing difference (in ms) between the time at which presynaptic spike arrives at postsynaptic neuron (i.e. presynaptic neuron spike time plus synaptic delay) and postsynaptic neuron spike time in ms. The constants are directly taken from the ref., in which the values were obtained by least-square fits to the experimental data. For L2/3-L2/3 excitatory connections, the rule was as follows (Banerjee et al 2014):

$$dA = 0.53/100 * exp(-\Delta t/18), \qquad \Delta t > 0$$

$$-0.32/100 * exp(-\Delta t/18), \qquad \Delta t < 0$$

The synaptic weight change was additive for potentiation and multiplicative for depression; repeating the simulations with an additive rule for potentiation and depression did not change the results and are not shown herein. Plasticity rules for excitatory-inhibitory and inhibitory connections are less commonly studied. Inclusion of the empirically identified learning curves (Haas et al 2006, Lu et al 2007) did not qualitatively alter the results and are not included in the rest of the Chapter.

In vitro recordings

The quadratic neuron model, as postulated by Izhikevich (see above), generates action potential at a set threshold. In biological networks, however, the threshold depends on the recent history of the membrane state (see Chapter 4). To empirically determine the relationship between the membrane depolarization and the action potential threshold we performed *in vitro* whole-cell current-clamp recordings in acutely prepared slices of the barrel cortex (P18-21) as described before (Allen et al. 2003) but with minor modifications. Oblique thalamocortical slices (300 mm, Finnerty et al. 1999) were cut 45° from the midsagittal plane in chilled low-calcium, low-sodium Ringer's solution (in mM; sucrose, 250; KCl, 2.5; $MgSO_4.7H_2O$, 4; $NaH_2PO_4.H_2O$, 1; HEPES, 15; D-(+)-glucose, 11; $CaCl_2$, 0.1). Slices were first incubated at 37ºC for 45 minutes and were subsequently kept in room temperature in carbonated (5% oxygen) bath solution (pH 7.4, normal Ringer's solution: in mM, NaCl, 119; KCl, 2.5; $MgSO_4$, 1.3; NaH_2PO_4, 1; $NaHCO_3$, 26.3; D-(+)-glucose, 11; $CaCl_2$, 2.5).

Visualized whole-cell recordings were performed using an Axoclamp-2B amplifier under an IR-DIC objective (Olympus) at room temperature. A bipolar extracellular stimulation electrode (inter-tip distance 150 micrometer) was placed in the lower half of a L4 barrel representing a mystacial vibrissa. A recording electrode (3-4 MOhm) containing an internal solution (pH 7.25; in mM; potassium gluconate, 116; KCl, 6; NaCl, 2; HEPES, 20 mM; EGTA, 0.5; MgATP, 4; NaGTP, 0.3) was placed orthogonal to the stimulation electrode within 150-300 µm of the cortical surface. For whole cell recordings, putative excitatory cells were selected based on pyramidal shaped somata, apical dendrites and distal tuft orientation, and regular pattern of spiking to somatic current injections (500 ms). Data was low-pass filtered (2 kHz), digitized at 5 kHz using a 12-bit National Instruments data acquisition board and acquired using Strathclyde Electrophysiology Suite for offline data analysis.

Results

In this study, to develop a computational model of the barrel cortex, we have first reconstructed the somatosensory cortex in soma resolution, then employed a mathematical model of the cortical neuron based on Izhikevich's quadratic neuron model (see above) and finally connected the each node in the network (i.e soma across the different cell classes) according to Peter's rule (see above). Here we first provide experimental data on the network formation and then perform network simulations to characterize sensory representations and network plasticity *in silico*.

Anatomical organization of the barrel cortex

Just like most other neocortical areas barrel columns consists of six layers and tens of different neural classes (Thomson & Lamy 2007, Markram et al 2004, Oberlaender et al 2012a). The reconstruction of the network in soma resolution (Figure 3.5) showed that cell-type specific cortical columns (Figure 3.5F) have distinct laminar organization. Similar to the laminar borders observed in the traditional Nissl stainings, staining the column with neuronal nuclear antibody anti-NeuN, hereafter NeuN, results in high cellular density in Layer (L)4 and lower layers of L3, while L5 and L2/3 display a gradient of cell density (Figure 3.5G). Inhibitory neurons stained with anti-GAD65 (i.e. GAD65), on the other hand, do not obey the laminar borders as outlined by the NeuN and display near equal density in lower L 4, L5b and L1. A major contributor to this distinct lamination is the parvalbumin positive interneurons (Figure 3.5G, compare GAD65 to PV). While calretinin neurons predominantly found in the L4/L3 border, somatostatin neurons are preferentially located in the infragranular layers (Figure 3.5).

Given that the average area of one barrel in D row, 1-3 column was $6.64 \pm 0.43 \times 10^4$ (Figure 3.3, data measured from 3 animals, 7 barrels; values show mean±std, which is the same for all values reported in this paragraph), based on the cell density measurement (Figure 3.5G), we estimated that in an average D row barrel column there are 2410±154 NeuN+ cells in L2/3 (N=5), 6.5±0.7% of which are GAD65+, 5.3±1.2% are PV+, 1.5±0.5% are SST+, and 0.9±0.1% are CR+; in L4 there are 1557±192 NeuN+ cells (N=5), in which 5.5±0.6% are GAD65+, 3.3±0.4% are PV+, 1.5±1.1% are SST+, and

1.2±0.2% are CR+; in L5a there are 709±133 NeuN+ cells (N=5), in which 9.5±1.7% are GAD65+, 13.0±5.6% are PV+, 3.1±3.4% are SST+, and 0.8±0.5% are CR+; in L5b there are 811±68 NeuN+ cells (N=3), in which 10.2±3.9% are GAD65+, 9.4±3.1% are PV+, 1.7±1.8% are SST+, and 0.4±0.2% are CR+; in L6 there are 1226±232 NeuN+ cells (N=2), in which 6.8±1.7% are GAD65+, 5.3±0.3% are PV+, 1.7±1.0% are SST+, and 0.6±0.5% are CR+.

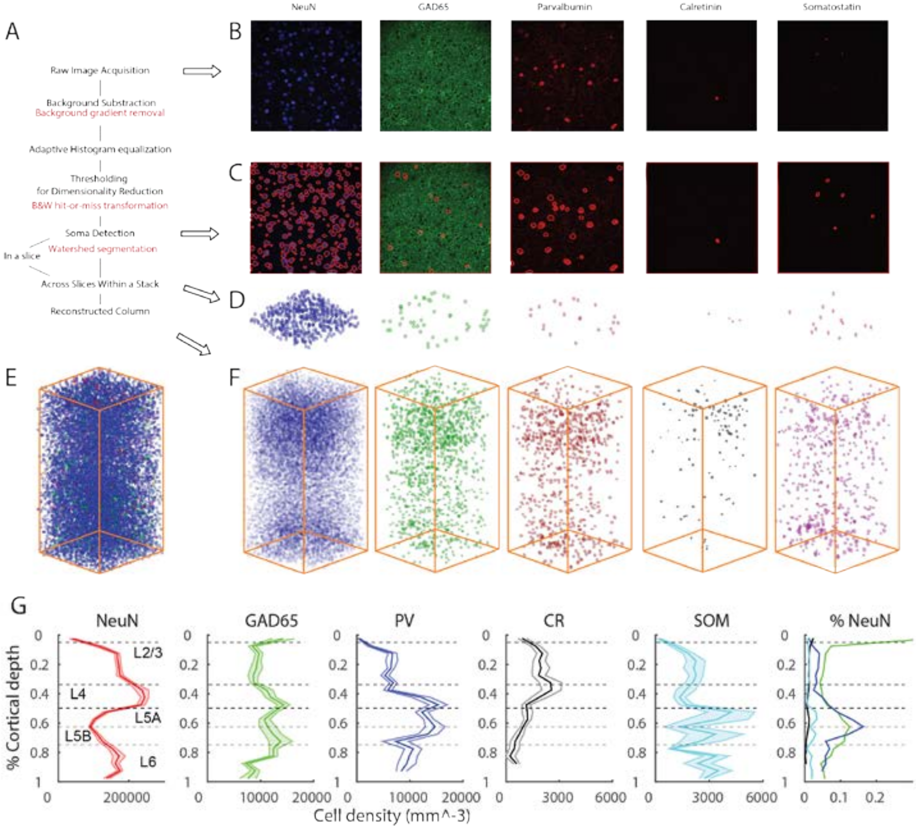

Figure 3.5. Anatomical reconstruction of an average column in the mouse barrel cortex. (A) The flow chart depicts a simplified pipeline for anatomical reconstructions, starting with confocal scanning. (B) Example confocal images from different antibody staining channels. Note that GAD65 has a very high background staining due to the GAD65 positive synapses. Somatostatin staining is cytosolic. (C) Identified cells in each antibody staining channel by the automatic cell count algorithm (see Materials and Methods). Red open circles denote identified cells. (D) Automatically detected cells in a 300x300x25 μm volume of fixed barrel cortex tissue. The sections are not corrected for the shrinkage (i.e 50% in the current set of data).

(E, F) Cell-type specific (reconstructed) cortical columns. Different colors correspond to different cell types. (G) Density distribution of different types of cells across the normalized cortical depth. Cortical layer boundaries were determined based on NeuN+ cell density (see methods). The shaded area shows 2 times the standard error.

Action potential threshold in real neurons

To rescue the quadratic neuron model from the dependence of a fixed spike-threshold, we performed in vitro whole-cell current clamp experiments in L2/3 while stimulating the presynaptic neurons in L4 using a bipolar electrode (see Materials and Methods). Resting membrane potential of the neurons were clamped at predetermined membrane potentials at -80, -70 and -60 mV across trials and the slope of the current injection through the bipolar electrode was modulated linearly to introduce changes in spike-timing in the postsynaptic neurons.

The analysis of the membrane dynamics prior to the action potential generation in the postsynaptic neuron showed that there is a negative correlation between the action potential threshold and the 1st derivative of the rising EPSP slope. As such the faster the EPSP rises the more hyperpolarized the spike threshold is (Figure 3.6A), while action potential threshold varied between -44 and -49 mV.

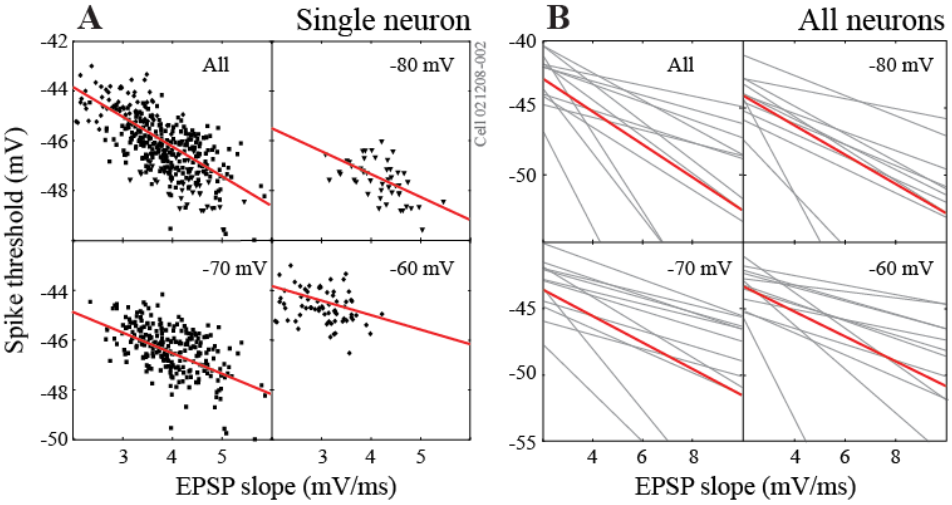

Figure 3.6. Action potential threshold is inversely correlated with the EPSP slope independent from the membrane state. (A) A representative neuron. (B) All neurons recorded in this study. Spike threshold is inversely correlated with EPSP slope, and

the correlation is independent of resting membrane states.

With a systematic shift in the EPSP slope across the membrane potentials, the actual action potential threshold varied across states, hyperpolarizing about 2 mV for every 10 mV change in the resting membrane potential (Figure 3.6A). Although this relationship between the membrane state and the rate of change in the action potential threshold varied across experiments, the slope of the fit between the spike threshold and 1st derivative of the membrane potential was constant across all experiments (Figure 3.6B).

Stimulus representations *in silico*

The identification of the relationship between the speed of EPSP rise and the action potential threshold enabled us to model the spike threshold as an emergent property of the network activity (instead of a stationary value as commonly used). This modification in the quadratic model did not affect the model's ability to generate different firing patterns upon sustained current in soma (see Figure 3.7 compare middle column to the Izhikevich 2004), and also correctly predicted the rate and timing changes associated with the resting membrane state at a single neuron resolution.

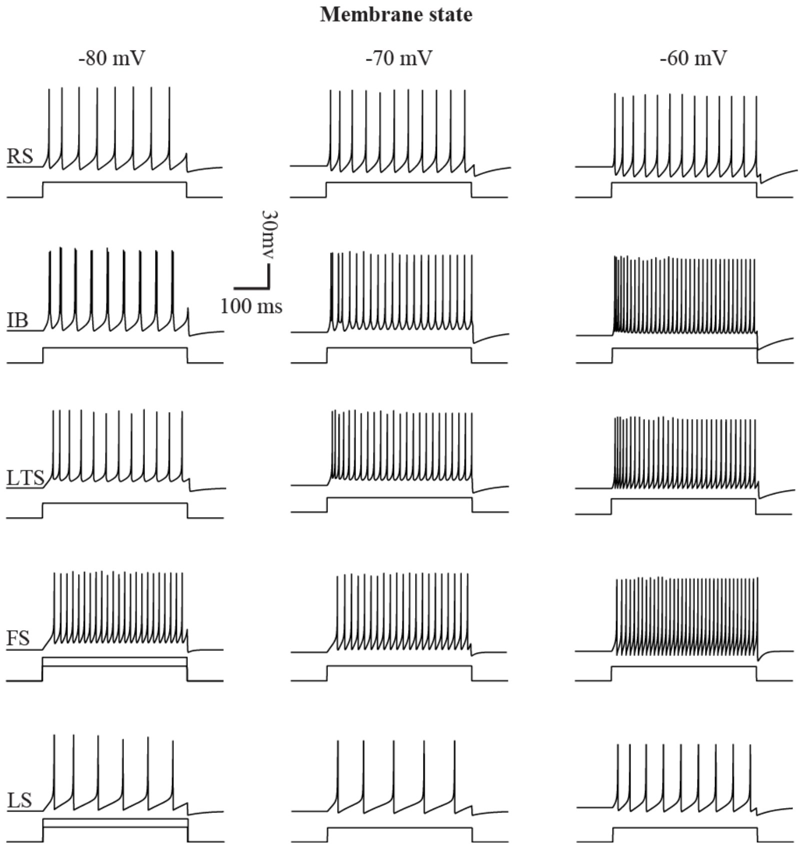

Figure 3.7. The neuronal model with adaptive action potential threshold replicates known changes in temporal pattern of spiking across membrane states. Simulated model neuron responses to somatic current injection at different resting membrane states. Five major classes of electrically identified neurons were simulated: regular spiking (RS), intrinsically bursting (IB), low-threshold spiking (LTS), fast spiking (FS) and late spiking (LS). Columns show firing patterns at different resting membrane potential.

With the anatomy of the cortical column in soma resolution being constructed (Figure 3.5), a statistical model of connectivity between any given two neurons in this network (see Materials and Methods) and a functional model of action potential generation in single neurons (see above) we constructed a biologically constrained barrel cortical column *in silico*. Due to the general lack of experimental work on the pairwise connectivity between infragranular layer neurons and the rest of the network, in this version of the column we have constrained the network to the top 630 µm (Figure 3.8A), which includes the supragranular and granular layers. Since granular layers are the principal recipient of the thalamic inputs and strongly drive the supragranular layers, before the cross-columnar integration takes place across the upper L2/3, this model provides an *in silico* simulation environment for the first three stages of thalamocortical and intracortical information processing that involves supragranular and granular layers.

Stimulus evoked activity, as stimulus encoded at the level of the thalamic ventroposterior medial nucleus (VPM; see Materials and Methods), spread across the network with latencies similar to those observed experimentally under anaesthesia (Figure 3.8B, Armstrong-James et al 1992, Allen et al 2003, Celikel et al 2004). In the simulated network, inhibitory neurons have an earlier onset of spiking than thw excitatory neurons with a peak latency of 8.2±0.6 ms (mean±std) in L4 (Figure 3.8B,C) which corresponds to <3 ms conduction delay as previously observed *in vivo* (Swadlow 1995, 2003). In terms of the latency to action potential, neurons across the entire depth of L4 were homogenous with the exception that those closer to the L3 border had a delayed spiking (Figure 3.8B). Since the feed-forward projections originating from L4 are the main inputs to the L2/3 neurons, the activity *in silico* naturally follows the latency code observed *in vivo* across the cortical layers with L2 neurons generating action potential up to 4 ms later than the lower L3 neurons (Celikel et al 2004; Figure 3.8C). Independent from the actual location of the neuron within the *silico* network, however, inhibitory neurons have an earlier onset of spiking as compared to the neighbouring excitatory neurons within the layer.

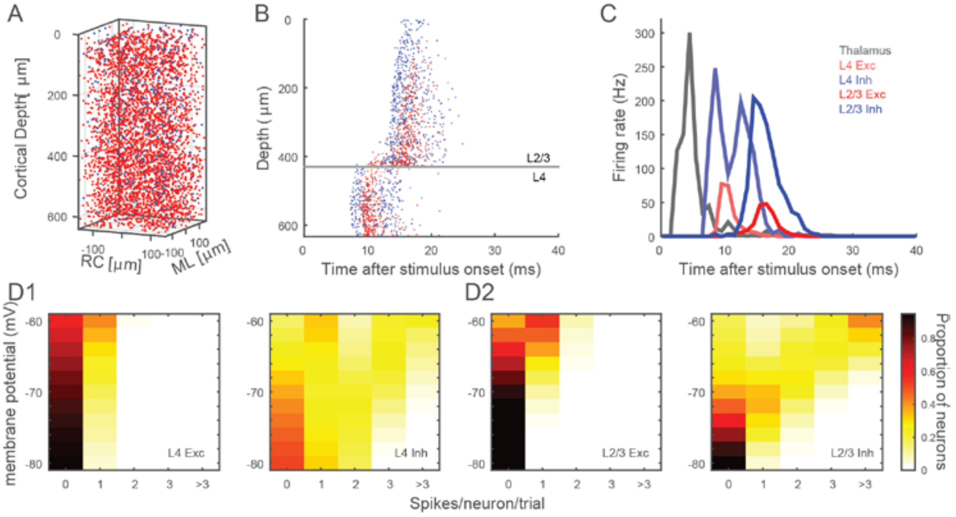

Figure 3.8. Response to thalamic input in the supragranular and granular layers of the mouse barrel cortex in silico. (A) Cellular distribution of neurons across the supragranular and granular layers (see Materials and Methods). Although the in silico network consists of 13 different classes of neurons, for simplicity neurons are visualized as excitatory (red) and inhibitory (blue) during the rest of this Chapter. RC, rostral-caudal axis; ML, medial-lateral axis. (B) Raster plot of spiking activity as a function of cortical depth in a given trial upon VPM activation. (C) Peristimulus time histograms (PSTHs) of spiking across thalamus, L4 and L2/3. (D1) Probability distribution of spike counts in excitatory and inhibitory neuron populations in L4. Note that sparse spiking in the excitatory population is independent from the resting membrane potential states, and that inhibitory neurons spike at higher rates across states. (D2) Same as in D1, but for L2/3 neuron population.

The spiking probability varies significantly across layers and neuron types *in vivo* (Celikel et al 2004, de Kock et al 2007, O’Connor et al 2010, Gentet et al 2010, 2012) and *in silico* (Figure 3.8D1,D2). Excitatory neurons encode the stimulus with a sparse neural code: the probability of a given neuron to generate action potential at a given trial is low, and when the stimulus yields an action potential, the neuron typically generates a single action potential (Figure 3.8D1, left). The response probability and the number of action potential/stimulus depend on the laminar location of the neuron as well as the resting membrane potential state of the network. While excitatory neurons are practically silent upon stimulation arrived in a hyperpolarized membrane state, membrane depolarization invariably results in reduced failure rate and increased likelihood of spiking. Inhibitory neurons fire significantly more action potentials *in vivo* (Gentet et al 2010, 2012, Sachidhanandam et al 2013) and across resting membrane states *in silico* (Figure 3.8D1,D2) compared to excitatory neurons. Even in quiescent hyperpolarized membrane potentials inhibitory neurons exhibit a higher probability of firing. In depolarized membrane potential states not only the rate of failures are reduced but also the number of action potentials per stimulus increased among the inhibitory neural populations. The laminar position of the neuron, be it excitatory or inhibitory, does not have a role for state dependent change in excitability at the single neuron level, although neurons in the supragranular layers on average respond to stimulus more reliably. The only exception to the rule is when the stimulus arrives in the hyperpolarized membrane states; if the resting membrane potential prior to the stimulus onset averaged <-75 mV, both excitatory and inhibitory neurons display failure rates higher than corresponding L4 neurons in the same membrane state (compare Figure 3.8D2 to D1). This suggests that the resting membrane potential state dependent changes in the network activation effectively uncouple supragranular activity from the bottom-up sensory input during quiescent states.

The source of response variability *in silico*

In a network where information propagates across synaptically coupled neurons via weak and failure prone connections; identical stimuli will evoke distinct spiking patterns, even if the measured spike rate and time stay constant across the presynaptic population, simply due to the stochasticity of the presynaptic population contributing to the postsynaptic spiking. Accordingly neural representations *in silico* should vary as this *effective connectivity* across the layers change across trials.

To quantify the contribution of response variability to the stimulus representations *in silico* we have simulated the cortical responses to thalamic inputs in two conditions while keeping the population PSTH in thalamus the same across conditions: 1) The thalamic spiking response is drawn from a Poisson distribution, constrained by the population PSTH (see method), in every trial; 2) the thalamic activation patterns (i.e. firing rate and spike time at single neuron level) stay the same across trials while the rate and timing of the population response is constrained by the population PSTH. While the former condition creates variability in spike timing and rate at the single thalamic neuron resolution, the latter preserves the rate and timing of the single thalamic neuron input onto the postsynaptic cortical neurons across trials.

The results (Figure 3.9) confirmed the prediction that effective connectivity, i.e. presynaptic neurons that contribute to firing of a postsynaptic neuron in a given trial, is a major contributor to the observed response variability across trials. This contribution was independent from the membrane state and the neuron classes studied, although the variance increased with membrane depolarization.

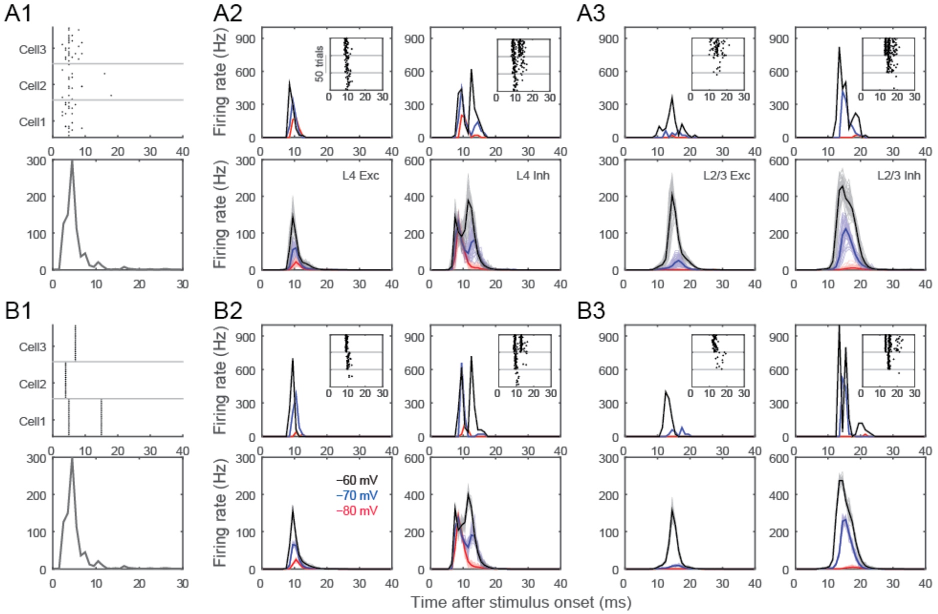

Figure 3.9. Variability of stimulus representations in silico. (A1) The population activity in thalamus is constrained by the PSTH as spike timing for individual cells are drawn according to Poisson-distributions. Raster plots exemplify the spiking responses of 3 representative thalamic neurons across 20 trials (upper panel) drawn from the population PSTH (lower panel). (A2) Representation of the thalamic input in single (upper panels) neurons and populations (lower panels). Left column: L4 excitatory, right column: L4 inhibitory neurons. PSTHs represent neural responses to 50 thalamic stimulation across three different membrane states (black: -60 mV, blue: -70 mV, red: -80 mV) (A3) Same as in A2, but for L2/3 excitatory and inhibitory neurons. (B1) The population PSTH in thalamus is the same as in A1 (lower panel), but spike timing and rate of individual thalamic neurons' spiking is constant across trials (see raster plots in upper panel). (B2, B3) same as in A2, A3, but show cortical response to stereotypic thalamic inputs. Note that even when the same thalamic input pattern was used to stimulate the network, neurons still showed spike timing variability due to synaptic failures and synaptic strength variations although the variance was greatly reduced as the effective connectivity in the network was kept constant.

Response to stimulus presentation in L4 *in silico*

Thalamic neurons project extensively to cortical L4, and diffusely to the L3/L4 and L5b/6 borders (Arnold et al 2001, Oberlaender et al 2012a). This thalamocortical input is the principal pathway that carries the feed-forward excitatory drive representing the bottom-up sensory information.

The response of L4 neurons to the sensory input is characterized by sparse neural representations *in vivo* (Celikel et al 2004, de Kock et al 2007) and *in silico* (Figure 3.10). Thalamic input modeling the principal whisker's stimulation *in vivo* (Aguilar & Castro-Alamancos 2005) results in on average 0.02-0.45 to 0.8-2.2 spikes/stimulus/cell in the network depending on the membrane state prior to the stimulus arrival in L4 as well as the neuronal class studied (at *vr*=-80 mV, excitatory neurons fire 0.06±0.11 spikes/stimulus/cell, range 0-0.82; inhibitory neurons fire 0.68±0.71 spikes/stimulus/cell, range 0-2.22; at *vr*=-60mV, excitatory neurons fire 0.44±0.30 spikes/stimulus/cell, range 0-1.96; inhibitory neurons fire 2.13±1.48 spikes/stimulus/cell, range 0.02-6.54; values show mean±std); While excitatory neurons fire sparsely (Figure 3.10A1), inhibitory neurons spike with higher reliability (Figure 3.10A2).

The resting membrane potential acts as a state switch for the excitatory neurons as L4 excitatory neurons switch from a sparse coding, where probability of spiking per neuron per stimulus is low, and when neurons spike they typically fire single action potentials, to less sparse spiking at more depolarized membrane potentials (Figure 3.10A1). The inhibitory neural population, on the other hand, undergoes rate scaling as the resting membrane potential is depolarized (Figure 3.10A2). Hence for the neural coding of stimulus in L4, membrane state acts as a state-switch for excitatory neurons and a gain-modulator for the inhibitory neurons.

The spatial distribution of neural responses in a network is primarily constrained by the axo-dendritic overlap across the pre- and postsynaptic neurons. Accordingly, with the diffuse axonal projections of thalamic neurons and spatially constrained L4 neuronal dendritic branching within the barrel borders, both excitatory and inhibitory L4 neurons along the rostro-caudal (RC) and medio-lateral (MC) planes have comparable response statistics (Figure 3.10B1-3). Although this connectivity patterns ensures topographical representations across the entire barrel cortex, within a single barrel column the input is homogenously represented throughout the RC and ML planes. In contract to this spatial homogeneity of L4 responses to the stimulus along the RC and ML axis, preferential laminar targeting of the thalamic input results in a higher likelihood of spiking in the center-bottom portion of the barrel, especially for postsynaptic excitatory neurons (Figure 3.10 C1-3).

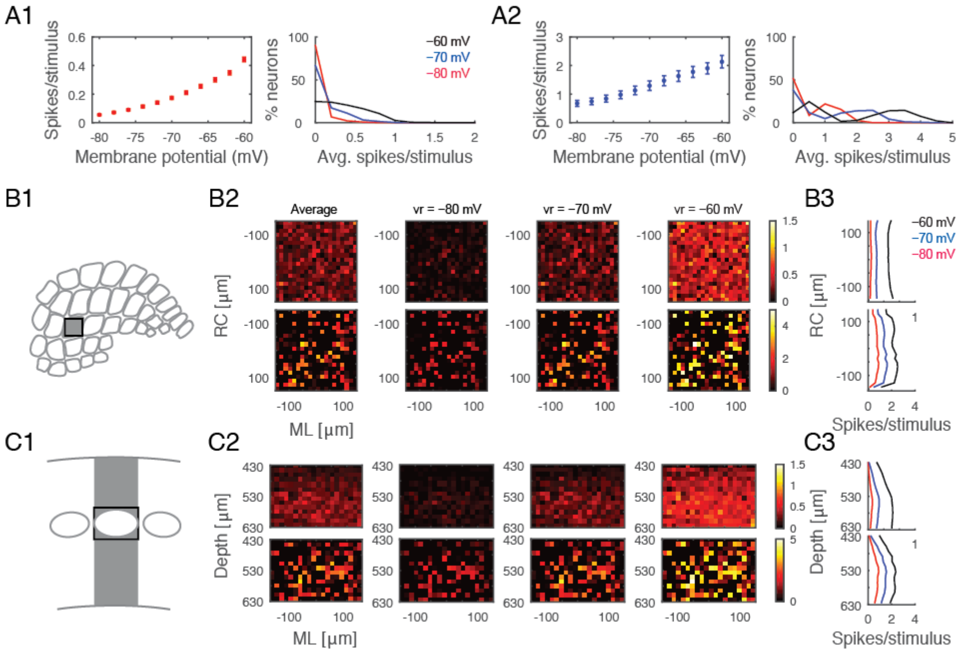

Figure 3.10. Response to Stimulus presentation in the principal whisker's cortical Layer 4 in silico. (A1) Left: Average firing rate in the network as a function of the resting membrane potential before stimulus onset. Right: histogram of spiking rate in the network across membrane states. (A2) same as A1, but for L4 inhibitory neuron population. (B) Spatial distribution of L4 response as visualized in a tangential plane cutting across all columns in L4. (B1) The schematic drawing illustrates spatial dimensions and orientation of the visual displays in B2. The dark edged square labels the analyzed region in B2-3, and the gray region indicates the principal (stimulated) whisker barrel. (B2) Average excitatory (upper panel) and inhibitory (lower panel) neuronal response at different spatial location mapped onto rostro-caudal (RC) and medio-lateral (ML) planes, across different resting membrane states. Each bin is a 15x15 µm window. (B3) Average excitatory (upper panel) and inhibitory (lower panel) neuronal responses along the RC axis. (C) Spatial distribution of the L4 response as visualized in a coronal plane cutting across layers. (C1-C3) Same as B1-B3, but analyzed in a coronal plane.

The topographical nature of the neural response to whisker touch dictates that each neuron has a preferred whisker, called principal whisker, which evokes the largest number of action potentials upon deflection (Brecht & Sakmann 2002, Foeller et al 2005). However cortical neurons' receptive fields are rarely (if ever) constrained to a single whisker as multi-whisker receptive fields in the thalamus (Simons and Carvell 1989, Armstrong-James and Callahan 1991, Diamond et al 1992, Aguilar & Castro-Alamancos 2005, Kwegyir-Afful et al 2005) and cross-columnar projections in the cortex (Egger et al 2008) ensure that each neuron receives information from multiple whiskers. Responses to the surround whiskers are always less strong (lower in number of spikes per stimulus), and arrive with a delay compared to the principal whisker deflection (Brecht & Sakmann 2002). This relationship is also preserved in the *in silico* model (Figure 3.11).

In many respect principal *vs* surround whiskers activate excitatory and inhibitory neurons similarly, although evoked responses from the surround whiskers are invariably weaker (Figure 3.11A1-2). Similar to the principal whisker deflection, surround whisker stimulation results in largely homogenous representations across the RC-ML axis (Figure 3.11B1-3) even though the postsynaptic spiking is constrained to depolarized membrane states. Sublaminar activation pattern in L4 of the principle whisker column results in higher likelihood of spiking in the bottom half of L4 of the surround whisker column even after surround whisker stimulation (Figure 3.11C1-3).

One main difference between the principal vs surround responses is the role of the resting membrane state in modulating the network activity. The contribution of the different membrane potentials to surround whisker representation slowly (but predictably) varies across different membrane states (Figure 3.11A1-2), unlike the differential role of the resting membrane potential in the response to principal whisker touch. Most excitatory and inhibitory neurons in L4 of the surround whisker column do not respond to whisker touch during the quiescent hyperpolarized membrane state, resulting in principal whisker specific cortical responses. In the depolarized membrane states, the probability of spiking disproportionally increases for the inhibitory neurons.

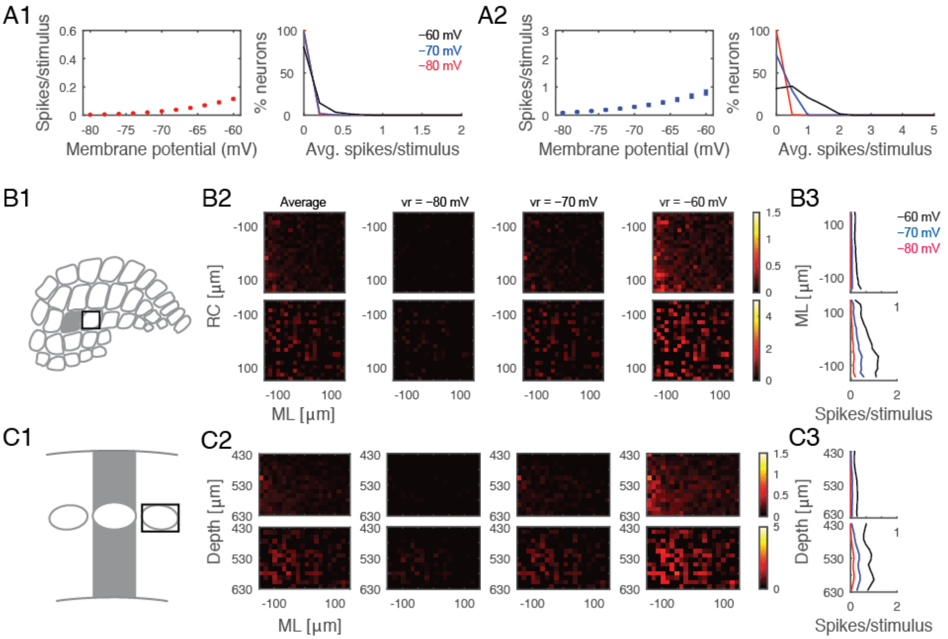

Figure 3.11. Response to Stimulus presentation in the surround whisker's cortical Layer 4 in silico. (A1) Left: Average firing rate in the network as a function of the resting membrane potential states, right: histogram of spiking rate in the network across membrane states. (A2) same as A1, but for L4 inhibitory neuron population. (B) Spatial distribution of L4 response as visualized in a tangential plane cutting across all columns in L4. (B1) This schematic drawing illustrates spatial dimensions and orientation of the visual displays in B2. The dark edged square labels the analyzed region in B2-3, and the gray region indicates the principal (stimulated) whisker barrel. (B2) Average excitatory (upper panel) and inhibitory (lower panel) neuronal response at different spatial location mapped onto RC-ML plane, across different resting membrane states. Each bin is a 15x15 µm window. (B3) Average excitatory (upper panel) and inhibitory (lower panel) neuronal responses along the RC axis. (C) Spatial distribution of the L4 response as visualized in a coronal plane cutting across layers. (C1-C3) Same as B1-B3, but analyzed in a coronal plane.

Response to Stimulus presentation in L2/3 *in silico*

Feed-forward L4 projections are powerful modulators of supragranular layers, and bring the bottom-up information from the sensory periphery for eventual cross-columnar integration within L2. The responses to sensory stimuli in L2/3 *in silico* are generally similar to the L4 ones, with the exceptions that (1) supragranular neurons have an increased, albeit slightly, probability of firing; (2) the resting membrane states gate stimulus representations, and (3) the spatial location of a neuron has a predictive power for its response properties.

Network responses in L2/3, let they be excitatory (Figure 3.12A1 and Figure 3.13A1) or inhibitory (Figure 3.12A2 and Figure 3.13A2), or located in the principal (Figure 3.12) or surround whisker's column (Figure 3.13), entails increased number of spikes per stimulus although probability of a given L2/3 neuron firing an action potential is similar to that of a L4 neuron (for principal whisker stimulation, L2/3 excitatory neurons, 0.23±0.22 spikes/stimulus/neuron, range 0-1.71; L2/3 inhibitory neurons, 1.32±0.86, range 0-3.78; L4 excitatory neurons, 0.20±0.20, range 0-1.06; L4 inhibitory neurons, 1.33±1.08, range 0.002-4.34; for 1st order surround whisker stimulation, L2/3 excitatory neurons, 0.10±0.15, range 0-1.03, L2/3 inhibitory neurons, 0.38±0.35, range 0-1.91; L4 excitatory neurons, 0.04±0.06, range 0-0.46; L4 inhibitory neurons, 0.36±0.30, range 0-1.11. Values are mean±std, averaged across all cortical states simulated). Hence single L2/3 neuronal responses are statistically comparable to corresponding L4 neurons when studied under similar conditions.

Unlike the L4 responses to the stimulus in the quiescent membrane states, L2/3 excitatory neurons are completely silent at hyperpolarized membrane potentials, suggesting that the bottom-up thalamocortical information is decoupled from the rest of the cortical circuits that originate from the supragranular layers. The lack of spiking is not specific to the excitatory neurons (Figure 3.12B2, top - C2, top), as inhibitory neurons are similarly unresponsive to the L4 input if the resting membrane potential was hyperpolarized (Figure 3.12B2, bottom - C2, bottom). Although spikes from inhibitory neuron population is observed in less hyperpolarized membrane potentials (> -70 mV), compared to the excitatory neurons' responses, the net effect of the membrane potential on suppressing cortical propagation of information via L2 is maintained (Figure 3.12). The lack of stimulus evoked spiking in the surround column (Figure 3.13) in resting membrane potentials < -70 mV and the changes in the spike probability described before suggest that sensory representations are weak but specific to the principal whisker column during the quiescent states *in vivo*.

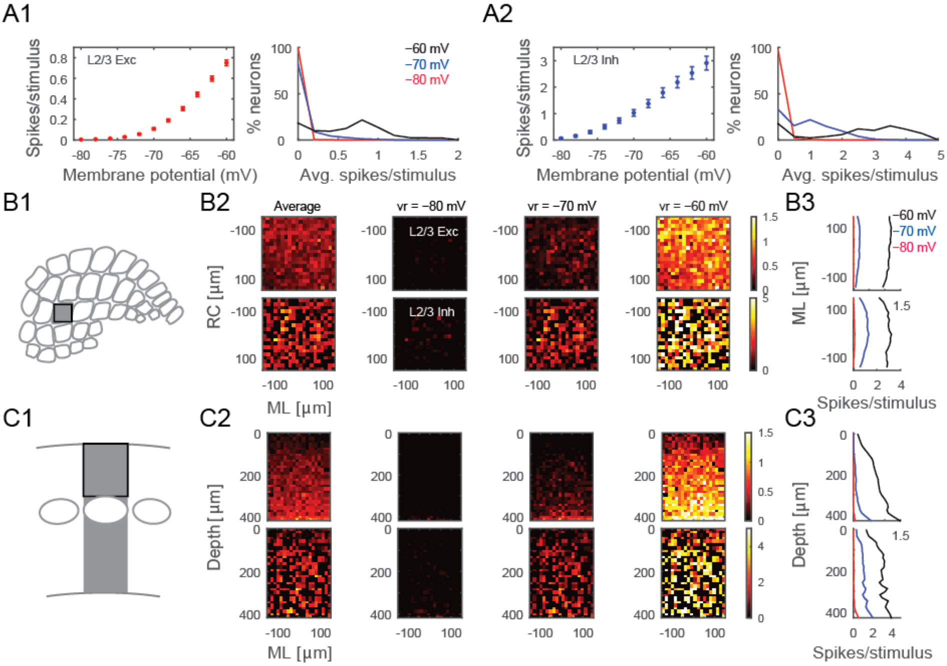

Figure 3.12. Response to Stimulus presentation in the principal whisker's cortical Layer 2/3 in silico. (A1) Left: Average firing rate in the network as function of the resting membrane potential states, right: histogram of spiking rate in the network across membrane states. (A2) same as A1, but for L2/3 inhibitory neuron populations. (B) Spatial distribution of L2/3 response as visualized in a tangential plane cutting across all columns in L2/3. (B1) The schematic drawing illustrates spatial dimensions and orientation of the visual displays in B2. The dark edged square labels the analyzed region in B2-3, and the gray region indicates the principal (stimulated) whisker barrel. (B2) Average excitatory (upper panel) and inhibitory (lower panel) neuronal response at different spatial location mapped onto RC-ML plane, across different resting membrane states. Each bin is a 15x15 µm window. (B3) Average excitatory (upper panel) and inhibitory (lower panel) neuronal responses along the RC axis. (C) Spatial distribution of the L2/3 response as visualized in a coronal plane cutting across layers. (C1-C3) Same as B1-B3, but analyzed in a coronal plane.

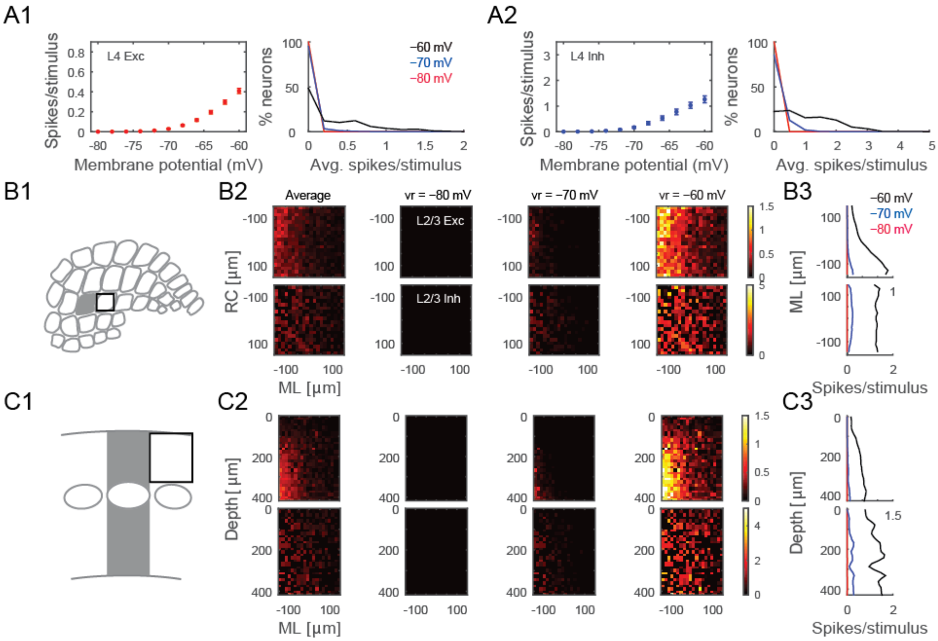

Figure 3.13. Response to Stimulus presentation in the surround whisker's cortical Layer 2/3 in silico. (A1) Left: Average firing rate in the network as function of resting membrane potential states, right: histogram of spiking rate in the network across membrane states. (A2) same as A1, but for L2/3 inhibitory neuron population. (B) Spatial distribution of L2/3 response as visualized in a tangential plane cutting across all columns in L2/3. (B1) The schematic drawing illustrates spatial dimensions and orientation of the visual displays in B2. The dark edged square labels the region analyzed in B2-3, and the gray region indicates the principal (stimulated) whisker barrel. (B2) Average excitatory (upper panel) and inhibitory (lower panel) neuronal response at different spatial location mapped onto RC-ML plane, across different resting membrane states. Each bin is a 15x15 µm window. (B3) Average excitatory (upper panel) and inhibitory (lower panel) neuronal responses along the RC axis. (C) Spatial distribution of the L2/3 response as visualized in a coronal plane cutting across layers. (C1-C3) Same as B1-B3, but analyzed in a coronal plane.

Given that the neuronal excitability changes with the resting membrane state, and that each neuron is an integrator that will sum its inputs until the non-linear transformation of the input into spikes, the functional connectivity within the network should change with the membrane potential state of the postsynaptic neuron. To visualize the effective connectivity we spatially mapped the synaptically connected presynaptic neurons that fired action potential(s) prior to the spiking of a postsynaptic neuron (Figure 3.14). As expected the functional connectivity varied with the resting membrane state, although the relative contribution of the L4 input to trigger a spike in L2/3 neurons remained constant across states. With an increasing probability of L2/3 spiking in the depolarized membrane states, the contribution of the intralaminar input to the spiking increased, suggesting that at depolarized membrane states sensory responses are a function of feed-forward drive originating from L4 and local recurrent excitation in L2/3. The latter component is likely to be modulated by top-down modulations or as the state of the animal changes during. For instance, active sensing could provide a mechanistic model how the bottom-up sensory information can be integrated with the top-down neuromodulatory influences.

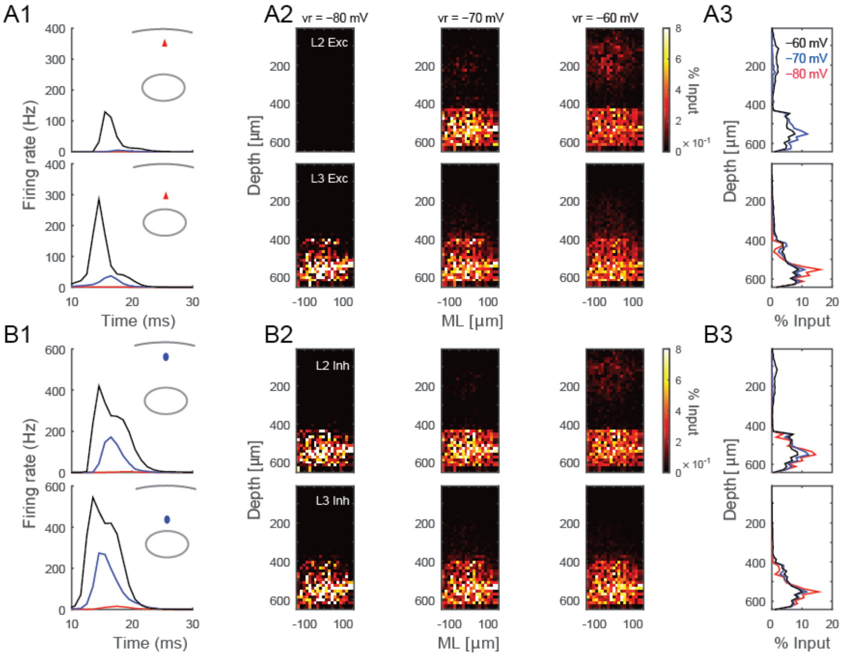

Figure 3.14. Visualization of the presynaptic population contributing to a postsynaptic action potential. We spatially mapped the neural activity across the granular and supragranular layers prior to an action potential in a given layer. The maps were averaged across all postsynaptic neurons that fire evoked action potentials during the simulations. (A1) Population activity that drives an L2 (upper panel) or L3 (lower panel) excitatory neurons to spike in response to thalamic input. The first spike fired by either an L2 or L3 excitatory neurons is used as the trigger to calculate the spike-triggered input map. Insert: schematic representation of the location of different cell population in the barrel column. (A2) Spike triggered spatial averaging for L2 (upper panel) and L3 (lower panel) excitatory neuron population at

different resting membrane potentials. (A3) Average depth distribution of excitatory inputs to drive a spike in L2 (upper panel) and L3 (lower panel) excitatory neurons. (B1-B3) Same as A1-A2, but using L2 and L3 inhibitory neurons as triggers, respectively.

Experience-dependent plasticity of synaptic strength *in silico*

Neurons in the barrel cortex adapt to the changes in sensory organ use as cortical circuits undergo plastic changes upon altered sensory input statistics (Allen et al 2003, Celikel et al 2004, Feldman & Brecht 2005, Clem et al 2008). These adaptive changes have long lasting consequences in neural representations of touch and might help to functionally bridge neural representations to touch perception. We have, therefore, integrated a spike-timing-dependent-plasticity learning rule (Celikel et al 2004) to enable plastic changes in neural representations of touch *in silico*. Figure 3.15 shows the implementation of the model on a 3-column model of the barrel cortex, layers 1-4 (Figure 3.15A1). Each column receives their major synaptic input from their own respective whiskers in the form of thalamic representation of whisker touch (see above; Figure 3.15A2), with the exception that the center column lacks a principal whisker, mimicking the whisker deprivation condition (Figure 3.15A2).

Employing empirically observed the STDP rules across the feed-forward projections originating from L4 (Figure 3.15B) and intracolumnar projections of L2/3 (Figure 3.15C) resulted in reorganization of touch already within 100 trials, in agreement with the experimental observations in barrel cortical slices (Allen et al 2003, Celikel et al 2004). The model correctly predicted all the known pathways that are modified upon whisker deprivation including the potentiation in the spared whiskers' L4-L2/3 projections (Clem et al 2008), slow depression in the deprived cortical column's L4-L2/3 projections (Bender et al 2006), and plasticity of the oblique projections from L4 onto the neighboring L2/3 (Hardingham et al 2011). The model further predicted that a number of circuit changes, including the bidirectional changes across the cross-columnar projections between the spared and deprived columns, which could potentially bridge the receptive field plasticity to topographic map reorganization.

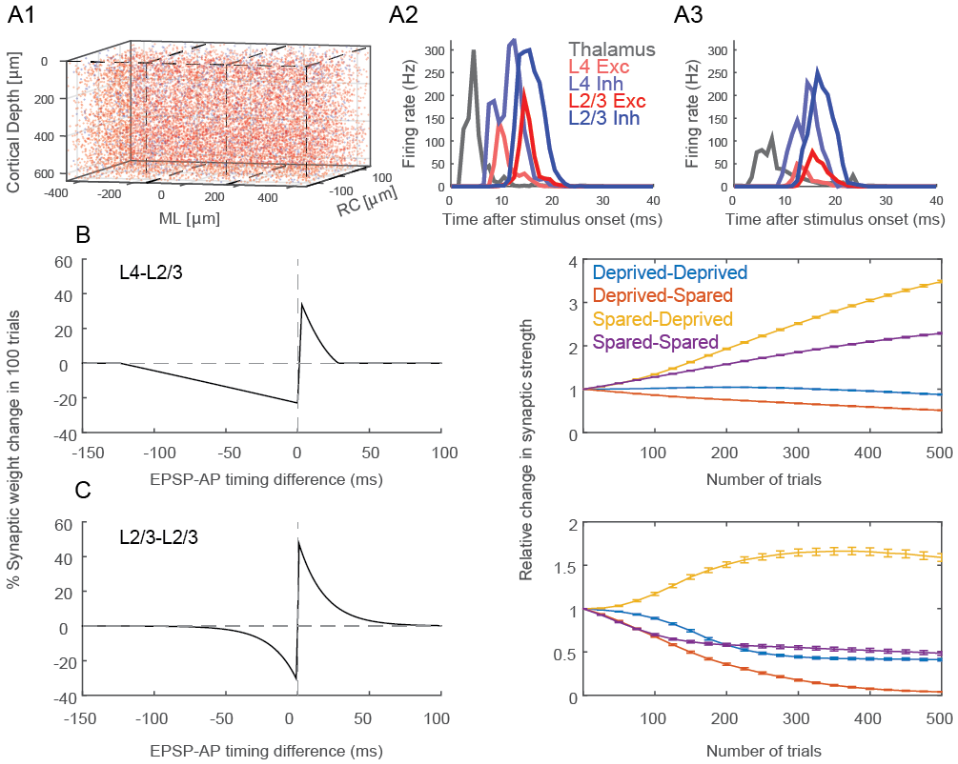

Figure 3.15. Spike-timing dependent map plasticity in silico. (A1) A network model with 3 barrels. Cells in each column are randomly generated using distributions quantified in Figure 5. (A2) Population PSTH for the spared columns, i.e most medial and most lateral columns in A1. (A3) Population PSTH for the deprived, i.e. center, column. (B) Left: Experimentally observed STDP learning rule in L4-L2/3 projections (Celikel et al 2004; see Materials and Methods). Right: Change in synaptic efficacy as a function of whisker deprivation in the simulated network. Color codes denote the whisker deprivation status of pre- and postsynaptic neurons' location. Note that presynaptic neurons are always located in L4. (C) Same as in B, but for L2/3-L2/3 connections. STDP rule was taken from Banerjee et al 2014.

Discussion

Understanding the circuit mechanisms of touch will require studying the somatosensory cortex as a dynamical complex system. Given that the majority of research in the barrel system has thus far focused on the identification circuit components one neuron at a time without linking structure to function, the development of a computational model of the barrel cortex is not only necessary, but also feasible (thanks to these careful and plentiful observations on the circuit organization). Accordingly, here we employed a three-tiered approach to (1) reconstruct the barrel cortex in soma resolution, (2) develop a model neuron whose spiking is a function of the network activity impinging onto postsynaptic neurons, and (3) axo-dendritically connect neurons in the column based on Peter's rule and experimentally observed pairwise network connectivity (see Materials and Methods). We finally performed simulations in this network to compare neural responses to whisker touch *in silico* to experimental observations from biological networks *in vivo*. As extensively discussed in the Results section simulations correctly replicate experimental observations *in vivo* with high accuracy. Here we will first discuss technical considerations and finally conclude the chapter with a brief discussion on the future developments for this barrel cortical column *in silico*.

Technical considerations for anatomical reconstruction of an stereotypical barrel column

One of the essential steps towards building a biologically plausible in *silico* model of the mouse barrel cortex is to obtain the distribution pattern of different neuron types throughout the barrel cortex. To reconstruct the cortex in soma resolution, we directly visualized these distributions by labeling different types of neurons using cell-type specific markers in tangential section and digitized these data using confocal scanning microscopy. We automatized the identification and counting of all neurons independent from whether the markers were nuclear or cyctoplasmic. The advantage of using tangential sections is that the identities of individual barrels in L4 can be reliably recognized based on GAD65 immunostaining (Figure 3.3A). However, due to difficulties in aligning images across consecutive sections, we could not consistently follow every barrel column across the entire cortical depth. Therefore, in the current study we only report average cell density across a canonical barrel cortex rather than reconstructing the barrel cortex while preserving the columnar identity. It should be noted that, in the rat barrel cortex, the cell density across different barrel columns has been shown to be relatively constant (Meyer et al 2013). Thus our density estimation is likely to be accurate as we employed a normalized volume for the entire column. Obviously, however, the absolute cell number in a particular barrel column could vary depending on the exact location of the barrel within the barrel cortex (Meyer et al 2013).

Our automatic cell counting algorithm for nuclear cell counts is functionally similar to that employed in Oberlaander et al. (2009). Compared to their method, we employed lower threshold values to separate foreground objects from background in order to capture weakly stained cells. This comes at the expense of an increased number of connected clusters. Therefore we employed more sophisticated methods to separate clusters of connected cells based on both intensity and shape information, rather than simply assuming that there exists a single dominate cell population based on volume, which could lead to a bias when this assumption is not met (Oberlaender et al 2009). Our method does not require manual correction, and the counting results are comparable with manual counts (Table 3.1). Furthermore we also developed algorithms to enable source localization for the cytoplasmic signals which allowed us to quantify cellular classes, for instance somatostatin neurons, which are characterized by non-nuclear markers. Together these approaches have resulted in more detailed quantification of the network, going beyond the two-neuron group (i.e. excitatory vs inhibitory) clustering available in the literature.

Tissue shrinkage could affect the cell density estimates. Although we project cell densities onto a normalized volumetric column, and although we have quantified the shrinkage of the sections, the cell density estimates might somewhat differ using alternative reconstruction methods. Another potential error could be introduced by cutting cells located at slice borders – these cells will appear in both slices, resulting in overestimation of the cell number. We corrected for the overestimation by including only those cells within a given radius along the z- direction (which is orthogonal to cutting plane) and no smaller than half of the average radius along x- and y- direction. This ensured that the overwhelming majority of the cells were located within the same slice, as confirmed by the human observer quantifications.

Comparison with past cell counts

In our data the average neuronal density, as identified by NeuN staining, across all layers of the mouse barrel cortex was found to be 1.66×10^5 per mm^3, before correcting for tissue shrinkage. After immunostaining the average optical thickness of slices was found to be 32.5 µm, indicating a 34.8% shrinkage in z direction, assuming that each slice in our sample was cut precisely as 50 µm section. The shrinkage along x-y plane was generally much smaller in our protocol: imaged cells with voxel size of 0.73-by-0.73-by-0.45 or 1.46-by-1.46-by-0.9 µm showed a similar voxel radius along x-, y- and z- axes (data not shown). If we assume that the real neurons have similar radius along the 3 axes, the data suggests a shrinkage factor of ~2.3% along x- and y- axes. After correcting for the estimated average shrinkage factors, the average neuronal density became 1.03×10^5 per mm^3, which is within the range of previously reported values in the C57B6 mouse (i.e. 0.6×10^5-1.6×10^5 per mm^3, Ma et al 1999, Hodge et al 2005, Irintchev et al 2005, Lyck et al 2007, Tsai et al 2009).

Comparison with other simulated networks

Researchers make network models in order to explain network dynamics and information processing on many levels. Therefore, these models exist at many different scales of complexity. On the one extreme, simplified network models investigate a single or a few aspects of the network (connectivity) properties on network behavior. For instance, randomly connected balanced networks use integrate-and fire neuron models (Brunel 2000), binary neuron models (van Vreeswijk and Sompolinsky 1996, 1998), or rate neuron models (Sompolinsky and Crisanti 1988) to investigate the effects of synaptic sparseness, connectivity strength and the balance between excitation and inhibition on network dynamics. Similarly, like discussed in the introduction, feed-forward networks like the perceptron (Rosenblatt 1958) can explain the increasing abstraction of receptive fields in sensory perception using similar simplified neuron models (Seung and Yuste 2012) and randomly connected symmetric networks (Hopfield 1982) can explain associative memory. Finally, the dynamics of small-world networks (Watts and Strogatz 1998) have several special properties such as rapid (near-critical) synchronization, low wiring costs and a balance between locally specialized and large-scale distributed information processing (Bassett and Bullmore 2006, Stam and Reijneveld 2007).

Although simplified networks are often very powerful in giving (analytical) explanations about the influence of connectivity on network behaviour, they are biologically not very realistic. A middle ground can be found in biologically-inspired networks that use the main connectivity schemes found in the brain. These model networks often make specific predictions about the effects of network properties on dynamics, although analytical solutions are mostly not feasible. For instance, Tort et al. (Tort et al 2007) explain the role of O-LM interneurons in gamma-band coherence in a hippocampal network using known network motives and single- and multi-compartment conductance-based cell models. A second example of such models is by Rubin and Terman (Rubin and Terman 2004), who make a network of the basal ganglia and thalamus, using simplified conductance-based models, to successfully explain the effects of deep-brain stimulation of the subthalamic nucleus in patients suffering from Parkinson’s disease. A final example from Wendling et al. (Wendling et al 2002) shows how epileptiform EEG activity can be explained by making a difference between fast and slow feedback inhibition in a macroscopic rate-based model of the hippocampus.

Another intermediate level of modelling networks is fitting functional models to whole-network recordings (e.g. Generalized Linear Models (GLMs) (Paninski 2004, Pillow et al 2008, Truccolo et al 2005), Generalized Integrate-and-Fire models (GIF models) (Gerstner and Kistler 2002, Jolivet et al 2004), etc). With these types of models, the spiking behaviour and functional connectivity of entire networks can be fitted to network recordings. The results from such an analysis can be difficult to link to biophysical properties of the neurons and networks, but it is a very successful method for describing the functional connectivity of for instance the macaque, salamander, cat and rabbit retina (Denk and Detwiler 1999, Doi et al 2012, Keat et al 2001, Li et al 2015, Marre et al 2012, Pillow et al 2005, Reich et al 1998) (for a review see Field and Chichilnisky 2007) and *c. elegans* (Kato et al 2015).

Finally, on the other extreme, are biologically reconstructed networks, like the one we present here. For some systems, complete or partial wiring diagrams have been published (*c. elegans*: Varshney et al 2011, mouse retina: Helmstaedter et al 2013), that can be used to construct such models. These networks are biologically realistic, but because of their complexity, it is more difficult to analyse the influence of specific network properties on network dynamics and function. Moreover, one concern is that with the current methods, it still impossible to measure all relevant parameters (molecular cell-type, electrophysiological cell-type, cell location, structural connectivity, functional connectivity) in a single sample. Therefore, every biologically reconstructed network so far is a combination of properties from different animals. Whether such a synthesized model is a good approximation of the actual functional neural network remains to be seen (Edelman and Gally 2001, Marder and Taylor 2011). Despite these limitations, biologically reconstructed network models are very important as a testing ground for hypotheses based on more simplified networks, or to assess biological parameters that are difficult or impossible to measure experimentally. In table 3.4, we have summarized the properties of several biologically reconstructed networks that have been published over the last few years. Note that until now, all these reconstructed networks have to be run on a cluster of computers or on a supercomputer, because a simple desktop computer simply lacked the computational power to run a biologically reconstructed network. Our model is slightly smaller than existing models, which makes it run on a normal desktop computer. Because our model exists of a single column, it is easily scalable: to include more columns, only the inter-columnar connectivity has to be modelled. Finally, like the recent model by Markram et al. (Markram et al 2015), we used no parameter tuning to construct this model, other than making the different cell-types of the Izhikevich-model and controlling the cell-type specific connection probabilities. All this makes the model very accessible for quickly testing fundamental hypotheses.

Authors	**Brain area, animal**	**Neuron models**	**Number of modelled neurons**	**Short term synaptic**	**Long term plasticity**	**platform**

				plasticity		
Izhikevich & Edelman, 2008	(human) thalamus, cortex, brainstem neuromodulation	Izhikevich (2003, 2004) 'simple model', multicompartmental	1,000,000	Yes	STDP	Cluster
Markram et al., 2015	Layers 1-6, hind-limb somatosensory cortex of rat with thalamic input	Multicompartment conductance model	31,000	Yes	Yes, but unspecified	Supercomputer
Markram, 2006	Cortical column	Multicompartment conductance model	10,000	Yes	No	Supercomputer
Sharp et al., 2014	Barrel cortex, rodent	Leaky integrate-and-fire model	50,000	No	No	Cluster
Huang et al., 2015	L4-L2/3 somatosensory column of mouse, with thalamic input	Izhikevich (2003, 2004) 'simple model'	4,200	Yes	STDP	PC
Ananthanarayanan et al.,	Thalamus, visual	Izhikevich (2003, 2004)	>1,000,000,000	No	STDP	Supercomputer

2009	cortex, cat	‘simple model’				
Traub et al., 2005	Thalamus, cortex	Multicompartment conductance model	3560	No	No	Cluster

Table 3.4. Summarization of the properties of several recently published biologically reconstructed or biology-inspired network models.

Work in progress for the next generation of the barrel cortex *in silico*

The current model is sufficiently detailed and accurate enough to start addressing fundamental questions in systems neuroscience as shown in the results section above and in the following chapters. In the interim we are updating the model with new anatomical data where the entire network is visualized in transparent brain (which solves the problem of section alignment) and using an extended combination of antibodies (which improves the accuracy of neuronal class identifications). It is important to note however that not all new data will directly benefit the network *in silico* in the short run as combinatorial subclassification of inhibitory neurons results in superclustering. In the absence of connectivity and electrophysiological characterization for the new clusters, their inclusion to the model is best an approximation of their function.

References

Ananthanarayanan, R., Esser, S. K., Simon, H. D., & Modha, D. S. (2009). The cat is out of the bag: cortical simulations with 109 neurons, 1013 synapses. *In Proceedings of the Conference on High Performance Computing Networking, Storage and Analysis,* 1-12.

Aguilar, J. R., & Castro-Alamancos, M. A. (2005). Spatiotemporal gating of sensory inputs in thalamus during quiescent and activated states. *The Journal of Neuroscience*, 25(47), 10990–1002.

Ali, A. B. (2003). Involvement of post-synaptic kainate receptors during synaptic transmission between unitary connections in rat neocortex. *The European Journal of Neuroscience*, *17*(11), 2344–50.

Armstrong-James, M., & Callahan, C. A. (1991). Thalamo-cortical processing of vibrissal information in the rat. II. spatiotemporal convergence in the thalamic ventroposterior medial nucleus (VPm) and its relevance to generation of receptive fields of S1 cortical “barrel” neurones. *The Journal of Comparative Neurology, 303*(2), 211–24.

Armstrong-James, M., Fox, K., & Das-Gupta, A. (1992). Flow of excitation within rat barrel cortex on striking a single vibrissa. *Journal of Neurophysiology*, *68*(4), 1345–58.

Arnold, P. B., Li, C. X., & Waters, R. S. (2001). Thalamocortical arbors extend beyond single cortical barrels: an in vivo intracellular tracing study in rat. *Experimental Brain Research, 136*(2), 152–68.

Banerjee, A., González-Rueda, A., Sampaio-Baptista, C., Paulsen, O., & Rodríguez-Moreno, A. (2014). Distinct mechanisms of spike timing-dependent LTD at vertical and horizontal inputs onto L2/3 pyramidal neurons in mouse barrel cortex. *Physiological Reports, 2*(3), e00271.

Bassett, D. S., & Bullmore, E. (2006). Small-world brain networks. The Neuroscientist : A Review Journal Bringing Neurobiology, Neurology and Psychiatry, 12(6), 512–23.

Beierlein, M., Gibson, J. R., & Connors, B. W. (2003). Two dynamically distinct inhibitory networks in layer 4 of the neocortex. *Journal of Neurophysiology*, 90(5), 2987–3000.

Bender, K. J., Allen, C. B., Bender, V. A., & Feldman, D. E. (2006). Synaptic basis for whisker deprivation-induced synaptic depression in rat somatosensory cortex. *The*

Journal of Neuroscience : The Official Journal of the Society for Neuroscience, *26*(16), 4155–65.

Blatow, M., Rozov, A., Katona, I., Hormuzdi, S. G., Meyer, A. H., Whittington, M. A., ... Monyer, H. (2003). A Novel Network of Multipolar Bursting Interneurons Generates Theta Frequency Oscillations in Neocortex. *Neuron, 38*(5), 805-817.

Brecht, M. (2007). Barrel cortex and whisker-mediated behaviors. *Current Opinion in Neurobiology*, *17*(4), 408–16.

Brecht, M., & Sakmann, B. (2002). Dynamic representation of whisker deflection by synaptic potentials in spiny stellate and pyramidal cells in the barrels and septa of layer 4 rat somatosensory cortex. *The Journal of Physiology, 543,* 49–70.

Brecht, M., Roth, A., & Sakmann, B. (2003). Dynamic receptive fields of reconstructed pyramidal cells in layers 3 and 2 of rat somatosensory barrel cortex. *The Journal of Physiology*, 553, 243–65.

Brunel, N. Dynamics of sparsely connected networks of excitatory and inhibitory spiking neurons. *Journal of Computational Neuroscience*, 8(3), 183–208.

Bruno, R. M., & Sakmann, B. (2006). Cortex is driven by weak but synchronously active thalamocortical synapses. *Science, 312*(5780), 1622–7.

Caputi, A., Rozov, A., Blatow, M., & Monyer, H. (2009). Two Calretinin-Positive GABAergic Cell Types in Layer 2/3 of the Mouse Neocortex Provide Different Forms of Inhibition. *Cerebral Cortex, 19*(6), 1345-1359.

Celikel, T., & Sakmann, B. (2007). Sensory integration across space and in time for decision making in the somatosensory system of rodents. *Proceedings of the National Academy of Sciences of the United States of America, 104*(4), 1395–400.

Celikel, T., Szostak, V. A., & Feldman, D. E. (2004). Modulation of spike timing by sensory deprivation during induction of cortical map plasticity. *Nature Neuroscience, 7*(5), 534-541.

Clem, R. L., Celikel, T., & Barth, A. L. (2008). Ongoing in vivo experience triggers synaptic metaplasticity in the neocortex. *Science, 319*(5859), 101–4.

Crochet, S., Poulet, J. F. A., Kremer, Y., & Petersen, C. C. H. (2011). Synaptic mechanisms underlying sparse coding of active touch. *Neuron*, *69*(6), 1160–75.

De Kock, C. P. J., Bruno, R. M., Spors, H., & Sakmann, B. (2007). Layer- and cell-type-specific suprathreshold stimulus representation in rat primary somatosensory cortex. *The Journal of Physiology*, *581*, 139–54.

Denk, W., & Detwiler, P. B. (1999). Optical recording of light-evoked calcium signals in the functionally intact retina. *Proceedings of the National Academy of Sciences of the United States of America*, 96(12), 7035–40.

Doi, E., Gauthier, J. L., Field, G. D., Shlens, J., Sher, A., Greschner, M., Machado, T. a, Jepson, L.H., Mathieson, K., Gunning, D.E., Litke, A.M., Paninski, L., Chichilnisky, E.J., Simoncelli, E. P. (2012). Efficient coding of spatial information in the primate retina. *The Journal of Neuroscience*, 32(46), 16256–64.

Diamond, M. E., Armstrong-James, M., & Ebner, F. F. (1992). Somatic sensory responses in the rostral sector of the posterior group (POm) and in the ventral posterior medial nucleus (VPM) of the rat thalamus. *The Journal of Comparative Neurology*, *318*(4), 462–76.

Douglas, R. J., & Martin, K. A. C. (2004). Neuronal circuits of the neocortex. *Annual Review of Neuroscience*, *27*, 419–51.

Douglas, R. J., & Martin, K. A. C. (2007). Mapping the matrix: the ways of neocortex. *Neuron*, *56*(2), 226–38.

Egger, V., Nevian, T., & Bruno, R. M. (2008). Subcolumnar dendritic and axonal organization of spiny stellate and star pyramid neurons within a barrel in rat somatosensory cortex. *Cerebral Cortex*, *18*(4), 876–89.

Edelman, G. M., & Gally, J. A. (2001). Degeneracy and complexity in biological systems. *Proceedings of the National Academy of Sciences of the United States of America*, 98(24), 13763–8.

Feldman, D. E., & Brecht, M. (2005). Map plasticity in somatosensory cortex. *Science*, *310*(5749), 810–5.

Feldmeyer, D., Lübke, J., & Sakmann, B. (2006). Efficacy and connectivity of intracolumnar pairs of layer 2/3 pyramidal cells in the barrel cortex of juvenile rats. *The Journal of Physiology*, 575, 583–602.

Feldmeyer, D., Brecht, M., Helmchen, F., Petersen, C. C. H., Poulet, J. F. A., Staiger, J. F., … Schwarz, C. (2013). Barrel cortex function. *Progress in Neurobiology*, *103*, 3–

27.

Feldmeyer, D., Lübke, J., Silver, R. A., & Sakmann, B. (2002). Synaptic connections between layer 4 spiny neurone- layer 2/3 pyramidal cell pairs in juvenile rat barrel cortex: Physiology and anatomy of interlaminar signalling within a cortical column. *The Journal of Physiology*, *538*(3), 803-822.

Field, G. D., & Chichilnisky, E. J. (2007). Information processing in the primate retina: circuitry and coding. *Annual Review of Neuroscience*, 30, 1–30.

Fino, E., & Yuste, R. (2011). Dense Inhibitory Connectivity in Neocortex. *Neuron*, *69*(6), 1188-1203.

Foeller, E., Celikel, T., & Feldman, D. E. (2005). Inhibitory sharpening of receptive fields contributes to whisker map plasticity in rat somatosensory cortex. *Journal of Neurophysiology*, *94*(6), 4387–400.

Furuta, T., Deschenes, M., & Kaneko, T. (2011). Anisotropic Distribution of Thalamocortical Boutons in Barrels. *Journal of Neuroscience*, *31*(17), 6432-6439.

Gentet, L. J., Avermann, M., Matyas, F., Staiger, J. F., & Petersen, C. C. H. (2010). Membrane potential dynamics of GABAergic neurons in the barrel cortex of behaving mice. *Neuron*, *65*(3), 422–35

Gentet, L. J., Kremer, Y., Taniguchi, H., Huang, Z. J., Staiger, J. F., & Petersen, C. C. H. (2012). Unique functional properties of somatostatin-expressing GABAergic neurons in mouse barrel cortex. *Nature Neuroscience*, *15*(4), 607–12.

Gerstner, W., Kistler, W.M. (2002). Spiking Neuron Models: Single Neurons, Populations, Plasticity. Cambridge University Press.

Gil, Z., Connors, B. W., & Amitai, Y. (1999). Efficacy of Thalamocortical and Intracortical Synaptic Connections. *Neuron*, *23*(2), 385–397.

Gupta, a., Wang, Y., & Markram, H. (2000). Organizing principles for a diversity of GABAergic interneurons and synapses in the neocortex. *Science*, *287*(5451), 273–8.

Hardingham, N. R., Gould, T., & Fox, K. (2011). Anatomical and sensory experiential determinants of synaptic plasticity in layer 2/3 pyramidal neurons of mouse barrel cortex. *The Journal of Comparative Neurology*, *519*(11), 2090–124.

Hodge, R. D., D'Ercole, A. J., & O'Kusky, J. R. (2005). Increased expression of insulin-like growth factor-I (IGF-I) during embryonic development produces neocortical overgrowth with differentially greater effects on specific cytoarchitectonic areas and cortical layers. *Brain Research. Developmental Brain Research*, *154*(2), 227–37.

Haas, J. S., Nowotny, T., & Abarbanel, H. (2006). Spike-Timing-Dependent Plasticity of Inhibitory Synapses in the Entorhinal Cortex. *Journal of Neurophysiology, 96*(6), 3305-3313.

Heckbert, P. S. (1994). *Graphics gems IV*. Boston: AP Professional.

Helmstaedter, M., Briggman, K. L., Turaga, S. C., Jain, V., Seung, H. S., & Denk, W. (2013). Connectomic reconstruction of the inner plexiform layer in the mouse retina. *Nature*, 500(7461), 168–174.

Helmstaedter, M., Staiger, J. F., Sakmann, B., & Feldmeyer, D. (2008). Efficient Recruitment of Layer 2/3 Interneurons by Layer 4 Input in Single Columns of Rat Somatosensory Cortex. *Journal of Neuroscience, 28*(33), 8273-8284.

Holmgren, C., Harkany, T., Svennenfors, B., & Zilberter, Y. (2003). Pyramidal cell communication within local networks in layer 2/3 of rat neocortex. *The Journal of Physiology, 551*(1), 139-153.

Hopfield, J. J. (1982). Neural networks and physical systems with emergent collective computational abilities. *Proceedings of the National Academy of Sciences of the United States of America*, 79(8), 2554–8.

Izhikevich, E. M., & Edelman, G. M. (2008). Large-scale model of mammalian thalamocortical systems. *Proceedings of the National Academy of Sciences, 105*(9), 3593-3598.

Izhikevich, E. (2004). Which Model to Use for Cortical Spiking Neurons? *IEEE Transactions on Neural Networks, 15*(5), 1063-1070

Izhikevich, E. M. (2007). Dynamical systems in neuroscience: The geometry of excitability and bursting. Cambridge, MA: MIT Press.

Izhikevich, E. M., & Edelman, G. M. (2008). Large-scale model of mammalian thalamocortical systems. *Proceedings of the National Academy of Sciences of the United States of America*, 105(9), 3593–8.

Irintchev, A., Rollenhagen, A., Troncoso, E., Kiss, J. Z., & Schachner, M. (2005). Structural and functional aberrations in the cerebral cortex of tenascin-C deficient mice. *Cerebral Cortex (New York, N.Y. : 1991)*, *15*(7), 950–62.

Kapfer, C., Glickfeld, L. L., Atallah, B. V., & Scanziani, M. (2007). Supralinear increase of recurrent inhibition during sparse activity in the somatosensory cortex. *Nature Neuroscience*, *10*(6), 743-753.

Jolivet, R., Lewis, T. J., & Gerstner, W. (2004). Generalized integrate-and-fire models of neuronal activity approximate spike trains of a detailed model to a high degree of accuracy. *Journal of Neurophysiology*, 92(2), 959–76.

Kato, S., Kaplan, H. S., Schrödel, T., Skora, S., Lindsay, T. H., Yemini, E., Lockery, S., Zimmer, M. (2015). Global Brain Dynamics Embed the Motor Command Sequence of Caenorhabditis elegans. *Cell*, 163(3), 656–69.

Kawaguchi, Y. (1997). GABAergic cell subtypes and their synaptic connections in rat frontal cortex. *Cerebral Cortex*, *7*(6), 476-486.

Keat, J., Reinagel, P., Reid, R. C., & Meister, M. (2001). Predicting every spike: a model for the responses of visual neurons. *Neuron*, 30(3), 803–17.

Koelbl, C., Helmstaedter, M., Lübke, J., & Feldmeyer, D. (2015). A barrel-related interneuron in layer 4 of rat somatosensory cortex with a high intrabarrel connectivity. *Cerebral Cortex*, *25*(3), 713–25.

Kwegyir-Afful, E. E., Bruno, R. M., Simons, D. J., & Keller, A. (2005). The role of thalamic inputs in surround receptive fields of barrel neurons. *The Journal of Neuroscience*, *25*(25), 5926–34.

Lefort, S., Tomm, C., Floyd Sarria, J.-C., & Petersen, C. C. H. (2009). The excitatory neuronal network of the C2 barrel column in mouse primary somatosensory cortex. *Neuron*, *61*(2), 301–16.

Li, P. H., Gauthier, J. L., Schiff, M., Sher, A., Ahn, D., Field, G. D., Greschner, M., Callaway, E.M., Litke, A.M., Chichilnisky, E. J. (2015). Anatomical identification of extracellularly recorded cells in large-scale multielectrode recordings. *The Journal of Neuroscience*, 35(11), 4663–75.

Lu, J., Li, C., Zhao, J., Poo, M., & Zhang, X. (2007). Spike-Timing-Dependent Plasticity of Neocortical Excitatory Synapses on Inhibitory Interneurons Depends on

Target Cell Type. *Journal of Neuroscience*, *27*(36), 9711-9720.

Lübke, J., & Feldmeyer, D. (2007). Excitatory signal flow and connectivity in a cortical column: focus on barrel cortex. *Brain Structure & Function*, *212*(1), 3–17.

Lyck, L., Krøigård, T., & Finsen, B. (2007). Unbiased cell quantification reveals a continued increase in the number of neocortical neurones during early post-natal development in mice. *The European Journal of Neuroscience*, *26*(7), 1749–64.

Ma, D., Descarries, L., Micheva, K. D., Lepage, Y., Julien, J. P., & Doucet, G. (1999). Severe neuronal losses with age in the parietal cortex and ventrobasal thalamus of mice transgenic for the human NF-L neurofilament protein. *The Journal of Comparative Neurology*, *406*(4), 433–48.

Marder, E., & Taylor, A. L. (2011). Multiple models to capture the variability in biological neurons and networks. *Nature Neuroscience*, 14(2), 133–8.

Markram, H., Muller, E., Ramaswamy, S., Reimann, M. W., Abdellah, M., Sanchez, C. A., Ailamaki, A., Alonso-Nanclares, L., Antille, N., Arsever, S., Kahou, G.A.A., Berger, T.K., Bilgili, A., Buncic, N., Chalimourda, A., Chindemi, G., Courcol, J.-D., Delalondre, F., Delattre, V., Druckmann, S., Dumusc, R., Dynes, J., Eilemann, S., Gal, E., Gevaert, M.E., Ghobril, J.-P., Gidon, A., Graham, J.W., Gupta, A., Haenel, V., Hay, E., Heinis, T., Hernando, J.B., Hines, M., Kanari, L., Keller, D., Kenyon, J., Khazen, G., Kim, Y., King, J.G., Kisvarday, Z., Kumbhar, P., Lasserre, S., Le Bé, J.-V., Magalhães, B.R.C., Merchán-Pérez, A., Meystre, J., Morrice, B.R., Muller, J., Muñoz-Céspedes, A., Muralidhar, S., Muthurasa, K., Nachbaur, D., Newton, T.H., Nolte, M., Ovcharenko, A., Palacios, J., Pastor, L., Perin, R., Ranjan, R., Riachi, I., Rodríguez, J.-R., Riquelme, J.L., Rössert, C., Sfyrakis, K., Shi, Y., Shillcock, J.C., Silberberg, G., Silva, R., Tauheed, F., Telefont, M., Toledo-Rodriguez, M., Tränkler, T., Van Geit, W., Díaz, J.V., Walker, R., Wang, Y., Zaninetta, S.M., DeFelipe, J., Hill, S.L., Segev, I., Schürmann, F. (2015). Reconstruction and Simulation of Neocortical Microcircuitry. *Cell*, 163(2), 456–492.

Markram, H., Toledo-Rodriguez, M., Wang, Y., Gupta, A., Silberberg, G., & Wu, C. (2004). Interneurons of the neocortical inhibitory system. *Nature Reviews Neuroscience*, *5*(10), 793-807.

Marre, O., Amodei, D., Deshmukh, N., Sadeghi, K., Soo, F., Holy, T. E., & Berry, M. J. (2012). Mapping a complete neural population in the retina. *The Journal of Neuroscience*, 32(43), 14859-73

Meyer, F. (1994). Topographic distance and watershed lines. *Signal Processing, 38*(1), 113-125.

Meyer, H. S., Wimmer, V. C., Oberlaender, M., de Kock, C. P. J., Sakmann, B., & Helmstaedter, M. (2010). Number and laminar distribution of neurons in a thalamocortical projection column of rat vibrissal cortex. *Cerebral Cortex*, *20*(10), 2277–86.

Meyer, H. S., Egger, R., Guest, J. M., Foerster, R., Reissl, S., & Oberlaender, M. (2013). Cellular organization of cortical barrel columns is whisker-specific. *Proceedings of the National Academy of Sciences, 110*(47), 19113-19118.

Oberlaender, M., Dercksen, V. J., Egger, R., Gensel, M., Sakmann, B., & Hege, H.-C. (2009). Automated three-dimensional detection and counting of neuron somata. *Journal of Neuroscience Methods, 180*(1), 147–60.

Oberlaender, M., Kock, C. P., Bruno, R. M., Ramirez, A., Meyer, H. S., Dercksen, V. J., ... Sakmann, B. (2012a). Cell Type-Specific Three-Dimensional Structure of Thalamocortical Circuits in a Column of Rat Vibrissal Cortex. *Cerebral Cortex, 22*(10), 2375-2391.

Oberlaender, M., Ramirez, A., & Bruno, R. (2012b). Sensory Experience Restructures Thalamocortical Axons during Adulthood. *Neuron, 74*(4), 648-655.

Otsu, N. (1979). A Threshold Selection Method from Gray-Level Histograms. (1979, 12). *IEEE Transactions on Systems, Man, and Cybernetics, 9*(1), 62-66.

O'Connor, D. H., Huber, D., & Svoboda, K. (2009). Reverse engineering the mouse brain. *Nature, 461*(7266), 923–9.

O'Connor, D. H., Peron, S. P., Huber, D., & Svoboda, K. (2010). Neural activity in barrel cortex underlying vibrissa-based object localization in mice. *Neuron, 67*(6),

Packer, A. M., & Yuste, R. (2011). Dense, Unspecific Connectivity of Neocortical Parvalbumin-Positive Interneurons: A Canonical Microcircuit for Inhibition? *Journal of Neuroscience, 31*(37), 13260-13271.

Paninski, L. (2004). Maximum likelihood estimation of cascade point-process neural encoding models. *Network*, 15(4), 243–62.

Peng, H., Ruan, Z., Long, F., Simpson, J. H., & Myers, E. W. (2010). V3D enables real-time 3D visualization and quantitative analysis of large-scale biological image data sets. *Nature Biotechnology*, *28*(4), 348-353.

Peters, A., Feldman, M., & Saldanha, J. (1976). The projection of the lateral geniculate nucleus to area 17 of the rat cerebral cortex. II. Terminations upon neuronal perikarya and dendritic shafts. *Journal of Neurocytology*, 5(1), 85–107.

Pfeffer, C. K., Xue, M., He, M., Huang, Z. J., & Scanziani, M. (2013). Inhibition of inhibition in visual cortex: the logic of connections between molecularly distinct interneurons. *Nature Neuroscience*, *16*(8), 1068–76.

Pillow, J. W., Paninski, L., Uzzell, V. J., Simoncelli, E. P., & Chichilnisky, E. J. (2005). Prediction and decoding of retinal ganglion cell responses with a probabilistic spiking model. *The Journal of Neuroscience*, 25(47), 11003–13.

Pillow, J. W., Shlens, J., Paninski, L., Sher, A., Litke, A. M., Chichilnisky, E. J., & Simoncelli, E. P. (2008). Spatio-temporal correlations and visual signalling in a complete neuronal population. *Nature*, 454(7207), 995–9.

Porter, J. T., Cauli, B., Staiger, J. F., Lambolez, B., Rossier, J., & Audinat, E. (1998). Properties of bipolar VIPergic interneurons and their excitation by pyramidal neurons in the rat neocortex. *European Journal of Neuroscience*, *10*(12), 3617-3628.

Reich, D. S., Victor, J. D., & Knight, B. W. (1998). The power ratio and the interval map: spiking models and extracellular recordings. *The Journal of Neuroscience*, 18(23), 10090–104.

Reyes, a, Lujan, R., Rozov, A., Burnashev, N., Somogyi, P., & Sakmann, B. (1998). Target-cell-specific facilitation and depression in neocortical circuits. *Nature Neuroscience*, *1*(4), 279–85.

Rosenblatt, F. (1958). The perceptron: a probabilistic model for information storage and organization in the brain. *Psychological Review*, 65(6), 386–408.

Rozov, a, Jerecic, J., Sakmann, B., & Burnashev, N. (2001). AMPA receptor channels with long-lasting desensitization in bipolar interneurons contribute to synaptic depression in a novel feedback circuit in layer 2/3 of rat neocortex. *The Journal of Neuroscience*, *21*(20), 8062–71.

Rubin, J. E., & Terman, D. High frequency stimulation of the subthalamic nucleus eliminates pathological thalamic rhythmicity in a computational model. *Journal of*

Computational Neuroscience, 16(3), 211–35.

Sachidhanandam, S., Sreenivasan, V., Kyriakatos, A., Kremer, Y., & Petersen, C. C. H. (2013). Membrane potential correlates of sensory perception in mouse barrel cortex. *Nature Neuroscience*, *16*(11), 1671–7.

Schubert, D., Kötter, R., & Staiger, J. F. (2007). Mapping functional connectivity in barrel-related columns reveals layer- and cell type-specific microcircuits. *Brain Structure & Function*, *212*(2), 107–19.

Seung, H.S., Yuste, R. (2012). Neural Networks. In: Principles of Neural Science. pp. 1580 – 1600. McGraw-Hill.

Sharp, T., Petersen, R., & Furber, S. (2014). Real-time million-synapse simulation of rat barrel cortex. *Frontiers in Neuroscience,* 8, 131.

Simons, D. J., & Carvell, G. E. (1989). Thalamocortical response transformation in the rat vibrissa/barrel system. *Journal of Neurophysiology*, *61*(2), 311–30.

Sompolinsky, H., Crisanti, A., & Sommers, H. J. (1988). Chaos in Random Neural Networks. *Physical Review Letters*, 61(3), 259–262.

Staiger, J. F., Flagmeyer, I., Schubert, D., Zilles, K., Kötter, R., & Luhmann, H. J. (2004). Functional diversity of layer IV spiny neurons in rat somatosensory cortex: quantitative morphology of electrophysiologically characterized and biocytin labeled cells. *Cerebral Cortex*, 14(6), 690–701.

Stam, C. J., & Reijneveld, J. C. (2007). Graph theoretical analysis of complex networks in the brain. *Nonlinear Biomedical Physics*, 1(1), 3.

Swadlow, H. A. (1995). Influence of VPM afferents on putative inhibitory interneurons in S1 of the awake rabbit: evidence from cross-correlation, microstimulation, and latencies to peripheral sensory stimulation. *J Neurophysiol*, *73*(4), 1584–1599.

Swadlow, H. A. (2003). Fast-spike Interneurons and Feedforward Inhibition in Awake Sensory Neocortex. *Cerebral Cortex*, *13*(1), 25–32.

Sun, Q., Huguenard, J., Prince, D. (2006). Barrel Cortex Microcircuits: Thalamocortical Feedforward Inhibition in Spiny Stellate Cells Is Mediated by a Small Number of Fast-Spiking Interneurons. *Journal of Neuroscience*, *26*(4), 1219-1230.

Tamas, G., Lorincz, A., Simon, A., Szabadics, J. (2003). Identified Sources and Targets of Slow Inhibition in the Neocortex. *Science, 299*(5614), 1902-1905. doi: 10.1126/science.1082053

Thomson, A. M., Lamy, C. (2007). Functional maps of neocortical local circuitry. *Frontiers in Neuroscience, 1*(1), 19-42.

Tort, A. B. L., Rotstein, H. G., Dugladze, T., Gloveli, T., & Kopell, N. J. (2007). On the formation of gamma-coherent cell assemblies by oriens lacunosum-moleculare interneurons in the hippocampus. *Proceedings of the National Academy of Sciences of the United States of America*, 104(33), 13490–5.

Traub, R. D., Contreras, D., Cunningham, M. O., Murray, H., LeBeau, F. E. N., Roopun, A., Bibbig, A., Wilent, W. B., Higley, M. J., Whittington, M. A. (2005). Single-column thalamocortical network model exhibiting gamma oscillations, sleep spindles, and epileptogenic bursts. Journal of Neurophysiology, 93(4), 2194–232.

Truccolo, W., Eden, U. T., Fellows, M. R., Donoghue, J. P., & Brown, E. N. (2005). A point process framework for relating neural spiking activity to spiking history, neural ensemble, and extrinsic covariate effects. *Journal of Neurophysiology*, 93(2), 1074–89.

Tsai, P. S., Kaufhold, J. P., Blinder, P., Friedman, B., Drew, P. J., Karten, H. J., … Kleinfeld, D. (2009). Correlations of neuronal and microvascular densities in murine cortex revealed by direct counting and colocalization of nuclei and vessels. *The Journal of Neuroscience*, *29*(46), 14553–70.

Uematsu, M., Hirai, Y., Karube, F., Ebihara, S., Kato, M., Abe, K., ... Kawaguchi, Y. (2007). Quantitative Chemical Composition of Cortical GABAergic Neurons Revealed in Transgenic Venus-Expressing Rats. *Cerebral Cortex, 18*(2), 315-330.

van Vreeswijk, C., & Sompolinsky, H. (1996). Chaos in neuronal networks with balanced excitatory and inhibitory activity. *Science*, 274(5293), 1724–6.

Varshney, L. R., Chen, B. L., Paniagua, E., Hall, D. H., & Chklovskii, D. B. (2011). Structural properties of the Caenorhabditis elegans neuronal network. *PLoS Computational Biology*, 7(2), e1001066.

Von H van Vreeswijk, C., & Sompolinsky, H. (1998). Chaotic balanced state in a model of cortical circuits. *Neural Computation*, 10(6), 1321–71.

eimendahl, M., Itskov, P. M., Arabzadeh, E., & Diamond, M. E. (2007). Neuronal activity in rat barrel cortex underlying texture discrimination. *PLoS Biology*, *5*(11), e305.

Vincent, L. (1993). Morphological grayscale reconstruction in image analysis: Applications and efficient algorithms. *IEEE Transactions on Image Processing, 2*(2), 176-201.

Watts, D. J., & Strogatz, S. H. (1998). Collective dynamics of “small-world” networks. *Nature*, 393(6684), 440–2.

Wendling, F., Bartolomei, F., Bellanger, J. J., & Chauvel, P. (2002). Epileptic fast activity can be explained by a model of impaired GABAergic dendritic inhibition. *The European Journal of Neuroscience*, 15(9), 1499–508.

White, E. L. (1979). Thalamocortical synaptic relations: A review with emphasis on the projections of specific thalamic nuclei to the primary sensory areas of the neocortex. *Brain Research Reviews, 1*(3), 275-311.

Wozny, C., & Williams, S. R. (2011). Specificity of Synaptic Connectivity between Layer 1 Inhibitory Interneurons and Layer 2/3 Pyramidal Neurons in the Rat Neocortex. *Cerebral Cortex, 21*(8), 1818-1826.

Xu, X., Roby, K. D., & Callaway, E. M. (2006). Mouse cortical inhibitory neuron type that coexpresses somatostatin and calretinin. *The Journal of Comparative Neurology, 499*(1), 144-160.

Zheng, Y., Lin, S., Kambhamettu, C., Yu, J., & Kang, S. B. (2009). Single-Image Vignetting Correction. *IEEE Transactions on Pattern Analysis and Machine Intelligence, 31*(12), 2243-2256.

Chapter 4. COMPUTATIONAL PROPERTIES OF NEURONS WITH ADAPTIVE THRESHOLD

Abstract

Neural processing rests on the intracellular transformation of information as synaptic inputs are translated into action potentials. This transformation is governed by the spike threshold, which depends on the history of the membrane potential on many temporal scales. While the adaptation of the threshold after spiking activity has been addressed before both theoretically and experimentally, it has only recently been demonstrated that the subthreshold membrane state also influences the effective spike threshold. The consequences for neural computation are not well understood yet. We address this question here using neural simulations and whole cell intracellular recordings in combination with information theoretic analysis.

We show that an adaptive spike threshold leads to better stimulus discrimination for tight input correlations than would be achieved otherwise, independent from whether the stimulus is encoded in the rate or pattern of action potentials. Encoding information using adaptive thresholds further ensures robust information transmission across cortical states i.e. decoding from different states is less state dependent in the adaptive threshold case, if the decoding is performed in reference to the timing of the population response. Results from *in vitro* neural recordings were consistent with simulations from adaptive threshold neurons.

In summary, the adaptive spike threshold reduces information loss during intracellular information transfer, improves stimulus discriminability and ensures robust decoding across membrane states in a regime of highly correlated inputs, similar to those seen in sensory nuclei during the encoding of sensory information.

Introduction

The essential computation performed by neurons is the (non-linear) integration of synaptic inputs and subsequent generation of a spike. This summation is determined by multiple factors, including the passive membrane properties, active currents, and the neuronal geometry (Magee, 2000, Destexhe et al 2003, Spruston and Nelson 2008). The currents at the axon hillock have voltage-dependent activation dynamics, which accelerate and then self-sustain the depolarization, eventually leading to a spike. The voltage at which this acceleration occurs is commonly referred to as the voltage threshold of spiking or spike threshold. Recently, several studies have empirically demonstrated that this threshold is not constant as recorded in cortical (Azouz and Gray 2000, Azouz and Gray 2003, Polavieja et al 2005, Wilent and Contreras 2005, Goldberg et al 2008) and in subcortical (Henze and Buzsaki 2001, Farries et al 2010, Fontaine et al. 2014) neurons. Rather, the spike threshold exhibits a dependence on the slope of the depolarization, such that fast depolarizations produce spikes at lower thresholds, and slower depolarizations at higher thresholds. The relationship is monotonically decreasing over a range of a few millivolts. This phenomenon is qualitatively different from the thoroughly studied spike-frequency adaptation, which acts on longer time scales (Brenner et al. 2000, Benda et al. 2010, Bohte et al. 2013) and depends on suprathreshold activity. The effects of the adaptation investigated here, will manifest already before the ‘first’ spike, e.g. at response onset.

Recently, Fontaine and colleagues (2014) have demonstrated that this threshold dependence can be captured using a threshold which itself ‘chases’ the membrane potential, however, does not instantly adapt to the new membrane potential but approaches its new value with a certain time-constant. Consequently, if one considers two fluctuations of equal size, but different speed, the faster fluctuation will encounter a lower threshold (still in the approach of its final value) and thus already lead to a spike, whereas the slower fluctuation may encounter a higher threshold and thus lead to a spike at a greater depolarization (or fail to spike). Hence, the propensity to spike depends on the recent history of the membrane potential and in particular on the most recent rate of depolarization leading up to a potential spike. Multiple mechanisms could underlie this modulation in spike threshold, including adaptive changes in sodium channel inactivation (Azouz and Gray 2000, Azouz and Gray 2003, Wilent and Contreras 2005, Platkiewicz and Brette 2011) and potassium conductances (Goldberg et al 2008, Higgs and Spain 2011). Given that the existence of these conductances is common among spiking neurons, an adaptive spike threshold is likely to be ubiquitous features of neurons.

An adaptive threshold could have important computational consequences, since this would rapidly modulate the gain of neurons. Several authors (Azouz and Gray 2000, Azouz and Gray 2003, Wilent and Contreras 2005, Higgs and Spain 2011, Fontaine et al 2014) have speculated on the possible relevance of an adaptive threshold in the sense described above, however, to our knowledge, no study has thoroughly investigated its computational consequences.

Hence, here we set out to evaluate the effect of an adaptive threshold on the level of single neurons in feed-forward excitatory networks in the context of stimulus processing. We investigate how a single neuron's response to different rates and patterns of inputs varies as the action potential generation is gated by fixed, i.e. constant, or adaptive thresholds. Furthermore, we investigate how the state of the neuron (resting membrane potential prior to stimulus onset) influences the response behavior using both recordings from barrel cortex as well as neuronal simulations. The results suggest that neurons with adaptive threshold perform better than with a constant threshold when the stimulus is encoded by highly correlated inputs. Such a neuron encodes the stimulus more robustly, even in the context of noisy fluctuations of the membrane potential. For the state differences, we find the temporal reference used for decoding - internal or external - to play a major role: If the time reference is computed internally based on the timing information from the correlated spiking of local populations, an adaptive threshold turns out to be beneficial. Together these results show the usefulness of adaptive thresholds in performing temporally precise and robust computations.

Materials and Methods

Neural recordings

Mice from either sex were used according to the Guidelines of National Institutes of Health, and experiments were approved by the local Institutional Animal Care and Use Committee.

In vitro whole-cell current-clamp recordings were performed in acutely prepared slices of the barrel cortex (P18-21) as described before with minor modifications (Allen et al 2003; Celikel et al, 2004). Animals were anesthetized using Isofluorane before they were decapitated. Oblique thalamocortical slices (Finnerty et al 1999)(300 mm) were cut 45° from the midsagittal plane in chilled low-calcium, low-sodium Ringer's solution (in mM; sucrose, 250; KCl, 2.5; $MgSO_4 \cdot 7H_2O$, 4; $NaH_2PO_4 \cdot H_2O$, 1; HEPES, 15; D-(+)-glucose, 11; $CaCl_2$, 0.1). Slices were incubated at 37ºC for 45 minutes and kept in room temperature in carbonated (5% oxygen) bath solution (pH 7.4, normal Ringer's solution: in mM, NaCl, 119; KCl, 2.5; $MgSO_4$, 1.3; NaH_2PO_4, 1; $NaHCO_3$, 26.3; D-(+)-glucose, 11; $CaCl_2$, 2.5).

Visualized whole-cell recordings were performed using an Axoclamp-2B amplifier under an IR-DIC objective (Olympus) in room temperature. A bipolar extracellular stimulation electrode was placed in the lower half of a L4 barrel representing a mystacial vibrissa. A recording electrode (3-4 MOhm) containing an internal solution (pH 7.25; in mM; potassium gluconate, 116; KCl, 6; NaCl, 2; HEPES, 20 mM; EGTA, 0.5; MgATP, 4; NaGTP, 0.3) was placed orthogonal to the stimulation electrode within 150-300 µm of the cortical surface. For whole cell recordings, putative excitatory cells were selected based on pyramid-shaped somata, apical dendrites and distal tuft orientation, and regular pattern of spiking to somatic current injections (500 ms). Data was filtered (2 kHz), digitized at 5 kHz using a 12 bit National Instruments data acquisition board and acquired using Strathclyde Electrophysiology Suite for offline data analysis.

All analyses were performed offline in MATLAB (MathWorks, Inc). Raw voltage traces were smoothed using running window averaging (1 ms window size), and resting membrane potential (Vm, in mV) was calculated as the average membrane potential in a 40 ms time window prior to the stimulus onset. For those sweeps in which spike was observed, spike threshold (Vt) and spike latency (St) in respect to stimulus onset were calculated. Spike threshold was defined as the membrane potential value at which second derivative of membrane potential reached maximum as described before (Wilent & Contreras 2004).

Neural simulations

Single Neuron Dynamics

We used the exponential integrate and fire model (Fourcaud-Trocme et al 2003) to simulate postsynaptic neuron membrane dynamics:

$$C_m \cdot dV_m/dt = -g_L(V_m - E_L) + g_L \cdot \Delta_T exp((V_m - \theta)/\Delta_T) + I$$

where C_m=50 nF is the membrane capacitance, g_L=10 ns is the leak conductance, E_L=-70 mV is the leak reversal potential, and Δ_T=1 mV is the slope factor which characterize the sharpness of spike initiation. V_m is the membrane potential in mV, and θ is the spike threshold. For neurons with adaptive threshold, θ is determined by (Fontaine et al 2014):

$$\tau_\theta \cdot d\theta/dt = \theta_\infty(V_m) - \theta$$

where τ_θ=6 ms is the time constant of the threshold dynamics, $\theta_\infty$is the steady-state spike threshold and is determined by V_m:

$$\theta_\infty(V_m) = \alpha(V_m - V_i) + V_T + k_a \cdot log(1 + exp((V_m - V_i)/k_i))$$

where α=0.3, β=1.1, k_a=7, k_i=8.75, V_T=-50 mV and V_i=-55mV were as determined by Fontaine et al. (2014). For neurons with fixed spike threshold, the θ was set to values ranging from -52--53.8 mV, so that the overall average firing rate were comparable between adaptive and fixed spike threshold model across all conditions in one experiment. Spikes were detected when V_m>θ+3mV, and following a 0.5ms refractory period the V_m was reset to -70 mV. I is the input current neurons receive. All simulations were performed using 1st order Euler method with 0.1 ms time steps in MATLAB.

Network structure

To study the properties of neurons with or without adaptive threshold, we constructed a simple feed-forward excitatory neural network, where N=100 presynaptic input neurons connect to a single postsynaptic neuron. Each connection was identical to each other (amplitude, 15 pA; failure rate, 0.03; coefficient of variation of amplitude, 0.3; connection strength resembles typical layer 4 - layer 2/3 excitatory connections found in rat barrel cortex, see Feldmeyer et al 2002) except for the synaptic latencies, which were normally distributed with standard deviation σ ranged from 0-4 ms. When presynaptic neurons fire at the same time, the normally distributed synaptic delays effectively result in excitatory postsynaptic currents (EPSCs) arriving at postsynaptic neuron with a temporal jitter of σ. The EPSC was modeled as an exponential function with time constant of 5 ms. Short-term synaptic dynamics were not included.

Stimulation and network activity

We considered two types of presynaptic encoding strategies: 1) a classic “rate code”, in which the stimulus was defined as number of presynaptic neurons activated in each trial, and across trials a random subset of presynaptic neurons were selected to be active. In this case the postsynaptic neuron tries to decode how many presynaptic neurons are active in any given trial. 2) a “pattern code” (or “timing code”), in which the stimulus was defined as presynaptic activation pattern, i.e. in response to the same stimulus the same neuron had exactly the same activity across trials, and numbers of activated presynaptic neurons were the same across different stimuli. Under this condition the postsynaptic cell tried to decode which presynaptic activity pattern was present in any given trial. Under both conditions, when a presynaptic neuron was decided to be activated in a given trial it generated a spike at a fixed time, which was 60 ms after stimulation started. In other word, the temporal delay of action potential arrival time at postsynaptic neuron was purely caused by the synaptic latency; the presynaptic spike time was chosen so that the postsynaptic neuron was at steady state when presynaptic cells spiked. The activation state of the postsynaptic neuron was modulated by setting the leak reversal potential E_L to different values; mathematically it is equivalent to drive the cell with a constant current. Each stimulus was delivered 150 times for a given condition (different σ and/or different states); for each condition we simulated 500 such randomly generated networks.

In both models the temporal delay of action potentials in respect to the presynaptic neurons' activity is predominantly caused by the synaptic latency. The presynaptic spike onsets were chosen so that the postsynaptic membrane potential was at a steady state when the presynaptic neurons generated action potentials. The activation state of the postsynaptic neuron was modulated by setting the leak reversal potential E_L to different values; mathematically this is equivalent to drive the cell with a constant current. Each stimulus was delivered 150 times for a given condition (different σ and/or different states); for each condition we simulated 500 such randomly generated networks.

Noise in the network was introduced by inserting spikes generated from a Poisson process in the presynaptic neurons. The mean event rate of the Poisson process (expressed as mean noise spike rate from a single presynaptic neuron in Hz) determined the overall noise strength

Analysis of stimulus capacity

We employed Shannon information theory (Shannon 1948) to analyze the stimulus representation capacity of neurons with either adaptive or fixed spike threshold. The mutual information *I* between the stimulus *S* and neuronal response *R* is calculated as

$$I(S,R) = H(R) - H(R|S)$$

in which *H(R)* denotes the entropy of the response variable *R*:

$$H(R) = -\sum_{i=1}^{n} p(r_i) log_2(p(r_i))$$

and *H(R|S)* is given as

$$H(R|S) = -\sum_{i=1}^{n} p(s_i) \sum_{j=1}^{m} p(r_j|s_i) log_2(p(r_j|s_i))$$

where *m*, *n* is the number of possible response and stimulus patterns and *p(r)* and *p(s)* is the occurrence probability of these patterns, respectively. Intuitively, the mutual information measures how much uncertainty about one variable, either *R* or *S*, can be accounted for if an ideal observer had knowledge about the other variable. It is theoretically the upper bound of knowledge about the stimulus can be gained from the neuronal response under the exact condition (i.e. no other source of additional information).

To construct response patterns, we binned the spike trains from individual trials using various temporal bin sizes (0.5 ms, 1 ms, 2 ms, 5 ms or 30ms). The analysis window was chosen to be 0-30 ms after stimulus onset, which included all spikes elicited by the stimulus. The number of spikes in each temporal bin was counted, and the resulting numeric vector with different lengths, depending on temporal bin size, was used to calculate the mutual information. When calculating the mutual information between stimulus and neural response knowing the states (Figure 4.4-4.6), the states was supplied to the binned response vector as an additional dimension. The mutual information calculation was performed using the Spike Train Analysis toolbox (Goldberg et al 2009), with shuffle correction combined with the Panzeri-Treves estimator (Panzeri and Treves 1996) as the bias correction method (Ince et al 2010).

Results

We simulated neuronal models with an adaptive or fixed threshold (Figure 4.1A) and quantified their ability to encode stimulus information using information theoretic methods (Figure 4.1D/E). Further, we recorded from L2/3 pyramidal neurons in the barrel cortex *in vitro* while stimulating in layer 4 of the same column to experimentally quantify the relationship between the spike threshold and the membrane potential (Figure 4.1C, 4.6A) and experimentally test the quality of the stimulus encoding with biological circuits across membrane states (Figure 4.6).

Parameterization of the input-output behaviour

While the variability in threshold is typically described in relation to the slope or the membrane potential (Azouz & Gray 2000, Azouz & Gray 2003, Henze & Buzsáki 2001, Wilent & Contreras 2005; Figure 4.1), for computational purposes it is more insightful to describe it in relation to the properties of the synaptic input to the postsynaptic neuron. On a mechanistic level, Fontaine et al (2014) identified the membrane potential itself as a valuable predictor of the threshold (see Materials and Methods). While this choice is practically useful, it does not - or only indirectly - allow one to address questions such as the dependence on the input rate, pattern, or correlation. Therefore, we first directly relate the amplitude and slope of the incoming excitatory postsynaptic potential (EPSP), to the number of synaptic inputs N_{input} and their temporal dispersion σ, which parameterizes the Gaussian distribution from which the EPSP arrival times are drawn.

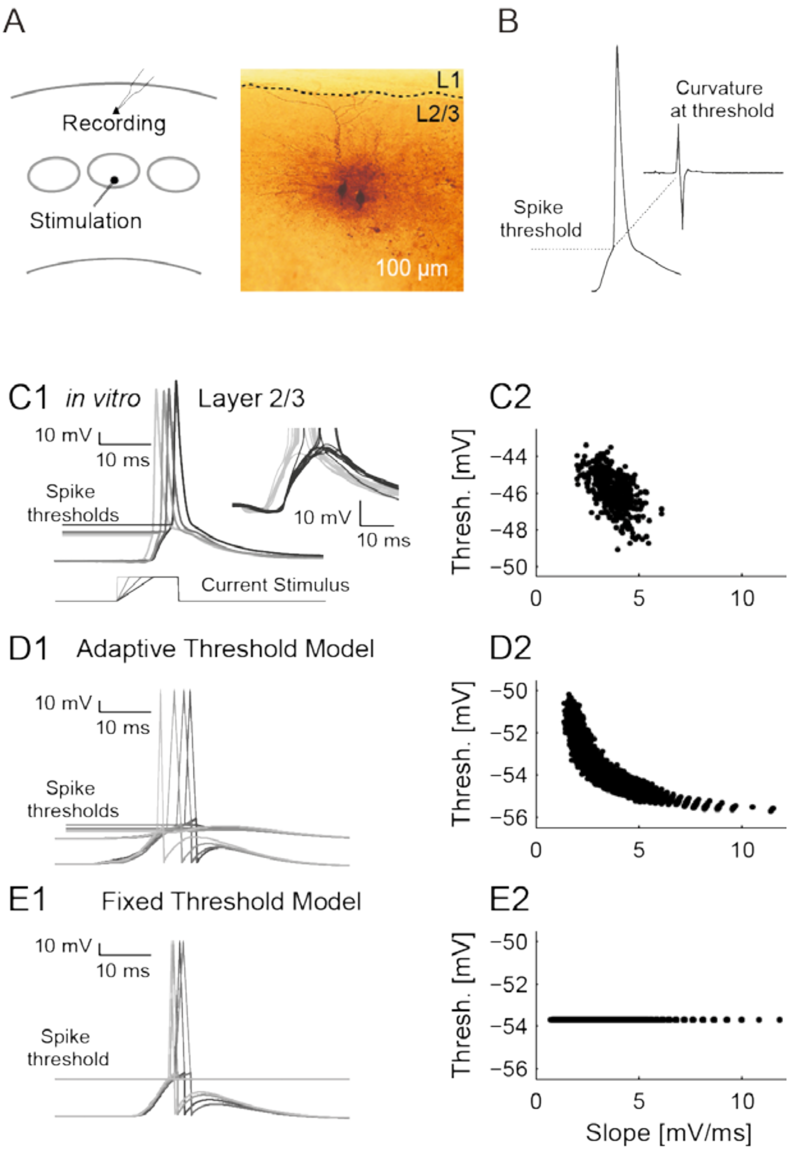

•

Figure 4.1. The spike threshold depends on the history of the membrane potential in both real and simulated data. (A) We performed patch-clamp recordings in layer 2/3 pyramidal neurons in vitro, in response to population input from stimulation in layer 4 (left). The pyramidal neuron identity was confirmed in a subset by filling the targeted neuron using biotin (middle). (B) Spike threshold is estimated as the maximal positive peak of the second derivative of the membrane potential (bottom).

(C1) A cortical neuron stimulated with current inputs of different slopes (bottom, different shades of gray) exhibits different thresholds for spike initiation (top, fine flat lines in corresponding colors to the stimulus). Intersect, randomly selected 10 traces from both the stimulation with fastest (light grey lines) and slowest (dark grey lines) slopes. Spikes are truncated at -40 mV. (C2) As in previous studies, thresholds were found to vary with the slope of the preceding membrane voltage. In the current stimulation settings, only a limited range of input slopes was realized. (D1) Neurons with an adaptive threshold were simulated on the basis of the model by Fontaine et al. (2014), after adapting the parameterization to cortical excitatory neurons (see Methods). As for the in vitro data, a dependence on the stimulus slope is observed. Consequently, when the threshold is re-estimated (D2) from the voltage trace, we obtain an adaptive dependence on slope, as observed in the experimental data. The relationship between EPSP slope and spike threshold is overall captured by an exponential function especially when the wider range of EPSP slopes was used, which could be explore in the model (compare C2 and D2); see also Azouz and Gray 2000. (E1) Neurons with a fixed threshold were also simulated. The threshold was set to equalize firing probability with the adaptive threshold model. (E2) Re-estimating the threshold, we obtain the expected constant threshold.

This reformulation of input variables is valid and broadly applicable, since the combination of N_{input} and σ predicts the amplitude (Figure 4.2 A1/B1) and slope (Figure 4.2 A2/B2) of the resulting EPSPs with little variance (dark surface at the bottom of each panel). The quality of prediction and the shape of dependence, albeit at a lesser extent, are independent of whether the adaptive or the fixed threshold model is considered (Figure 4.2 A1 vs. B1 and A2 vs. B2). As expected, increases in N_{input} and decreases in σ generally, increase A_{EPSP} and EPSP slope. Hence, values of N_{input} and σ map approximately to corresponding values of A_{EPSP} and EPSP slope and thus span the space of EPSPs (w.r.t. to these two experimentally relevant parameters).

Based on these parameters we investigated the transition between sub- and suprathreshold activity via the spike probability. Throughout this study, the only source of variability across repeated trials is the trial-to-trial variation in synaptic strength (including failures, see Methods).

The adaptive threshold model exhibits overall a steeper transition to spiking as a joint function of σ and N_{inputs} than the fixed threshold model (Figure 4.2C1 vs C2). Analyzing the two parameters separately, however, shows that the transition is only steeper for the temporal precision of the input, σ (Figure 4.2D1 vs D2), but not for the input rate, N_{inputs} (Figure 4.2E1 vs E2). Spike probability follows generally a similar shape as a function of σ and N_{inputs}. Spike probability as a function of only σ, is fit well by a sigmoid, with the adaptive model exhibiting a steeper slope as a function of different σ's (adaptive: s =

0.16, fixed: s = 0.28). Fitting sigmoids to the spike probability as a function of the N_{inputs} shows an inverse relationship in steepness between (adaptive: s = 0.98, fixed s = 0.63, E1 vs. E2). In addition, the midpoint of the transition is located at a lower σ for the adaptive than for the fixed threshold (2.6 vs. 3.5 ms), while the midpoints for the dependence on N_{inputs} differ only slightly (34 vs. 37 inputs). The latter is a consequence of setting the fixed threshold matched to the average of the adaptive threshold.

The adaptive threshold model is thus able to respond to a wider dynamic range of the number of inputs contributing to a stimulus, restricted to a smaller range of integration time-windows (given here by the lower lowpass limit w.r.t. σ, compare Figure 4.2D1 to D2).

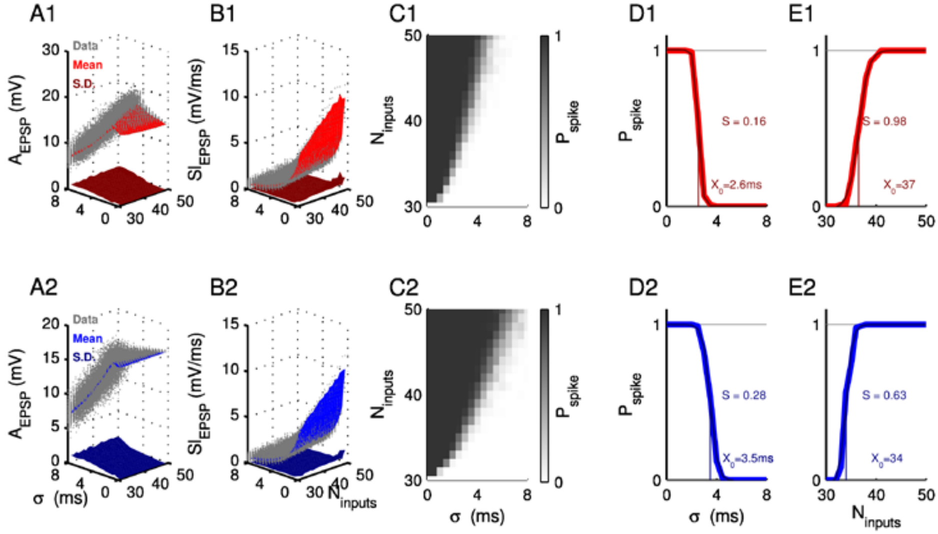

Figure 4.2. The input-output relationship is sharpened due to the adaptive threshold. Conventionally, EPSP amplitude (A_{EPSP}) and slope (Sl_{EPSP}) are measured to visualize the spike threshold dependence to changes in membrane potential. Both measures can be reliably predicted by the combination of temporal input spread (σ) and the number of contributing neurons (N_{inputs}) in point neurons. (A) The A_{EPSP} (data: gray, mean: red) is predicted with small standard deviation (S.D.) (maroon) by σ and N_{inputs} across a wide range of values for the adaptive threshold model (A1). Prediction quality was similarly good for the fixed threshold model (mean: blue, S.D. : dark blue, A2). (B) Similarly, the Sl_{EPSP} amplitude is predicted well with small S.D. on the basis of σ and N_{inputs}, for both adaptive (B1) and fixed (B2). (C) Spike probability

follows generally a similar shape as a function of σ and N_{inputs}*. However, the speed of transition between spiking and non-spiking domain is overall greater for the adaptive threshold model (C1 vs.C2), translating into a steeper decision criterion as a function of the input parameters. (D) Spike probability as a function of only σ, is fit well by a sigmoid, with the adaptive model (D1 vs. D2) exhibiting a steeper slope as a function of different σ's (adaptive: s = 0.18, fixed: s=0.28) as well as a lower midpoint, indicating overall operation on a faster time-scale However, the inverse is the case for the dependence on* N_{inputs} *(E1 vs. E2). Error bars represent 2x SEMs and are barely visible.*

Information transmission for rate and pattern codes

Neural integration by the postsynaptic neuron ensures projection of a high-dimensional pattern of synaptic input onto a binary time-series. While a certain amount of information always has to be ignored in this process, the goal of mutual information analysis is to quantify the ability of neurons to encode different inputs with quantitatively discriminable spiking patterns. In the present context, we focus on two encoding schemes on the input side, population rate and population pattern (which will be abbreviated as rate and pattern below).

In the case of population rate (Figure 4.3 top), the studied neuron receives input from a population of presynaptic neurons, and inputs differ in firing rate, i.e. each presynaptic neuron generates at most one spike in a given trial, and the spikes from the presynaptic neuron population are normally distributed as a function of time with standard deviation σ. The input rate is varied by increasing the number of neurons that contribute to the current input, thus leading to a Gaussian distributed set of synaptic inputs with temporal standard deviation σ. Spike times are redrawn for each trial, while only the number of participating neurons stays the same across trials for a given input. For the simulations reported, in total 11 different stimuli were given (range of active neuron number, 40-60, incremented by 2), thus the total stimulus entropy was $\log_2(11) \approx 3.46$ bit.

Adaptive threshold neurons performed slightly better for low σ, but substantially worse for larger σ for rate encoded inputs (Figure 4.3A). In these simulations noise exists as variability in the synaptic weights (according to Feldmeyer et al. 2002), but no additional inputs were added. Adding additional noise inputs generally reduces the recoverable mutual information (Figure 4.3 B1/2), but does not change the qualitative finding of a better coding of rate by fixed threshold neurons for larger σ (Figure 4.3 B3). Overall, both neuron types exhibit a low-pass behavior, which results from the fact that a greater σ at some point exhausts the integration window of each model.

In the case of the population pattern encoding (Figure 4.3 bottom), the different inputs are created by setting distinct predetermined patterns across neurons, which do not vary in their population firing rate ($N_{input} = 50$). Under this condition, the same number but a different subset of neurons are activated by different stimulus, and in response to the same stimulus the same neuron has exactly the same response across different trials. Hence, distinction between different stimuli has to rely on the temporal differences between different input spike patterns. As above, 11 different stimuli were delivered, resulting in ~3.46 bit stimulus entropy.

Adaptive threshold neurons perform substantially better for low σ, but again substantially worse for greater σ. Additional independent Poisson noise inputs change the relation between the models qualitatively, with the clear difference between them progressively giving way to a weak, but inverted relationship (Figure 4.3D). This is due to the adaptive threshold models lower σ edge for performance shifting faster to higher values than in the case of the fixed model (Figure 4.3 D1 vs. D2). Interestingly now, both model neurons exhibit a band-pass behavior, in contrast to the low-pass behavior for rate coding, which follows from the fact that patterns with very small σ effectively get squeezed to the same, single-time pattern.

In summary, adaptive threshold neurons are only useful or even superior encoders for precisely timed, or well correlated, inputs. Interpreted inversely, the shortened integration window of the adaptive threshold model, allows it to ignore inputs outside a certain period, and thus make more decisions per second.

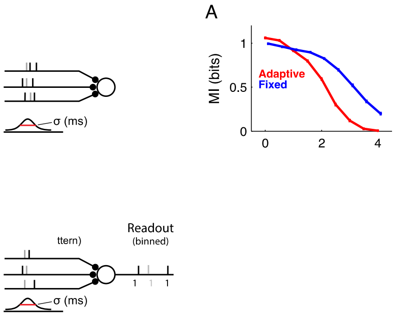

Figure 4.3. Adaptive threshold is more informative for high temporal precision and low noise. Two codes were investigated on the input side, a classical rate code (top), where the number of EPSPs indicate the information, and a pattern code (bottom), where the spatiotemporal pattern of inputs encodes the information. In both cases,

the temporal precision with which the inputs arrive is important (σ). (A) Responses of the adaptive threshold model neurons (red) encode information mostly at low temporal spread σ, which the fixed threshold neurons (blue) possess a wider range of encoding w.r.t. to σ if information is rate-encoded. (B) This relationship holds across a wide range of noise inputs, with adaptive threshold neurons encoding generally better for low values of σ, and fixed threshold neurons for high values of σ. Color mapping here represents information. (C) A similar relationship in information encoding between the models is observed for pattern-encoded information. Again the adaptive threshold model performs better for low σ, and vice versa. (D) This relationship holds only for a limited range of noise, after which point the relationship between the differences between the models becomes fairly small.

State dependence of information transmission

Cortical populations undergo state changes, depending on the wakefulness or attentional state of the brain (Hasenstaub et al 2007, Tan et al 2014). The state changes manifest themselves on the single cell level as a shift in the subthreshold membrane potential, thus bringing each cell to a different voltage distance to its spiking threshold. While the sources of the state changes are not fully understood, their presence will either change network computation, or require network computation to be robust against the changes. An adaptive threshold could be a contributor to robust processing under different states. We therefore investigated the robustness of adaptive compared with fixed threshold neurons for different initial membrane voltages for rate-encoded inputs (range 50 – 60, with increment step size of 2; in total 6 stimuli with log2(6) ≈ 2.58 bit entropy). An ideal observer could decode the stimulus from the spiking activity of the simulated neuron, with or without knowing the resting membrane potential state of the simulated neuron. Robustness was defined as the difference in mutual information between unknown and known state, supplied as an additional dimension in the mutual information analysis. A neuron that is perfectly robust to state-differences would not show any improvement by knowing the state. Differences are typically positive, since adding state-information always increases the mutual information due to part of the variability being explained by state knowledge.

The adaptive threshold model exhibited a reduced dependence of spike times as a function of different initial states (Figure 4.4 A). For a small difference of only 3mV state difference (-65 vs. -62mV, Figure 4.4 A1) the spike times of the adaptive threshold neuron are almost identical (red, different shades indicate different N_{input}, with more solid colors corresponding to greater N_{input}), while the times are already noticeably shifted for the fixed threshold neuron (blue). Correspondingly the mutual information with state knowledge (Figure 4.4 B1, solid colors), is only slightly larger in the adaptive case, but substantially larger in the fixed case than the mutual information without state knowledge (light colors). The differences between mutual information remain fairly constant as a function of σ (Figure 4.4 B1 bottom).

If one considers larger differences in state (Figure 4.4 A2, -72 vs. -62mV), the changes in spike time due to the state change become more severe. Especially for the fixed threshold model, the set of spike times becomes essentially disjoint, and in the more hyperpolarized state (-72mV) the dispersion of the spike times increases substantially. In addition, failures of spike elicitation are observed (Data on top, marked as NS). For the adaptive threshold model the shift becomes stronger, but in comparison to the fixed threshold, it remains more limited in temporal shift and dispersion. Interestingly, from an information theoretic perspective, this leads to an inversion of the situation: The fixed model is now less dependent on the knowledge of state (Figure 4.4 B2, top), again almost independently from σ (Figure 4.4 B2, bottom). This inversion rests on the fact that in the case of disjoint response times, decoding across states is not impeded by confusions introduced by temporal overlaps, i.e. a response time in one state would be related to a different N_{input} than in another state.

The differential robustness of the models observed for the example state differences holds more generally across a wider range of state differences. The differential behavior described above rests on the overlap between the response distributions across different states (Figure 4.4C, quantified by the correlation coefficient across PSTH-bins). For small state differences the PSTHs are almost identical, leading to a correlation coefficient close to 1. For large state differences, the PSTHs are not correlated and hence the correlation coefficients are close to 0. For the conditions between the two extremes, the fixed threshold model exhibits a faster decay in correlation coefficient, thus indicating a faster drift of onset times.

Qualitatively, the correlation coefficient between PSTHs is a good predictor for the resulting difference in mutual information between knowing and not-knowing the state (ΔMI) during decoding (Figure 4.4 D). Low ΔMI, i.e. high robustness, is achieved both for highly similar ($CC_{PSTH}=1$) and dissimilar responses ($CC_{PSTH}=0$). Correspondingly ΔMI varies also non-monotonically as a function of state difference, with the adaptive threshold neuron being more robust for small state differences, and the fixed threshold neuron being more robust for larger state differences (Figure 4.4 E).

Hence, the adaptive nature of the threshold does improve robustness of the spike-timing across membrane states, but improves information transmission for a limited range of small state differences. For larger state differences, the ambiguity in decoding generated by small shifts in timing is outweighed by the possibility to decode across different time-windows. This becomes feasible in the fixed threshold case due to the larger shift in average spike timing, thus providing it with an advantage in information transmission (see Discussion for a dependence on decoding scheme).

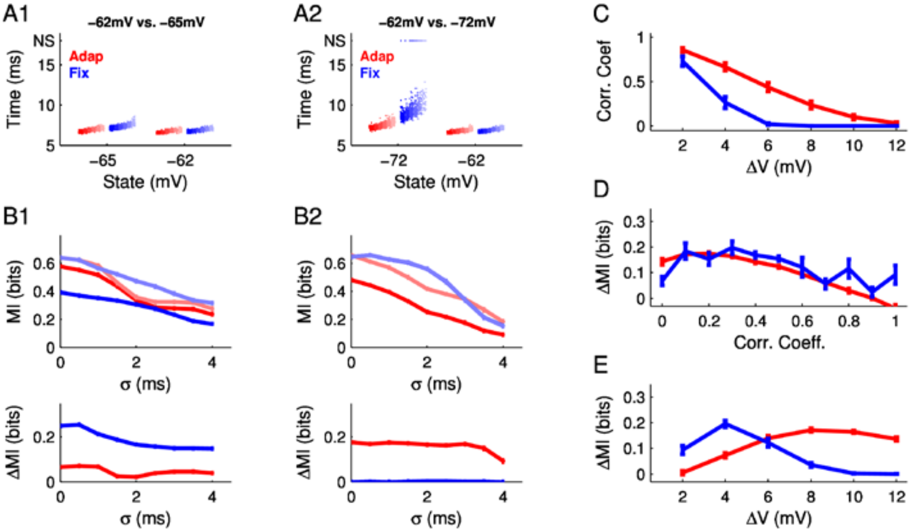

Figure 4.4. Information decoding across different membrane states and spike threshold types for a 'stimulus-centered' time reference. (A) For small differences in state (A1: -62mV vs. -65mV) both adaptive (red) and fixed (blue) threshold models show a shallow dependence on stimulus strength (different rates, range [50:2:60] inputs, total stimulus entropy ~ 2.58 bit, dark color = 60, light color = 50 EPSPs). The adaptive threshold model compensates partly for the difference in initial voltage, and thus exhibits smaller differences in spiking behavior across states. During larger fluctuations in membrane potential (A2: -62mV vs. -72mV) this behavior is qualitatively retained. The different states also scale the slope (average spike times vs. input strength) and spike time variability for each model, with the fixed model being influenced more strongly in both cases. NS, non-spiking trials. (B) Mutual information is estimated across all states with the state known (light colors) or unknown (dark colors) to the decoder. For small state differences (B1) the adaptive model's MI is independent of state knowledge (bottom: ΔMI across states), while the adaptive model shows a strong dependence to membrane state (~40% of MI added by state knowledge). For larger state differences, this relationship inverts (B2). Note that in B2 upper panel the dark blue curve almost fully overlaps with the light blue curve. (C) To understand this inversion, we relate the response distributions to state difference. The correlation coefficient between response PSTHs measures similarity

across state differences. The adaptive threshold neuron (red) retains similar responses for larger state differences than the fixed threshold neuron (blue). (D) The correlation coefficient of response distributions predicts qualitatively the advantage of knowing state during decoding. (E) The adaptive model encodes information in a state independent manner for small state differences, while the fixed threshold model becomes more state independent only for larger state differences. This switch is caused by a shift from overlapping to non-overlapping temporal decoding ranges, as indicated by the correlation coefficients of the PSTHs across different states (see Figure 4.4C). Hence, the adaptive threshold model compensates for a part of the initial state, however, does not encode more information independently if a stimulus-based fixed decoding reference is used. Error bars indicate SEMs across all state differences of a given size.

Decoding across states with a moving reference frame

Classically, information theoretic decoding is performed in reference to the timing of the stimulus, e.g. spike-times are computed in relation to the time of stimulus onset (‘stimulus-centered’, Panzeri et al, 2001, Petersen et al, 2001, Quiroga and Panzeri, 2009). While this provides an objective reference, the brain's internal decoding mechanisms may not have direct access to the (external) information about stimulus onset. Alternatively, responses can be decoded in relation to the response timing of other neurons (Thorpe et al. 2001, Panzeri and Diamond, 2010). Use of this 'response-centered' decoding is not only closer to the brain's internal perspective, but also provides more accurate decoding if the time of stimulus onset is uncertain (Panzeri and Diamond, 2010).

In the case of response-centered timing, the adaptive threshold model is found to be generally more robust to differences in state than the fixed threshold model. The internal reference time was defined as the peak-time of the population response (termed 'columnar synchronous response' in Panzeri and Diamond 2010). Since the neural population encompasses a range of tuning preferences, this leads to an average response time of the neural population to the stimulus set (see Experimental Procedures). Effectively, the spike-times of the analyzed neuron are thus shifted to a common average response time of all simulated neurons, which will, however, depend on the membrane state and neural response properties, e.g. threshold type (see Figure 4.5A).

For small differences in state, both adaptive and fixed threshold models show little difference in their response time and variation in response time (Figure 4.5A1, red vs. blue, different shades indicate different stimuli). Consequently the difference between decoding with or without state information is quite small (Figure 4.5B1, especially bottom). For larger state differences, the response time distributions differ strongly in their variance, with the fixed threshold model exhibiting a larger increase in spread for the more hyperpolarized state (Figure 4.5A2). The reduced variance across states and stimuli here exemplifies the effect of the adaptive threshold. The quality of unified decoding across states deteriorates for the fixed threshold model, thus leading to a larger information gain from the inclusion of state information (Figure 4.5B2).

As a function of state-difference, both the fixed and the adaptive threshold model exhibited better conserved PSTHs across states (compare Figure 4.5C with Figure 4.4C) when ‘response-centered’ reference was used. However, the adaptive threshold model profits more and thus a wider gap between fixed and adaptive threshold model results in terms of PSTH correlation coefficients. As before, the correlation coefficient between the PSTHs remains a good predictor for the information contributed by knowing the state (Figure 4.5D), although the shape slightly differs from the previous case (Figure 4.4D).

For 'response-centered' decoding, the robustness across states is generally higher for the adaptive than the fixed threshold model (Figure 4.5E), independent of the size of the state-difference (compare to Figure 4.4E). While the robustness partially depends on the particular combination of states (combinations averaged in Figure 4.5E), the variability is small compared to the effect size (errorbars in Figure 4.5E).

In summary, an adaptive threshold neuron can be decoded more robustly than a fixed threshold neuron, if the stimulus timing is known from the brain's internal perspective. Under these circumstances, the absolute timing is converted to a relative timing in the population, and the reduction in response variance in the adaptive threshold model renders responses across different states more comparable.

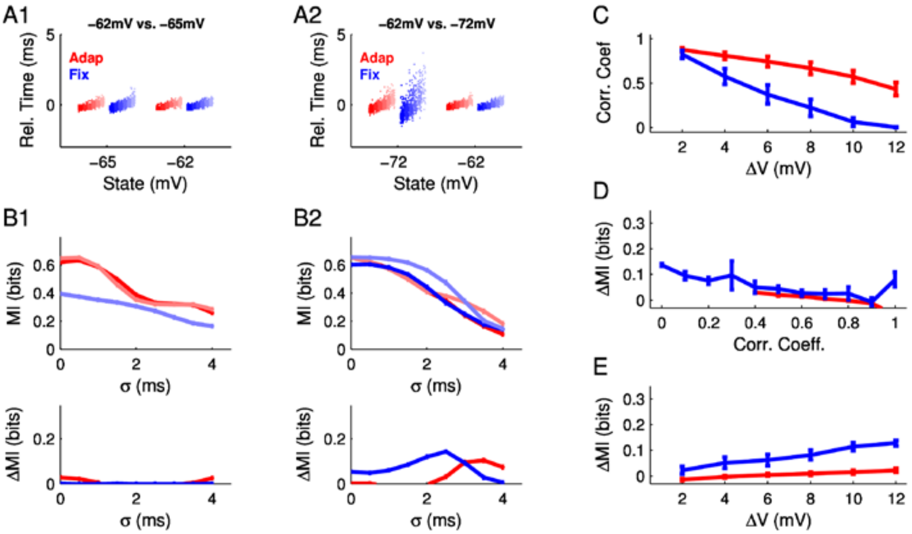

Figure 4.5. An adaptive threshold neuron represents information more robustly across membrane states for a 'response-centered' time reference. Since stimulus onset is not known internally, a population-based decoding reference has been suggested to serve a biologically relevant surrogate for stimulus timing (Panzeri and Diamond, 2010). With this reference, spike-timing is measured relative to the peak-time of the population response, i.e. local maxima of the population peristimulus time histogram (PSTH). (A) For small differences in state, adaptive and fixed threshold models show little difference in their relative-time response (A1) and consequently the contribution of the knowledge about the state becomes negligible (B1). All colors are as in the preceding figure. (B) For larger state differences, the response time distributions now differ significantly in their variance, with the fixed threshold model exhibiting a much larger increase in spread for the more hyperpolarized membrane state (A2). Consequently, decoding across states becomes less robust for the fixed model than for the adaptive threshold model (B2). (C) While the 'response-centered' time reference increases the robustness of the PSTH for both the fixed and the adaptive threshold model, the latter profits more, widening the gap between the models for larger state differences. (D) As before, the correlation coefficient between the PSTHs remains a good predictor for the information contributed by knowing the state. (E) In the case of the moving decoding reference, the adaptive model is generally more robust than the fixed threshold model across all state differences investigated. Error bars indicate SEMs across all state differences of a given size.

State dependence of information transmission

The relationship between membrane potential and spike threshold appears to not be strongly dependent on the resting membrane potential (Figure 4.6A/B). However, active conductances like the hyperpolarization activated cation currents (Robinson and Siegelbaum, 2003) could potentially alter the integration time course, ultimately changing the interaction between the membrane potential and the spike threshold. To investigate the effect of resting membrane potential states on the spike threshold, we made whole-cell patch clamp recordings from pyramidal neurons in L2/3 mouse barrel cortex in acute slice preparations, and delivered the stimuli after having clamped the somatic membrane potential across different resting potentials. In the following the *stimulus-centered* and *response-centered* decoding analyses are compared, taking the average 1st spike time from all recorded neurons as the time reference for the response-centered decoding (in Figure 4.6).

The recorded neurons (N=11) exhibited an adaptive threshold that depended on the slope of the input for all states (-80, -70, -60mV) investigated (Figure 4.6A/B). The slopes across the different states were comparable, i.e. -0.99 (0.27), -0.92 (0.19), and 0.90 (0.23) ms respectively ($p = 0.48$, one-way ANAOVA with correlated samples).

The neurons also exhibited a high PSTH similarity (Figure 4.6E), as well as a high robustness of information encoding across states (Figure 4.6G), reminiscent of the adaptive threshold model. For small state differences, both the response patterns (Figure 4.6C1), the decoded information and the gain remain comparable (Figure 4.6D1) across *stimulus-centered* (orange) and *response-centered* (red) decoding. For larger state differences the improved robustness of decoding with a *response-centered* threshold becomes evident (Figure 4.6D2).

The correlation coefficient between PSTHs at different states remained high for a range of state differences that exceeded the magnitude of similarity of even the adaptive model for *response-centered* decoding (compare to Figure 4.6E to Figure 4.5C). This difference between real and simulated neurons could either stem from an additional mechanism present in real neurons or be based on a difference in the properties between real and modeled dynamics.

Robustness across states exhibits a shape that stays closer to the adaptive threshold model behavior with a slow rise and especially for the static decoding a much later decay than the fixed threshold model (Figure 4.6G compared to Figure 4.4E).

In summary, the information transmission behavior of cortical neurons exhibited similar features of robustness across states as the adaptive threshold model. An adaptive threshold could therefore be a mechanism which contributes to achieving this robustness, providing a functional reason for its widespread existence in the mammalian nervous system.

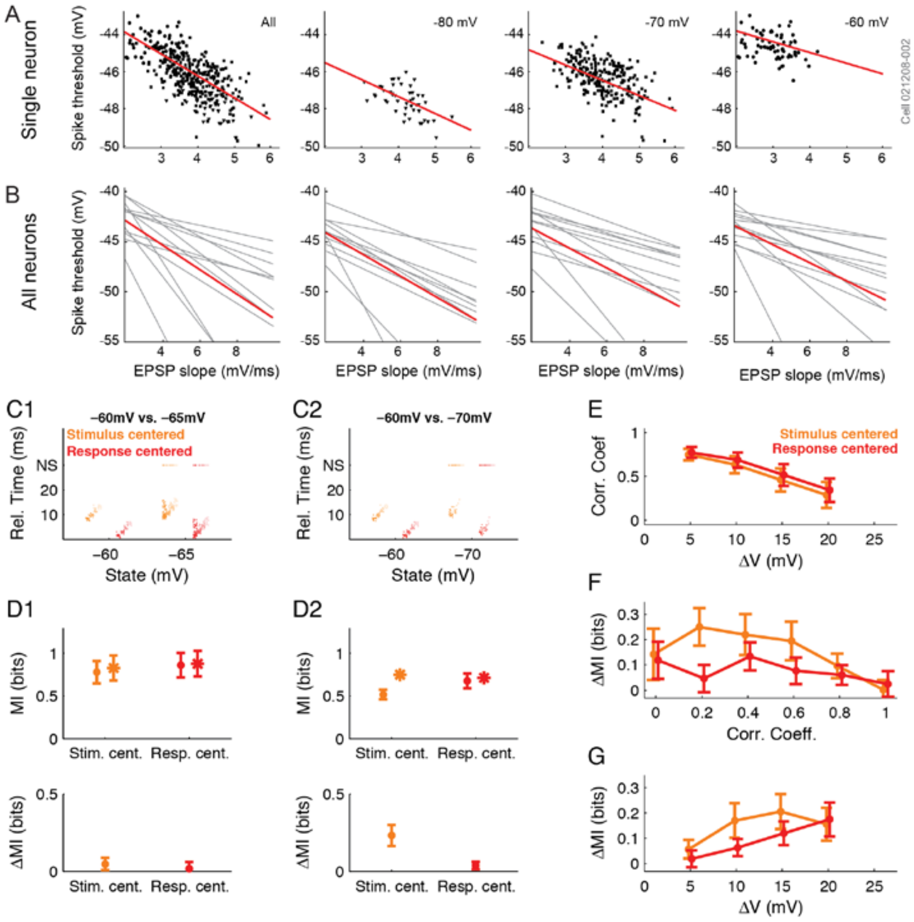

Figure 4.6. The state dependence of neural data corresponds closely to adaptive threshold behavior. Identical analyses were carried out as for the model data in the preceding figures. (A) Across three initial states of voltage (-80, -70, -60mV) an adaptive threshold w.r.t. the slope of the EPSP was observed, i.e. a negative dependence between spike threshold and EPSP slope. Red lines, least-square linear fit to the data. (B) All recorded neurons (N=11) exhibited this behavior. The slopes across the different states were across the three states, i.e. -0.99 (0.27), -0.92 (0.19), and 0.90 (0.23) ms respectively. Red lines, average across all the neurons. (C) For small state differences, both the response patterns (C1), the decoded information and

the gain remain comparable (D1) across stimulus-centered (orange) and response-centered (red) decoding. N.S., non-spiking trials. (D) For larger state differences the advantage of decoding with an adaptive threshold becomes evident (D2). Stim. cent., stimulus-centered; Resp. cent., response-centered. (E) The similarity of PSTHs as a function of state difference reflects the behavior of the adaptive threshold model (Fig. 4C/5C, red) exhibiting a slow decay, based on a similar robustness in mean and variance of the spike-timing. (F) Robustness in decoding across states (measured as ΔMI between knowing and not knowing the state during decoding) shows a similar dependence on the correlation coefficient as for the model data (compare orange to Fig. 4D, and red to Fig. 5D), validating the analysis across real and model data. (G) Robustness across states exhibits a shape that stays closer to the adaptive threshold model behavior with a slow rise and especially for the static decoding a much later decay than the fixed threshold model (Fig. 4E).

Discussion

We addressed the computational properties of neuron models with an adaptive spike threshold. The results showed that a neuron with an adaptive threshold supports selective information processing for well-correlated inputs both for rate and pattern codes in the input. Furthermore, the adaptive threshold provides a higher level of robustness against variations in the initial state if the decoding is performed relative to the average response-time. The experimental data behave similar to the adaptive threshold model with respect to robustness against changes in initial resting membrane potential state. Below we explore the consequences of these results for neural coding, and discuss a range of assumptions and limitations for the present study.

Relation to previous studies

Threshold adaptation has been observed in a range of systems and modalities, and therefore appears to be the norm rather than the exception. In cortical neurons, the spike threshold is shown to be correlated with the average membrane potential prior to a spike (Azouz and Gray 2003, Hu et al 2009), as well as inversely correlated with the rate of membrane potential depolarization in both excitatory (Azouz and Gray 2000, Azouz and Gray 2003, De Polavieja et al 2005, Wilent and Contreras 2005) and fast-spiking interneurons (Goldberg et al 2008). The adaptive threshold increases the sensitivity to synchronized presynaptic inputs, while suppressing uncorrelated inputs, thus potentially increasing stimulus selectivity. Similar forms of spike threshold adaptation have been reported in the thalamus (Henze and Buzsáki 2001), the subthalamic nucleus (Farries et al 2010) and the auditory brainstem (Fontaine et al 2014).

Previous studies have speculated and partially linked the adaptive nature of the spike threshold to improvements in neural coding, but not performed corresponding analyses to quantitatively test this hypothesis. The clearest investigation of the mechanism is found in Fontaine et al. (2014), where the difference between the adapting threshold and the membrane potential is identified as the 'effective signal', which determines under what conditions the neuron will spike. They demonstrate directly, in the context of neurons from the barn owl's inferior colliculus, that the response selectivity shifts towards temporally more tightly tuned coincidences. The present reparametrization of the EPSPs in terms of the input temporal precision is partially guided by this finding. Their analysis, however, does not proceed to a full coding analysis as presented here. We recover their result in a more general form for the decoding analysis (Fig.3), with more tightly tuned input leading to superior encoding in the adaptive threshold neurons than in the fixed threshold neurons, both with respect to rate and pattern codes in the input. The analysis of the state dependence reveals that the robustness to changes in state for the adaptive neuron model only holds for a limited range of states, whereas the fixed threshold model becomes more uniquely decodable for larger steps in prior state.

Robustness in information transmission to initial state

While the functional significance of state changes is still debated, research over the last decade has indicated that (subthreshold voltage) state changes occur under a variety of conditions, ranging from different states of wakefulness (Hasenstaub et al. 2007), movement (McGinley et al. 2014) or task involvement (Tan et al. 2014), to rapid changes during sensing (Yamashita et al 2013). While the activity of neurons will undoubtedly be modulated by the change in subthreshold membrane potential, it is not clear how the decoding will be affected. We presently addressed this question on the basis of modeled and real data, by computing the mutual information between stimulus and response for responses from neurons in different states. In particular, we investigated how insensitive the decoding was to the influence of subthreshold state, by comparing decoding with and without state knowledge.

The results suggest that an adaptive threshold confers an increased robustness across states, especially if the decoding is performed based on an internal time reference. As we argue below, a decoding scheme consistent with the internal perspective of the nervous system has to rely solely on quantities which are internally available. Consequently, an adaptive threshold provides support to the idea that the processes of decoding can remain unchanged, if the encoding/dynamics are changed the influence of state. While other schemes of regularity of processing are conceivable, this would provide a contribution to explain the relative constancy of perception for against different subthreshold states.

Internal vs. external timing reference

Neural communication occurs in continuous time, i.e. there is no clock that determines the start and end of a message. The interpretation of a message depends on the temporal reference used, and can determine the meaning of the message, as well as the set of messages distinguishable, and hence the capacity of the channel. For example, a given spike pattern "1011" (binned over time) can be interpreted as "0101100" and "0001011" depending on the time reference. These messages may carry different information. This becomes particularly evident in the typical scenario of neural integration of messages (spike-trains) from multiple sources at the same time, where a time-shift between two spike-trains will affect their integration by the post synaptic neurons (Levitan et al. 1968, Svirskis and Rinzel 2000).

Since a neuron only has access to information from its own inputs (including modulatory inputs), a time reference has to be generated from the brain's internally available information. A time reference can be generated in multiple ways. For example, in vocal communication, pauses between words or sentences are used as markers to define starting points for interpreting parts of the entire message. Given the onset response properties of sensory neurons, these pauses will generate volleys of spikes, which can be used as a temporal reference. As suggested by Panzeri and Diamond (2010), a similar interpretation could hold for the onset responses generated by tactile events in the somatosensory system (Voigts et al, 2008; Voigts et al, 2015) as cortical neurons integrate spatiotemporal information on behaviorally relevant time scales (Celikel and Sakmann, 2007). More generally, a given neuron could derive a time reference from the common responses in its input population. One proposition for the case of peripheral sensory neurons is to use the peak of the population activity as the temporal reference. The existence of such timing references is more generally suggested by the existence of large-scale oscillatory signals both on the cortical (Engel et al 1991, Lakatos et al 2007, 2008) and subcortical level.

As demonstrated here, an adaptive threshold provides advantages in information representation, since the variance of the response time of a neuron with an adaptive threshold is more restricted than that of a neuron with a fixed threshold, both across stimuli and across subthreshold initial states. In combination with the use of a population-based time reference, this attributes a role in generating robust information transmission to the use of an adaptive threshold.

Assumptions in information-theoretic analysis

Results from a decoding method are only accurate descriptions of how the brain processes information if they are compatible with the internal decoding performed by the brain.

Information theoretic methods have been an invaluable to test decoding mechanisms, since they are quite general, make only few assumptions and lead to objective performance estimates, which allow comparison between different codes. However, information theoretic decoding as well as the particular choices in the present work comes with some limitations/caveats.

First, we used the entire spike train (binned at several temporal precisions ranging from 0.5-30 ms) as the response of the neuron. While this approach guarantees that we used all the available information, it also assumes that the decoder can wait for the entire time-span to decide whether and how to respond. A closer approximation to the decoding performance of a (point) neuron would be a decoder with a limited integration-time and a memory term, that weights recent inputs stronger than past inputs. As the processing is performed online and in real-time, multiple decoders of this kind could be lined up in sequence to perform classification of longer responses. Alternatively, one could assume that (internal) decoding only happens on short timescales and thus restricts the view to a single decoder. This would result in information loss, but it will not significantly affect the computational power of the adaptive threshold over the fixed threshold as described herein.

Second, the present comparison between the adaptive threshold and the fixed threshold neuron on decoding across states assumed that the decoder was based on the set of responses from all states. While it is a reasonable assumption that this information is available over time in the brain, one could postulate that a decoder should be optimally matched to one state (e.g. the up state), in which case robustness would then be a transfer of the optimally matched decoding strategy to other states. This complicates the analysis, since now the comparison between states becomes asymmetric (i.e. a decoder can be optimal for only one state at a time). Given the current set of data, the effect of the adaptive threshold may be similar to the above proposed *response-centered* decoding, as the decoder would be focused around the response within a state.

Consequences for intrinsic network dynamics

The integration and transfer characteristics of individual neurons are relevant as they form the basis for processing on the network level. The adaptive threshold neuron's sensitivity for correlated inputs could contribute to a much discussed property of neural representation, namely sparseness. Limiting the responses to only well correlated inputs limits responsiveness to a smaller subset of input patterns/rates for reach neuron, and thus reduces the overall number of spikes in the network. Hence, a side-effect could be more energy efficient operation based on the limited number of spikes.

The adaptive threshold neuron's general ability to follow changes in preceding voltage reduces the variability in the time to spike. Consequently, the dispersion of responses to the same stimulus is reduced with respect to the state or noise contributed variability (see Figure 4.4 A). Consequently, in a network with multiple levels, the dispersion of spike timing would accumulate at a lower rate (per neuron), than in the case of a fixed threshold. To make use of this precision, as discussed above, the timeframe for decoding should not be fixed to the presynaptic response onset, but rather be defined by the average timing on the postsynaptic side (Panzeri & Diamond, 2010).

While certain consequences of single neuron properties to the network level can be predicted well, explicit simulations or theoretical explorations are required to test these hypotheses in further detail.

Alternate models of adaptive threshold

We modeled the adaptive nature of the threshold based on the explicit, phenomenological description of the threshold by Fontaine et al. (2014), which was shown to make accurate predictions for the case of subcortical neurons in the inferior colliculus of the Barn owl. Alternative accounts for the adaptive threshold could be based on biophysical mechanisms, such as the inactivation of Na^+ channels (Platkiewicz & Brette 2011) and activation of K^+ channels (e.g. low-voltage activated Kv1 channels, Higgs & Spain 2011). These accounts would be directly related to the biological basis and could therefore be tested more directly using specific tools e.g. Na+-channel blockers together with a dynamic clamp-based electrical substitution of conductance (Sharp et al 1993). However, for the present purpose, i.e. a neural coding analysis, the phenomenological properties of the model are more relevant than its basis. As long as the Fontaine model is consistent on the phenomenological level, the present results should transfer to more biologically realistic models and bring about the usual advantages w.r.t. simplified simulation and a more direct link between an underlying mechanism with its computational consequence. In the opposite direction, despite the elegance of the Fontaine model, one may ask whether simpler models could still account for the adaptive threshold and produce realistic spiking behavior, relevant for large network simulations.

Future directions

While the present work addresses many questions relevant to the computational effects of an adaptive threshold, a range of questions remains open. In particular, including other neural constraints (e.g. limited memory) would be of interest, as well as the explicit study of network activity, and the consequences on sparseness and efficiency on the network level. Experimentally, it would be of interest to map thresholds' adaptiveness across different systems with a focus on directly modulating the adaptive nature, and discovering systems which exhibit a fixed threshold (if they exist).

References

Allen, C. B., Celikel, T., and Feldman, D. E. (2003). Long-term depression induced by sensory deprivation during cortical map plasticity in vivo. *Nature Neuroscience*, 6(3), 291–299.

Azouz, R., and Gray, C. M. (2000). Dynamic spike threshold reveals a mechanism for synaptic coincidence detection in cortical neurons in vivo. *Proceedings of the National Academy of Sciences of the United States of America*, 97(14), 8110–8115.

Azouz, R., and Gray, C. M. (2003). Adaptive coincidence detection and dynamic gain control in visual cortical neurons in vivo. *Neuron*, 37(3), 513–523.

Benda, J., Maler, L., & Longtin, A. (2010). Linear versus nonlinear signal transmission in neuron models with adaptation currents or dynamic thresholds. *Journal of Neurophysiology*, 104(5), 2806–2820.

Bohte, S. M. (2012). Efficient Spike-Coding with Multiplicative Adaptation in a Spike Response Model. In *Advances in Neural Information Processing Systems* (pp. 1835–1843).

Brenner, N., Bialek, W., & de Ruyter van Steveninck, R. (2000). Adaptive Rescaling Maximizes Information Transmission. *Neuron*, 26(3), 695–702.

Celikel, T., Szostak, V. A., and Feldman, D. E. (2004). Modulation of spike timing by sensory deprivation during induction of cortical map plasticity. *Nature Neuroscience*, 7(5):534-541.

Celikel, T., and Sakmann, B. (2007). Sensory integration across space and in time for decision making in the somatosensory system of rodents. *Proceedings of the National Academy of Sciences of the United States of America*, 104(4), 1395–1400.

Clem, R. L., Celikel, T., and Barth A. L. (2008). Ongoing in vivo experience triggers synaptic metaplasticity in the neocortex. Science, 319(5859),101-104.

Destexhe, A., Rudolph, M., and Paré, D. (2003). The high-conductance state of neocortical neurons in vivo. *Nature Reviews. Neuroscience*, 4(9), 739–751.

De Polavieja, G. G., Harsch, A., Kleppe, I., Robinson, H. P. C., and Juusola, M. (2005). Stimulus history reliably shapes action potential waveforms of cortical neurons. *The Journal of Neuroscience*, 25(23), 5657–5665.

Engel, A. K., König, P., Kreiter, A. K., and Singer, W. (1991). Interhemispheric synchronization of oscillatory neuronal responses in cat visual cortex. *Science*, 252(5010), 1177–1179.

Farries, M. A., Kita, H., and Wilson, C. J. (2010). Dynamic spike threshold and zero membrane slope conductance shape the response of subthalamic neurons to cortical input. *The Journal of Neuroscience*, 30(39), 13180–13191.

Feldmeyer, D., Lubke, J., Silver, R. a., and Sakmann, B. (2002). Synaptic connections between layer 4 spiny neurone- layer 2/3 pyramidal cell pairs in juvenile rat barrel cortex: physiology and anatomy of interlaminar signalling within a cortical column. *The Journal of Physiology*, 538(3), 803–822.

Finnerty, G. T., Roberts, L. S., and Connors, B. W. (1999). Sensory experience modifies the short-term dynamics of neocortical synapses. *Nature*, 400(6742), 367–371.

Fontaine, B., Peña, J. L., and Brette, R. (2014). Spike-threshold adaptation predicted by membrane potential dynamics in vivo. *PLoS Computational Biology*, 10(4), e1003560.

Fourcaud-Trocme, N., Hansel, D., van Vreeswijk, C., and Brunel, N. (2003). How Spike Generation Mechanisms Determine the Neuronal Response to Fluctuating Inputs. *J. Neurosci.*, 23(37), 11628–11640.

Goldberg, E. M., Clark, B. D., Zagha, E., Nahmani, M., Erisir, A., and Rudy, B. (2008). K+ channels at the axon initial segment dampen near-threshold excitability of neocortical fast-spiking GABAergic interneurons. *Neuron*, 58(3), 387–400.

Hasenstaub, A., Sachdev, R. N. S., and McCormick, D. A. (2007). State changes rapidly modulate cortical neuronal responsiveness. *The Journal of Neuroscience*, 27(36), 9607–9622.

Henze, D. A., and Buzsáki, G. (2001). Action potential threshold of hippocampal pyramidal cells in vivo is increased by recent spiking activity. *Neuroscience*, 105(1), 121–130.

Higgs, M. H., and Spain, W. J. (2011). Kv1 channels control spike threshold dynamics and spike timing in cortical pyramidal neurones. *The Journal of Physiology*, 589(Pt 21), 5125–5142.

Hodgkin, A. L., and Huxley, A. F. (1952). A quantitative description of membrane current and its application to conduction and excitation in nerve. *The Journal of Physiology*, 117(4), 500–544.

Hu, W., Tian, C., Li, T., Yang, M., Hou, H., and Shu, Y. (2009). Distinct contributions of Na(v)1.6 and Na(v)1.2 in action potential initiation and backpropagation. *Nature Neuroscience*, 12(8), 996–1002.

Izhikevich, E. M. (2004). Which model to use for cortical spiking neurons. *IEEE Trans. Neural Netw*, 15(5), 1063–1070.

Lakatos, P., Chen, C.-M., O'Connell, M. N., Mills, A., and Schroeder, C. E. (2007). Neuronal oscillations and multisensory interaction in primary auditory cortex. *Neuron*, 53(2), 279–292.

Lakatos, P., Karmos, G., Mehta, A. D., Ulbert, I., and Schroeder, C. E. (2008). Entrainment of neuronal oscillations as a mechanism of attentional selection. *Science*, 320(5872), 110–113.

Levitan, H., Segundo, J. P., Moore, G. P., and Perkel, D. H. (1968). Statistical analysis of membrane potential fluctuations. Relation with presynaptic spike train. *Biophysical Journal*, 8(11), 1256–1274.

Magee, J. C. (2000). Dendritic integration of excitatory synaptic input. *Nature Reviews. Neuroscience*, 1(3), 181–190.

Martens, M. B., Celikel, T., and Tiesinga, P. H. (2015). A developmental switch for Hebbian Plasticity. *PLOS Computational Biology*, 11(7):e1004386.

Panzeri, S., and Treves, A. (1996). Analytical estimates of limited sampling biases in different information measures. *Network: Computation in Neural Systems*, 7, 87–107.

Panzeri, S., and Diamond, M. E. (2010). Information Carried by Population Spike Times in the Whisker Sensory Cortex can be Decoded Without Knowledge of Stimulus Time. *Frontiers in Synaptic Neuroscience*, 2, 17.

Platkiewicz, J., and Brette, R. (2011). Impact of fast sodium channel inactivation on spike threshold dynamics and synaptic integration. *PLoS Computational Biology*, 7(5), e1001129.

Rall, W. (1967). Distinguishing theoretical synaptic potentials computed for different soma-dendritic distributions of synaptic input. *J Neurophysiol*, 30(5), 1138–1168.

Rall, W. (1969). Time constants and electrotonic length of membrane cylinders and neurons. *Biophysical Journal*, 9(12), 1483–1508.

Robinson, R. B., and Siegelbaum, S. A. (2003). Hyperpolarization-activated cation currents: From molecules to physiological function. *Annual Reviews of Physiology*, 65:453-480.

Shannon, C. E. (1948). A mathematical theory of communication. *The Bell System Technical Journal*, 27(1), 379–423.

Sharp, A. A., O'Neil, M. B., Abbott, L. F., and Marder, E. (1993). Dynamic clamp: computer-generated conductances in real neurons. *Journal of Neurophysiology*, 69(3), 992–995.

Spruston, N. (2008). Pyramidal neurons: dendritic structure and synaptic integration. *Nature Reviews. Neuroscience*, 9(3), 206–221.

Svirskis, G., and Rinzel, J. (2000). Influence of temporal correlation of synaptic input on the rate and variability of firing in neurons. *Biophysical Journal*, 79(2), 629–637.

Tan, A. Y. Y., Chen, Y., Scholl, B., Seidemann, E., and Priebe, N. J. (2014). Sensory stimulation shifts visual cortex from synchronous to asynchronous states. *Nature*, 509(7499), 226–229.

Thorpe, S., Delorme, A., and Van Rullen, R. (2001). Spike-based strategies for rapid processing. *Neural Networks*, 14(6-7), 715–725.

Voigts, J., Sakmann, B., and Celikel, T. (2008). Unsupervised whisker tracking in unrestrained behaving animals. *Journal of Neurophysiology*, 100(1),504-515.

Voigts, J., Herman, D. H., and Celikel, T. (2015). Tactile object localization by anticipatory whisker motion. *Journal of Neurophysiology*, 113(2),620-632.

Wilent, W. B., and Contreras, D. (2005). Stimulus-dependent changes in spike threshold enhance feature selectivity in rat barrel cortex neurons. *The Journal of Neuroscience*, 25(11), 2983–2991.

Yamashita, T., Pala, A., Pedrido, L., Kremer, Y., Welker, E., and Petersen, C. C. H.

(2013). Membrane potential dynamics of neocortical projection neurons driving target-specific signals. *Neuron*, 80(6), 1477–1490.

Chapter 5. INFORMATION TRANSFER AND RECOVERY IN THE SOMATOSENSORY CORTEX

Abstract

Neurons process information by transforming postsynaptic potentials (PSPs) into action potentials (APs). The efficiency of this intracellular information transfer is at the core of stimulus processing in sensory cortices. Using whole-cell recordings in the barrel cortex, we show herein that somatic PSPs accurately represent stimulus location on a trial-by-trial basis in single layer (L) 2/3 neurons. This information is largely lost during AP generation, but can be recovered within the layer in <20ms. In a computational model of the barrel cortex we further show that L4 coding properties are crucial for optimization of information recovery in L2/3 as excitatory and inhibitory neurons act as distinct information bearing channels. While excitatory neurons recover information from single neuron spike timing, inhibitory neuronal decoding is primarily based on population firing rates in L4. These results suggest that cortical processing retains complete stimulus information to enable lossless information representation along the ascending somatosensory circuits.

Introduction

Neural information processing requires signal transformation every time the information is transferred from one neuron to another. This transformation is performed in postsynaptic neurons by integrating spatiotemporally distributed synaptic inputs to generate action potentials, which ultimately ensures propagation of information in neural circuits. During this intracellular information transfer how much information is retained, how much of it is transferred to the postsynaptic neuron and whether the local networks can fully recover the lost information are unknown. Moreover, because the effectiveness of this operation to preserve stimulus information depends on the code used between the sender (i.e. presynaptic neurons) and the receiver (i.e. postsynaptic neurons) as well as the noise characteristics of the communication channel (i.e. synaptic communication) between them, mechanistic description of the rules that govern information processing within and across neurons have been traditionally challenging.

We used a multilevel approach to address these questions both on the level of single neurons and neural populations of different sizes in the barrel cortex subregion of the primary somatosensory cortex where facial whiskers (i.e. macro vibrissae) are represented. Information transmission in single cells is first addressed using *in vitro* whole cell patch-clamp recordings in response to L4 stimulation mimicking different whisker stimulations recorded *in vivo*. Information is found to be fully available on the subthreshold level, i.e. in the post-synaptic potential at the soma, yet, up to 90% of this information is lost in the transition to supra-threshold action potential output, in agreement with previous observations on the information content of action potentials in barrel cortical neurons (Panzeri et al 2001, Petersen et al 2001). In vivo, information loss is likely to exceed this value. Information recovery on the population level is found to be almost complete, based on the analysis using bootstrapped groups of in-vitro cells. This is only reached for temporal codes, with time-resolutions of 2-3ms and group sizes of about 100 neurons.

Next, we turn to a realistic and well-constrained simulation of a barrel column, to study relationship between encoding strategies in L4 between decoding strategies in L2/3. Comparing candidate codes in the L4 population, we find that a population rate code (using in vivo peristimulus time histograms) is unsuitable for information transfer in a cortical network. Codes with higher trial-to-trial reliability in timing and rate for individual neurons perform substantially better, with optimal performance reached if neurons response stereotypically across trials, which can be fully decoded by small groups (~25 cells) of both excitatory and inhibitory neurons in L2/3.

In summary, we find that early stages of intracortical information processing, i.e projections from L4 to L2/3, to be highly lossy, and thus potentially selective on the level of individual cells. Concurrently it is complementary across the population, thus retaining the possibility for full stimulus reconstruction.

Materials and Methods

Juvenile rats from either sex were used according to the Guidelines of National Institutes of Health. Experiments were approved by the local Institutional Animal Care and Use Committee.

Electrophysiological Recordings

In vitro whole-cell current-clamp recordings were performed in acutely prepared slices of the barrel cortex (P18-21) as described before with minor modifications (Allen et al. 2003). Animals were anesthetized using isofluorane before they were decapitated. Oblique thalamocortical slices (300 mm, Finnerty et al. 1999) were cut 45° from the midsagittal plane in chilled low-calcium, low-sodium Ringer's solution (in mM; sucrose, 250; KCl, 2.5; $MgSO_4.7H_2O$, 4; $NaH_2PO_4.H_2O$, 1; HEPES, 15; D-(+)-glucose, 11; $CaCl_2$, 0.1). Slices were first incubated at 37ºC for 45 minutes and were subsequently kept in room temperature in carbonated (5% oxygen) bath solution (pH 7.4, normal Ringer's solution: in mM, NaCl, 119; KCl, 2.5; $MgSO_4$, 1.3; NaH_2PO_4, 1; $NaHCO_3$, 26.3; D-(+)-glucose, 11; $CaCl_2$, 2.5).

Visualized whole-cell recordings were performed using an Axoclamp-2B amplifier under an IR-DIC objective (Olympus) at room temperature. A bipolar extracellular stimulation electrode (intertip distance 150 micrometer) was placed in the lower half of a L4 barrel representing a mystacial vibrissa. A recording electrode (3-4 MOhm) containing an internal solution (pH 7.25; in mM; potassium gluconate, 116; KCl, 6; NaCl, 2; HEPES, 20 mM; EGTA, 0.5; MgATP, 4; NaGTP, 0.3) was placed orthogonal to the stimulation electrode within 150-300 µm of the cortical surface (Figure 5.1 B). For whole cell recordings, putative excitatory cells were selected based on pyramidal shaped somata, apical dendrites and distal tuft orientation, and regular pattern of spiking to somatic current injections (500 ms). Data was low-pass filtered (2 kHz), digitized at 5 kHz using a 12-bit National Instruments data acquisition board and acquired using Strathclyde Electrophysiology Suite for offline data analysis.

In vivo whole-cell current-clamp recordings were performed under ketamine/xylazine anesthesia at P28-30. Anesthesia was induced using 100 mg/kg (ketamine) and 10 mg/kg (xylazine) mixture and maintained with intraperitoneal ketamine-only injections (20% of the initial dose) as necessary. Upon complete loss of facial and hind-limb motor reflexes, the skull was exposed. A head-bolt was fixed posterior to lambda using cyanoacrylate and used to immobilize the animal during experiments. The surface over the primary somatosensory cortex (from Bregma, -0.5mm to -2.5mm, from Midline -2.5mm to -4.5mm was thinned using a dental drill. The surface was kept moist with a thin layer of low-viscosity mineral oil to maintain the transparency of the thinned skull. Cortical representation of the D2 whisker was localized in the contralateral hemisphere using intrinsic optical imaging as described before (Stewart et al. 2013) while deflecting individual whiskers using piezoelectric actuators as described elsewhere (Celikel et al. 2004). The skull above the center of mass of the functional whisker representation was punctured using a 28 gauge needle to allow patch electrode to access the cortical region of interest. All electrode penetrations were perpendicular to the cortical surface. *In vivo* whole-cell recordings were performed as described before (Margrie et al. 2002) with recording electrodes (6-7 MOhm) filled with the same intracellular solution used in slice experiments. Throughout the experiment the animal's core body temperature was maintained at 36.5±0.5°C.

Two different whisker deflection protocols were used: During optical mapping experiments single whiskers were deflected along the dorsoventral axis at 5 Hz with 8° deflections for 20 times with an intertrial interval of 20 sec (Stewart et al. 2013). During electrophysiological recordings single dorsoventral whisker deflections were delivered at 0.2 Hz for 200 times. In each trial 4° whisker deflections were delivered at 10 Hz for 1s.

Data analysis

All analyses were performed off-line in Matlab (Mathworks, Inc). Raw voltage traces were smoothed using running window averaging (1ms window size) and the following variables were calculated for all evoked responses: Onset time (*Ot*, in ms): Latency of the postsynaptic potential (PSP) onset in respect to onset of the stimulus; Rise time (*Rt*, in ms): Time it takes for the membrane to reach 90% of the PSP amplitude relative to the onset of PSP; PSP slope (*Sl*, in mV/ms) between 10-90% of the PSP amplitude and amplitude of the EPSP (*Amp*, in mV). If the trial included an action potential, the peak of the EPSP was set to the spike threshold (*Vt*). The spike threshold was defined as the membrane potential value at which the second derivative of the membrane potential reached a maximum as described before (Wilent & Contreras 2004). In slice recordings, resting membrane potential (*Vm*, in mV) was calculated as the average membrane potential in a 40 ms time window prior to the stimulus onset. For *in vivo* recordings the same time window was used but the sweep was included in the data analysis only if the variance of the membrane potential was < 0.5mV during the time window. For those sweeps in which a spike was observed, the spike threshold and spike latency (St) were also calculated.

Mutual information analysis for single neuron.

Only cells with more than 250 acceptable sweeps (summed across all stimulus conditions) were used to perform Shannon information analysis. The mutual information (MI) between any two variables S, R can be calculated as

$$I(S;R) = H(R) - H(R|S)$$

in which H is the entropy of a given variable R:

$$H(R) = -\sum_{i=1}^{n} p(r_i) log_2(p(r_i))$$

and H(R|S) is defined as

$$H(R|S) = -\sum_{j=1}^{m} p(s_j) \sum_{i=1}^{n} p(r_i|s_j)\ log_2 p(r_i|s_j)$$

where j, i ranges over the stimulus/response types. Similarly, the mutual information between one variable S and multiple $\boldsymbol{R}$ (joint mutual information) can also be calculated using above equations. In this case, the synergistic effect of $\boldsymbol{R}$ can be expressed as the difference between the linear sum of the mutual information between S and each individual R and the joint information $I(S;\boldsymbol{R})$:

$$syn(S;\boldsymbol{R}) = I(S;\boldsymbol{R}) - \sum_{i=1}^{n} I(S;R_i)$$

Information calculations were performed using the Information Breakdown toolbox (Magri et al, 2009) in Matlab (Mathworks. Inc). In short, each variable was first digitized using the equal space (*'eqspace'*) binning method with 7 bins. The effect of different binning method as well as number of bins on MI values are also explored (Figure 5.i). Because in most trials only one spike was observed, only the first spike was considered when calculating the information in St. Thus, the spike latency St can be digitized to a single word, which has (number of bin + 1) possible outcomes, instead of a binary list which could have 2^(number of bin) possible values. Shuffle correction combined with Panzeri-Treves (PT) bias correction was used to perform all information calculations for neural recordings. The performance of the algorithm was evaluated by randomly selecting a subset of trials to calculate the mutual information (*I(S;PSP)*, *I(PSP;Vt)* and *I(PSP;St)*; *PSP* is the 3-dimentional vector composed of *Ot*, *Rt* and *Sl*), and subsequently checking the number of trials (*Ns*) needed for the calculated information values to reach asymptote (Figure 5.ii). When the 'eqspace' binning method was used, all information values reached asymptote after *Ns* > 70, well below the average *Ns* in the present data set (124±33.2 (range: 78-220) stimulus repetitions per stimulus).

A. equal # of observations in each bin

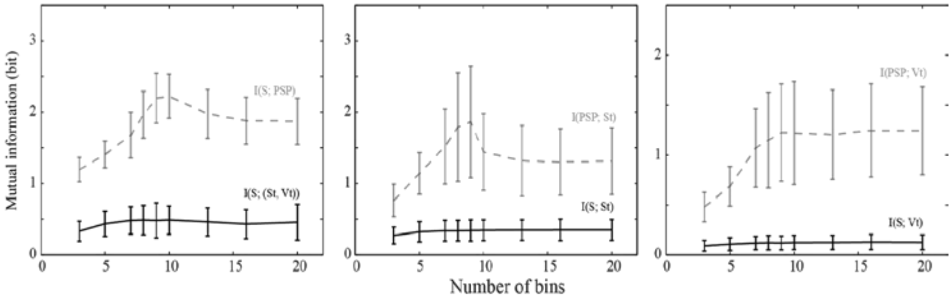

B. equal bin size

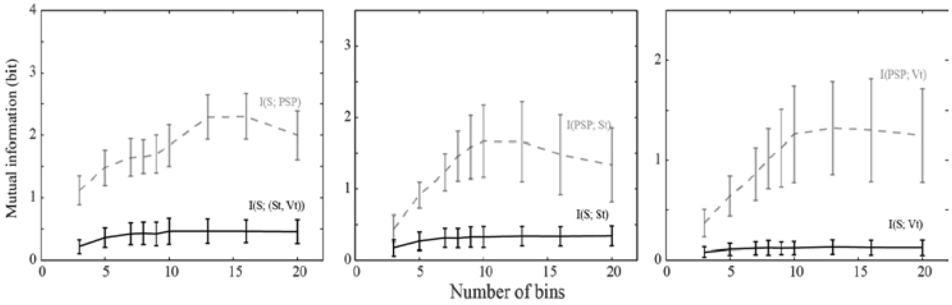

Figure 5.i. Effect of the bin number on mutual information calculations. Two different binning methods were considered: (A) equal number of observations in each bin and (B) equal bin size. Independent of the bin number used in calculations, PSP channels contain significantly more information about Stimulus (or the suprathreshold response) compared to action potential threshold (Vt) or spike timing (St).

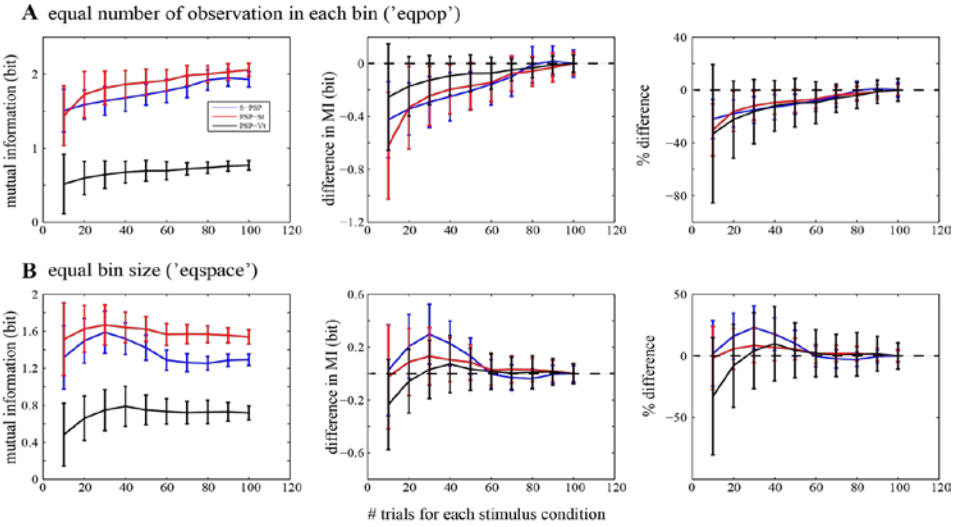

Figure 5.ii. Calculated mutual information value as a function of the number of trials in each stimulus condition. A random subset of trials in each stimulus condition was selected to perform calculation on I(S; PSP), I(PSP; St) and I(PSP; Vt). (A) Analysis based on 'eqpop' binning method, in which the size of individual bins was modified so roughly equal number of observation was placed in each bin. (B) Analysis based on 'eqspace' binning method, in which the size of individual bins was kept constant. All three information value reach asymptote after ~70 trials in each stimulus condition. Therefore calculations in the main text were performed using >70 trials per condition (78-220, on average 124±33.2 trials/stimulus). Dash lines donate zero difference, compared with the information value calculated with 100 trials per stimulus condition.

Calculation of minimum observation size

An essential step in the information calculation method listed above is the estimation of stimulus-response probability distributions from the experimental data. Following Panzeri and colleagues (Ince et al. 2010) we calculated the number of experimental trials per stimulus condition, *Ns*, to be ~32 times larger than the number of possible response pattern, N_R, to get an accurate estimation ($Ns/N_R \approx 32$). This also means that to accurately estimate information between the subthreshold responses (*Am*, *Sl*, *Ot*, all binned to 7 bins) and the stimulus, 32×7×7×7 = 10976 trials/ stimulus =91h continuous recordings will be needed. Given technical infeasibility of maintaining whole cell access for such a long period we performed bias corrections to account for the upward bias in information estimation with limited sample sizes (see Ince et al. (2010) and Victor (2006) for further discussion). Methods like quadratic extrapolation (QE), Panzeri-Trevez (PT) correction (Treves, & Panzeri. 1995) and Nemenman-Shafee-Bialek (NSB) (Nemenman, Shafee, & Bialek 2002) correction greatly reduced the Ns needed to $Ns/N_R \approx 2\text{-}4$ or less. Furthermore, combining shuffle correction method with bias correction methods mentioned above further reduced the necessary Ns/N_R to 1/4~1/8[7]. Thus, for the same calculation above, only 1/8~1/4×7×7×7 = 43~86 trials/stimulus condition was needed. Therefore we collected 124±33.2 (range: 78-220) trials/stimulus in *in vitro* experiments and 94±25.6 (range, 60-146) trials/stimulus for the *in vivo* whole-cell recordings.

Mutual information analysis for multiple neurons

For multi neuron MI analysis we followed the approach to first decode and then estimate the MI between stimuli and the confusion matrix of the decode (Quian Quiroga et al. 2009, Panzeri & Diamond 2010, Ince et al. 2010) using support vector machine (SVM) in MATLAB with radial basis functions as the kernel transform. We utilized 90/10% cross validation during decoding to obtain an estimate of the generalized performance of the decoder. SVM decoding outperformed other decoders with an average performance of 94%, compared with some other decoders (diagonal linear (77%), linear (79%), quadratic (80%)). The use of an intermediate decoder ensured that the calculation was bias free (given that we observe the correct value of 0 bits for an uninformative set of stimuli, with otherwise very similar properties (see Figure 5.3G)), but came at the expense of lower bound in MI estimates since a (potentially existing) better decoder would improve the MI.

For the *in vitro* recordings we first had to generate bootstrapped populations of sufficient size to perform the population MI calculations. In order to preserve the within-cell variability of responses across stimulus and trials, we only drew bootstrap samples from the trials of each cell independently. As in the simulations we drew 100 samples of groups of each population size. Curves in Figure 5.4 display averages over these samples.

Network Simulations

The reconstruction of information in the neural network was performed in an *in silico* model of the barrel cortex. The model included a realistic account of the number and connectivity with a barrel column for Layers 2/3, with inputs arriving from the L4, mimicking the conditions in the *in vitro*/*in vivo* experiments.

Neuronal model

The neuronal model was originally based on Izhikevich's quadratic model (Izhikevich 2004)

$$\frac{dv}{dt} = 0.04(v - vr)(v - vt) - u + I$$

where v, vr and vt are the membrane potential, resting membrane potential without stimulus and the spike threshold of the neuron, respectively. For excitatory cells, vt is determined by the EPSP slope s as shown before (Wilent & Contreras 2005):

$$vt = -\frac{10}{7}s - 48$$

u is the recovery variable and its evolution is determined by:

$$\frac{du}{dt} = a[b(v - vr) - u]$$

With the following reset condition:

$$if\ v \geq 30$$

$$v \leftarrow c$$

$$u \leftarrow u + d$$

I is the synaptic current the neuron received (see below). *a, b, c, d* are dimensionless variables which together determine the firing pattern of the model neuron (Table 5.1; for more details see Izhikevich 2004). For the simulations a first order Euler method with step size of 0.1 ms was used.

	a	**b**	**c**	**d**
Excitatory neurons	0.020±0.006	0.225±0.014	-60.0±4.4	11.0±1.7
Fast-spiking interneuron	0.100±0.012	0.213±0.015	-69.7±3.0	10.6±1.7
Non-fast-spiking interneuron	0.021±0.007	0.225±0.020	-64.2±10.3	8.5±3.4

Table 5.1. Neuronal parameters for different type of neurons in the layer 2/3. All values are in mean±std.

Neural network

A two-layer neural network that models the first order feed-forward projections from L4 to L2/3 along with reverberatory connections within L2/3 was constructed based on anatomical reconstruction of the barrel cortex (data not shown). L4 contained 1330 excitatory neurons; L2/3 contained 2657 neurons of which 2263 (85.2%) are excitatory. Of the 394 interneurons in layer 2/3, 97 are fast-spiking (FS) interneurons, and the rest are non-fast-spiking (NFS) interneurons. These neurons were distributed in a 640-by-300-by-300 µm region (L4, 210-by-300-by-300; L2/3, 430-by-300-by-300). The density and ratio of the neurons matched published data (Feldmeyer et al. 2002, Uematsu et al. 2008). L4 sent projections to L2/3 and recurrent connections were included in L2/3. There were no feedback connections from L2/3 to L4.

Connectivity was determined using axonal and dendritic projection patterns (Feldmeyer et al. 2002, Lubke et al. 2003, Feldmeyer et al. 2006, Helmstaedter et al. 2008), which were approximated by 2-D Gaussian functions, with the assumption that the probability that two neurons are connected is proportional to the degree of axonal-dendritic overlap between these two neurons (i.e. Peter's rule, White 1979). For each pre-synaptic *i* and post-synaptic neuron *j*, we calculated the axonal-dendritic overlapping index I_{ij}, which is the sum of product of presynaptic axonal distribution A_i and postsynaptic dendritic distribution D_j:

$$I_{i,j} = \int_x \int_y A_i D_j dxdy, \qquad x, y \in SD_j$$

where SD_j is the 2-D space contains 99.9% of D_j. We then converted I_{ij} into connection probability P_{ij} between neuron *i* and *j*, by choosing a constant k for each unique pre- and post-synaptic cell type pair so that the average connection probability within experimentally measured inter-soma distances (usually 100 µm) matches empirically measured values between these two types of cells (Feldmeyer et al. 2002, Lubke et al. 2003, Helmstaedter et al. 2008, Feldmeyer et al.2008, Blatow et al. 2003, Holmgren et al. 2003, Caputi et al. 2009, Avermann et al. 2011) (Table 5.2):

$$P_{i,j} = kI_{i,j}$$

Finally a binary connectivity matrix was randomly generated using pairwise connection probability P_{ij}, in which connected pairs were labelled as 1.

Synaptic currents in this network were modeled by a double-exponential function. Parameters of those functions (peak amplitude, rise time, half width, and pair-pulse ratio) were adjusted to match experimentally measured PSPs in barrel cortex (Table 5.2; See Thomson & Lamy 2007 for review). The onset latency was calculated from the distance between cell pairs; the conduction velocity of action potential was set to 190µm/ms.

Differences in activation state of cortex were included in the model by setting the common initial voltage and the equilibrium potential ***vr*** of all cells to either -80, -70, or -60mV in a third of the trials, thus accounting for potential up- and down-states as well as an intermediate state.

Post vs Presynaptic	**Layer 4 neuron**	**Excitatory neuron**	**FS interneuron**	**NFS interneuron**
Excitatory neuron				
Pconn	0.11	0.03	0.14	0.10
uPSP strength, mV	0.7±0.6	1.0±0.7	-2.96±2.52	-0.49±0.49
uPSP rise time, ms	0.8±0.3	0.7±0.2	6.5±3.7	5.4±2.2
uPSP half width, ms	12.7±3.5	15.7±4.5	55.9±22.6	56.2±24.1
PPR	0.90±0.39	0.61±0.41	0.46±0.17	0.91±0.56
FS interneuron				
Pconn	0.20	0.21	0.06	0.09
uPSP strength, mV	0.96±0.93	3.48±2.52	-2.96±2.52	-0.37±0.33
uPSP rise time, ms	0.89±0.31	2.32±1.00	6.5±3.7	3.1±2.0
uPSP half width, ms	15.0±8.2	16.3±5.8	55.9±22.6	20.0±12.1
PPR	0.99±0.66	0.70±0.14	0.46±0.17	0.91±0.56
NFS interneuron				
Pconn	0.20	0.14	0.07	0.11
uPSP strength, mV	1.2±0.9	1.36±0.78	-2.96±2.52	-0.49±0.56
uPSP rise time, ms	0.42±0.1	1.3±0.5	6.5±3.7	4.9±5.4
uPSP half width, ms	14.0±9.1	14.0±6.2	55.9±22.6	33.3±12.0
PPR	1.00±0.62	0.96±0.51	0.46±0.17	0.91±0.56

Table 5.2. Connection probability and unitary PSP parameters between different neuron populations. Pconn, connection probability; uPSP, unitary postsynaptic

potential; PPR, pair-pulse ratio. Values are mean±std.

Synaptic input from layer 4

Layer 4 stimulation was provided in the model based on population PSTHs collected extracellularly in anesthetized animals *in vivo* (Celikel et al, 2004). We used PSTHs of principal and 1st order surround whisker stimulation, as well as two linear interpolations between the two, yielding 4 stimuli with 2 bits total entropy, matching the numbers in the in vitro experiments. The PSTHs only specified the population firing rate in L4. We further explored population coding properties, by modifying the variability of spike timing across trials. If response times and spike counts were conserved across multiple trials, spike timing and counts within and between neurons start to carry additional information.

In the ‘Rate + Poisson’ condition, we assumed no trial-to-trial reliability beyond that given by the PSTH. Spike times were drawn based on Poisson statistics for each time with the PSTH modulating the firing rate (see Figure 5.4D left). This condition forms a lower bound on the transferred information between L4 and L2/3, under the experimental constraints on the model. On the other extreme, in the ‘Rate + Trial Reliability’ condition, the PSTHs varied as before, but in addition neurons emitted the same sequence of spikes for every trial, hence, preserving timing and count perfectly. This condition forms an upper bound on the information transfer, since within the experimental constraints, no additional variability is introduced, which would reduce the mutual information. Finally, we considered the ‘No Rate + Trial Reliability’ condition, where the population PSTHs are uninformative across stimuli, and stimulus information is only contained in the trial-to-trial reliability of individual neurons. This case if provided for reference for other stimulus scenarios, where the PSTH may not vary much (e.g. texture-type stimuli), and individual timing becomes more important.

We also explored conditions between these extremes (Figure 5.6), where the information in population or single neuron response was systematically varied. For the case of the population response we varied the different in time and firing rate of the PSTHs for different stimuli (Figure 5.6A). Time differences were implemented by simply shifting the entire PSTH in time (tested shifts: [0,1,2,3] ms per stimulus, i.e. maximum shift was 9 ms). Rate differences were implemented as the fraction between the maximal and the minimal stimulus (tested fractions were [1,2,3,4], where e.g. 4 corresponds to the weakest stimulus being 25% of the strongest stimulus at the peak of the PSTH). The case of time shift 0 ms and rate fraction 1 is uninformative on the level of population rate. Single neuron reliability in this case was chosen as a medium level of single unit reliability (SD_T = 3 ms, SD_C = 20%). Single neuron reliability in response was also explored in timing and rate (Figure 5.5B). Starting from perfect timing and rate, we degraded the information extractable from single neurons, buy introducing timing variability (spike times were shifted by Gaussian-distributed noise with standard deviation SD_T) and rate/count variability (spikes were deleted or added, by linearly mixing between Poisson and perfectly reliable spiking, with mixing parameter SD_C, denoted as % in the figure). For both procedures, the modifications were performed while keeping the population PSTH approximately unchanged, i.e. for timing the overall timing distribution was contracted to keep the original PSTH, and for rate, spikes were shifted between neurons, rather than only removed from individual neurons.

These independent variations of population and single unit responses allowed us to separate the contribution of these two information sources to the information available in groups of L2/3 excitatory and inhibitory neurons (see Results).

Results

We performed whole-cell current-clamp recordings of Layer (L) 2/3 pyramidal neurons (N=6) in the juvenile rat primary somatosensory cortex, in the barrel cortex subregion, *in vivo* and *in vitro*. During *in vivo* recordings, sensory stimulation was provided with direct stimulation of the principal and 1st order surround whiskers (Figure 5.1A) and the resulting somatic post-synaptic potential (PSP) was characterized in terms of onset latency, slope, and peak amplitude (Figure 5.1B-D). Principal whisker evoked PSPs exhibited shortest latency, as well as highest slope and amplitude, in comparison to stimulation of surrounding whiskers in agreement with previous observations (Brecht et al 2003). Although the synaptic transmission was highly reliable across trials (percentage of trials with subthreshold response, PW: 99.8%, SW: 91.8%), action potentials were sparse even after principal whisker deflections (percentage of trials with suprathreshold response, PW: 6.2%±8.6%, SW: 1.7%± 2.9%, mean±STD). Knowledge of the *in vivo* response properties to different whisker stimulations provided us the basis for recreating stimulation conditions that match *in vivo* PSP statistics *in vitro*, where a substantially larger number of trials with action potentials can be recorded for a given neuron while presynaptic neuronal activity can be modulated with precision. *In vitro* whisker stimulation was emulated by providing current input with different slopes to L4 of the same barrel column (Figure 5.1E-G); PSP responses of L2/3 neurons with shallower slopes corresponded to stimulation of neighboring whiskers, exhibiting delayed PSP onset times as well as lower slopes and amplitudes (Figure 5.1H-J). Action potential responses showed a similar dependence when averaged across multiple trials, with delayed spike times, increased threshold and decreased spike probability for shallower slopes of stimulation (Figure 5.1K-M).

Sub- & supra-threshold encoding properties

The across trials analysis shown above indicate that individual cells are tuned to spatial stimuli, however, during sensory processing stimuli have to be recognized on single trials, which is only possible with low trial-to-trial variability. Action potential probability exhibited far greater temporal trial-to-trial variability than PSPs (Figure 5.1N-P). PSP onset times showed an average progression with small trial-to-trial variability (Figure 5.1N, SD = 0.42-0.63 ms) as spike time variability increased threefold (Figure 5.1P, SD = 1.2-2.3 ms). Correspondingly, PSP onset time only had a limited predictability for spike time, with action potentials often occurring with significant and variable delays (Figure 5.1P, 2.8-4.7 (SD 1.1-2.1) ms). Action potential generation was also failure prone as average spike failures rates reached 31.7% (Range: 0-85%). To study the influence of trial-to-trial variability in timing and rate on stimulus information we next employed mutual information in Shannon’s formulation (Shannon 1948, Panzeri et al, 2001, Petersen et al 2001, Quian Quiroga and Panzeri, 2009). Mutual information provides largely agnostic estimates of transmitted information between stimulus and response, conceiving of the sensory processing as a communication channel between the environment and the internal state of the neural system.

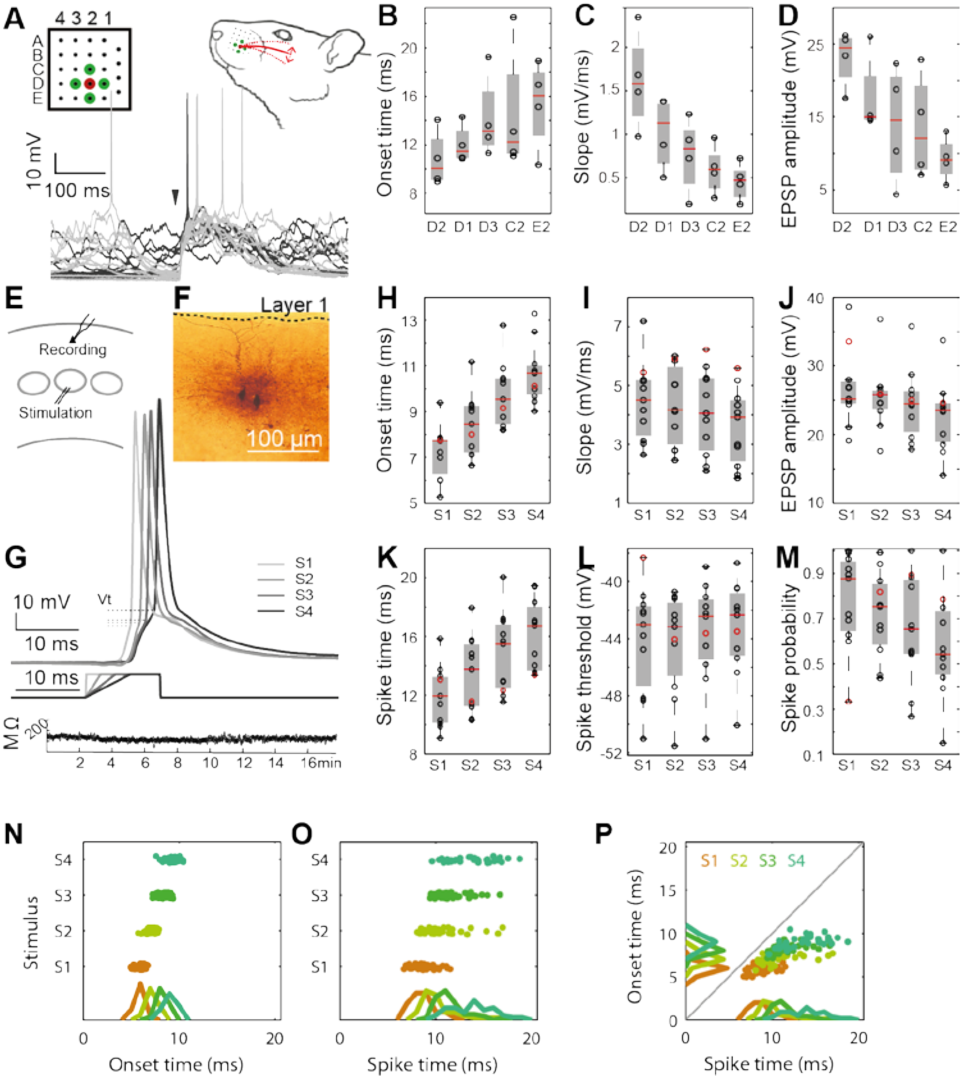

Figure 5.1. Stimulus representation in single somatosensory cortical neurons. (A) We stimulated whisker D2 and direct neighbors (D1, D3, C2, E2) individually to compare their responses in barrel cortex in vivo using whole cell recordings. Randomly selected 10 traces from primary whisker (D2, in light grey lines) stimulation and 10 traces from surround whisker (D1, D3, C2, E2, in dark grey lines) stimulation are shown. The dark triangle indicates the onset of whisker stimulation. (B-D) EPSP parameters of somatosensory L4 pyramidal neurons in the D2 barrel show a dependence on relative stimulus location, with earlier onset times (B), larger

slopes (10-90%) (C) and larger amplitudes (D) at the D2 whisker in comparison to its neighbors. Onset time was the latency between stimulus onset and time it takes for the membrane to reach 10% of the somatic EPSP amplitude. (E) In vitro recording configuration in acute slices of the mouse barrel cortex. (F) Biotin filled, DAB processed, L2/3 neurons. (G) Top: Representative action potentials. Dashed lines denote spike thresholds. Color codes correspond to four presynaptic stimuli with varying slopes, S1:S4 with reducing rising slope, delivered via a bipolar electrode in L4 (middle). Bottom: Input resistance of the neuron labeled with a red circle in Figure 5.1H-M. (H-M) L2/3 pyramidal neurons' responses to L4 stimulation. Each circles shows the mean response of one neuron (N=11). H: Onset time, I: Slope, J: EPSP amplitude; K: Spike time, i.e latency to spike after stimulus onset; L: Spike threshold, described as the membrane potential at which its second derivative reaches global (positive) maximum; M: Action potential (i.e. spike) probability, across trials. (N-P) While both EPSP and spike parameters displayed average dependence on the stimulus, EPSP parameters are more accurately determined on single trials by the stimulus, than the spike parameters.

Information transmission between somatic PSP and Action Potential

How much information does a somatosensory neuron carry about the sensory stimulus (S) in the periphery and how much of this information does it transfer to its postsynaptic targets? Surprisingly, a single somatic PSP contains the bulk (~95%, $I(S;PSP)$ vs. $H(S)$, Figure 5.2A) of the information present in the sensory stimulus. The information in the onset time (81%, Figure 5.2B), slope (8.4%, Figure 5.2B) and amplitude (6.4%, Figure 5.2B) of the PSP contribute largely independently to the total information content of a PSP (Figure 5.2 C). However most of this information is lost upon action potential generation (down to 24%, $I(S;(St,Vt))$, Figure 5.2A), where spike time (*St*, 16%, Figure 5.2D) and voltage threshold (*Vt*, 6.2%, Figure 5.2D) carry about equal amounts of stimulus information.

To quantify how much of the stimulus information in the PSP is transferred to post-synaptic neurons via action potentials we first calculated the total entropy of the PSP (i.e across onset, slope and amplitude together; 6.4 bits, 3.2-fold, Figure 5.2E). The transferred information from PSP to action potential was limited to 50% and 70% of the stimulus information for St and *Vt*, respectively (Figure 5.2E). Most of this information is apparently contributed by other sources than the stimulus, e.g. network structure (see below), since the actual amount of stimulus information contained in an action potential is drastically lower (0.41 bit, Figure 5.2A). Nonetheless, individual PSP properties contribute synergistically, albeit only minimally, to the timing information in the spike (Figure 5.2F, 6.4%, $p<10^{-5}$). Consequently, while a substantial amount of this information is transferred from the PSP to the spike, this information is insufficient to encode the stimulus using information in spike timing at the single neuron level on a given trial.

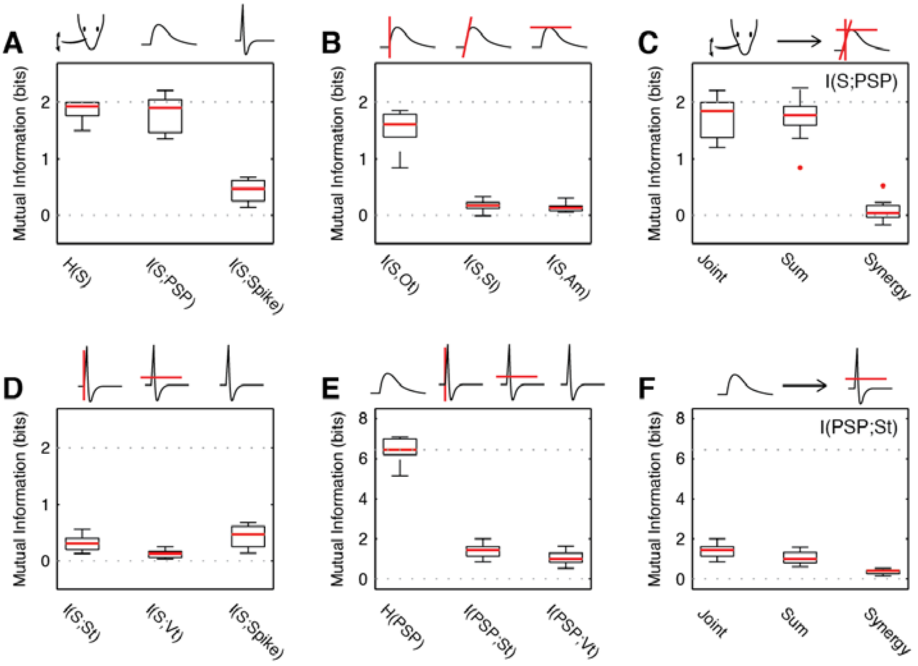

Figure 5.2. Postsynaptic potentials encode substantially more stimulus information than spikes. (A) The transformation from PSP to the spike significantly reduces the information single neurons transmit about the stimulus. While the PSP contains a large fraction of the stimulus information (95%, I(S;PSP), 1.81±0.31 bit vs. H(S), 1.86±0.17 bit, p = 0.16), most of this information is not transferred to the spike (0.47 bit, 24%). (B) The majority of the information in the PSP is carried by the onset timing (Ot, 1.6 bit, 85%), while slope (Sl, 0.17 bit, 10%) amplitude (Am, 0.13 bit, 5%) carry only small amounts of information. (C) Ot, Sl, and Am add their information independently, as the synergy between them is close to 0 (Synergy: 0.03 bit, p = 0.15, t-test). (D) The information in the spike is contributed by spike time (St, 0.31 bit, 16%) and threshold (Vt, 0.12 bit, 6.2%), and jointly only reach 21% of the total information (repeated from A). (E) Substantial information transfer occurs between the PSP and the spike, although this constitutes only 22% (St) and 15% (Vt) of the entropy in the PSP. (F) The information in the properties of the PSP adds largely independently to the joint information, with a small but highly significant synergistic contribution of different PSP properties (0.41 bit, 6.4%, p<10-5). In all figures data is plotted as inter-quartile intervals and red lines denote the median of each

distribution. Outliers are plotted as red dots.

Information recovery in local neural populations

If the intracellular information transfer via PSP-to-action potential transformation causes a dramatic drop of stimulus information carried in the neural activity, how can the somatic PSP of single L2/3 neurons carry near complete information about the stimulus on a trial-to-trial basis (Figure 5.2A)? Since these neurons are four synapses away from the sensory periphery, the recovery of information has to occur at the network level.

We quantified the information recovery both on bootstrapped populations of real data, and in an anatomically and physiologically well-constrained network model of a rat barrel column (see Materials and Methods). The model has anatomically correct numbers and laminar locations of major classes of inhibitory and excitatory neurons in L4 and L2/3 (Figure 5.3A), as well as statistically defined connectivity, synaptic transmission parameters and single neuron dynamics based on experimental observations (see Materials and Methods). Stimulation was provided analogously to the *in vitro* stimulation in L4, sampling from previously collected L4 peristimulus time histograms (PSTH) of principal and surround whisker stimulation *in vivo* (Figure 5.3B, L4 response to principal whisker in grey; (Celikel et al, 2004)). PSTHs of simulated L2/3 excitatory and inhibitory neurons correspond to experimentally observed ones under similar conditions (Celikel et al 2004, de Kock et al 2007, Figure 5.3B red and blue, respectively). Information in PSPs and action potentials in this simulated network closely matched the properties of the real neurons in biological networks (see above). Trial-to-trial variability in spike timing was substantial and significantly larger than the variability in PSP timing (Figure 5.3C, compare with Figure 5.1K-M). Similar to the observations in real neurons (Figure 5.2A) stimulus information was nearly fully retained in the PSP in excitatory neurons (Figure 5.3D, red, 88.8%), yet, reduced substantially (20.1%) during action potential generation. Interestingly, inhibitory neurons carried significantly less information in their PSPs (Figure 5.3D, blue, 77.3%), but also exhibited less of an information loss during spike generation (43.6%).

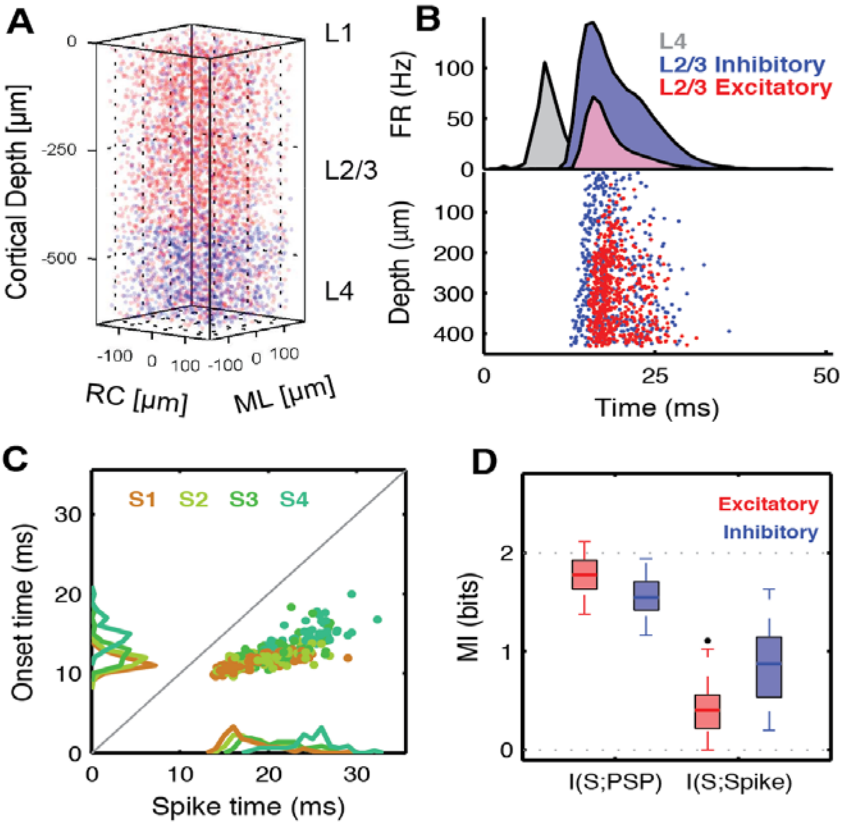

Figure 5.3. Anatomically constrained barrel column in silico reproduces the relationships between sub- and supra-threshold information. (A) An anatomically based model of a barrel column for L2/3/4 was generated to analyze the information transfer between L4 and L2/3 in analogy to the physiological recordings (see Methods for details). (B) In response to stimulation in L4 with a whisker-like PSTH (grey), excitatory (red) and inhibitory (blue) cells respond in L2/3, with inhibitory activity eventually extinguishing the total activity in the network. (C) Corresponding to the in-vitro/in-vivo data, the timing of PSPs for a given stimulus is more precise than the spikes they evoke (compare to Figure 5.1P). (D) The relationship between PSPs and spikes in terms of timing and reliability leads to single cell mutual information very similar to the recorded data (excitatory cells, compare to Figure 5.2A). Inhibitory cells (not recorded), show less information in their PSP response, but more information in the spikes (all properties combined for both cell-types).

Stimulus information could be almost fully recovered from populations of excitatory L2/3 neurons *in vitro* (>81.1%, Figure 5.4B). As expected the amount of recovered information was substantially greater when information in timing considered (81.1%, in timing of the 1st spike, binned at 2ms, 100 cells), compared to rate based decoding (50.5%, red vs. light red), and was largely independent of the population size. To avoid overestimation of information from high-dimensional population data due to limited sampling bias, we first decoded the stimulus from single trial responses before computing the MI using a support vector machine (SVM) based decoder (Figure 5.4A). To verify that this method does not introduce a positive bias we computed the information in artificial uninformative stimulus set (same PSTH for all stimuli, independent Poisson spiking), which yielded near zero MI values (Figure 5.4C). The performance of the SVM provided significantly better results (94%) than linear (79%) or quadratic (80%) decoders. Although better decoders than the SVM may still exist, the data presented here constitutes a very close approximation of the lower bound on the available information in the population data.

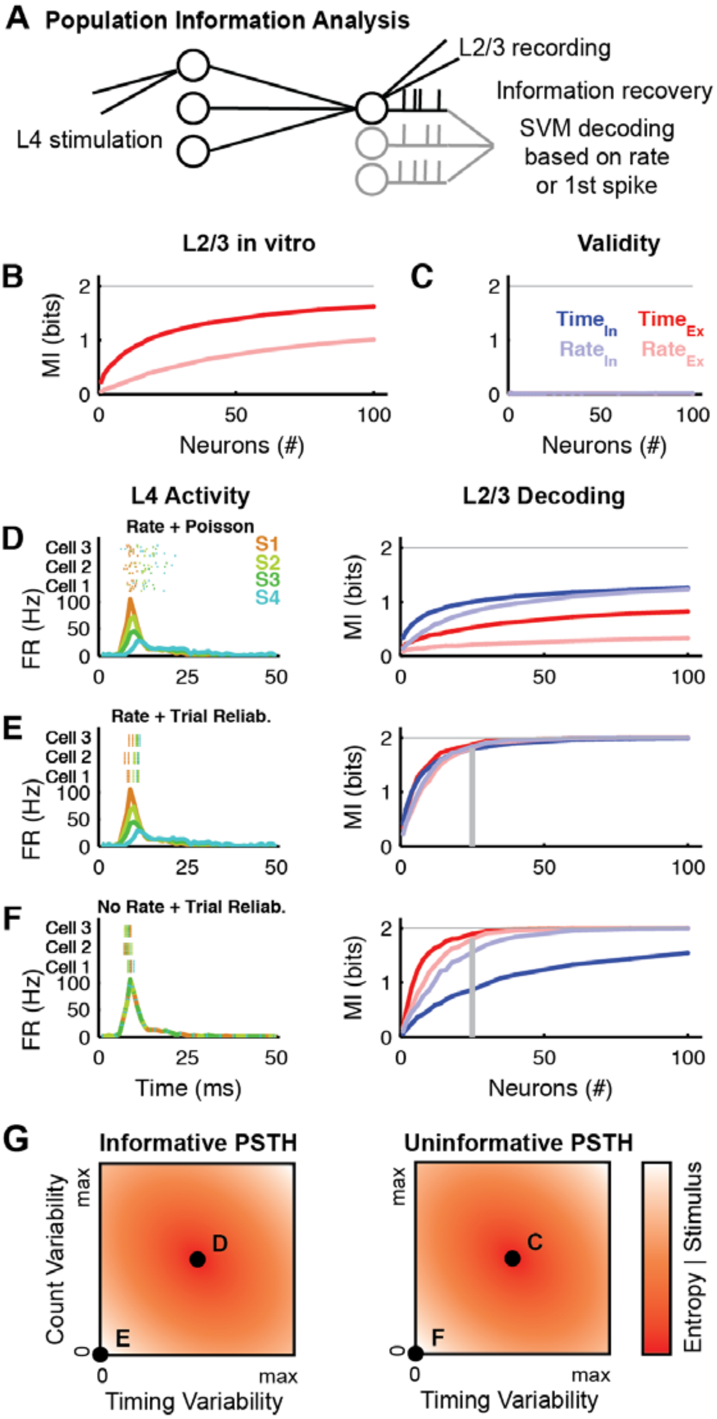
A Population Information Analysis
L2/3 recording
Information recovery
SVM decoding
based on rate
or 1st spike
L4 stimulation
L2/3 in vitro
Validity
B
MI (bits)
2
1
0
0
50
100
Neurons (#)
C
Time_In
Time_Ex
Rate_In
Rate_Ex
L4 Activity
L2/3 Decoding
D
Rate + Poisson
Cell 3
Cell 2
Cell 1
S1
S2
S3
S4
FR (Hz)
100
50
0
25
E
Rate + Trial Reliab.
F
No Rate + Trial Reliab.
Time (ms)
G
Informative PSTH
Uninformative PSTH
Count Variability
max
Timing Variability
D
E
C
F
Entropy | Stimulus

Figure 5.4. Information recovery in neural populations possible from small neuronal groups. (A) To address the question of information recovery in neural populations in L2/3, we evaluate the mutual information from population spike trains of groups of excitatory or inhibitory neurons. To prevent the sampling bias, MI is estimated between the stimulus and an SVM decoding from the population response. (B) Population information estimated from bootstrapped in vitro recordings show nearly complete recovery of stimulus information. Asymptote is reached above 81% for 100 neurons for temporal decoding (dark red), and remains systematically lower for the rate-based decoding (light red). (C) Estimating population information for non-informative stimuli (identical PSTH, Poisson-spiking) leads to vanishingly low MI values, demonstrating that the analysis does not introduce a positive bias. (D) If the population activity in L4 is only constrained by the PSTH and otherwise spikes are drawn according to Poisson-distributions (bottom left, different colors = different stimuli), then inhibitory neurons carry more information for both time (dark blue) and rate (light blue) decoding, than excitatory neurons (dark & light red respectively). (E) If PSTHs differ across stimuli but spike timing is stereotypic across trials ('Rate + Trial Reliability', top left, multiple trials per neuron above each other), coding becomes highly effective and independent of cell-type and coding strategy (~25 cells). (F) If L4 PSTHs do not distinguish stimuli, but only the timing of individual neurons across trials is stereotypic (No Rate + Trial Reliability, top left), a remarkable shift occurs, with excitatory neurons reaching almost complete information for much smaller group sizes (~25 cells). In all plots the vertical grey line indicates where 90% of the information is represented.

Contribution of timing/rate reliability for information recovery

While a well-defined stimulus can be provided *in vitro*, the details of the population activity cannot be well controlled. From the perspective of information transmission in single trials, the most important property of the neural response is the reliability across trials. We therefore constructed a barrel column *in silico* (described above and in Materials and Methods) to investigate the influence of reliability in spike-timing and spike-count in L4 on the information transfer to L2/3, and determine its limits in comparison with the experimentally observed data.

We first considered three extreme cases of encoding in L4, with a more systematic exploration in the following section. In the first case ('Rate + Poisson'), stimuli are encoded only by the population PSTH, but spikes across trials and neurons are drawn with Poisson statistics. In the second case ('Rate + Trial Reliability'), stimuli are encoded by the population PSTH, but also by the spike timing and count of individual neurons. Within the constraints of the experimentally observed PSTHs, these two cases constitute the lower and upper bound of trial-to-trial reliability in L4. In the third case (‘No Rate + Trial Reliability’), the population PSTH carries no information about the stimulus, but is encoded in the spike timing and count of individual neurons. The latter case is added for comparison with other stimulus paradigms, where the population PSTH does not distinguish between stimuli, e.g. certain texture recognition tasks. These cases are illustrated in Fig. 4G in relation to the effective reliability in spike count and timing, as well as the stimulus dependent entropy. More details regarding the construction of these cases are given in Experimental Procedures.

The results have shown that in the ‘**Rate + Poisson**’ case, information transfer is overall low, with interneurons providing superior readout of stimulus information in L2/3 for both decoding the information in rate or spike-timing (Figure 5.4D right, light and solid colors respectively, excitatory (red) vs. inhibitory (blue) neurons). While timing and rate codes are similarly efficient in interneurons, substantially larger populations of excitatory neurons are required to decode information in rate than in time. Given that timing information is only present on the population level in L4, the dominance of this temporal readout in L2/3 is remarkable. As the regenerated stimuli *in silico* approximate the stimuli *in vitro* with high accuracy (see above), the ‘**Rate + Poisson**’ coding cannot account for the L4 encoding scheme in the present experiments.

Information transfer using ‘**Rate + Trial Reliability**’ is overall substantially higher (Figure 5.4E right) and requires the least number of neurons (~25) to reconstruct the information available in the presynaptic pool of neurons and the stimulus. This information maximization is qualitatively expected, as two sources of information - rate and timing - are simultaneously encoded. Remarkably, both cell-types and decoding strategies yield very similar information values, suggesting that encoding information with ‘**Rate + Trial Reliability**’ ensures optimal information transfer. Predictably, information encoding in the absence of rate modulation, i.e. ‘**No Rate + Trial Reliability**’, results in information loss, although information recovery with this decoding schema is still superior to the ‘**Rate + Poisson**’ coding (Figure 5.4E). Unlike the ‘**Rate + Poisson**’ coding, however, excitatory neurons are substantially more efficient at representing information for similar group sizes than inhibitory neurons (compare Figure 5.4D and 5.4E).

These results show that stimulus information represented in L2/3 neurons is highly dependent on the properties of the encoding within the layer. While information encoded in the rate of the population response to the stimulus is better transferred using inhibitory neurons, information in single neurons’ action potential timing is better represented in excitatory neurons.

Population and single unit information selectively influence inhibitory or excitatory cells

Next, we modulated the information content in L4 more fine grained along meaningful dimensions, to investigate the consequences for L2/3 information availability. Note that the real data falls between the extremes, suggesting the availability of a limited amount of single unit information.

While we only considered the extreme cases of L4 encoding above, realistic encoding will necessarily cover a range of cases between these extremes. Different stimuli will often lead to different population PSTHs, however, not always, as different textures may well lead to similar PSTHs, but rather differ in the single unit responses. Conversely, even in cases where the population PSTH carries substantial information about stimulus identity, spiking may well not be Poisson (especially at response onset, Amarasingham et al. 2006), although likely not as reliable as posited above.

We investigated contributions from the population and the single unit separately. Information on the population level was represented as the average PSTH of the population (see Figure 5.5A1). Stimulus information was encoded either as timing or rate differences. Timing differences were implemented as shifts of the PSTHs (Δ_T), whereas rate differences were implemented as rate factors between the PSTHs (Δ_C). If Δ_T = 0ms and $\Delta_C = 1$, then no information is contained in the population PSTH. Conversely, if Δ_T = 4ms and $\Delta_C = 4$, the combined difference between the PSTHs is similar to the experimentally observed. These parameters allow us to study the susceptibility of L2/3 neurons to the information on the population level in L4 (Examples of spike patterns are shown in Figure 5.6A1 above the PSTHs, 10 trials each).

For decoding using spike times, inhibitory neurons exhibited substantially greater susceptibility to variations in the distinguishability of stimuli on the L4 population level compared to excitatory neurons (blue vs. red, Figure 5.5A2). This was true for both variations in time (Δ_T) and rate (Δ_C) in L4. Similarly for rate decoding, inhibitory neurons were more susceptible to changes in rate than excitatory neurons (Figure 5.5A3). Timing had little effect on rate decoding, since this corresponds mostly to a shift in the analysis window (unrestricted here), with no change in rate information in L2/3.

Next, we considered the influence of various levels of single unit variability on the stimulus reconstruction in L2/3. Here, the population PSTH is kept fixed, but the temporal and count reliability are varied on a per neuron basis (see Figure 5.5B1). The timing reliability was varied by introducing a temporal jitter to individual neurons (SD_T), while contracting spiking patterns to remain consistent with the population PSTH. Count reliability was varied by selectively by a linear transition between a complete reliable and a Poisson model, while maintaining overall PSTHs, by shifting spikes between neurons and maintaining temporal variability at the same time.

For time decoding, now excitatory neurons showed much greater susceptibility to single unit differences in reliability in L4, both for rate and time (Figure 5.5B2). Interestingly this carried over to rate decoding to an even greater degree, which may have been suspected to be rather the domain for inhibitory neurons (Figure 5.5B3).

In summary, population and single unit level information translates quite clearly into modulations of the information content of inhibitory and excitatory neurons in L2/3, respectively. Hence, a fairly clean line is drawn between the lines with respect to their putative use in extracting stimulus information from the L4 level. Together they thus have the ability to represent the entire information efficiently in small populations (see Figure 5.4D).

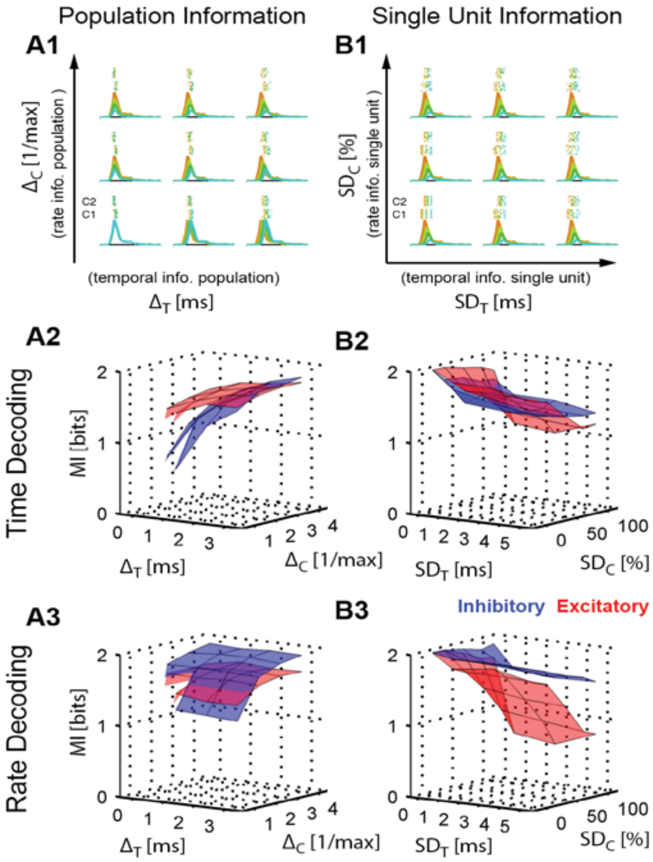

Figure 5.5. L4 population and single unit encoding selectively influence inhibitory or excitatory cell information. The stimulus encoding in L4 is a mixture of population level and single unit level. Excitatory and inhibitory cells show opposite sensitivities to these encoding dimensions in L4. (A1) Stimulus information can be encoded in differences in rate or timing on the level of the population PSTH. Different combinations of these two coding dimensions are varied, with Δ_T *(abscissa) indicating different timing for different stimuli (different colors), and* Δ_C *(ordinate) indicating different rates for different stimuli. Maximal information is achieved for high values of* Δ_T *and* Δ_C*. For each condition the population PSTHs and two example cells are shown (raster plot for 10 trials, above). Spike-times of individual neurons are Poisson-distributed given the PSTH. (A2) Decoding of first spike timing reveals a greater sensitivity of inhibitory neurons (blue) to the level of information in the L4 population response, both for time and rate information in L4. Conversely, excitatory neurons (red) are comparatively insensitive. (A3) Decoding of rate again reveals a greater sensitivity of inhibitory neurons to the level of information in the L4 response for different rates. Since we did not limit the time window of analysis, neither of the cell types is influenced by variation in time, since they leave the rate information unchanged. (B1) Stimulus information can also be encoded in the reliable discharge of single units. We modulated the reliability by introducing variability in timing (*SD_T*) or variability in count (*SD_C*) independent of each other. Maximal information is achieved for* SD_T *and* SD_C *both close to 0, i.e. perfectly reliable responses. Colors and raster plots as in A1. (B2) Decoding of first spike timing reveals a great sensitivity of excitatory neurons to the L4 information in single unit responses for both variability in time (*SD_T*) and rate (*SD_C*). (B3) Decoding of rate shows a very strong sensitivity of excitatory neurons on the single unit information. Conversely, inhibitory neurons exhibit almost no sensitivity to single unit information in L4, and are thus dominated by L4 population information.*

Information recovery occurs rapidly within a few milliseconds

Processing in the sensory cortices is under severe temporal constraints, especially in S1 where the sensory part is tightly integrated with the motor output for the purpose of precise and adaptive whisking control (Voigts et al. 2008, Voigts et al. 2015). The state of processing at a given time can be estimated by computing the mutual information over limited time windows, which progressively include a larger part of the neural response (Figure 5.6A, all excitatory and inhibitory neurons separated for a single trial). In combination with varying the group size, we can thus obtain a ‘neurotemporal’ overview over the process of information availability in L2/3 as a function of neuron type.

We consider again three different representations of the L4 input, ‘Rate + Poisson’, ‘Rate

+ Trial Reliability’ and ‘No Rate + Trial Reliability’ encoding of stimulus identity (Figure 5.6B-D). In the ‘Rate + Poisson’ case the mutual information begins to increase with interneurons leading over excitatory neurons (Figure 5.6B, left, group size = 10 cells) around 12-14ms after stimulus onset (in L4). The inhibitory neurons reach maximal stimulus information after about 25ms, whereas the excitatory neurons take until about 30ms, and do not achieve full stimulus information. Groups of inhibitory neurons encode more information than excitatory neurons, independent of time relative to stimulus onset and almost independent of group size (Figure 5.6B, right).

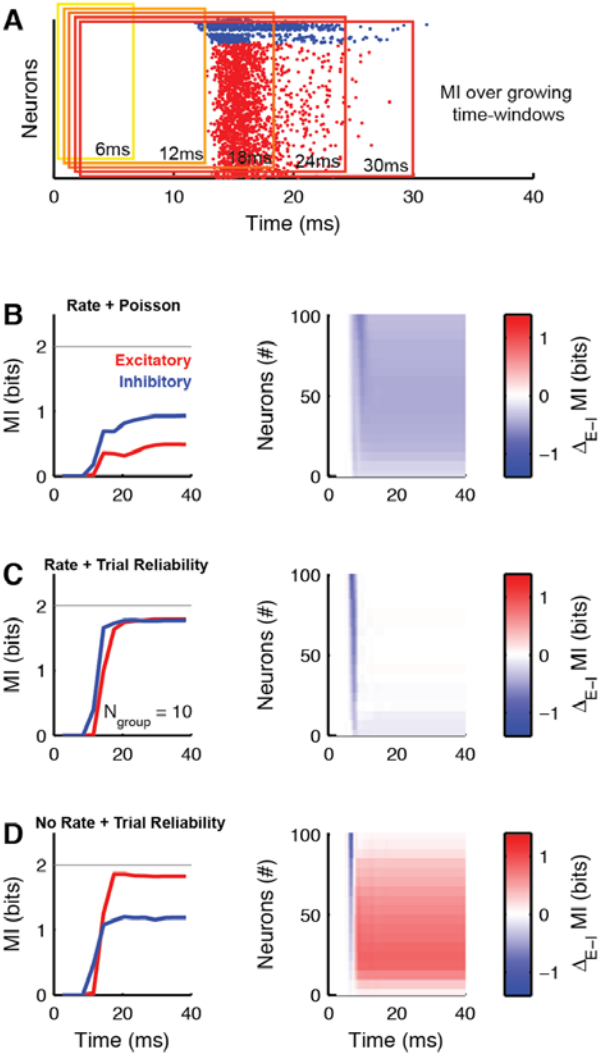

Figure 5.6. Neuronal information recovery completes within <20ms after stimulus onset. (A) Sensory processing operates under strict time-constraints, given by the sensory-motor loop. We analyze the time-scales of information recovery by computing the MI over time-windows of increasing length (6-30ms at 3ms steps), here for the first spike time code. (B) For the 'Rate + Poisson' encoding in L4, both excitatory (red) and inhibitory (blue) neurons in L2/3 reach their respective maximal information (here shown for groups sizes of 10 cells) around 25-30ms after stimulus onset. L2/3 inhibitory neurons (blue) encode more information, independent of peri-stimulus time and group size (right). The color code shows the different in MI between the excitatory and inhibitory groups, with red for larger MI in the excitatory, and blue for greater MI for the inhibitory neurons. (C) For the 'Rate + Trial Reliability' condition in L4, the information content of the two populations is quite similar (left) with a slight advantage for the inhibitory neurons at early times, but no dependence on group size (right). (D) In the 'No Rate - Trial Reliability'' case, divergence between information content only begins around 12ms after stimulus onset, after which excitatory neurons achieve a substantial coding advantage, especially for smaller group sizes.

Finally, for the 'Rate + Trial Reliability' encoding condition in L4, the difference in the information content between cell types in L2/3 is small, with inhibitory neurons carrying slightly more information at early peri-stimulus times and group-sizes (Figure 5.6C, right). The difference in onset timing renders the information content higher only during the initial 1-2ms after response onset, due to the earlier response times of the inhibitory neurons (Figure 5.6C, left).

In the 'No Rate + Trial Reliability' condition the time when information content increases are very comparable for excitatory and inhibitory neurons, however, after a few ms, excitatory neurons prevail over inhibitory neurons. This advantage stays preserved over time, whereas the difference in information content is strongly reduced as a function of group size, with inhibitory neurons, eventually catching up to excitatory neurons (Figure 5.6D, right).

In summary, the representation of stimulus information is rapidly completed within only a few milliseconds (3-5) after response onset, while the principal encoders are determined by the encoding type in L4 (corresponding potentially to different stimulus paradigms), and not much on peri-stimulus time. As before, pure rate coding on the level of L4 is identified as an insufficient coding strategy.

Discussion

Here we showed that although the PSP-to-action potential transformation results in significant information loss about the stimulus, local networks overcome this loss by integrating residual information across a small, experimentally tractable, number of neurons. Therefore, the somatic PSPs received by a single neuron contain nearly complete information about the stimulus, even several synapses away from the sensory periphery. The efficiency in information recovery is determined by a conjunction between encoding scheme, neuronal class and decoding strategy. Excitatory and inhibitory cells take complementary roles when decoding single unit and population information, respectively.

Contribution of temporal coding in somatosensory cortex

Encoding information in fine temporal bins can enrich the information content of neural activity over coarser average rates (Rieke et al. 1999). Previous work has pointed to the presence of temporally encoded information in the somatosensory (Petersen et al. 2001, Alenda et al. 2010, Panzeri & Diamond 2010) and other sensory cortices (Kayser et al. 2010, Kayser et al. 2012). Consistently we find the majority of information in the PSP to be encoded in its timing. However, spike initiation timing is substantially more variable, such that only little of the information in the PSP is transferred to the spike (Figure 5.2). The amount of information loss could even be more substantial *in vivo* in the presence of ongoing activity. On the population level, we find temporal information to also be highly relevant during information recovery. Information content in the population asymptotes within 5 ms after response onset, consistent with the time-scales of neuronal read-out in whisker cortex estimated before (5-8 ms, Stüttgen & Schwarz 2010).

The temporal information described above can be fully characterized by single neuron variations in rate, and hence does not include more specialized temporal codes, such as patterns of interspike intervals. Due to the sparse response nature of excitatory neurons to simple stimulations, such a temporal code could only exist in the interspike intervals of inhibitory neurons or spike-patterns across multiple (excitatory or inhibitory) neurons. The term temporal code is still appropriate, since the time scales of the response are not only reflecting dynamics in the stimulus, but correspond to intrinsic computations of the neural network (Nemenman et al. 2011).

For the present dataset, mutual information was computed with responses aligned to stimulus onset. Recent work by Panzeri and colleagues (Panzeri et al. 2010, Panzeri & Diamond 2010) have pointed out that this reference time is not necessarily available to a decoder in S1. How would a change to an internal reference time, such as the efference copy of the whisking signal (Crochet & Petersen 2006, Poulet & Petersen 2008, Crochet et al. 2011) or a populaton-based timing (e.g. the CSR event defined by Panzeri & Diamond 2010), affect the present results? Assuming that the population response can be approximated by a set of individually recorded neurons (as in Petersen & Diamond 2010), the influence of such an intrinsic reference on our results would be only minor, since the relative timing - and thus the relative trial-to-trial variability in timing - would be the same as in the stimulus locked case. Hence, the information content would not be modified. If on the other hand, synchronization between neural groups occurs, results could be significantly influenced, since then variability could be transferred from spikes to PSPs (in which case the alignment would be based on the near-synchronous CSR). According to Petersen et al. (2001), covariability, measured as noise correlation, was assessed to be ~0.1, and subsequent studies have found even lower values (Renart et al. 2010), suggesting that stimulus-independent synchronization is not substantial.

Implications of high information availability for neural codes

Neural activity of excitatory neurons in layer 2/3 is generally considered to be more sparse than in Layer 4 (see Barth & Poulet 2012 for review, although the evidence is not yet fully conclusive). This sparsity of activation has been linked to higher selectivity of encoding, in terms of fewer, more specific features represented per neuron. This increased selectivity could be the reason for the information loss during the transformation of PSPs to spikes - observed presently - which discards some part of the information, in favor of another part. However, as shown presently as well, the entire stimulus information persists to be encoded in a distributed fashion. Importantly from a decoding perspective, the information can be recovered already on the basis of a small subset of neurons (~10-20, if single unit information is present) on short time-scales (~5ms relative to response onset).

While the residual presence of this information may not be a surprise, it is remarkable that the intrinsic variability of the network (contributed primarily by synaptic failures) does not outgrow the information, as quantified here using mutual information. The distributed persistence of complete stimulus information could provide a solution to one of the classical problems of neural encoding: the compatibility between a specific feature representation and the context of the entire stimulus space. Concretely, a readout neuron of L2/3 in S1 may have dominantly access to neurons selective for one type of feature, but in addition a wide range of inputs from a random subset of the population. It could thus evaluate the dominant feature in relation to the entire stimulus representation. This becomes especially relevant in the case of multiple concurrent stimulations on different whiskers, corresponding to the natural situation an animal is exposed to during active exploration. Multiplexed codes have been discussed recently in the context of local field oscillations (Alenda et al., 2010), and the present combined presence of selective and general information may provide an additional example of multiplexing.

An important question for future in-vivo imaging studies will be, whether this complete information representation persists if larger stimulus sets/spaces are considered. Due to the requirements of accurate estimation of mutual information, we had to restrict the stimulus space to four stimuli in the context of whole-cell recordings (leading to ~300 trials per recorded cell). Note, however, that even under these conditions, trial-to-trial variability could have prevailed and prevented complete information representation on the single neuron and population level.

The present results can only provide a lower bound on the available information, since not all possible codes were explored and the decoding step between stimulus and response renders all results lower bounds (Quian Quiroga & Panzeri 2009). In contrast to a previous study in the auditory cortex, we find more complex decoding methods to provide improved decoding quality and hence higher mutual information. Concretely, support vector machine decoding with radial basis functions provided superior performance (94%) than either diagonal linear (77%), linear (79%), or quadratic (80%). In order for the neural system to achieve this quality of decoding, it would, however, have readout mechanisms, which use decoding strategies beyond linear or quadratic combinations.

Predictions for cell-type specific coding strategies

The cortical population of neurons is composed of various cell-types, which differ in their morphology, location and physiology (Oberländer et al. 2012). These differences suggest different roles in information processing, some of which have recently been elegantly elucidated (Hofer et al. 2011). Coarsely, on the level of their firing patterns, inhibitory neurons can be distinguished from excitatory neurons, by more dense responses, based on a greater convergence of connections (reviewed in Harris & Mrsic Flogel, 2013). The connectivity in the present model was set in precise accordance with the latest results from the literature from identified, pairwise recordings (see Methods for detailed references), and consequently recreates these differences in firing behavior. Going beyond previous work, we find the coding balance to lean to either cell class, depending on the encoding strategy used in L4.

We explored these encoding strategies in L4, finding that excitatory neurons more effectively convey information encoded in L4 single units, requiring a level of reliability in L4 beyond Poisson-spiking (Figure 5.6B). Conversely, inhibitory neurons are more effective in carrying L4 population rate information (Figure 5.6A). Hence, together, excitatory and inhibitory neurons make effective use of the combined information in population rate and single units responses in L4.

The encoding in L4 is likely not unique, but depends on the stimulus condition: Many stimuli will induce time-varying population rates, which distinguish them from other stimuli. However, exceptions exist, such as the comparison of different texture examples, which have only small differences in population rate, and differ more in their fine-structure. On the other hand, temporally structured inputs (e.g. many natural stimuli) lead to stronger time locking between neurons in L4 (Amarasingham et al. 2012, Litwin-Kumar & Doiron 2012). Based on our results, excitatory and inhibitory neurons could focus on individual and population information to optimize the availability of stimulus information. Since long-range projections of inhibitory neurons are rare (Thomson & Lamy, 2007), the information content in the spiking of the inhibitory neurons is likely to be most relevant in determining local processing. It is challenging to address this hypothesis, since the inhibitory neurons cannot be removed from the network without influencing the overall dynamics.

In summary, timing of spikes consistently appears to play an important role as a coding dimension for stimulus information both on the level of individual neurons as well as the recovery of information on the population level. Whether it is used for a similar purpose in the neural system as a whole will have to be addressed using in vivo population recordings in tasks such as object localization by whisker touch (Celikel & Sakmann 2007), where timing of contact is likely to play an important role in relation to the whisking cycle.

References

Adibi, M., Clifford, C. W. G., & Arabzadeh, E. (2013). Informational basis of sensory adaptation: entropy and single-spike efficiency in rat barrel cortex. *The Journal of neuroscience, 33,* 14921–6.

Adibi, M., McDonald, J. S., Clifford, C. W. G., & Arabzadeh, E. (2014). Population Decoding in Rat Barrel Cortex: Optimizing the Linear Readout of Correlated Population Responses. *PLoS Computational Biology, 10.*

Alenda, A., Molano-Mazón, M., Panzeri, S., & Maravall, M. (2010). Sensory input drives multiple intracellular information streams in somatosensory cortex. *The Journal of neuroscience, 30,* 10872–10884.

Allen, C. B., Celikel, T., & Feldman, D. E. (2003). Long-term depression induced by sensory deprivation during cortical map plasticity in vivo. *Nature neuroscience, 6,* 291–299.

Arabzadeh, E., Panzeri, S., & Diamond, M. E. (2004). Whisker vibration information carried by rat barrel cortex neurons. *The Journal of neuroscience, 24,* 6011–6020.

Arabzadeh, E., Panzeri, S., & Diamond, M. E. (2006). Deciphering the spike train of a sensory neuron: counts and temporal patterns in the rat whisker pathway. *The Journal of neuroscience, 26,* 9216–9226.

Avermann, M., Tomm, C., Mateo, C., Gerstner, W., & Petersen, C. C. H. (2012). Microcircuits of excitatory and inhibitory neurons in layer 2/3 of mouse barrel cortex. *Journal of Neurophysiology*.

Barth, A. L., & Poulet, J. F. A. (2012). Experimental evidence for sparse firing in the neocortex. *Trends in Neurosciences.*

Blatow, M., Rozov, A., Katona, I., Hormuzdi, S. G., Meyer, A. H., Whittington, M. A., … Monyer, H. (2003). A novel network of multipolar bursting interneurons generates theta frequency oscillations in neocortex. *Neuron, 38,* 805–817.

Brecht, M., Roth, A., & Sakmann, B. (2003). Dynamic receptive fields of reconstructed pyramidal cells in layers 3 and 2 of rat somatosensory barrel cortex. *The Journal of physiology, 553,* 243–265.

Celikel, T., & Sakmann, B. (2007). Sensory integration across space and in time for decision making in the somatosensory system of rodents. *Proceedings of the National Academy of Sciences of the United States of America*, *104*, 1395–1400.

Celikel, T., Szostak, V. A., & Feldman, D. E. (2004). Modulation of spike timing by sensory deprivation during induction of cortical map plasticity. *Nature neuroscience*, *7*, 534–541.

Dayan, P., & Abbott, L. F. (2001). *Theoretical Neuroscience: Computational and Mathematical Modeling of Neural Systems*.(p. 480).

De Kock, C. P. J., Bruno, R. M., Spors, H., & Sakmann, B. (2007). Layer- and cell-type-specific suprathreshold stimulus representation in rat primary somatosensory cortex. *The Journal of Physiology*, *581*, 139–54.

De Ruyter van Steveninck, R. R., Lewen, G. D., Strong, S. P., Koberle, R., & Bialek, W. (1997). Reproducibility and variability in neural spike trains. *Science*, *275*, 1805–1808.

Destexhe, A., Rudolph, M., & Paré, D. (2003). The high-conductance state of neocortical neurons in vivo. *Nature Reviews Neuroscience*, *4*, 739–751.

Feldmeyer, D., Lübke, J., & Sakmann, B. (2006). Efficacy and connectivity of intracolumnar pairs of layer 2/3 pyramidal cells in the barrel cortex of juvenile rats. *The Journal of physiology*, *575*, 583–602.

Feldmeyer, D., Lübke, J., Silver, R. A., & Sakmann, B. (2002). Synaptic connections between layer 4 spiny neurone-layer 2/3 pyramidal cell pairs in juvenile rat barrel cortex: physiology and anatomy of interlaminar signalling within a cortical column. *The Journal of physiology*, *538*, 803–822.

Finnerty, G. T., Roberts, L. S., & Connors, B. W. (1999). Sensory experience modifies the short-term dynamics of neocortical synapses. *Nature*, *400*, 367–371.

Ghazanfar, A. A., Stambaugh, C. R., & Nicolelis, M. A. (2000). Encoding of tactile stimulus location by somatosensory thalamocortical ensembles. *The Journal of neuroscience*, *20*, 3761–75.

Helmstaedter, M., Staiger, J. F., Sakmann, B., & Feldmeyer, D. (2008). Efficient recruitment of layer 2/3 interneurons by layer 4 input in single columns of rat somatosensory cortex. *The Journal of neuroscience*, *28*, 8273–8284.

Holmgren, C., Harkany, T., Svennenfors, B., & Zilberter, Y. (2003). Pyramidal cell communication within local networks in layer 2/3 of rat neocortex. *The Journal of physiology*, *551*, 139–153.

Ince, R. A. A., Senatore, R., Arabzadeh, E., Montani, F., Diamond, M. E., & Panzeri, S. (2010). Information-theoretic methods for studying population codes. *Neural Networks*, *23*, 713–727.

Izhikevich, E. M. (2004). Which model to use for cortical spiking neurons? *IEEE transactions on neural networks / a publication of the IEEE Neural Networks Council*, *15*, 1063–1070.

Keller, A., & Carlson, G. C. (1999). Neonatal whisker clipping alters intracortical, but not thalamocortical projections, in rat barrel cortex. *The Journal of comparative neurology*, *412*, 83–94.

Magri, C., Whittingstall, K., Singh, V., Logothetis, N. K., & Panzeri, S. (2009). A toolbox for the fast information analysis of multiple-site LFP, EEG and spike train recordings. *BMC neuroscience*, *10*, 81.

Maravall, M., Petersen, R. S., Fairhall, A. L., Arabzadeh, E., & Diamond, M. E. (2007). Shifts in coding properties and maintenance of information transmission during adaptation in barrel cortex. *PLoS Biology*, *5*, 0323–0334.

Margrie, T. W., Brecht, M., & Sakmann, B. (2002). In vivo, low-resistance, whole-cell recordings from neurons in the anaesthetized and awake mammalian brain. *European journal of physiology*, *444*, 491–498.

Montani, F., Ince, R. A. A., Senatore, R., Arabzadeh, E., Diamond, M. E., & Panzeri, S. (2009). The impact of high-order interactions on the rate of synchronous discharge and information transmission in somatosensory cortex. *Philosophical transactions. Series A, Mathematical, physical, and engineering sciences*, *367*, 3297–3310.

Nemenman, I., Bialek, W., & de Ruyter van Steveninck, R. (2004). Entropy and information in neural spike trains: progress on the sampling problem. *Physical review. E, Statistical, nonlinear, and soft matter physics*, *69*, 056111.

Panzeri, S., Ince, R. a a, Diamond, M. E., & Kayser, C. (2014). Reading spike timing without a clock: intrinsic decoding of spike trains. *Philosophical transactions of the Royal Society of London. Series B, Biological sciences*, *369*, 20120467.

Panzeri, S., Petersen, R. S., Schultz, S. R., Lebedev, M., & Diamond, M. E. (2001). The role of spike timing in the coding of stimulus location in rat somatosensory cortex. *Neuron*, *29*, 769–777.

Panzeri, S., Petroni, F., Petersen, R. S., & Diamond, M. E. (2003). Decoding neuronal population activity in rat somatosensory cortex: role of columnar organization. *Cerebral Cortex*, *13*, 45–52.

Petersen, R. S., Panzeri, S., & Diamond, M. E. (2001). Population coding of stimulus location in rat somatosensory cortex. *Neuron*, *32*, 503–514.

Pouget, A., & Snyder, L. H. (2000). Computational approaches to sensorimotor transformations. *Nature neuroscience*, *3 Suppl*, 1192–1198.

Quian Quiroga, R., & Panzeri, S. (2009). Extracting information from neuronal populations: information theory and decoding approaches. *Nature Reviews Neuroscience*, *10*, 173–185.

Reich, D. S., Mechler, F., & Victor, J. D. (2001). Formal and attribute-specific information in primary visual cortex. *Journal of neurophysiology*, *85*, 305–318.

Rieke, F., Warland, D., De Ruyter Van Steveninck, R., & Bialek, W. (1997). *Spikes: Exploring the Neural Code*. *Computational Neuroscience* (Vol. 20, p. xvi, 395 p.).

Sachidhanandam, S., Sreenivasan, V., Kyriakatos, A., Kremer, Y., & Petersen, C. C. H. (2013). Membrane potential correlates of sensory perception in mouse barrel cortex. *Nature neuroscience*, *16*, 1671–7.

Shannon, C. E. (1948). A Mathematical Theory of Communication. *Bell System Technical Journal*, *27*, 379–423.

Stewart, R. S., Huang, C., Arnett, M. T., & Celikel, T. (2013). Spontaneous oscillations in intrinsic signals reveal the structure of cerebral vasculature. *Journal of neurophysiology*, *109*, 3094–104.

Sreenivasan, V., Karmakar, K., Rijli, F. M., & Petersen, C. C. H. (2015). Parallel pathways from motor and somatosensory cortex for controlling whisker movements in mice. *The European Journal of Neuroscience*, *41*(3), 354–67.

Thomson, A. M., & Lamy, C. (2007). Functional maps of neocortical local circuitry. *Frontiers in neuroscience*, *1*, 19–42.

Treves, A., & Panzeri, S. (1995). The Upward Bias in Measures of Information Derived from Limited Data Samples. *Neural Computation*, *7*, 399-407.

Uematsu, M., Hirai, Y., Karube, F., Ebihara, S., Kato, M., Abe, K., … Kawaguchi, Y. (2008). Quantitative chemical composition of cortical GABAergic neurons revealed in transgenic venus-expressing rats. *Cerebral Cortex*, *18*, 315–330.

Victor, J. D. (2006). Approaches to Information-Theoretic Analysis of Neural Activity. *Biological Theory*, *1*, 302-316.

Voigts, J., Sakmann, B., & Celikel, T. (2008). Unsupervised whisker tracking in unrestrained behaving animals. *Journal of Neurophysiology*, *100*(1), 504–15.

Voigts, J., Herman, D. H., & Celikel, T. (2015). Tactile object localization by anticipatory whisker motion. *Journal of Neurophysiology*, *113*(2), 620–32.

White, E. L. (1979). Thalamocortical synaptic relations: A review with emphasis on the projections of specific thalamic nuclei to the primary sensory areas of the neocortex. *Brain Research Reviews*, *1*(3), 275-311.

Wilent, W. B., & Contreras, D. (2005). Dynamics of excitation and inhibition underlying stimulus selectivity in rat somatosensory cortex. *Nature Neuroscience*, *8*, 1364–1370.

Yu, J., & Ferster, D. (2010). Membrane potential synchrony in primary visual cortex during sensory stimulation. *Neuron*, *68*, 1187–1201.

Chapter 6. CONCLUSIONS

"**What does a sensory neuron in the brain know about the world**" is one of the most fundamental questions in systems neurosciences. In the somatosensory cortex, the quantitative work of Panzeri, Petersen and colleagues (Panzeri et al 2001, Petersen et al 2001, Quian Quiroga and Panzeri 2009) have originally shown that spiking activity of individual (or pairs of) cortical neurons is minimally informative about the world these sensory neurons are tuned to encode (Panzeri et al 2001, Petersen et al 2001, Bale & Petersen 2009). In this thesis, using *in vitro* and *in vivo* whole cell-recordings, neural network simulations (after having reconstructed the somatosensory cortical columns *in silico*) and Shannon mutual information calculations, we found that somatosensory cortical neurons surprisingly carry complete information about the stimulus location in the periphery even four synapses away from the mechanoreceptors, but *only* in their evoked subthreshold responses. This sensory information in the somatic EPSP is lost when the same neuron generates action potential. Interestingly local networks can recover the lost information efficiently and rapidly, i.e in <~20 ms, using action potentials of experimentally tractable number of local neurons. Not every neuron contributes to information recovery equally; while inhibitory neurons readily decode the rate information in the presynaptic pool of neurons, excitatory neurons effectively decode the timing information in single neurons.

These results suggest a novel theory of somatosensory information processing along neural circuits and show that as the sensory information is transferred from one loci to another (let it be a subcortical nucleus or a cortical layer) the circuits reconstruct the stimulus with high fidelity, thus remaining close to the general bound imposed by the Information Processing Inequality. On the contrary to the traditional model, which argues degradation of information as the information is transferred from one locus to another, this model has the advantage that lossless information representation can be achieved along the sensory path. This new model of sensory processing has powerful features that can also provide a mechanistic explanation to a plethora of experimental observations (e.g. Arenz et al., 2008; Houweling & Brecht, 2008; Petersen & Crochet, 2013; Sachidhanandam et al., 2013) while providing support to the emerging field of lossless information processing in cerebral and cerebellar circuits (Billings et al, 2014).

Multiplexed sensing

In a network that consists of multiple circuit components, information flow is dictated by the integration properties of each node, channel capacity and the network connectivity. Besides the complementary functions that they play in integration of information in individual neurons, excitatory and inhibitory neurons are fundamentally different in all aspects of the network formations (see Chapter 1); Sensory evoked spiking activity in interneurons is dense (as opposed to sparse), more reliable and less selective compared to sensory representations of excitatory neurons. This difference is partially due to higher excitability in interneurons, as some interneuron populations have comparable (to excitatory neurons) subthreshold tuning (Bruno & Simons 2002, Cardin et al 2007, Wu et al 2008, Nowak et al 2008), and cannot be generalized across all different subclasses of inhibitory neurons. PV+ interneurons, for examples, have broad receptive fields with generally show strong, unselective and short latency response to stimulus compared to SST+ interneurons; While SST+ interneurons show weak, more selective and delayed response in the visual cortex (Ma et al 2010), in barrel cortex they are inhibited by whisker contacts (Gentet et al 2012).

Given the fundamental differences in network organization and the nature of sensory representations by excitatory and inhibitory neurons, it is not surprising that not every neuron contributes to information recovery equally, as shown in Chapter 5. While inhibitory neurons readily decode the rate information in the presynaptic pool of neurons, excitatory neurons effectively decode the timing information in single neurons. This differential coding suggests that sensory circuits might employ a multiplexed coding schema for representing information (Figure 6.1).

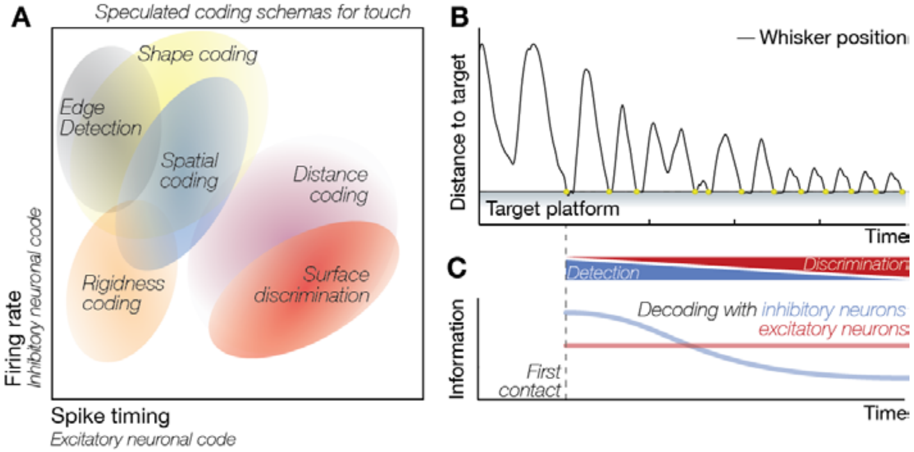

Figure 6.1. Multiplexed coding of touch. See text for details.

Multiplexed sensing suggests that two (or more) information bearing channels (in this case excitatory and inhibitory neurons jointly represent information. Given the information content across the excitatory and inhibitory neural populations (see Chapter 5), we speculate that distinct tactile features are encoded as excitatory and inhibitory neurons differentially vary the rate and timing of spiking during information encoding (Figure 6.1A). If an animal were to use its whiskers to locate a tactile target in space for example (see Celikel & Sakmann 2007), this model predicts that, inhibitory neurons would carry the largest amount of information during the first contact as the animal detects the edge of the tactile target. The information content of each information-bearing channel is temporally constrained as the animal continues to explore its immediate environment, and make additional whisker contacts with the tactile target (Figure 6.1B; Voigts et al 2008, Voigts et al 2015) presumably to predict object distance and extract additional surface feature information about the target. With the change in pattern of whisking, the sensory history and the statistics of the local network activity relative information in the excitatory will eventually dominate (Figure 6.1C).

References

Arenz, A., Silver, R. A., Schaefer, A. T., & Margrie, T. W. (2008). The contribution of single synapses to sensory representation in vivo. *Science (New York, N.Y.)*, *321*(5891), 977–80.

Bale, M. R., & Petersen, R. S. (2009). Transformation in the neural code for whisker deflection direction along the lemniscal pathway. *Journal of Neurophysiology*, *102*(5), 2771–80.

Billings, G., Piasini, E., Lőrincz, A., Nusser, Z., & Silver, R. A. (2014). Network structure within the cerebellar input layer enables lossless sparse encoding. *Neuron*, *83*(4), 960–74.

Bruno, R. M., & Simons, D. J. (2002). Feedforward mechanisms of excitatory and inhibitory cortical receptive fields. *The Journal of Neuroscience : The Official Journal of the Society for Neuroscience*, *22*(24), 10966–75.

Cardin, J. A., Palmer, L. A., & Contreras, D. (2007). Stimulus feature selectivity in excitatory and inhibitory neurons in primary visual cortex. *The Journal of Neuroscience : The Official Journal of the Society for Neuroscience*, *27*(39), 10333–44.

Celikel, T., & Sakmann, B. (2007). Sensory integration across space and in time for decision making in the somatosensory system of rodents. *Proceedings of the National Academy of Sciences of the United States of America*, *104*(4), 1395–400.

Gentet, L. J., Kremer, Y., Taniguchi, H., Huang, Z. J., Staiger, J. F., & Petersen, C. C. H. (2012). Unique functional properties of somatostatin-expressing GABAergic neurons in mouse barrel cortex. *Nature Neuroscience*, *15*(4), 607–12.

Houweling, A. R., & Brecht, M. (2008). Behavioural report of single neuron stimulation in somatosensory cortex. *Nature*, *451*(7174), 65–8.

Ma, W., Liu, B., Li, Y., Huang, Z. J., Zhang, L. I., & Tao, H. W. (2010). Visual representations by cortical somatostatin inhibitory neurons--selective but with weak and delayed responses. *The Journal of Neuroscience : The Official Journal of the Society for Neuroscience*, *30*(43), 14371–9.

Nowak, L. G., Sanchez-Vives, M. V, & McCormick, D. A. (2008). Lack of orientation and direction selectivity in a subgroup of fast-spiking inhibitory interneurons: cellular and synaptic mechanisms and comparison with other electrophysiological cell types. *Cerebral*

Cortex (New York, N.Y. : 1991), *18*(5), 1058–78.

Panzeri, S., Petersen, R. S., Schultz, S. R., Lebedev, M., & Diamond, M. E. (2001). The role of spike timing in the coding of stimulus location in rat somatosensory cortex. *Neuron*, *29*(3), 769–77.

Petersen, C. C. H., & Crochet, S. (2013). Synaptic computation and sensory processing in neocortical layer 2/3. *Neuron*, *78*(1), 28–48.

Petersen, R. S., Panzeri, S., & Diamond, M. E. (2001). Population coding of stimulus location in rat somatosensory cortex. *Neuron*, *32*, 503–514.

Quian Quiroga, R., & Panzeri, S. (2009). Extracting information from neuronal populations: information theory and decoding approaches. *Nature Reviews. Neuroscience*, *10*(3), 173–85.

Sachidhanandam, S., Sreenivasan, V., Kyriakatos, A., Kremer, Y., & Petersen, C. C. H. (2013). Membrane potential correlates of sensory perception in mouse barrel cortex. *Nature Neuroscience*, *16*(11), 1671–7.

Voigts, J., Sakmann, B., & Celikel, T. (2008). Unsupervised whisker tracking in unrestrained behaving animals. *Journal of Neurophysiology*, *100*(1), 504–15.

Voigts, J., Herman, D. H., & Celikel, T. (2015). Tactile object localization by anticipatory whisker motion. *Journal of Neurophysiology*, *113*(2), 620–32.

Wu, G. K., Arbuckle, R., Liu, B.-H., Tao, H. W., & Zhang, L. I. (2008). Lateral sharpening of cortical frequency tuning by approximately balanced inhibition. *Neuron*, *58*(1), 132–43.

Summary

How the brain processes the information is one of the central questions in system neuroscience. Just like humans use their fingers, rodents use an array of sensory hairs (whiskers) to explore their local environment and gather haptic information to guide their behavior; And just like fingers, whiskers are represented topographically as somatosensory and motor maps in the neocortex. Sensory information embodied in whisker contacts with a tactile target propagates along the sensorimotor axis via action potentials (APs); the rate and timing of APs have been shown to carry information about the sensory world throughout cortical and subcortical networks, and are believed to be the neural basis of sensory representations in the brain. As a result, in the primary somatosensory cortex (S1) of rodents, neurons encode egocentric localization of the tactile target they are exploring by varying the rate and/or the timing of APs.

Information in AP rate and timing is not necessarily redundant. Single unit recordings in S1 suggest that while timing of an AP is more informative than its rate for determining the position of the object in space, information in AP rate gradually increases following whisker contact. Furthermore changes in relative AP timing, but not in its rate, alter the efficacy of monosynaptic connections in the very same somatosensory network. Despite the importance of modulated changes in AP rate and timing dynamics for sensory processing and reorganization of neural circuits, network mechanisms of AP rate and timing modulation are not completely understood. This thesis addresses the circuit mechanisms of touch representations during spatial localization (i.e. which whisker is in contact with the tactile target), and specifically addresses the nature of intra- and interneuronal information transfer along the somatosensory axis to mechanistically determine how information is aggregated, transferred and recovered using a combination of experimental (i.e. functional imaging of whisker evoked activity, whole-cell recordings *in vitro* and *in vivo*, and cortical network reconstructions in single soma resolution with multi-channel serial mosaic scanning) and computational (i.e. construction of a biologically realistic computational model of the primary somatosensory cortex and spiking network analysis) approaches.

Functional imaging of intrinsic signals allows minimally invasive spatiotemporal mapping of stimulus representations in the cortex; but representations are often corrupted by stimulus-independent spatial artifacts, especially those originating from the blood vessels. In **Chapter 2** of the thesis we present novel algorithms for unsupervised identification of cerebral vascularization, allowing blind separation of stimulus representations from noise, and detail how to locate cortical region of interest for subsequent electrophysiological experiments. Application of these methods for removal

of stimulus-independent changes in reflectance permits isolation of stimulus-evoked representations even if the representation spatially overlaps with blood vessels. The algorithms can further be expanded to extract temporal information on blood flow, monitoring of revascularization following a focal stroke, and distinguish arterioles from venules and parenchyma.

To understand how neural circuits perform their functions, it is necessary to quantify the interactions among each individual elements of the circuit, i.e. neurons of different types. Thanks to the advances in high-density microelectrode array recordings and two-photon imaging it is now possible to observe tens to hundreds of neurons simultaneously in action. However, experimental study of every neuron in a functionally relevant circuit is still several decades away. Thus, establishing a biologically plausible and computationally efficient model of neural circuits has an outstanding potential to greatly advance our understanding on the neuronal basis of circuit behavior. In **chapter 3** of the thesis I present such a model of the primary somatosensory cortex (S1) of the mouse. The location (i.e. columnar and laminar) and identity (i.e. excitatory vs inhibitory, including subclassification of the major inhibitory subclasses) of the nodes in this topological network of the canonical cortical column is based on cell body reconstructions of the somatosensory cortex using multifluorescence serial confocal microscopy. The statistics and efficacy of functional connectivity between pairs of cells across and within Layer (L) 4 and L2/3 are modeled after previously published data. The mathematical model of individual neurons was based on the quadratic model neuron originally introduced by Izhikevich with an adaptive spike threshold which adapts to the rate of ongoing network activity impinging onto the postsynaptic neuron (see also Chapter 4). Simulation of whisker touch representations in this network showed that the *in silico* network predicts the population response of touch representations in the barrel cortex *in vivo* while providing new insights on the role of membrane states in gating, otherwise gain-modulation of sensory representations in a layer, column and input specific manner.

The spike threshold plays an important role on governing information processing at single neuron level by gating the information transformation from synaptic inputs (i.e. the information the neuron receives) to spikes (i.e. the information the neuron transmits). This spike threshold is not fixed, as recently it has been demonstrated that the subthreshold membrane state influences the effective spike threshold. However the consequences of the spike threshold adaptation on neural computation are not well understood. In **Chapter 4** of the thesis we address this question using neural simulations and whole cell intracellular recordings in combination with information theoretic analysis. The results indicate that the adaptive spike threshold reduces information loss during intracellular information transfer, improves stimulus discriminability and ensures robust decoding across membrane states in a regime of highly correlated inputs, similar to those seen in sensory nuclei during the encoding of sensory information.

In **chapter 5** of the thesis we study the principles of information transfer in rodent somatosensory cortex, using both electrophysiological and computational methods. Using whole-cell recordings in the barrel cortex, we show that although significant amount of information about the stimulus is lost during the PSP-to-action potential transformation, local networks overcome this loss by integrating residual information across a small, experimentally tractable, number of neurons. As a consequence, the somatic PSPs received by a single neuron contain nearly complete information about the stimulus, even several synapses away from the sensory periphery. Using the computational model developed in Chapter 3, we further show that L4 coding properties are crucial for optimization of information recovery in L2/3 as excitatory and inhibitory neurons act as distinct information bearing channels. While excitatory neurons are more robust on recovering information from single neuron firing patterns, inhibitory neuronal decoding is primarily based on population firing rates in L4. Thus, while information processing in primary sensory cortex appears to be highly lossy at single neuron level, the neural network could still reconstruct the full information by combining spikes from multiple complementary information bearing channels

Based on the data obtained, in **chapter 6** of the thesis we propose a model of early somatosensory information processing in rodent, in which the sensory information is transferred from one loci to another with high fidelity even though there is a significant amount of information loss when a single neuron converts the information it received (i.e. the information in PSPs) to the information it transmits (i.e. the information in spikes). Furthermore, different sub-circuits in the somatosensory neural network carry different but complementary information about the sensory feature space, thus could differentially contribute to the sensory processing depending on which behavior task the animal is currently engaging. Our results could potentially guide the development of prosthetic devices.

Acknowledgement

This thesis work would not be possible with the help of many people. First I would like to thank my parents for their understandings, encouragement and support. The Ph.D study was long and sometimes frustrating; it is their warm support that carried me through. The same goes to Xida; I wish I could spend more time with you.

I also would like to thank my supervisor, Tansu Celikel. First of all thank you for giving me the opportunity to enter your lab as a Ph.D student. It was an exciting adventure, with lots of new knowledge and techniques to pick up, lots of fun people to meet, and a great atmosphere to enjoy the science as well as the break times. Thanks for the help and advice, and also thanks for letting us win (sometimes) at the dart game – someday we will build a robot and let it compete with you. Also thanks for the beer and coffee – the beer was very good, however I am sorry to say that I have not been very impressed by the coffee yet. Maybe simply the coffee just not fit to my genetics? Especially, thanks for all the enthusiastic encouragements and support– I tend to look from a somewhat pessimistic side on many things, and your kind words mean a lot to me.

Bernhard, thanks for all the help and advice – both on works and on others. This thesis will not be at its current stage without you. Working with you is also extremely fun, which partially results from your “nerdiness” in my opinion. However you will never admit it, am I correct? I learned a lot and could still learn a lot from you, and I am very grateful that I could have you both as my co-supervisor and a friend. The only complaint I have is that your taste of tea is still very wrong – but I guess it is ok as long as it is more efficient right?

People from Los Angleles, Thank you all for the fun and fulfilling time we spent together. Florian, you have always been like a big brother to me, and I hope very thing goes well with you. Dr. Judith Hirsch, Dr. Bartlett Mel, and Dr. Norberto Grzywacz, thank you for your critical and invaluable suggestions and advices both on my project and my future plan. Dr. Aaron McGee, thank you for providing the finicial support during my transition period. Dave, Megan, and Jean, it was very fun working together, and your drastically different characters and views on many things made the lab time extremely interesting. Especially Dave, thank you so much for helping me start the very different and sometimes difficult life in the U.S., as well as the fun and sometimes very deep discussions and debatings. Hope you have not forgetten all the Chinese dishes. Wanqing, thank you for all the help and the cheerful, inspring discussions. And all the other people in the Neuroscience Graduate Program, as well as the friends in Los Angleles, thank you for making the time enjoyable and memorable.

Moving to a new country to continue the Ph.D was not easy. There are many people who offered me with great help and guidance, and without them I would be totally lost. Dr. Richard van Wezel, thank you very much for giving me the opportunity to work on the 2-photon microscope and helping me get started. Also Dr. Wim Scheenen, thank you for your technical support and insightful advices. I wish I could spend more time working on the system. Fleur, thank you for helping me with the writing as well as the many suggestions and advices. Frouwke, thanks for the hard and skilful immunostaining works, as well as the introduction to the glider club. I hope you enjoy your new job. Ron, we should go to the football game together again some time. Debbie, thank you so much for putting some order onto the otherwise (sort of) chaotic lab space, and organizing these awesome parties- hopefully you are still not afraid of the dumplings. Gea, thank you for the administrative work and help that made my life here much easier. Elisabeth, you are a true master of the confocal system, and thank you very much for your help and invaluable suggestions on my project.

My sinsere thank also goes to the wonderful fellow students, collegues and friends here in the department and at the Radboud University. It is a fun and dynamic environment with people from diverse background, and I learned from many of them on a broad spectrum of topics. It is very difficulty to write down the name of every one of them; I just would like to thank you all for the fun both in science and in life. Especially, Remi, we should go to some real Chinese tea shop together some time. And Koen and Laurens, it is great to have you to back me up at the defense. I will stop here with a piece of my favorate Chinese poems, and hope we will see each other often in the future.

海内存知己，天涯若比邻。

–When one has close friends in this world, the far ends of the heaven are like next door.

Curriculum Vitae

Chao Huang was born in Yunnan, China. He obtained the Bechelor's degree on biological science from Tinghua University, China with the study investigating the effect of magnesium on the learning and memory of rodents, under the supervision of Prof. Guosong Liu. Afterwards he started his Ph.D work in the group of Prof. Dr. Tansu Celikel at the Neuroscience Graduate Program of the University of Southern California, U.S. investigating the cellular and circuit mechanisms of touch representation in the rodent somatosensory system. He then moved to Radoud University Nijmegen, the Netherlands together with his supervisor to finish his Ph.D project.

Donders Graduate School for Cognitive Neuroscience Series

1. Van Aalderen-Smeets, S.I. (2007). *Neural dynamics of visual selection.* Maastricht University, Maastricht, the Netherlands.
2. Schoffelen, J.M. (2007). *Neuronal communication through coherence in the human motor system.* Radboud University Nijmegen, Nijmegen, the Netherlands.
3. De Lange, F.P. (2008). *Neural mechanisms of motor imagery.* Radboud University Nijmegen, Nijmegen, the Netherlands.
4. Grol, M.J. (2008). *Parieto-frontal circuitry in visuomotor control.* Utrecht University, Utrecht, the Netherlands.
5. Bauer, M. (2008). *Functional roles of rhythmic neuronal activity in the human visual and somatosensory system.* Radboud University Nijmegen, Nijmegen, the Netherlands.
6. Mazaheri, A. (2008). *The influence of ongoing oscillatory brain activity on evoked responses and behaviour.* Radboud University Nijmegen, Nijmegen, the Netherlands.
7. Hooijmans, C.R. (2008). *Impact of nutritional lipids and vascular factors in Alzheimer's disease.* Radboud University Nijmegen, Nijmegen, the Netherlands.
8. Gaszner, B. (2008). *Plastic responses to stress by the rodent urocortinergic Edinger-Westphal nucleus.* Radboud University Nijmegen, Nijmegen, the Netherlands.
9. Willems, R.M. (2009). *Neural reflections of meaning in gesture, language and action.* Radboud University Nijmegen, Nijmegen, the Netherlands.
10. Van Pelt, S. (2009). *Dynamic neural representations of human visuomotor space.* Radboud University Nijmegen, Nijmegen, the Netherlands.
11. Lommertzen, J. (2009). *Visuomotor coupling at different levels of complexity.* Radboud University Nijmegen, Nijmegen, the Netherlands.
12. Poljac, E. (2009). *Dynamics of cognitive control in task switching: Looking beyond the switch cost.* Radboud University Nijmegen, Nijmegen, the Netherlands.
13. Poser, B.A. (2009). *Techniques for BOLD and blood volume weighted fMRI.* Radboud University Nijmegen, Nijmegen, the Netherlands.
14. Baggio, G. (2009). *Semantics and the electrophysiology of meaning. Tense, aspect, event structure.* Radboud University Nijmegen, Nijmegen, the Netherlands.
15. Van Wingen, G.A. (2009). *Biological determinants of amygdala functioning.* Radboud University Nijmegen Medical Centre, Nijmegen, the Netherlands.
16. Bakker, M. (2009). *Supraspinal control of walking: Lessons from motor imagery.* Radboud University Nijmegen Medical Centre, Nijmegen, the Netherlands.
17. Aarts, E. (2009). *Resisting temptation: The role of the anterior cingulate cortex in adjusting cognitive control.* Radboud University Nijmegen, Nijmegen, the Netherlands.
18. Prinz, S. (2009). *Waterbath stunning of chickens – Effects of electrical parameters on the electroencephalogram and physical reflexes of broilers.* Radboud University Nijmegen, Nijmegen, the Netherlands.
19. Knippenberg, J.M.J. (2009). *The N150 of the Auditory Evoked Potential from the rat amygdala: In search for its functional significance.* Radboud University Nijmegen, Nijmegen, the Netherlands.
20. Dumont, G.J.H. (2009). *Cognitive and physiological effects of 3,4-methylenedioxymethamphetamine (MDMA or 'ecstasy') in combination with alcohol or cannabis in humans.* Radboud University Nijmegen, Nijmegen, the Netherlands.

21. Pijnacker, J. (2010). *Defeasible inference in autism: A behavioral and electrophysiogical approach.* Radboud University Nijmegen, Nijmegen, the Netherlands.
22. De Vrijer, M. (2010). *Multisensory integration in spatial orientation.* Radboud University Nijmegen, Nijmegen, the Netherlands.
23. Vergeer, M. (2010). *Perceptual visibility and appearance: Effects of color and form.* Radboud University Nijmegen, Nijmegen, the Netherlands.
24. Levy, J. (2010). *In cerebro unveiling unconscious mechanisms during reading.* Radboud University Nijmegen, Nijmegen, the Netherlands.
25. Treder, M. S. (2010). *Symmetry in (inter)action.* Radboud University Nijmegen, Nijmegen, the Netherlands.
26. Horlings C.G.C. (2010). *A weak balance: Balance and falls in patients with neuromuscular disorders.* Radboud University Nijmegen, Nijmegen, the Netherlands.
27. Snaphaan, L.J.A.E. (2010). *Epidemiology of post-stroke behavioural consequences.* Radboud University Nijmegen Medical Centre, Nijmegen, the Netherlands.
28. Dado – Van Beek, H.E.A. (2010). *The regulation of cerebral perfusion in patients with Alzheimer's disease.* Radboud University Nijmegen Medical Centre, Nijmegen, the Netherlands.
29. Derks, N.M. (2010). *The role of the non-preganglionic Edinger-Westphal nucleus in sex-dependent stress adaptation in rodents.* Radboud University Nijmegen, Nijmegen, the Netherlands.
30. Wyczesany, M. (2010). *Covariation of mood and brain activity. Integration of subjective self-report data with quantitative EEG measures.* Radboud University Nijmegen, Nijmegen, the Netherlands.
31. Beurze S.M. (2010). *Cortical mechanisms for reach planning.* Radboud University Nijmegen, Nijmegen, the Netherlands.
32. Van Dijk, J.P. (2010). *On the Number of Motor Units.* Radboud University Nijmegen, Nijmegen, the Netherlands.
33. Lapatki, B.G. (2010). *The Facial Musculature - Characterization at a Motor Unit Level.* Radboud University Nijmegen, Nijmegen, the Netherlands.
34. Kok, P. (2010). *Word order and verb inflection in agrammatic sentence production.* Radboud University Nijmegen, Nijmegen, the Netherlands.
35. van Elk, M. (2010). *Action semantics: Functional and neural dynamics.* Radboud University Nijmegen, Nijmegen, the Netherlands.
36. Majdandzic, J. (2010). *Cerebral mechanisms of processing action goals in self and others.* Radboud University Nijmegen, Nijmegen, the Netherlands.
37. Snijders, T.M. (2010). *More than words - Neural and genetic dynamics of syntactic unification.* Radboud University Nijmegen, Nijmegen, the Netherlands.
38. Grootens, K.P. (2010). *Cognitive dysfunction and effects of antipsychotics in schizophrenia and borderline personality disorder.* Radboud University Nijmegen Medical Centre, Nijmegen, the Netherlands.
39. Nieuwenhuis, I.L.C. (2010). *Memory consolidation: A process of integration – Converging evidence from MEG, fMRI and behavior.* Radboud University Nijmegen Medical Centre, Nijmegen, the Netherlands.
40. Menenti, L.M.E. (2010). *The right language: Differential hemispheric contributions to language production and comprehension in context.* Radboud University Nijmegen, Nijmegen, the Netherlands.

41. Van Dijk, H.P. (2010). *The state of the brain, how alpha oscillations shape behaviour and event related responses.* Radboud University Nijmegen, Nijmegen, the Netherlands.
42. Meulenbroek, O.V. (2010). *Neural correlates of episodic memory in healthy aging and Alzheimer's disease.* Radboud University Nijmegen, Nijmegen, the Netherlands.
43. Oude Nijhuis, L.B. (2010). *Modulation of human balance reactions.* Radboud University Nijmegen, Nijmegen, the Netherlands.
44. Qin, S. (2010). *Adaptive memory: Imaging medial temporal and prefrontal memory systems.* Radboud University Nijmegen, Nijmegen, the Netherlands.
45. Timmer, N.M. (2011). *The interaction of heparan sulfate proteoglycans with the amyloid protein.* Radboud University Nijmegen, Nijmegen, the Netherlands.
46. Crajé, C. (2011). *(A)typical motor planning and motor imagery.* Radboud University Nijmegen, Nijmegen, the Netherlands.
47. Van Grootel, T.J. (2011). *On the role of eye and head position in spatial localisation behaviour.* Radboud University Nijmegen, Nijmegen, the Netherlands.
48. Lamers, M.J.M. (2011). *Levels of selective attention in action planning.* Radboud University Nijmegen, Nijmegen, the Netherlands.
49. Van der Werf, J. (2011). *Cortical oscillatory activity in human visuomotor integration.* Radboud University Nijmegen, Nijmegen, the Netherlands.
50. Scheeringa, R. (2011). *On the relation between oscillatory EEG activity and the BOLD signal.* Radboud University Nijmegen, Nijmegen, the Netherlands.
51. Bögels, S. (2011). *The role of prosody in language comprehension: When prosodic breaks and pitch accents come into play.* Radboud University Nijmegen, Nijmegen, the Netherlands.
52. Ossewaarde, L. (2011). *The mood cycle: Hormonal influences on the female brain.* Radboud University Nijmegen, Nijmegen, the Netherlands.
53. Kuribara, M. (2011). *Environment-induced activation and growth of pituitary melanotrope cells of Xenopus laevis.* Radboud University Nijmegen, Nijmegen, the Netherlands.
54. Helmich, R.C.G. (2011). *Cerebral reorganization in Parkinson's disease.* Radboud University Nijmegen, Nijmegen, the Netherlands.
55. Boelen, D. (2011). *Order out of chaos? Assessment and treatment of executive disorders in brain-injured patients.* Radboud University Nijmegen, Nijmegen, the Netherlands.
56. Koopmans, P.J. (2011). *fMRI of cortical layers.* Radboud University Nijmegen, Nijmegen, the Netherlands.
57. van der Linden, M.H. (2011). *Experience-based cortical plasticity in object category representation.* Radboud University Nijmegen, Nijmegen, the Netherlands.
58. Kleine, B.U. (2011). *Motor unit discharges - Physiological and diagnostic studies in ALS.* Radboud University Nijmegen Medical Centre, Nijmegen, the Netherlands.
59. Paulus, M. (2011). *Development of action perception: Neurocognitive mechanisms underlying children's processing of others' actions.* Radboud University Nijmegen, Nijmegen, the Netherlands.
60. Tieleman, A.A. (2011). *Myotonic dystrophy type 2. A newly diagnosed disease in the Netherlands.* Radboud University Nijmegen Medical Centre, Nijmegen, the Netherlands.
61. Van Leeuwen, T.M. (2011). *'How one can see what is not there': Neural mechanisms of grapheme-colour synaesthesia.* Radboud University Nijmegen, Nijmegen, the Netherlands.
62. Van Tilborg, I.A.D.A. (2011). *Procedural learning in cognitively impaired patients and its application in clinical practice.* Radboud University Nijmegen, Nijmegen, the Netherlands.

63. Bruinsma, I.B. (2011). *Amyloidogenic proteins in Alzheimer's disease and Parkinson's disease: Interaction with chaperones and inflammation.* Radboud University Nijmegen, Nijmegen, the Netherlands.
64. Voermans, N. (2011). *Neuromuscular features of Ehlers-Danlos syndrome and Marfan syndrome; expanding the phenotype of inherited connective tissue disorders and investigating the role of the extracellular matrix in muscle.* Radboud University Nijmegen Medical Centre, Nijmegen, the Netherlands.
65. Reelick, M. (2011). *One step at a time. Disentangling the complexity of preventing falls in frail older persons.* Radboud University Nijmegen Medical Centre, Nijmegen, the Netherlands.
66. Buur, P.F. (2011). *Imaging in motion. Applications of multi-echo fMRI.* Radboud University Nijmegen, Nijmegen, the Netherlands.
67. Schaefer, R.S. (2011). *Measuring the mind's ear: EEG of music imagery.* Radboud University Nijmegen, Nijmegen, the Netherlands.
68. Xu, L. (2011). *The non-preganglionic Edinger-Westphal nucleus: An integration center for energy balance and stress adaptation.* Radboud University Nijmegen, Nijmegen, the Netherlands.
69. Schellekens, A.F.A. (2011). *Gene-environment interaction and intermediate phenotypes in alcohol dependence.* Radboud University Nijmegen, Nijmegen, the Netherlands.
70. Van Marle, H.J.F. (2011). *The amygdala on alert: A neuroimaging investigation into amygdala function during acute stress and its aftermath.* Radboud University Nijmegen, Nijmegen, the Netherlands.
71. De Laat, K.F. (2011). *Motor performance in individuals with cerebral small vessel disease: An MRI study.* Radboud University Nijmegen Medical Centre, Nijmegen, the Netherlands.
72. Mädebach, A. (2011). *Lexical access in speaking: Studies on lexical selection and cascading activation.* Radboud University Nijmegen, Nijmegen, the Netherlands.
73. Poelmans, G.J.V. (2011). *Genes and protein networks for neurodevelopmental disorders.* Radboud University Nijmegen, Nijmegen, the Netherlands.
74. Van Norden, A.G.W. (2011). *Cognitive function in elderly individuals with cerebral small vessel disease. An MRI study.* Radboud University Nijmegen Medical Centre, Nijmegen, the Netherlands.
75. Jansen, E.J.R. (2011). *New insights into V-ATPase functioning: the role of its accessory subunit Ac45 and a novel brain-specific Ac45 paralog.* Radboud University Nijmegen, Nijmegen, the Netherlands.
76. Haaxma, C.A. (2011). *New perspectives on preclinical and early stage Parkinson's disease.* Radboud University Nijmegen Medical Centre, Nijmegen, the Netherlands.
77. Haegens, S. (2012). *On the functional role of oscillatory neuronal activity in the somatosensory system.* Radboud University Nijmegen, Nijmegen, the Netherlands.
78. van Barneveld, D.C.P.B.M. (2012). *Integration of exteroceptive and interoceptive cues in spatial localization.* Radboud University Nijmegen, Nijmegen, the Netherlands.
79. Spies, P.E. (2012). *The reflection of Alzheimer disease in CSF.* Radboud University Nijmegen Medical Centre, Nijmegen, the Netherlands.
80. Helle, M. (2012). *Artery-specific perfusion measurements in the cerebral vasculature by magnetic resonance imaging.* Radboud University Nijmegen, Nijmegen, the Netherlands.
81. Egetemeir, J. (2012). *Neural correlates of real-life joint action.* Radboud University Nijmegen, Nijmegen, the Netherlands.

82. Janssen, L. (2012). *Planning and execution of (bi)manual grasping.* Radboud University Nijmegen, Nijmegen, the Netherlands.
83. Vermeer, S. (2012). *Clinical and genetic characterisation of autosomal recessive cerebellar ataxias.* Radboud University Nijmegen Medical Centre, Nijmegen, the Netherlands.
84. Vrins, S. (2012). *Shaping object boundaries: Contextual effects in infants and adults.* Radboud University Nijmegen, Nijmegen, the Netherlands.
85. Weber, K.M. (2012). *The language learning brain: Evidence from second language and bilingual studies of syntactic processing.* Radboud University Nijmegen, Nijmegen, the Netherlands.
86. Verhagen, L. (2012). *How to grasp a ripe tomato.* Utrecht University, Utrecht, the Netherlands.
87. Nonkes, L.J.P. (2012). *Serotonin transporter gene variance causes individual differences in rat behaviour: For better and for worse.* Radboud University Nijmegen Medical Centre, Nijmegen, the Netherlands.
88. Joosten-Weyn Banningh, L.W.A. (2012). *Learning to live with Mild Cognitive Impairment: development and evaluation of a psychological intervention for patients with Mild Cognitive Impairment and their significant others.* Radboud University Nijmegen Medical Centre, Nijmegen, the Netherlands.
89. Xiang, HD. (2012). *The language networks of the brain.* Radboud University Nijmegen, Nijmegen, the Netherlands.
90. Snijders, A.H. (2012). *Tackling freezing of gait in Parkinson's disease.* Radboud University Nijmegen Medical Centre, Nijmegen, the Netherlands.
91. Rouwette, T.P.H. (2012). *Neuropathic pain and the brain - Differential involvement of corticotropin-releasing factor and urocortin 1 in acute and chronic pain processing.* Radboud University Nijmegen Medical Centre, Nijmegen, the Netherlands.
92. Van de Meerendonk, N. (2012). *States of indecision in the brain: Electrophysiological and hemodynamic reflections of monitoring in visual language perception.* Radboud University Nijmegen, Nijmegen, the Netherlands.
93. Sterrenburg, A. (2012). *The stress response of forebrain and midbrain regions: Neuropeptides, sex-specificity and epigenetics.* Radboud University Nijmegen, Nijmegen, The Netherlands.
94. Uithol, S. (2012). *Representing action and intention.* Radboud University Nijmegen, Nijmegen, The Netherlands.
95. Van Dam, W.O. (2012). *On the specificity and flexibility of embodied lexical-semantic representations.* Radboud University Nijmegen, Nijmegen, The Netherlands.
96. Slats, D. (2012). *CSF biomarkers of Alzheimer's disease: Serial sampling analysis and the study of circadian rhythmicity.* Radboud University Nijmegen Medical Centre, Nijmegen, the Netherlands.
97. Van Nuenen, B.F.L. (2012). *Cerebral reorganization in premotor parkinsonism.* Radboud University Nijmegen Medical Centre, Nijmegen, the Netherlands.
98. van Schouwenburg, M.R. (2012). *Fronto-striatal mechanisms of attentional control.* Radboud University Nijmegen, Nijmegen, The Netherlands.
99. Azar, M.G. (2012). *On the theory of reinforcement learning: Methods, convergence analysis and sample complexity.* Radboud University Nijmegen, Nijmegen, The Netherlands.
100. Meeuwissen, E.B. (2012). *Cortical oscillatory activity during memory formation.* Radboud University Nijmegen, Nijmegen, The Netherlands.

101. Arnold, J.F. (2012). *When mood meets memory: Neural and behavioral perspectives on emotional memory in health and depression.* Radboud University Nijmegen, Nijmegen, The Netherlands.
102. Gons, R.A.R. (2012). *Vascular risk factors in cerebral small vessel disease: A diffusion tensor imaging study.* Radboud University Nijmegen Medical Centre, Nijmegen, the Netherlands.
103. Wingbermühle, E. (2012). *Cognition and emotion in adults with Noonan syndrome: A neuropsychological perspective.* Radboud University Nijmegen, Nijmegen, The Netherlands.
104. Walentowska, W. (2012). *Facing emotional faces. The nature of automaticity of facial emotion processing studied with ERPs.* Radboud University Nijmegen, Nijmegen, The Netherlands.
105. Hoogman, M. (2012). *Imaging the effects of ADHD risk genes.* Radboud University Nijmegen, Nijmegen, The Netherlands.
106. Tramper, J. J. (2012). *Feedforward and feedback mechanisms in sensory motor control.* Radboud University Nijmegen, Nijmegen, The Netherlands.
107. Van Eijndhoven, P. (2012). *State and trait characteristics of early course major depressive disorder.* Radboud University Nijmegen Medical Centre, Nijmegen, the Netherlands.
108. Visser, E. (2012). *Leaves and forests: Low level sound processing and methods for the large-scale analysis of white matter structure in autism.* Radboud University Nijmegen, Nijmegen, The Netherlands.
109. Van Tooren-Hoogenboom, N. (2012). *Neuronal communication in the synchronized brain. Investigating the functional role of visually-induced gamma band activity: Lessons from MEG.* Radboud University Nijmegen, Nijmegen, The Netherlands.
110. Henckens, M.J.A.G. (2012). *Imaging the stressed brain. Elucidating the time- and region-specific effects of stress hormones on brain function: A translational approach.* Radboud University Nijmegen, Nijmegen, The Netherlands.
111. Van Kesteren, M.T.R. (2012). *Schemas in the brain: Influences of prior knowledge on learning, memory, and education.* Radboud University Nijmegen, Nijmegen, The Netherlands.
112. Brenders, P. (2012). *Cross-language interactions in beginning second language learners.* Radboud University Nijmegen, Nijmegen, The Netherlands.
113. Ter Horst, A.C. (2012). *Modulating motor imagery. Contextual, spatial and kinaesthetic influences.* Radboud University Nijmegen, Nijmegen, The Netherlands.
114. Tesink, C.M.J.Y. (2013). *Neurobiological insights into language comprehension in autism: Context matters.* Radboud University Nijmegen, Nijmegen, The Netherlands.
115. Böckler, A. (2013). *Looking at the world together. How others' attentional relations to jointly attended scenes shape cognitive processing.* Radboud University Nijmegen, Nijmegen, The Netherlands.
116. Van Dongen, E.V. (2013). *Sleeping to Remember. On the neural and behavioral mechanisms of sleep-dependent memory consolidation.* Radboud University Nijmegen, Nijmegen, The Netherlands.
117. Volman, I. (2013). *The neural and endocrine regulation of emotional actions.* Radboud University Nijmegen, Nijmegen, The Netherlands.
118. Buchholz, V. (2013). *Oscillatory activity in tactile remapping.* Radboud University Nijmegen, Nijmegen, The Netherlands.

119. Van Deurzen, P.A.M. (2013). *Information processing and depressive symptoms in healthy adolescents*. Radboud University Nijmegen, Nijmegen, The Netherlands.
120. Whitmarsh, S. (2013). *Nonreactivity and metacognition in mindfulness*. Radboud University Nijmegen, Nijmegen, The Netherlands.
121. Vesper, C. (2013). *Acting together: Mechanisms of intentional coordination.* Radboud University Nijmegen, Nijmegen, The Netherlands.
122. Lagro, J. (2013). *Cardiovascular and cerebrovascular physiological measurements in clinical practice and prognostics in geriatric patients*. Radboud University Nijmegen Medical Centre, Nijmegen, the Netherlands.
123. Eskenazi, T.T. (2013). *You, us & them: From motor simulation to ascribed shared intentionality in social perception*. Radboud University Nijmegen, Nijmegen, The Netherlands.
124. Ondobaka, S. (2013). *On the conceptual and perceptual processing of own and others' behavior*. Radboud University Nijmegen, Nijmegen, The Netherlands.
125. Overvelde, J.A.A.M. (2013). *Which practice makes perfect? Experimental studies on the acquisition of movement sequences to identify the best learning condition in good and poor writers*. Radboud University Nijmegen, Nijmegen, The Netherlands.
126. Kalisvaart, J.P. (2013). *Visual ambiguity in perception and action*. Radboud University Nijmegen Medical Centre, Nijmegen, The Netherlands.
127. Kroes, M. (2013). *Altering memories for emotional experiences*. Radboud University Nijmegen, Nijmegen, The Netherlands.
128. Duijnhouwer, J. (2013). *Studies on the rotation problem in self-motion perception*. Radboud University Nijmegen, Nijmegen, The Netherlands.
129. Nijhuis, E.H.J (2013). *Macroscopic networks in the human brain: Mapping connectivity in healthy and damaged brains*. University of Twente, Enschede, The Netherlands
130. Braakman, M. H. (2013). *Posttraumatic stress disorder with secondary psychotic features. A diagnostic validity study among refugees in the Netherlands*. Radboud University Nijmegen, Nijmegen, The Netherlands.
131. Zedlitz, A.M.E.E. (2013). *Brittle brain power. Post-stroke fatigue, explorations into assessment and treatment*. Radboud University Nijmegen, Nijmegen, The Netherlands.
132. Schoon, Y. (2013). *From a gait and falls clinic visit towards self-management of falls in frail elderly*. Radboud University Nijmegen Medical Centre, Nijmegen, The Netherlands.
133. Jansen, D. (2013). *The role of nutrition in Alzheimer's disease - A study in transgenic mouse models for Alzheimer's disease and vascular disorders*. Radboud University Nijmegen, Nijmegen, The Netherlands.
134. Kos, M. (2013). *On the waves of language - Electrophysiological reflections on semantic and syntactic processing*. Radboud University Nijmegen, Nijmegen, The Netherlands.
135. Severens, M. (2013). *Towards clinical BCI applications: Assistive technology and gait rehabilitation*. Radboud University Nijmegen, Nijmegen, Sint Maartenskliniek, Nijmegen, The Netherlands.
136. Bergmann, H. (2014). *Two is not always better than one: On the functional and neural (in)dependence of working memory and long-term memory*. Radboud University Nijmegen, Nijmegen, The Netherlands.
137. Wronka, E. (2013). *Searching for the biological basis of human mental abilitites. The relationship between attention and intelligence studied with P3*. Radboud University Nijmegen, Nijmegen, The Netherlands.

138. Lüttjohann, A.K. (2013). *The role of the cortico-thalamo-cortical system in absence epilepsy.* Radboud University Nijmegen, Nijmegen, The Netherlands.
139. Brazil, I.A. (2013). *Change doesn't come easy: Dynamics of adaptive behavior in psychopathy.* Radboud University Nijmegen, Nijmegen, The Netherlands.
140. Zerbi, V. (2013). *Impact of nutrition on brain structure and function. A magnetic resonance imaging approach in Alzheimer mouse models.* Radboud University Nijmegen, Nijmegen, The Netherlands.
141. Delnooz, C.C.S. (2014). *Unravelling primary focal dystonia. A treatment update and new pathophysiological insights.* Radboud University Nijmegen Medical Centre, Nijmegen, The Netherlands.
142. Bultena, S.S. (2013). *Bilingual processing of cognates and language switches in sentence context.* Radboud University Nijmegen, Nijmegen, The Netherlands.
143. Janssen, G. (2014). *Diagnostic assessment of psychiatric patients: A contextual perspective on executive functioning.* Radboud University Nijmegen, Nijmegen, The Netherlands.
144. Piai, V. Magalhães (2014). *Choosing our words: Lexical competition and the involvement of attention in spoken word production.* Radboud University Nijmegen, Nijmegen, The Netherlands.
145. Van Ede, F. (2014). *Preparing for perception. On the attentional modulation, perceptual relevance and physiology of oscillatory neural activity.* Radboud University Nijmegen, Nijmegen, The Netherlands.
146. Brandmeyer, A. (2014). *Auditory perceptual learning via decoded EEG neurofeedback: a novel paradigm.* Radboud University Nijmegen, Nijmegen, The Netherlands.
147. Radke, S. (2014). *Acting social: Neuroendocrine and clinical modulations of approach and decision behavior.* Radboud University Nijmegen, Nijmegen, The Netherlands.
148. Simanova, I. (2014). *In search of conceptual representations in the brain: towards mind-reading.* Radboud University Nijmegen, Nijmegen, The Netherlands.
149. Kok, P. (2014). *On the role of expectation in visual perception: A top-down view of early visual cortex.* Radboud University Nijmegen, Nijmegen, The Netherlands.
150. Van Geldorp, B. (2014). *The long and the short of memory: Neuropsychological studies on the interaction of working memory and long-term memory formation.* Radboud University Nijmegen, Nijmegen, The Netherlands.
151. Meyer, M. (2014). *The developing brain in action - Individual and joint action processing.* Radboud University Nijmegen, Nijmegen, The Netherlands.
152. Wester, A. (2014). *Assessment of everyday memory in patients with alcohol-related cognitive disorders using the Rivermead Behavioural Memory Test.* Radboud University Nijmegen, Nijmegen, The Netherlands.
153. Koenraadt, K. (2014). *Shedding light on cortical control of movement.* Radboud University Nijmegen, Nijmegen; Sint Maartenskliniek, Nijmegen, The Netherlands.
154. Rutten-Jacobs, L.C.A. (2014). *Long-term prognosis after stroke in young adults.* Radboud University Nijmegen Medical Centre, Nijmegen, The Netherlands.
155. Herbert, M.K. (2014). *Facing uncertain diagnosis: the use of CSF biomarkers for the differential diagnosis of neurodegenerative diseases.* Radboud University Nijmegen Medical Centre, Nijmegen, The Netherlands.
156. Llera Arenas, A. (2014). *Adapting brain computer interfaces for non-stationary changes.* Radboud University Nijmegen, Nijmegen, The Netherlands.

157. Smulders, K. (2014). *Cognitive control of gait and balance in patients with chronic stroke and Parkinson's disease.* Radboud University Nijmegen Medical Centre, Nijmegen, The Netherlands.

158. Boyacioglu, R. (2014). *On the application of ultra-fast fMRI and high resolution multiband fMRI at high static field strengths.* Radboud University Nijmegen, Nijmegen, The Netherlands.

159. Kleinnijenhuis, M. (2014). *Imaging fibres in the brain.* Radboud University Nijmegen, Nijmegen, The Netherlands.

160. Geuze, J. (2014). *Brain Computer Interfaces for Communication: Moving beyond the visual speller.* Radboud University Nijmegen, Nijmegen, The Netherlands.

161. Platonov, A. (2014). *Mechanisms of binocular motion rivalry.* Radboud University Nijmegen, Nijmegen, The Netherlands.

162. Van der Schaaf, M.E. (2014). *Dopaminergic modulation of reward and punishment learning.* Radboud University Nijmegen Medical Centre, Nijmegen, The Netherlands.

163. Aerts, M.B. (2014). *Improving diagnostic accuracy in parkinsonism.* Radboud University Nijmegen Medical Centre, Nijmegen, The Netherlands.

164. Vlek, R. (2014). *From Beat to BCI: A musical paradigm for, and the ethical aspects of Brain-Computer Interfacing.* Radboud University Nijmegen, Nijmegen, The Netherlands.

165. Massoudi, R. (2014). *Interaction of task-related and acoustic signals in single neurons of monkey auditory cortex.* Radboud University Nijmegen, Nijmegen, The Netherlands

166. Stolk, A. (2014). *On the generation of shared symbols.* Radboud University Nijmegen, Nijmegen, The Netherlands.

167. Krause F. (2014). *Numbers and magnitude in the brain: A sensorimotor grounding of numerical cognition.* Radboud University Nijmegen, Nijmegen, The Netherlands.

168. Munneke, M.A.M. (2014). *Measuring and modulating the brain with non-invasive stimulation.* Radboud University Nijmegen Medical Centre, Nijmegen, The Netherlands.

169. Von Borries, K. (2014). *Carrots & Sticks - a neurobehavioral investigation of affective outcome processing in psychopathy.* Radboud University Nijmegen Medical Centre, Nijmegen, The Netherlands.

170. Meel-van den Abeelen, A.S.S. (2014). *In control. Methodological and clinical aspects of cerebral autoregulation and haemodynamics.* Radboud University Nijmegen Medical Centre, Nijmegen, The Netherlands.

171. Leoné, F.T.M. (2014). *Mapping sensorimotor space: Parieto-frontal contributions to goal-directed movements.* Radboud University Nijmegen, Nijmegen, The Netherlands.

172. Van Kessel, M. (2014). *Nothing left? How to keep on the right track - Spatial and non-spatial attention processes in neglect after stroke.* Radboud University, Nijmegen, The Netherlands.

173. Vulto-van Silfhout, A. T. (2014). *Detailed, standardized and systematic phenotyping for the interpretation of genetic variation.* Radboud University Medical Centre, Nijmegen, The Netherlands.

174. Arnoldussen, D. (2015). *Cortical topography of self-motion perception.* Radboud University, Nijmegen, The Netherlands.

175. Meyer, M.C. (2015). "*Inbetween Modalitiers combined EEG – fMR*". Radboud University, Nijmegen, The Netherlands.

176. Bralten, J. (2015). *Genetic factors and the brain in ADHD.* Radboud university medical center, Nijmegen, The Netherlands.

177. Spaak, E. (2015). *On the role of alpha oscillations in structuring neural information processing.* Radboud University, Nijmegen, The Netherlands.
178. Van der Doelen, R. (2015). *Translational psychiatry; the twists and turns of early life stress and serotonin transporter gene variation.* Radboud university medical center, Nijmegen, The Netherlands.
179. Lewis, C. (2015). *The structure and function of intrinsic brain activity.* Radboud University, Nijmegen, The Netherlands.
180. Huang, Lili. (2015). *The subiculum: a promising new target of deep brain stimulation in temporal lobe epilepsy. Investigation of closed-loop and open-loop high frequency stimulation of the subiculum in seizure and epilepsy models in rats.* Radboud University, Nijmegen, The Netherlands.
181. Maaijwee, N.A.M.M (2015). *Long-term neuropsychological and social consequences after stroke in young adults.* Radboud university medical center, Nijmegen, The Netherlands.
182. Meijer, F.J.A. (2015). *Clinical Application of Brain MRI in Parkinsonism: From Basic to Advanced Imaging.* Radboud university medical center, Nijmegen, The Netherlands.
183. Van der Meij, R. (2015). *On the identification, characterization and investigation of phase dependent coupling in neuronal networks.* Radboud University, Nijmegen, The Netherlands.
184. Todorovic, A. (2015). *Predictive adaptation in early auditory processing.* Radboud University, Nijmegen, The Netherlands.
185. Horschig, J.M. (2015). *Flexible control and training of posterior alpha-band oscillations.* Radboud University, Nijmegen, The Netherlands.
186. Vogel, S. (2015). *The runner-up: on the role of the mineralocorticoid receptor in human cognition.* Radboud University Medical Center, Nijmegen, The Netherlands.
187. Clemens, I.A.H. (2015). *Multisensory integration in orientation and self-motion perception.* Radboud University, Nijmegen, The Netherlands.
188. Nonnekes, J. (2015). *Balance and gait in neurodegenerative disease: what startle tells us about motor control.* Radboud university medical center, Nijmegen, The Netherlands.
189. Stapel, J.C. (2015). *Action prediction and the development thereof.* Radboud University, Nijmegen, The Netherlands.
190. De Grauwe, S. (2015). *The Processing of Derivations in Native and Non-Native Speakers of Dutch.* Radboud University, Nijmegen, The Netherlands.
191. Atucha Treviño, E. (2015). *Emotional Modulation of Memory: Mechanisms underlying strength and accuracy of Memory.* Radboud University, Nijmegen, The Netherlands
192. Bosch, M.P.C. (2015) *Needles on the Couch; acupuncture in the Treatment of Depression, Schizophrenia and Sleep Disorders.* Radboud University, Nijmegen, The Netherlands.
193. Marshall, T. (2015) *On the Control and manipulation of Alpha and Gamma oscillations in visual cortex.* Radboud University, Nijmegen, The Netherlands.
194. Rijken, N. (2015). *Balance and gait in facioscapulohumeral muscular dystrophy, relations with individual muscle involvement.* Radboud University Medical Center, Nijmegen, The Netherlands.
195. Blokpoel, M. (2015). *Understanding understanding: A computational-level perspective.* Radboud University, Nijmegen, The Netherlands.
196. Smyk, M. (2015). *Chronobiology of absence epilepsy.* Radboud University, Nijmegen, The Netherlands.
197. Richards, J. (2015). *Plasticity genes, the social environment, and their interplay in adolescents with and without ADHD – from behaviour to brain.* Radboud University Medical Center, Nijmegen, The Netherlands.

198. Janssen, C. (2015). *Nourishing the brain from cradle to grave: The role of nutrients in neural development and neurodegeneration.* Radboud University Medical Center, Nijmegen, The Netherlands.
199. Bertens, D. (2016). *Doin' it right: Assessment and errorless learning of executive skills after brain injury.* Radboud University, Nijmegen, The Netherlands.
200. Blokland, Y. M. (2015). *Moving towards awareness detection: From Brain-Computer Interfacing to anaesthesia monitoring.* Radboud University, Nijmegen, The Netherlands.
201. Lozano-Soldevilla, D. (2015). *GABAergic modulations of gamma and alpha oscillations: consequences for working memory performance.* Radboud University, Nijmegen, The Netherlands.
202. Bosch, S. E. (2015). *Reactivating memories in hippocampus and neocortex.* Radboud University, Nijmegen, The Netherlands.
203. Rhein von, D. (2015). *Neural mechanisms of reward processing in attention deficit hyperactivity disorder.* Radboud University, Nijmegen, The Netherlands/ Radboud University Medical Center, Nijmegen, The Netherlands.
204. Jiang, H. (2015). *Characterizing brain oscillations in cognition and disease.* Radboud University, Nijmegen, The Netherlands
205. Francken, J (2016). *Viewing the world through language-tinted glasses.* Radboud University, Nijmegen, The Netherlands
206. Sarwary, A.M.E. (2016). *Mechanisms of interference between motor memories.* Radboud University, Nijmegen, The Netherlands/ Radboud University Medical Center, Nijmegen, The Netherlands.
207. Vermeij, A. (2016). *Cognitive plasticity in normal aging and mild cognitive impairment: Shedding light on prefrontal activation.* Radboud University Medical Center, Nijmegen, The Netherlands.
208. Van den Elsen, G.A.H. (2016). *Tetrahydrocannabinol in the treatment of neuropsychiatric symptoms in dementia.* Radboud University Medical Center, Nijmegen, The Netherlands.
209. Ly, V. (2016). *Affective biasing of instrumental action: How emotion shapes behaviour.* Radboud University, Nijmegen, The Netherlands/ Radboud University Medical Center, Nijmegen, The Netherlands.
210. Brinkman, L. (2016). *A rhythmic view on the neurophysiological mechanisms of movement selection.* Radboud University, Nijmegen, The Netherlands.
211. Bouman Z. (2016). A measure to remember: Adaptation, standardization and validation of the Dutch version of the Wechsler Memory Scale - Fourth Edition (WMS-IV-NL). Radboud University, Nijmegen, The Netherlands/ Radboud University Medical Center, Nijmegen, The Netherlands.
212. Spronk, D.B. (2016). *Individual differences in the acute effects of cannabis and cocaine on cognitive control.* Radboud University Nijmegen Medical Center, Nijmegen, The Netherlands.
213. Müller, M. (2016). *Footprints of Alzheimer's disease. Exploring proteins and microRNAs as biomarkers for differential diagnosis.* Radboud University Medical Center, Nijmegen, The Netherlands.
214. Ekman, M. (2016). *Dynamic Reconfigurations in Human Brain Networks.* Radboud University, Nijmegen, The Netherlands.
215. Vollebregt, M.A. (2016). *Neuronal oscillations in children with ADHD. A journey towards the development of potential new treatments for children with ADHD.* Radboud University,

Nijmegen, The Netherlands/ Radboud University Medical Center, Nijmegen, The Netherlands.

216. Bruggink, K. (2016). *Amyloid-beta and amyloid associated proteins in the pathogenesis and diagnosis of Alzheimer's Disease.* Radboud University Medical Center, Nijmegen, The Netherlands or Radboud University Medical Center, Nijmegen, The Netherlands.
217. Van Os, N. (2016). *Role of the amygdala in chromatin remodeling effects underlying long-term memory. Radboud University Medical Center, Nijmegen, The Netherlands or Radboud University Medical Center, Nijmegen, The Netherlands.*
218. Kostermans, E. (2016). *Risky decision making: individual differences and dynamic aspects of real-life risk situations. Radboud University Medical Center, Nijmegen, The Netherlands or Radboud University Medical Center, Nijmegen, The Netherlands.*
219. Bosga-Stork, I.M. (2016). *A longitudinal study of preparatory handwriting: Developing efficiency in motor control.* Radboud University, Nijmegen, The Netherlands
220. Huang, C. (2016). *Cortical representation of touch: from whole-cell recordings to network simulations in silico.* Radboud University, Nijmegen, The Netherlands.